Screening of molluscan extrapallial proteins on $CaCO_3$ crystallisation *via* microfluidics

by
Bozhi Ji

Thesis submitted for the degree of Doctor of Philosophy (Ph.D.)

College of Science and Engineering
School of Geographical & Earth Sciences
School of Chemistry
School of Engineering

December-2011

Abstract

Many living systems produce mineral materials *via* organic-inorganic interactions; through a process known as biomineralisation. The formation of all biomineral structures is under exquisite biological control, concerning crystal morphology, polymorph selection and crystal orientation. The common blue mussel *Mytilus edulis* produces a shell structure composed of heterogeneous calcium carbonate polymorphs: an outer layer of prismatic calcite and an inner layer of aragonite nacre. The extrapallial (EP) fluid, confined to the space between the organic mantle and inner shell, is considered to be a key participant during shell growth. The existence of both organic components i.e. proteins, glycoproteins and inorganic ions in the extrapallial fluid supports such a hypothesis of functional involvement.

This study screens the influence of extrapallial (EP) proteins from *M. edulis* on *in vitro* crystallisation in the laminar flow microfluidic system. In laminar flow microfluidic systems, mass exchange between adjacent streams is driven by diffusion. This principle provides opportunities to simultaneously screen protein influences in a range of scenarios by mixing with different reagents. In addition, the combination of computational modelling and real-time crystallisation demonstrates the major influence of the microenvironment on crystal formation along microfluidic channels. The simulation of protein and ion concentration profiles, as well as the supersaturation ratio, contributes to our understanding of protein influence on crystal morphology and polymorph control.

In order to identify the influence of EP proteins on crystallisation, the total wild-type extrapallial (TWEP) proteins were initially used to produce oval calcite crystals. For further investigation, individual purified proteins were used to modify crystallisation, including the wild-type proteins directly extracted from living mussels and the expressed proteins provided from an *E.coli* expression system. Novel lemon-shaped structures precipitated in the microfluidic channel when the main wild-type 28 kDa extrapallial protein was mixed with $CaCl_2$ solution only. Similar structures were also generated in microfluidic channel with the expressed proteins in either $CaCl_2$ solution only or both reagent solutions. Multilayer calcite structures were induced in the microfluidic channel in the presence of biomineral proteins, mixed with Na_2CO_3 solution only. All of these results suggest that the extrapallial proteins influence $CaCO_3$ crystallisation.

Microcontact printing (μCP) has been used to create two-dimensional protein and polymer patterns for *in vitro* crystallisation. Polyacrylic acid (PAA) has been used as polymer patterns

to control $CaCO_3$ crystal formation, including precipitation and morphology. Calcite crystals, composed of nano-blocks, are the only structures precipitated in the patterned regions while PAA and calcium ions are both printed on the substrates. Although encouraging, further work is required to fully establish the protocol for protein patterning as a means of screening biomineral protein function.

Acknowledgements

This thesis would not have been finished without the help and support from many people. I am grateful to Lord Kelvin Adam Smith (LKAS) scholarship from the University of Glasgow for fully funding this four-year PhD project.

Many thanks to Prof. Maggie Cusack, Dr Huabing Yin and Dr Andy Freer, without their advice, patience and supervision, this would have been a much tougher project. I am also thankful to Dr Phil Dobson and Dr Nikolaj Gadegaard since they contributed knowledge and suggestions in their areas to this interdisciplinary work. Special thanks to Dr Jiahong Jiang and Dr Khedidja Mosbahi for their work on protein purification and supplement. Furthermore, thanks to Peter Chung for his assistance on SEM and EDS work on my samples.

Considerable mentions should also be given to many of the technical staff who have always been on hand and assist with queries and the inevitable equipment malfunctions. A great thanks to the James Watt Nanofabrication Centre (JWNC) staff for the help on the whole microfabrication process, especially to Mary Robertson for the training and help on SEM. I would thank all staff and research students in Biomedical Engineering in Jon Cooper's group who helped me during my PhD research. Special thanks to Dr Andrew Glidle who helped me on the initial setting of microfluidic system and modelling calculations, as well as Dr Norbet Klauke for his help on confocal microscope and Raman spectroscopy.

Finally, I would thank those who are most important to me and provide their support for me not just in this project: my Dad and Mum, brother and girlfriend.

Table of contents

List of figures

List of tables

Abbreviations:

ACC	amorphous calcium carbonate
BSA	bovine serum albumin
CBP	calcium-binding protein
CD	circular dichroism
EDTA	ethylenediaminetetraacetic acid
EDS	energy dispersive spectroscopy
EEP	expressed main extrapallial fluid protein
EP	extrapallial fluid
EST	expressed sequencing tag
FITC	Fluorescein isothiocyanate
GC	gas chromatography
HPLC	high pressure liquid chromatography
OMM	organic matrix mediating
PAA	polyacrylic acid
PDMS	Polydimethylsiloxane
P_e	Peclet number
PILP	polymer induced liquid precursor
Poly-Asp	poly aspartic acid
RACE	rapid amplification of cDNA ends
R_e	Reynolds number
RNAi	RNA interference
RT-PCR	reverse transcription polymerase chain reaction
SAMs	self-assembled monolayers
SDS-PAGE	sodium dodecyl sulfate polyacrylamide gel eletrophoresis
SEM	scanning electron microscope
TEM	transmission electron microscope
TWEP	total wild-type extrapallial fluid proteins
UV	Ultra violet
WEP	wild-type main extrapallial fluid protein
WCEP	wild-type extrapallial fluid complex proteins

μCP	microcontact printing
μTAS	micro total analysis system

Chapter 1

General introduction

1

1.1 Biomineralisation

For 550 million years, living systems have evolved to have exquisite control in mineral formation, enabling precise morphology and crystal orientation (Addadi and Weiner, 1992). There are more than 60 minerals produced in the biosphere, including amorphous minerals and inorganic crystals (Lowenstam, 1981, Lowenstam and Weiner, 1989). Early on in evolution, a major schism occurred with calcium phosphate forming the internal skeleton of vertebrates and calcium carbonate utilized for the external protective structures in invertebrates (Lowenstam and Weiner, 1989, Cusack and Freer, 2008). This phenomenon was induced by different biochemical and cellular processes engaged in the processes of vertebrates utilizing phosphate and invertebrates utilizing carbonate (Costa and Maquis, 1998, Weiner and Wagner, 1998, Mann, 2001, Weiner and Dove, 2003). In addition, other minerals such as magnetite and silica have been deposited by bacteria (Konhauser, 1998, Theil et al., 2006). The phenomenon of these mineral structures forming with organic materials is biomineralisation, the synthetic process of hierarchical mineral structures produced by living organisms in ambient conditions (Mann, 2001, Cusack and Freer, 2008).

Biomineral materials provide a variety of functions in living organisms. In invertebrates, the biomineral structures support and protect the inner bodies. For example, shells provide support and protection for the soft tissues of bivalves (Addadi and Weiner, 1992), oysters (MacDonald et al., 2010) and brachiopods (Pérez-Huerta et al., 2009). Avian eggshells, a composite structure of calcite in associated with organic components, provide protection for the developing embryos (Cusack et al., 2003, Dalbeck and Cusack, 2006). In addition, internal support from biominerals is found in vertebrates (Cusack et al., 2003, Nys et al., 2004). In vertebrates, bones have two major functions: the mechanical function of supporting various organs and metabolic function of serving as a conserver of calcium and phosphate for metabolism (Weiner and Wagner, 1998, Weiner et al., 1999, Nudelman et al., 2010).

There are other functions directly or indirectly related to biomineral materials. An example is

the membrane-enclosed magnetite crystal used uniquely by magnetotactic bacteria to navigate using the Earth's magnetic field (Scheffel et al., 2006). Another example is the calcite micro lenses of brittlestars, which acts as the optical elements regulating the light inside to the tissue (Aizenberg et al., 2001). In fish, the otolith is a calcified structure composed mainly of calcium carbonate, which is formed in the inner ear and participates in balance functions. (Murayama et al., 2002). In coccolithophorids, calcium carbonate plates (coccoliths) surround single algae cells and may provide protection for the inner cell from harmful UV light (Gauldie, 1996).

Biomineral formation can be considered in two classes (Lowenstam and Weiner, 1989, Weiner and Dove, 2003). Biominerals can be produced from the biologically-induced mineralisation, which has little biological control on precipitated minerals (Lowenstam and Weiner, 1989). In this process, minerals are induced by the environments employed by the biological metabolic process, such as pH and the increasing pressure of carbon dioxide (pCO_2) (Dove et al., 2003, Frankel and Bazylinski, 2003). Biogenic iron and manganese are common products from biologically induced mineralisation process. Fe- and Mn-oxidising bacteria are responsible for the precipitation of oxides of both metal, with oxidised Fe(III) and Mn(IV) are soluble and active mineralisation by organism at low pH (Frankel and Bazylinski, 2003).

However, thoroughly precise biological control is required to produce specific biomineral structures. This is biologically-controlled mineralisation (Lowenstam and Weiner, 1989). One distinctive aspect of biologically-controlled mineralisation is the spatial determination, which provides the crystal growing sites (Wilbur and Saleuddin, 1983, Dove et al., 2003, Frankel and Bazylinski, 2003). Spatial control is provided by the pre-existence of an organic matrix template. A good example is the nacre formation in molluscan shells, which is under control of the existing organic components (Nudelman et al., 2006). The mineralisation is not progressed until the ion concentrations are saturated in aqueous conditions. The possible mechanism is that cells control the ion concentrations, thereafter to modify the crystal nucleation and growth. Moreover, the crystal morphological modification is associated with the acidic proteins existing in the organic matrix (Lowenstam and Weiner, 1989, Nudelman et al., 2006). Thus, the biologically-controlled mineralisation demonstrates the vital correlation between the organic components and specific inorganic structures. As a consequence, the biomineral materials consist of both organic and inorganic components.

1.2 Mollusc shell structure

Mollusc shells are composed of calcium carbonate crystals (95%-99%) and organic component (less than 5%) (Weiner and Traub, 1984, Gotliv et al., 2003, Hou and Feng, 2006). Mollusc shells have different microstructures comprising one or two calcium carbonate polymorphs, calcite and aragonite (Weiss et al., 2002, Gotliv et al., 2003). Some bivalves such as oyster gastropod *Haliotis laevigata* and mollusc *Mytilus edulis* produce bimineralic shells with calcite prisms and aragonite nacre (England et al., 2007, De Paula and Silveira, 2009). Some bivalves produce only aragonite as both prism and nacre in a single shell, such as the freshwater mussels *Anodonta anatina* and *Anodonta cygnea* (Freer et al., 2009). On the other hand, the shell of the horse mussel, *Modiolus modiolus*, is almost entirely constructed of aragonite. However, here two forms of aragonite are present: prisms and nacre (Cusack et al., 2008).

Calcite (Figure 1.1A) is the most thermodynamically stable calcium carbonate polymorph in nature. Calcite crystals exist in a variety of morphologies, including rhombohedral, tabular, fibrous and prismatic (Feng et al., 2000, Hou and Feng, 2006, Li and Estroff, 2007b, Feng et al., 2009). Compared to calcite, aragonite is a less thermodynamically stable polymorph. The aragonite crystal lattice has a different crystal shape, an orthorhombic system with acicular structure, which creates a stronger crack resistant structure (Figure 1.1B) (De Villiers J. P. R., 1971). Aragonite forms more readily at elevated temperatures (>60 °C) in inorganic conditions without any additive (Dandeu et al., 2006). However, aragonite forms in the mollusc shell as nacre, mother of pearl, under ambient conditions as a result of biological control (Falini et al., 1996, Hou and Feng, 2006, Nudelman et al., 2006).

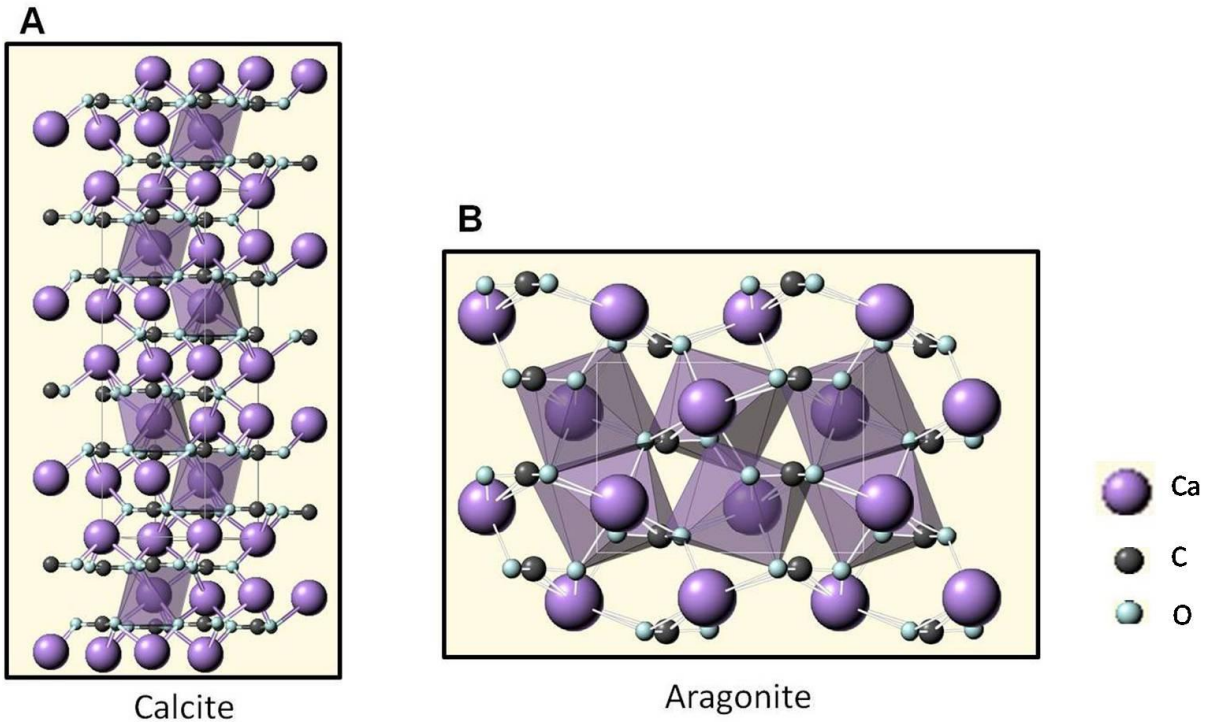

Figure 1.1. Schematic crystal structures of calcite and aragonite.

(A) Calcite and (B) Aragonite. Both are from Mineralogy Database.

The common blue marine mussel *Mytilus edulis* (Figure 1.2A) produces a bimineralic shell with an outer layer of prismatic calcite and an inner layer of aragonite nacre (Figure 1.2B) (Cusack et al., 2009). In natural conditions, a tough organic layer, the periostracum, covers the outside surface of the shell. The periostracum serves as a substrate on which mineralisation is initiated (Lowenstam and Weiner, 1989). The shell of *M. edulis* is ~98% by weight calcium carbonate, and the residual comprises organic material (Lowenstam and Weiner, 1989, Cusack and Freer, 2008).

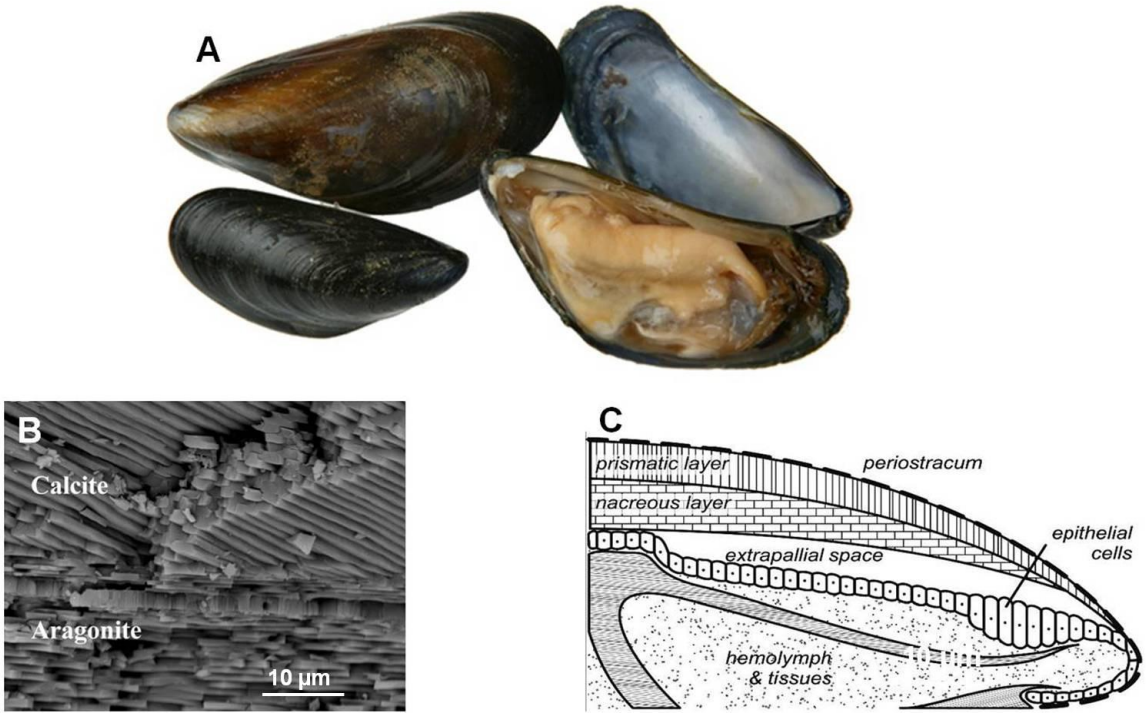

Figure 1.2. Shell structure of mussel *M. edulis*.

(A) The common blue mussel *M. edulis* has an external shell cover by organic periostracum. (B) The mollusc shell of *M. edulis* is composed of two $CaCO_3$ polymorphs, calcite in the outer layers and aragonite in the inner layer (Cusack and Freer, 2008). (C) Schematic diagram of transverse section of the mantle edge of a bivalve (Behrens and Baeuerlein, 2007).

1.2.1 Organic components

Organic macromolecules are associated with the formation of most biomineral structures, and they play a critical function in the control of mineralisation (Addadi and Weiner, 1992, Marin and Luquet, 2004, Nudelman et al., 2006, Saavedra and Bachère, 2006, Cartwright and Checa, 2007). According to the procedures of demineralisation using weak acids such as acetic acid or with a calcium-chelating agent like ethylenediaminetetraacetic acid (EDTA), the macromolecules can be divided into two subgroups; soluble and insoluble fractions (Lowenstam and Weiner, 1989, Marin and Luquet, 2005). The demineralisation process using EDTA was established in the 1980s and applied in the analysis of shell organic matrix proteins involved in biomineralisation by dissolving shell powder in 10% EDTA disodium salt dehydrate solution (pH 8) to separate organic matrix from inorganic crystals (Wheeler et al., 1987, Pereira-Mouriès et al., 2002).

In biomineral structures, the insoluble macromolecules are normally cross-linked and hydrophobic, namely framework hydrophobic macromolecules (Dove et al., 2003). These

hydrophobic organic components provide the template for mineralisation and protection of existing inorganic structures from degradation in aqueous conditions (Lowenstam and Weiner, 1989). This structural support and functional protection is determined by an inter-crystalline matrix (Weiner and Traub, 1984, Lowenstam and Weiner, 1989, Nudelman et al., 2007). The existing organic matrix framework in mollusc shells is spatially related to control mineral nucleation. Amino acid analysis shows that the protein nacre matrix is composed of silk-fibroin like proteins (Weiner and Wagner, 1998, Weiner et al., 1999, Weiner and Dove, 2003). The assembly of molluscan nacre induces the insoluble framework which is composed with chitin and hydrophobic proteins (Addadi and Weiner, 1992, Nudelman et al., 2006).

With respect to the soluble organic components, many shell proteins have been identified rich in aspartic acid. In addition, some of these molecules have covalently bound polysaccharides, classing them as glycoproteins (Chen et al., 1997, Zhang et al., 2003, Sarashina and Endo, 2006). These hydrophilic acidic proteins are proposed to fulfil several functions in biomineralisation, such as the control of crystal polymorph and morphology (Wilbur and Saleuddin, 1983, Weiss et al., 2002). This hypothesis has been confirmed by *in vitro* crystallisation experiments using shell matrix acidic proteins for crystal morphology and polymorph control (Falini et al., 1996, Belcher et al., 1996, Takeuchi et al., 2008, Feng et al., 2009). Pif, an acidic matrix protein form pearl oyster *Pinctada fucata* binds to aragonite layers only during *in vitro* crystallisation (Suzuki et al., 2009). Moreover, the *in vitro* experiments have determined that the calcite morphological modification and step-specific multilayer structures can be induced by the specific nacre protein, AP8 (De Yoreo and Dove, 2004).

Recently, there have been several reviews highlighting the diversity and function of many of the shell matrix proteins. Marin *et al.* (2008) classified 44 mollusc shell matrix proteins based on their isoelectric point. That approach divided the matrix proteins into three major groups according to their pI: the extremely acidic proteins, moderately acidic proteins and basic shell proteins. On a broader sense Marin and Luquet (2004) reviewed total 77 skeletal matrix proteins from a large range of invertebrates that had the shell matrix proteins of completed primary protein structures (Marin and Luquet, 2004). A complementary review focused on mollusc shell proteins located in the aragonite layer only, prismatic layer only or in both layers (Sarashina and Endo, 2006).

Several proteins have been identified in the aragonite only. The largest mollusc nacre protein, Lustrin A (molecular weight, 116 kDa), was identified by screening the mantle cell cDNA from abalone *Haliotis rufescens* (Shen et al., 1997). The deduced amino acid sequence showed that it had a modular structure consisting of several conserved domains: ten highly conserved

Cys-rich domains interspersed by 8 Ser-rich domains. The N16 protein family was purified from the aragonite layer of EDTA-insoluble matrix fraction from the pearl oyster *P. fucata* (Samata et al., 1999). The N16 mRNA was only expressed in the dorsal region of the oyster, which indicated that this protein family must be closely related to nacre formation (Samata et al., 1999). *In vitro* crystallisation experiments demonstrated that N16 can inhibit crystal formation in aqueous conditions but induced plate-like aragonite crystals when present in the insoluble organic matrix (Samata et al., 1999). Another nacreous protein, Perlucin, was identified from the nacre layer of the shell of the gastropod *Haliotis laevigata* after demineralisation using acetic acid. Perlucin is composed of 155 amino acid including a glycosylated asparagine (Mann et al., 2000).

Apart from the matrix proteins found in the nacreous layer, several proteins, especially the unusually acidic matrix proteins have been found in the prismatic layer of molluscs (Zhang and Zhang, 2006). MSP-1 was the first acidic protein characterised with an isoelectric point at 3.2. MSP-1 has a high ratio of acidic amino acid such as Ser (31%), Gly (25%), and Asp (20%), which is typical of acidic glycoproteins in mineralisation tissue (Sarashina and Endo, 1998). MSP-1 consists of a motif of two conserved Asp-rich domains interspersed by three Ser- and Gly-rich regions near the N-terminus, which is considered to be the calcium-binding site of this protein (Sarashina and Endo, 1998). Another extremely acidic protein, Aspein, was isolated from the prisms of *P. fucata*. This protein has an extreme isoelectric point at 1.45 and a very high proportion of Asp (60.4%) (Tsukamoto et al., 2004). *In vitro* crystallisation experiments showed that this protein induced calcite crystals even in a reagent solution containing Mg/Ca=5:1,which produces aragonite crystals without proteins (Takeuchi et al., 2008).

As well as the matrix proteins specifically found in either the aragonite layer or calcite layer, several proteins have been found distributed in non-specific regions of the whole shell (Zhang and Zhang, 2006). An example is the Gly-rich protein, MS17, which has been purified from the whole shell of *P. fucata* (Zhang et al., 2003). The cDNA sequence analysis indicates that this protein can be divided into three regions: an N-terminal hydrophilic region, a Gly-rich region considering as Ca^{2+}-binding site and a C-terminal hydrophobic region containing a β-sheet conformation (Zhang et al., 2003). Caspartin, also a calcium-binding protein, has been isolated from bivalve *P. nobilis*, and can be found in both the prismatic and nacreous layers (Marin et al., 2001). This protein is an acidic protein composed of 77% of acidic residues with an N-terminal signal region of 75 Asp (Marin et al., 2005).

In addition to isolating and studying the influence of proteins that are involved in

biomineralisation, there has been an increased interest in the role of polysaccharides in the process. Arias *et al.,* (2008) reviewed this area and showed that three types of polysaccharides are mainly involved in calcium carbonate biomineralisation: hydroxylated polysaccharide, polycarboxylated polysaccharide and sulfated polysaccharide. An example of a hydroxlated polysaccharide is chitin, which is a linear polysaccharide of α- or β-(1-4)-2-acetamido-2-deoxy-D-glucopyranose (Arias and Fernández, 2008). Chitin is wide-spread in biomineral structures, with α-chitin in crustacean carapaces and β-chitin being important for mollusc nacre formation (Arias and Fernández, 2003, Nudelman et al., 2006, Ehrlich et al., 2007). Chitin provides an insoluble two-dimensional template for crystal nucleation during nacre formation (Nudelman et al., 2006). Polycarboxylate polysaccharides have been found in coccoliths and can be divided into two subgroups: polyalduronic acid polymer and polymers of uronic, tartaric acid and glyoxylic acids (Arias and Fernández, 2008). Polycarboxylated polysaccharides are assumed to modify calcium carbonate crystallisation via cooperating with the bound calcium ions to form salt links (Marsh et al., 1992). The sulfated polysaccharides provide the main sulfate group in biominerals (Lootens et al., 2003). Demineralisation studies of mollusc shells have shown that crystal nucleation sites initiate on an organic matrix containing sulfate, acidic proteins and polysaccharides (Wilbur and Saleuddin, 1983, Nudelman et al., 2006).

1.2.2 Extrapallial fluid proteins

In bivalves, the extrapallial (EP) fluid is formed in the cavity between the organic mantle and the external shell (Figure 1.2C). Chemical analysis of the extrapallial fluid shows that the inorganic components in extrapallial fluid are regulated by the mantle (Crenshaw, 1972). The concentration of total cations is greater than that found in the environment (Crenshaw, 1972). The pH and calcium concentration are dynamically changing when the bivalve opens and closes. Compared to the mussel blood, the extrapallial fluid has a lower [K^+] and higher [Ca^{2+}], which implies that there is a provision of excess Ca^{2+} for the essential calcium-binding process of biomineralisation. All these findings illustrate that the ion concentrations in the extrapallial fluid are under the control of mantle cells. The calcium-binding capacity demonstrates the hypothetical roles of extrapallial fluid during shell formation (Crenshaw, 1972).

Macromolecules, including proteins, glycoproteins and peptides have been detected in molluscan extrapallial fluid (Misogianes and Chasteen, 1979, Wilbur and Bernhardt, 1984, Moura et al., 2000b, Cusack et al., 2008). Initially more than five proteins were identified from

the extrapallial fluid of *M. edulis* using sodium dodecyl sulfate polyacrylamide gel electrophoresis (SDS-PAGE) (Misogianes and Chasteen, 1979). This has been followed by specific protein identification from extrapallial fluid. Hattan *et al.,* (2001) firstly identified the most abundant protein in extrapallial fluid from *M. edulis* existing as a dimer with a monomeric molecular weight of ~28.3kDa. This 28 kDa EP protein is highly glycosylated with approximately 14% by weight carbohydrate. Ultracentrifugation and polyacrylamide gel electrophoresis showed the calcium-binding property of this protein. This protein-calcium-binding phenomenon influences the protein secondary structures as evidenced by circular dichroism (CD) (Hattan et al., 2001). Further work focused on the protein primary structure of this 28 kDa main EP protein (Yin et al., 2005). In their work, this protein was characterized with 213 amino acids and a signal peptide of 23 amino acids. In his study, previous molecular weight of 28 kDa was confirmed by the amino acid composition before post-translational modification of 24.3 kDa and the acidic N-linked glycan (~4kDa) (Yin et al., 2005). Highly rich in His, Glu and Asp acidic residues make this a prime candidate in the study of biomineralisation.

Extrapallial fluid from bivalves has been used previously for calcium carbonate *in vitro* crystallisation. Wilbur and Bernhardt (1984) initially identified the strong inhibition of *in vitro* crystallisation in the presence of extrapallial (EP) fluid from the oyster *Crassostrea virginica* and the clam *Mercenaria mercenaria* (Wilbur and Bernhardt, 1984). This inhibition was induced by the large number of negatively charged residues in the extrapallial proteins. An acidic 38 kDa extrapallial protein from pearl oyster, *P. funcata*, was identified to promote the formation of amorphous calcium carbonate (ACC) thereafter inhibit calcite growth during *in vitro* $CaCO_3$ crystallisation (Ma et al., 2007). In addition, *in vivo* crystallisation experiments using inorganic abiotic substrates implanted between the mantle and shell, the extrapallial cavity, demonstrated the influence of extrapallial fluid on shell formation (Fritz et al., 1994, Zaremba et al., 1996). In their studies, inorganic substrates such as glass, mica and MoS_2 were inserted into the extrapallial cavity of red abalone *Haliotis rufescens* for crystal growth. X-ray diffraction and SEM analysis of the biofabricated flat pearls reveals the biomineral process: it was initiated by the deposition of an organic components including EP proteins on the implanted substrate, and then followed by the formation of calcite layer and finally the growth of nacreous aragonite (Zaremba et al., 1996). Their results demonstrated the roles of EP proteins to mediate crystal nucleation *in vivo*.

1.2.3 Inorganic components

The comparison of inorganic components between the extrapallial fluid and sea water shows that there is control of ion concentration. Higher concentration of calcium present in the extrapallial fluid of *M. edulis* (11 mM) than in sea water (9.2 mM) (Crenshaw, 1972, Pietrzak et al., 1976). In addition, heavy metal ions such as Cd, Cu and Zn were detected in the extrapallial fluid and assumed to moderate the protein and glycosaminoglycan (GAG) composition in shells (Moura et al., 2000a).

In the biomineral process, not only organic components orchestrate *in vitro* crystallisation. Inorganic components also exert a strong influence on mineral formation (Moura et al., 2000a). Many inorganic components have been investigated in crystallisation control, including K^+, Sr^{2+} and Cd^{2+} (Falini et al., 2009). Sr^{2+} has complex effects on $CaCO_3$ crystallisation, with accelerating crystal formation in low [Sr^{2+}] and decreasing crystal growth in high [Sr^{2+}] in crystallisation solutions (de Leeuw, 2002, Falini et al., 2009). Also, both positive and negative ions contribute to the crystal morphological and polymorph control during *in vitro* crystallisation (Wasylenki et al., 2005).

The presence of Mg^{2+} has a significant impact on calcium carbonate crystallisation. *In vitro* experiments determined that Mg^{2+} inhibits calcium carbonate crystallisation by prolonging the crystal induction time (Wilbur and Bernhardt, 1984). This phenomenon has been further analysed in another set of *in vitro* crystallisation using Mg^{2+} on calcite formation (Loste et al., 2003b). The inhibition effect was illustrated by the effect of magnesium stabilising amorphous calcium carbonate (ACC) in aqueous conditions, where the stability of ACC strictly relies on the ratio of Mg/Ca (Loste et al., 2003b). Meanwhile, the Mg/Ca ratio also determines the crystal polymorph, producing a calcite lattice at a low ratio and aragonite at a sufficiently high ratio of greater than 3 (Loste et al., 2003b, Falini et al., 2009).

1.2.4 Nacre formation

Aragonite nacre or ‘mother of pearl’, has a distinctive morphology of mineral brick and organic mortar (Addadi and Weiner, 1992, Addadi et al., 2006). This unique structure has attracted significant research interesting on understanding biomineral process.

Weiner and Traub (1984) discussed the influence of the soluble and insoluble matrix during shell growth and provided a multilayer model of the macromolecules for nacre formation. The representative multilayer sandwich structure is consisting of the central layer of β-chitin and

surrounding layers of silk-fibroin like protein and the outer layers of acidic macromolecules (Weiner and Traub, 1984, Lowenstam and Weiner, 1989). The β-sheet is important in that reactive side chains are located to one side of the chain (Lowenstam and Weiner, 1989). This organic framework is assumed to provide well defined nucleation points, and the soluble macromolecules on the surface are assumed to have Ca^{2+}-binding ability, rich in Asp and Glu residues (Weiner and Traub, 1984, Lowenstam and Weiner, 1989). This model has been further developed by using Cryo-TEM with evidence identifying that the silk is absence from the matrix (Levi-Kalisman et al., 2001).

A modified model for molluscan nacre formation with the silk protein was provided by Addadi *et al.* (2006). In their model, silk proteins are present as a hydrogel phase which pre-fills the mineralisation space between two layers of β-chitin (Addadi et al., 2006). The matrix components, including acidic proteins and carbohydrates, are then absorbed onto β-chitin spatially differentiated (Figure 1.3A). The single-crystal nucleation sites are determined by the central ring structures of sulfate-rich protein surrounding a central spot of carboxylate-rich proteins (Addadi et al., 2006, Nudelman *et al*., 2006). The mineral phase is first produced as colloidal amorphous calcium carbonate (ACC) from specialised cells in vesicles (Addadi et al., 2006). The ACC is transported to the single-crystal nucleation sites by cells. The existing acidic proteins induce and control mineralisation to form nacreous layers (Figure 1.3B). The crystal growth proceeds vertically along the fast growing *c* axis until it reaches the β-chitin boundary. During growth, some of acidic proteins are assumed to incorporate into nacre formation, to adjust the mineral chemical and soluble properties. In this model, β-chitin, silk protein, carboxylate-rich protein and sulfate-rich protein are required to build each nacre tablet (Addadi et al., 2006).

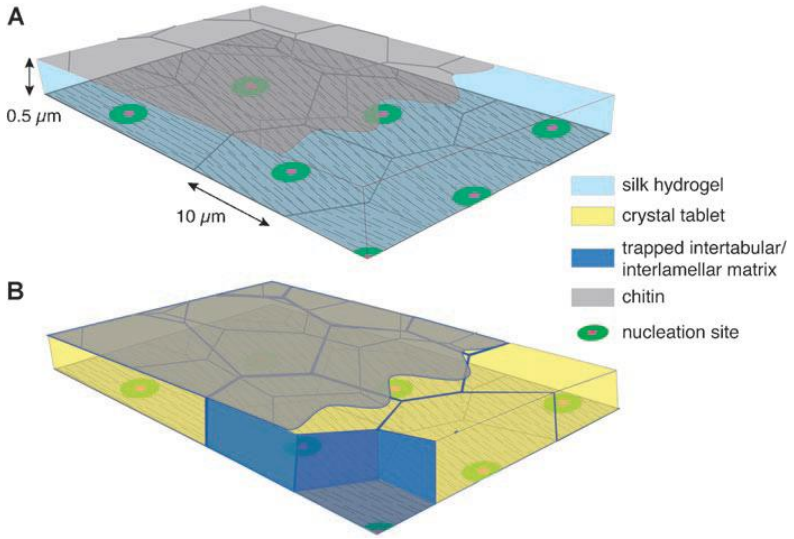

Figure 1.3. Schematic illustration of nacre formation.

(A) The organic matrix assembled prior to the mineral deposition. Organic components involved in nacre formation include silk proteins and nucleation sites. (B) Mineralised nacreous layer. The nucleation and growth of aragonite crystals is controlled by acidic proteins. As crystal growth proceeds, the water and silk are displaced. Crystal tablets are trapped by surrounding chitin between adjacent tablets (Addadi et al., 2006)

1.3 *In vitro* $CaCO_3$ crystallisation systems

Synthesis of inorganic crystals or hybrid inorganic-organic structures with precise control in morphology, orientation and size has attracted much research attention due to the importance and potential applications of new materials, such as catalysis, medicine and electronics (Dabbs and Aksay, 2000, Pinna et al., 2001, Lanting and Barfett, 2006, Lee et al., 2008). Calcium carbonate, an important biomineral material, has three main crystal polymorphs (calcite, aragonite and vaterite) two hydrated polymorphs (calcium carbonate monohydrate and calcium carbonate hexahydrate) and an amorphous phase (Peric et al., 1996, Nebel et al., 2008). In recent decades, this calcium mineral has attracted much research attention for *in vitro* crystallisation.

$CaCO_3$ crystals have been modified by additives such as proteins (Wilbur and Bernhardt, 1984, Ma et al., 2007, Politi et al., 2007, Takeuchi et al., 2008) and ions (Gebauer et al., 2009, Politi et al., 2010), since they occur in biominerals. In the presence of all of these additives, crystals follow the kinetic control of crystallisation, which is based on the modification of activation-energy barriers (Cölfen and Mann, 2003). In such circumstances, crystallisation is proceeded *via* a sequential process including structural and compositional modification, instead of a single-step pathway (Cölfen and Mann, 2003).

1.3.1 CO_2 diffusion system

In vitro calcium carbonate crystal formation was initially modified by dissolving $CaCO_3$ in a solution supersaturated with CO_2 (Kitano, 1962). In Kitano crystallisation system, $MgCl_2$ was used to produce pure aragonite crystals during recrystallisation of $CaCO_3$ upon escape of the CO_2 gas (Kitano, 1962). Another method, developed by Addadi *et al.,* was using vapour of ammonium carbonate slowly diffused into solutions containing Ca^{2+} in a sealed chamber (Addadi et al., 1987). This system of diffused CO_2 has been used during *in vitro* crystallisation experiments in screening both inorganic and organic components (Mann et al., 1988, Mann et al., 1993, Belcher et al., 1996, Aizenberg et al., 1999, Orme et al., 2001, Meldrum and Ludwigs, 2007, Stephens et al., 2010). However, in this crystallisation system, pH varies along this kinetic precipitation process, and a long incubation time was normally required for crystal growth (Matsushiro et al., 2003).

1.3.2 Templates for crystal growth

In recent biomineral studies, calcium carbonate crystallisation has been modified by polymers or organic components as templates *in vitro* (Kuther et al., 1998, Subburaman et al., 2006, Li and Estroff, 2007a, Meldrum and Ludwigs, 2007).Two major types of two-dimensional modified surface substrates with functional additives have been developed for crystallisation: Langmuir monolayers on aqueous surfaces and self-assembled monolayer on solid surfaces (Dey et al., 2010).

Langmuir monolayer substrates with ($CH_3(CH_2)_{16}COOH$) were first used to control $CaCO_3$ crystallisation and orientation (Mann et al., 1988). They used the stearic acid monolayer template to achieve oriented vaterite formation, instead of the rhombohedral calcite formation without monolayer substrates. Since the Langmuir monolayers provide an opportunity to control crystal nucleation, several organic components were used, including nitrilotriacetic acid and calixarenes (Archibald et al., 1996, Matsushiro et al., 2003, Volkmer et al., 2004). In subsequent studies, fatty acids have also been used to control $CaCO_3$ crystallisation, polymorph and morphology using a series of Langmuir monolayer substrates (Loste et al., 2003a). In these experiments, increasing the chain from C16 (palmitic acid) to C30 (triacontanoic acid) changed to crystal formation by promoting aragonite and vaterite formation. This has demonstrated that by using Langmuir monolayers with functional residues, the crystal outcome can be determined.

Aizenberg *et al*. (1999) revealed the effects of patterned self-assembled monolayers (SAMs)

of alkanethiols with a range of functional groups on Si surfaces on $CaCO_3$ crystallisation. Crystals specifically nucleated on polar regions with X group (X=CO_2H, SO_3H and OH) (Aizenberg et al., 1999, Aizenberg, 2004). A schematic pathway of crystal nucleation control under two-dimensional organic templates has been provided, starting from the pre-nucleation clusters in aqueous conditions (Pouget et al., 2009). In their hypothesis, the prenucleation clusters initially formed in the aqueous conditions with dimension of 0.6 to 1.1 nm. This is followed by the aggregation to form amorphous nanoparticles (~30 nm). These nanoparticles were associated with the template surface to mediate crystal growth. During crystallisation, crystal orientation was controlled through the interaction between crystals and organic templates (Figure 1.4).

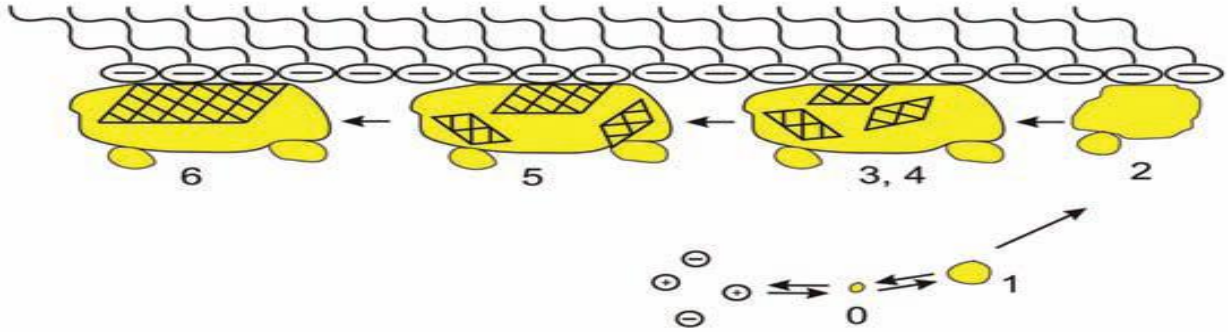

Figure 1.4. Illustration of schematic pathway of crystal formation in the presence of organic templates.

0: formation of pre-nucleation clusters in solution. 1: formation of amorphous calcium carbonate nanoparcitles. 2: growth of nano-particles on the template surface. 3,4: ACC aggregates to form crystalline domains. 5: stabilisation of crystalline domain by templates. 6: formation of single crystals (Pouget et al., 2009).

As described in Section 1.2.1, the insoluble organic matrix such as collagen in bone or chitin in bimineralic shell is considered to provide vital roles over crystallisation, especially at the initial stages. Therefore, apart from the two dimensional templates, three-dimensional insoluble organic or inorganic templates have been used to control crystal formation (Yue et al., 2006, Meldrum and Ludwigs, 2007, Kim et al., 2010). Porous single calcite crystals have been achieved in the presence of inorganic porous templates with a sea urchin skeleton structure (Yue et al., 2006). Porous calcite crystals also precipitated with replicated template structure of porous hexagonal morphology from colloid crystal templates (Hetherington et al., 2011). In addition, organic templates consisting of block copolymers of double-gyroid morphology of a polystyrene-*b*-polyisoprene (PS-*b*-PI) was used to produce gyroid calcite crystal structures (Finnemore et al., 2009). All these findings demonstrate that using 3-D templates can be used to produce crystals with composite morphologies and structures.

1.3.3 Additive components for crystallisation

In biomineral studies, soluble additives have been used to control $CaCO_3$ crystal morphology and polymorph in aqueous conditions. These additives including small inorganic ions and large organic molecules such as proteins and polymers are selected to construct the model experiments demonstrating their impact on crystal formation (Cölfen, 2007, Gebauer et al., 2009, Suzuki et al., 2009). As mentioned above, magnesium was initially assumed to inhibit crystal precipitation by prolonging the nucleation time (Misogianes and Chasteen, 1979). Later work has confirmed that Mg^{2+} has significant effects on calcium carbonate crystallisation, inducing stabilising ACC and formation of aragonite in the presence of a high ratio of Mg/Ca (Loste et al., 2003b, Politi et al., 2010). Further studies have illustrated that the ratio of Mg/Ca>3:1 has induced aragonite formation *via* forms of $Ca(MgCO_3)_2$ (Loste et al., 2003b, Dey et al., 2010). Moreover, other inorganic ions apart from Mg^{2+} have been identified to influence $CaCO_3$ crystal precipitation, including Na^+, Mn^{2+}, Cl^- and SO_4^{2-} (Gebauer et al., 2009).

Organic components, i.e. proteins, polysaccharides and poly amino acids, have been screened for crystallisation (Naka et al., 2000, Kuo and Ma, 2001, Politi et al., 2007, Cölfen, 2007, Gower, 2008). Both calcite and aragonite were induced in the presence of *in-situ* generation of polyacrylic acid (PAA) (Naka et al., 2000). A double hydrophilic copolymer consisting of an outer layer of positive polydiethylaminoethyl methacrylate (PDEAEMA) and inner layer of negative polymethacrylic acid (PMMA) was used for crystal growth by diffusing carbon dioxide vapour into $CaCl_2$ solution at 22 °C. Pure sable branched aragonite crystals were produced in this system (Nassif et al., 2005)

All of these crystallisation modifications are taking place with functional additives in aqueous conditions, which are probably following the particle-mediating crystallisation pathway to form crystals in the mesoscopic transformation (Cölfen, 2007). According to the presence of different additives, this crystal transformation includes several possible pathways (Figure 1.5) (Cölfen and Mann, 2003). In aqueous condition with no additives, crystals form along the classical crystallisation pathway, where clusters nucleate until approaching a critical size of primary nanoparticle and then grow to a single crystal (Pathway a in Figure 1.5). The primary nanoparticles can be arranged to form an iso-orientated crystal (Pathway b in Figure 1.5). When the primary particles correlated with polymers or organic additives, they undergo a mesoscale assembly to form mesocrystals (Pathway c in Figure 1.5). Mesocrystals are colloidal inorganic crystals with a well-defined outer surfaces built from individual nanoparticles (Cölfen and Mann, 2003). Mesocrystals can transfer into individual crystals as

nanoparticles re-aligned, when the surface is insufficiently stable (Cölfen and Mann, 2003). In addition, amorphous calcium carbonate (ACC) can also assemble into complex morphologies during the crystallisation process (Pathway d in Figure 1.5).

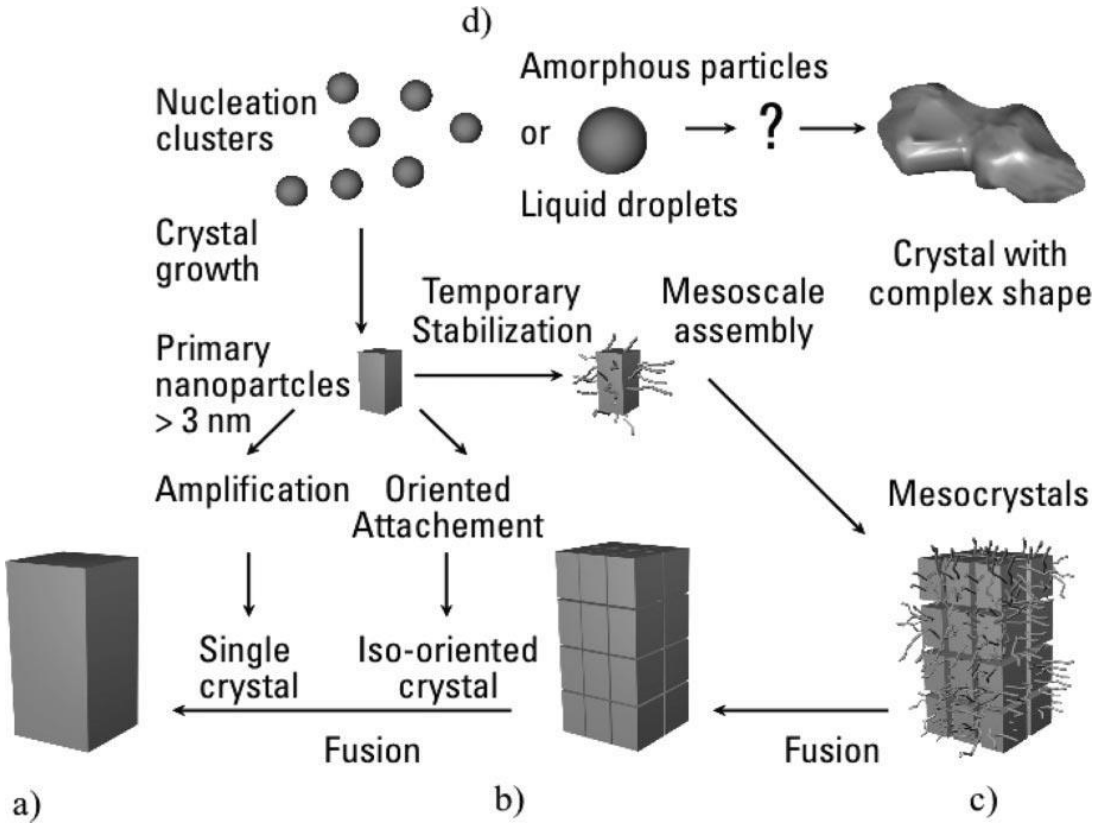

Figure 1.5. Schematic pathways of classical and non-classical crystallisation in aqueous condition (Cölfen, 2007).

1.3.4 Amorphous calcium carbonate (ACC) and pre-nucleation clusters

Amorphous calcium carbonate (ACC), the least stable phase of calcium carbonate, is highly soluble with a low density of crystalline mineral indicating that ACC is highly hydrated (Bolze et al., 2002). ACC can readily aggregate to form different crystalline materials i.e. calcite, aragonite or vaterite in aqueous conditions (Faatz et al., 2004, Stephens et al., 2010). Politi *et al.,* (2004) used the water etching, infrared spectroscopy, electron diffraction and environmental scanning electron microscopy to identify that sea urchin spine regenerated crystallisation *via* the amorphous calcium carbonate (ACC). In their research, this transformation was started from ACC induced into an isotropic non-crystal solid phase. The small amount (15%) of water position was expelled and subsequently, ACC transformed into

composite crystalline solid phase (Politi et al., 2004). In the later work, Politi *et al.,* (2008) used X-ray photoelectron emission spectromicroscopy to study the mechanism of transformation of ACC to calcite single crystals during sea urchin *in vivo* growth. Three distinctive mineral phases were detected during growth: the initial short-live hydrated ACC phase, the followed presumably hydrated ACC phase and the final crystals (Politi et al., 2008). They proposed the mechanism of ACC to crystal is via a secondary nucleation with the pre-existing amorphous units (40 to 100 nm) (Politi et al., 2008).

In vitro, acidic polymers including polyaspartic acid (Poly-Asp) and polyacrylic acid (PAA) have been used as a hydrated phase, called a polymer induced liquid-precursor (PILP) for calcium carbonate crystallisation (Gower and Odom, 2000, Gower, 2008). In this system, polyaspartate has been used to induce a liquid-liquid phase droplet as the mineral precursor, which induced solid amorphous calcium carbonate (ACC). Further work has demonstrated that in the presence of a low concentration of PAA, the ACC surface crystallised to form hollow vaterite structures (Gower and Tirrell, 1998, Gower, 2008, Gower and Odom, 2000). In addition, the solid amorphous calcium carbonate was induced by using Langmuir monolayer organic templates in aqueous condition (Pouget et al., 2009).

However, the schematic pathway of crystallisation in aqueous conditions has not been confirmed until recently. Gebauer *et al.* (2008) has demonstrated the initial stage of crystal precipitation in an aqueous system. Pre-nucleation clusters were detected on the basis of equilibrium thermodynamics, even in unsaturated solutions (Gebauer et al., 2008). They used *in-situ* measurement of [Ca^{2+}] at constant pH, enabling a quantitative analysis of all species during different stages of crystallisation. Based on their finding, the proposed mechanism of calcium carbonate crystallisation follows from the early formation of a nucleation cluster of around 70 ions in unsaturated solutions. This pre-nucleation cluster has also been demonstrated for the initial stage of $CaCO_3$ precipitation in a template controlled system (Pouget et al., 2009).

As mentioned above, calcium carbonate crystallisation has been widely studied in several different crystallisation systems as a means to fully understand the biomineralisation process. A large range of scenarios have to be considered for crystal precipitation to achieve exquisite crystal structures or the mechanism of biological control. In comparison to all of these systems, microfluidics can provide a platform to analyse a range of conditions providing a concentration gradient profile of ions and proteins. More information on biomineral protein screening can be achieved using microfluidic devices. In this project, rapid screening of *in vitro* calcium carbonate crystallisation has been demonstrated using microfluidics to present

this a novel platform for biomineralisation studies.

1.4 Microfluidics

1.4.1 Principle of microfluidics

Microfluidics is an emerging and relatively novel technique requiring a multi-disciplinary approach for building effective systems with applications in chemistry, biology and engineering. Microfluidics has derived from research focusing on the precise control encountered with decreasing amount of liquid and miniaturization needed when handling this fluidic size (Haeberle and Zengerle, 2007). The microfluidic technique was initially developed in 1950s, when research efforts focused on dispensing a small fluidic volume on the micro-litre and nano-litre scale (Mark et al., 2010). Later work by Terry *et al.* (1979) concentrated on a miniaturised gas chromatography (GC) instrument and achieved sub-micron cross-sections, which was seen as a milestone in microfluidic research (Terry et al., 1979, Mark et al., 2010). This technique was improved in 1990s by Manz *et al.,* (1990), who fabricated the first high pressure liquid chromatography (HPLC) using Si-Pyrex techniques (Manz et al., 1990). During the same period, several types of integrated microfluidic devices had been generated for complex fluidic analysis such as microvalves and micropumps (Shoji et al., 1988, van Lintel et al., 1988, Zengerle et al., 1995). This integration has generated the dramatic growth in this novel research field, namely micro total analysis system (μTAS) or lab-on-a-chip (Harrison et al., 1992, Weigl and Yager, 1999).

Lab-on-a-chip is the integrated microfluidic system designed to incorporate several phases including sample delivery, analysis and detection in a single chip (Haeberle and Zengerle, 2007). Typically, the microfluidic device is the combination of a microfluidic channel of tens to hundreds of micron wide and several fluidic control components, i.e. the tubing and valves (Mark et al., 2010). All of these components are required to control sample delivering, separation and mixing. Lab-on-a-chip has been reviewed recently by Mark and his co-workers for system design and the broader applications such as the polymer chain reactions (PCR) (Mark et al., 2010).

Nowadays, microfluidic systems have wide applications in biology and biochemistry, drug delivery, combinatorial chemistry and proteomics research (Weigl et al., 2003, Lau et al., 2007, Price and Kricka, 2007, Sauter et al., 2007, Kang et al., 2008, Teh et al., 2008). Several applications of microfluidic systems are seen in life science, such as cell culture and

tissue engineering (Andersson and Berg, 2004, El-Ali et al., 2006, Kimura et al., 2008). Ei-Ali *et al.* (2006) reviewed the highly integrated microfluidic devices applicable for biomedical and pharmaceutical studies. In their review, the microfluidics can be incorporated for cell culture and analysis in micro-systems, including cell stimulation by defining cells using temporal and spatial patterns, fractionating heterogeneous cell population into homogeneous population and even analysis of biomedical reaction in cells such as gene and protein analysis of cell lysates (El-Ali et al., 2006). In addition, in the studies of microfluidic applications in protein crystallisation, the droplet-based microfluidic device is essential for protein crystallisation using a minimal volume (Zheng et al., 2003, Song et al., 2006). Zhang *et al.,* (2003) successfully precipitated soluble protein crystals in micro-droplets based on a 150 μm wide microfluidic channel (Zheng et al., 2003). Moreover, novel strategies in small-scale such as micro-gels and diffusion controlled system have been involved in drug delivery and release (Weigl et al., 2003). These systems provide opportunities of small quantities consumption of drug for clinical studies (LaVan et al., 2003, Kang et al., 2008).

1.4.2 Classification of microfluidic systems

Depending on the type of liquid propulsion used, microfluidic systems can be divided into 5 subgroups: capillary, pressure-driven, centrifugal, electrokinetics and acoustic systems (Figure 1.6) (Haeberle and Zengerle, 2007, Mark et al., 2010). Each group has specific application in liquid handling, such as the frequency of rotation of the fabricated microstructure in a centrifugal microfluidic system (Haeberle and Zengerle, 2007, Mark et al., 2010). Another example is the delivery of acoustic shock waves in an acoustic microfluidic system to control the droplet residing frequency on substrate surfaces (Mark et al., 2010). In our biomineralisation experiments, a pressure-driven device is used and only that type of microfluidic system is considered here.

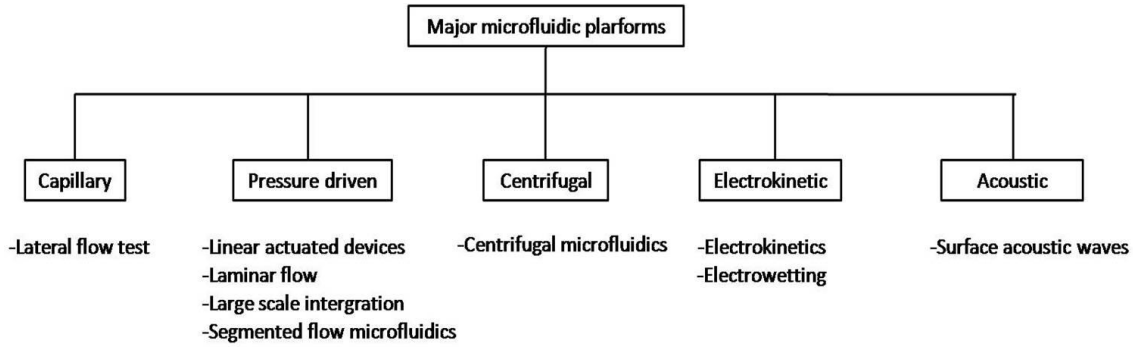

Figure 1.6. Classification of microfluidic systems according to the fluidic propulsion.

According to the fluidic propulsion, there are five major subgroups of microfluidic systems: capillary, pressure-driven, centrifugal, electrokinetic and acoustic systems, with respective applications in (bio-) chemical essays (Mark et al., 2010).

Pressure-driven microfluidic systems are characterized by the liquid delivery principles of pressure difference (Takayama et al., 2001, Teh et al., 2008, Meng and Kim, 2008). There are several methods to generate the pressure gradient, such as external syringe pumps and internal gas micropumps (Sia and Whitesides, 2003). In the laminar microfluidic system, several flow streams are running paralleling along the channel. In the turbulent flow system, the mass mixing is controlled by turbulence. Conditions of fluid delivery in this system also adjusted to obtain laminar flow throughout.

The Reynolds number (R_e) is the dimensionless parameter that characterise the fluidic flow region as laminar flow or turbulence flow. Also it is the ratio of the inertial forces to viscous forces. It can be defined as equation 1.1 (Chakraborty and Chakraborty, 2010).

$$R_e = \frac{\rho U d_h}{\mu} \qquad \textbf{(Equation 1.1)}$$

Where ρ is the fluidic density (kg/m^3),

U is the velocity (m/s),

d_h is the microfluidic channel length scale (m)

μ is viscosity (kg/(m·s))

The value of d_h varies according to the cross-sectional dimensions, i.e. the channel width (w) and height (h). In microfluidic systems, rectangular channels are commonly used, as a consequence, d_h for rectangular channels can be calculated using the equation of $d_h=2wh/(w+h)$.

When $R_e<2000$, viscous forces dominate. Under this circumstance, all fluidic streams run along the channel to form a stream line, leading to laminar flow formation. When $R_e>2000$, the inertial forces are predominate, which determines the turbulence flow (Beebe et al., 2002).

In this project, two types of pressure-driven microfluidic channels have been used for crystallisation. The diameters of the microfluidic channels are:

- Width= 100 µm, height =130 µm, flow rate of 2 µl/min (T-junction channel)
- Width=250 µm, height=50 µm with flow rate of 2.5 µl/min (Y-type channel)

As the protein samples and the reaction reagents are all aqueous solutions, the viscosity (µ) and the fluidic density (ρ) are considered the same as water, with respective numbers of 10^3 (kg/m^3) and $1.1x10^3$ kg/(m·s). After calculation, the Reynolds number for the microfluidic conditions used in this study is around 0.03, which is far less than 2000. Therefore, all fluidic streams in our microfluidic devices are laminar flow.

1.4.3 Mass transportation in the pressure-driven laminar flow system

In this project, the fluidic samples are delivered using external syringes achieving laminar flow, making the device a pressure-driven laminar flow microfluidic system. In the laminar flow system, mass transportation into adjacent streams is controlled by lateral diffusion, which takes place as the solutions flow through microfluidic channels (Takayama et al., 2001).

For example, with an aqueous solution of protein with a molecular weight of 100kDa and standard diffusion coefficient of $5x10^{-11}$ m^2/s (Chakraborty and Chakraborty, 2010), it requires only 30 seconds for this protein solution to diffuse across the 100 µm wide microfluidic channel. This time of lateral diffusion can be compared to that encountered with ion diffusion for Ca^{2+}, Cl^- and CO_3^{2-}, which will have a much smaller diffusion coefficient (Meechai et al., 1999, Guiot et al., 2000, Lide, 2006). Therefore, ions take a much shorter time to transport across the microfluidic channels. However, the process of flow through microfluidic channel is

dynamic, with flow directions towards the outlet of the channel and the latent mass diffusion across the channel occurring at the same time. Complex calculations are required to construct the in-channel mass concentration distribution profiles in aqueous conditions. This calculation of protein and ion concentration distributions along the channel was achieved by using modelling software, Comsol (Chapter 3 Section 3.2).

1.5 Microcontact printing (μCP)

1.5.1 Principle of microcontact printing

Microcontact printing (μCP) is a novel method to create patterned layers of organic components (Mrksich and Whitesides, 1995, Perl et al., 2009, Xu et al., 2009). This technique was initially designed to create patterned self assembled monolayers (SAMs) of hexadecanethiol on a gold substrate surface (Litman et al., 1983, Davey et al., 1986, Wilbur et al., 1994, Xia et al., 1996a, Xia et al., 1996b). In their procedures, photolithography was used to fabricate the elastomeric polydimethylsiloxane (PDMS) stamp (Figure 1.7), which was then used to transfer the 'inked' pattern onto the gold surface (Kumar and Whitesides, 1993).

Although μCP was originally used on a gold surface, a variety of substrate surfaces have been used, including palladium (Carvalho et al., 2002), silver (Xia et al., 1996a), copper (Xia et al., 1996b), and silicon (Offenhausser et al., 2007). Apart from the organic thiol solutions, microcontact printing was developed by researchers to generate the patterns with other substrates, including proteins, DNA and cells (Bernard et al., 2000, Loo et al., 2002, Rozkiewicz et al., 2007b, Hynd et al., 2007). Acetylene-modified oligonucleotides were immobilised by 'click' chemistry induced microcontact printing (Bernard et al., 2000, Loo et al., 2002, Rozkiewicz et al., 2007b).

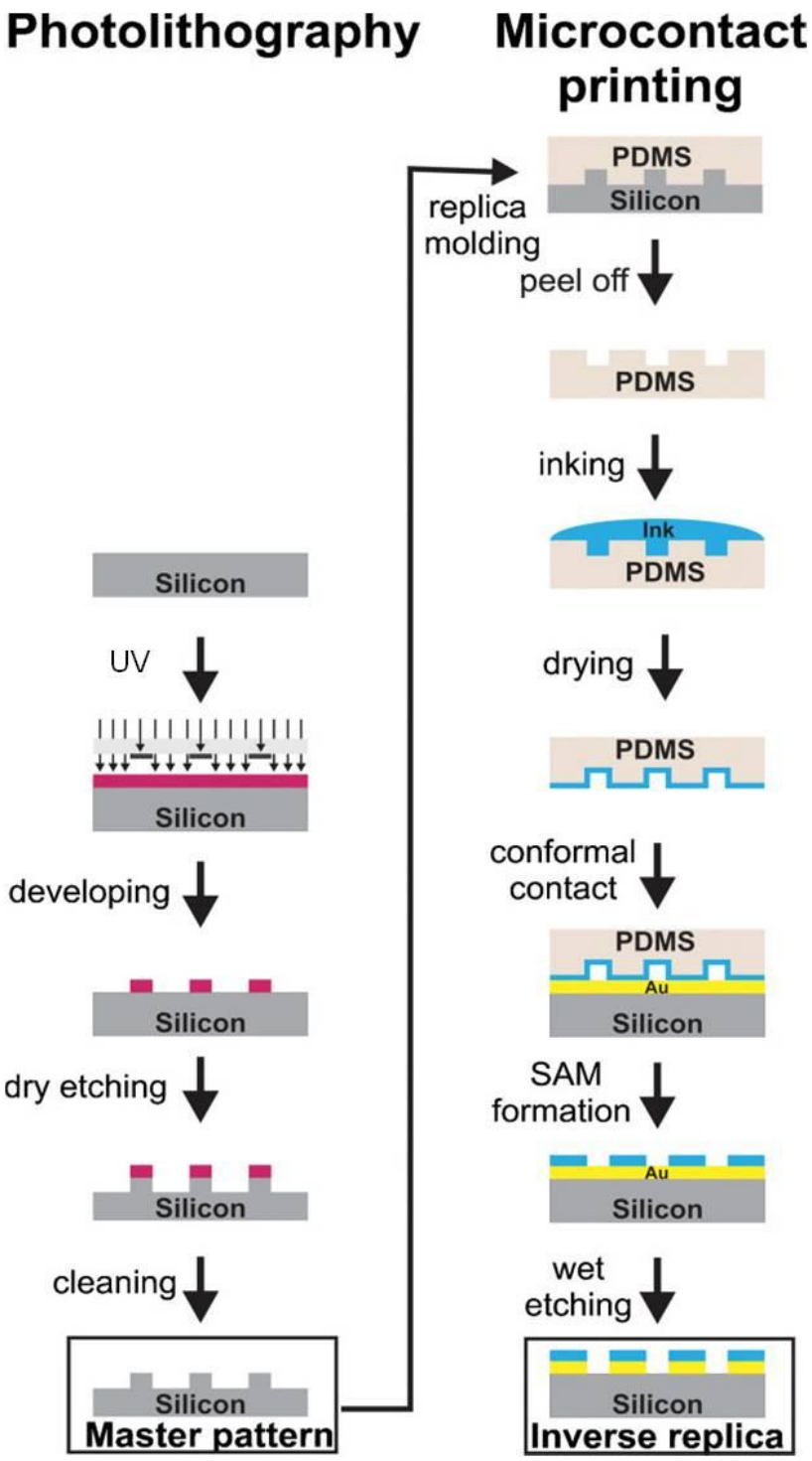

Figure 1.7. Schematic illustration of the procedures of microcontact printing.

The ultraviolet (UV) photolithography is the most commonly used techniques for the fabrication of Si substrates, which is used for PDMS stamps (Kumar and Whitesides, 1993). After fabrication, PDMS stamps are used to create SAMs on substrate surfaces, the microcontact printing process.

1.5.2 Applications of microcontact printing (µCP)

Since µCP can be used to generate different organic patterns on a variety of substrate surfaces, this novel technique has wide applications in biological assays and (bio-) chemistry. This technique was initially developed to achieve patterned SAMs substrates (Kumar and Whitesides, 1993, Wilbur et al., 1994). These substrates typically have a head domain binding to the surface and a long tail which regulates a highly ordered structure on the surface (Mrksich and Whitesides, 1995, Love et al., 2005). These patterned substrates are used for functional studies i.e. mineral crystallisation or cell alignment (Bain and Whitesides, 1988, Aizenberg et al., 1999, Love et al., 2005). Calcium carbonate crystal nucleation and orientation have been well controlled by using Si substrates with patterned SAMs of alkanethiol in a slow diffusion system (Figure 1.8B) (Aizenberg et al., 1999).

In addition, well-defined neural stem cell alignment was achieved using pre-patterned polypeptide substrates during cell culture (Figure 1.8A) (Ruiz et al., 2008). The substrates were generated by printing poly-L-lysine on a glass substrate which was pre-coated with poly-ethylene oxide film (Ruiz et al., 2008). This process enhances the cells immobilised only by the poly-lysine patterns.

Microcontact printing (µCP) has also been used for deoxyribonucleic acid (DNA) and ribonucleic acid (RNA) immobilisation and orientation (Lange et al., 2004, Rozkiewicz et al., 2007a, Rozkiewicz et al., 2007b). During the µCP process, DNA patterns were generated using DNA fragments in the range of 20 to 160 bp oligonucleaotides from PCR products (Lange et al., 2004, Ruiz and Chen, 2007).

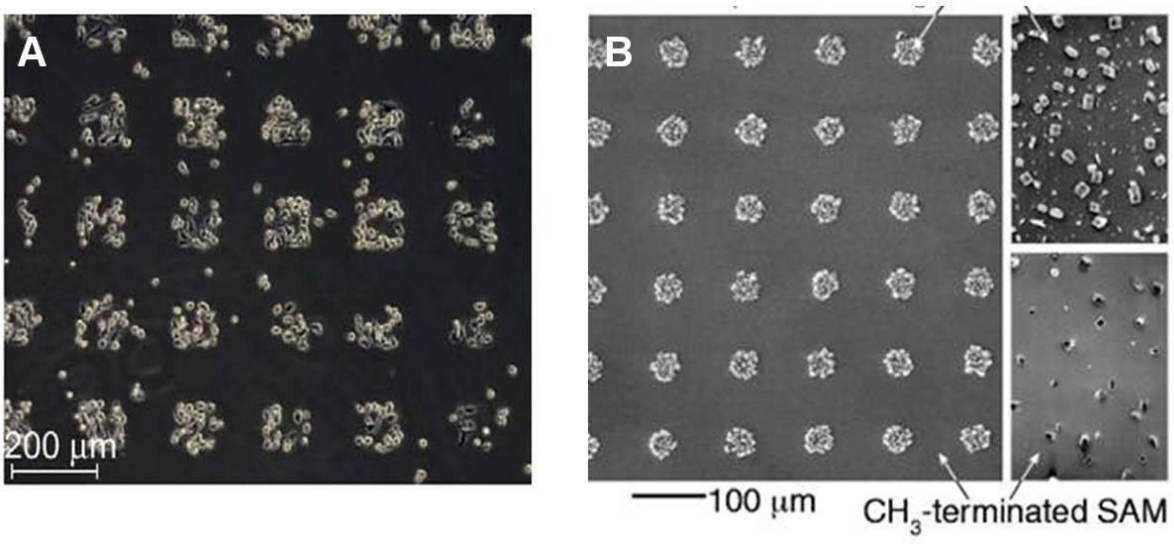

Figure 1.8. Examples of microcontact printing applications.

(A) SAMs of proteins created using µCP have been used to immobilise cells for further analysis (Ruiz et al., 2008). (B) Well modified substrates with alkanethiols patterns used to grow calcium carbonate crystals in a slow diffusion system. Crystals have been distributed under control of the patterned substrates (Aizenberg et al., 1999).

1.6 Aim of this study

The understanding of biomineral protein control in calcium carbonate crystallisation is essential to gain an insight into the biomineralisation process. In the bivalve mussel *Mytilus edulis,* the well-defined shell structure is composed of calcite and aragonite. The biochemical properties and location of the extrapallial (EP) fluid proteins imply that they play a critical role in providing the ingredients for *in vivo* shell formation. In order to investigate possible functions of these EP proteins *in vivo*, it is necessary to carefully analyse and assess protein influence on crystal growth *in vitro*. The aim of this study is to investigate the influence of the extrapallial fluid proteins on calcium carbonate crystallisation using a novel microfluidic platform. For that purpose, not only will the total EP protein mixture be screened, but also several isolated and purified proteins will be assessed.

A pressure-driven laminar flow microfluidic system has been used, where ion and protein concentrations are controlled in diffusion mode, generating a variety of conditions for crystallisation. The opportunity of using computational modelling to calculate ion and protein concentration distributions in the channel provides a theoretical on-site microenvironment for crystallisation prediction along the whole channel. Additionally, the extrapallial fluid proteins can be imprinted onto patterns *via* microcontact printing (µCP) process giving the possibility

of assessing protein function by a different route.

The experimental procedures of both microfluidic system and microcontact printing for crystallisation are described in Chapter 2. The computational modelling and the establishment of the procedure for on-chip crystallisation are given in Chapter 3 and Chapter 4 respectively. On-chip crystallisation control using individual extrapallial fluid proteins are detailed in Chapter 5. Initial experiments using extrapallial fluid protein as a template for crystallisation modification is described in Chapter 6.

Chapter 2

Materials and methods

2

2.1 Materials

In this study, reaction reagents for calcium carbonate ($CaCO_3$) crystallisation are calcium chloride ($CaCl_2$) and sodium carbonate (Na_2CO_3). Both were purchased from Sigma Aldrich and used without further purification. 3-(N-morpholino) propanesulfonic acid (MOPS), from Sigma Aldrich, was used to provide an environment for stable pH at 7.5. Poly acrylic acid (PAA), calcium-binding protein (CBP), bovine serum albumin (BSA) were commercially purchased and used for crystal growth as additives.

In micro-fabrication process, 4-inch Si wafers were purchased from Si-Mat Ltd. The positive photoresist SU-8 series and its developer were purchased from MicroChem®. Polydimethylsiloxane (PDMS) elastomer and the curing agent used for microfluidic chip fabrication and microcontact printing stamps were supplied by SYLGARD® Ltd. A full list of materials used in this study is listed in appendix 1.

2.2 Protein sample preparation

Two major types of mussel extrapallial proteins were screened in order to assess their influence on crystallisation: the wild-type proteins extracted and expressed proteins (Table 2.1). Wild-type EP proteins were extracted directly from the extrapallial (EP) cavity of living blue mussel, *Mytilus edulis*. To extract wild-type proteins, the bivalve shells were prized apart, clean needles gently inserted into the extrapallial space between shell and organic mantle. Extrapallial (EP) fluid was extracted from the mussels and dialysed against MOPS buffer (100mM, pH 7.5). Care was taken to avoid contamination from mussel blood and sea water. Centrifugation of the protein solution (5400 g force for 20 min) was used to pellet any sand and debris. Proteins were purified using the FPLC techniques of ion exchange and gel filtration chromatography.

In this study, there are two expressed extrapallial fluid proteins, the expressed main

extrapallial fluid protein (EEP) and the C1q domain of this protein, both were provided from an *E.coli* protein express system. Further protein purifications, including gel filtration chromatography and Ni-NTA chromatography, were used to ensure pure protein solutions.

Bovine serum albumin (BSA) and vitamin-D induced calcium-binding protein (Sigma Aldrich) were used as control experiments for *in vitro* crystallisation in the microfluidic experiments. Polyacrylic acid (PAA), average molecular weight (Mw) ~3500, was used as both an additive in the microfluidic experiment and a template molecule in the microcontact printing experimental protocols.

Table 2.1 Proteins selected for functional screening during $CaCO_3$ crystallisation

Protein name	Protein source	Mw (kDa)	carbohydrate
Total wild-type exptrapallial fluid proteins (TWEP)	Extracted directly from extrapallial fluid space from living mussel *Mytilus edulis*	*	**+**
Wild-type main extrapallial fluid protein (WEP)	Extracted directly from extrapallial fluid space from living mussel *Mytilus edulis*	~28kDa	**+**
Wild-type extrapallial fluid complex (WCEP) proteins	Extracted directly from extrapallial fluid space from living mussel *Mytilus edulis*	40-60kDa	**TBD**
Expressed main extrapallial fluid (EEP) protein	*E.coli* protein expression system	~24kDa	**-**
C1q domain (C1q)	*E.coli* protein expression system	~14kDa	**-**
Calcium binding protein (CBP)	Purchased from Sigma Aldrich Co.	~11 kDa	**-**
Bovine serum albumin (BSA)	Purchased from Sigma Aldrich Co.	~66kDa	**-**

For functional studies, wild-type and expressed extrapallial fluid proteins were involved. CBP and BSA were used as positive and negative control conditions. Where + stands for protein with carbohydrate, - stands for protein without carbohydrate. * stands for no fixed molecular weight since this is mixture with all extrapallial fluid proteins. TBD: To be determined

2.3 Microfluidic experiments for crystal growth

2.3.1 Microfluidic device design and computational modelling

In mollusc shell formation, calcium carbonate ($CaCO_3$) nucleation and growth are thermodynamic and kinetic processes that are dependent on the concentration of ions in the surrounding environment (Cölfen, 2007, Xu et al., 2007). In traditional experimental methods, a large range of crystallisation conditions has been investigated to determine the polymorph and morphology control. Understanding the diffusion control of proteins and ions in mineral formation is important in understanding the biomineral process.

Microfluidics provides a platform for investigating this process with a range of scenarios. Fixed concentration gradients of proteins and ions can be achieved in the laminar flow microfluidic system under appropriate flow rates (Takayama et al., 2001, Kuczenski et al., 2007). In this project, two types of pressure-driven laminar flow microfluidic devices were considered: the T-junction channel and the Y-type channels, each with two inlets and one outlet (Figure 2.1).

Fluidic computational modelling is a powerful method that reveals mass transport in this system. Therefore calculation of fluidic velocity in specific channel dimension determines the flow velocities at 5.2 mm/s for the T-junction channel and 5.1 mm/s for the Y-type device. Under these conditions, a range of mass concentration gradients along the channel can be realised providing a full range of conditions to study calcium carbonate crystal growth.

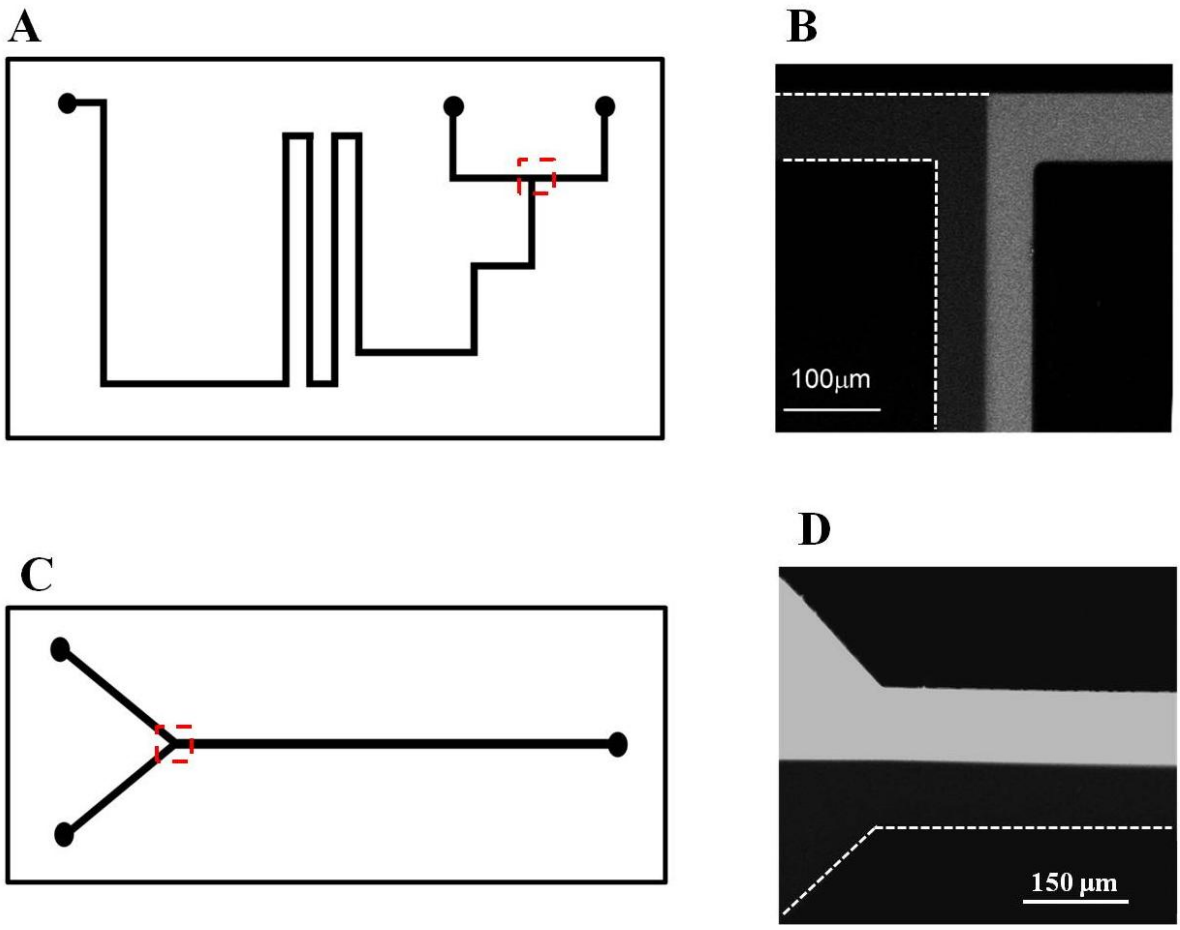

Figure 2.1. Two types of microfluidic chips used in this study.

(A) Illustration of the T-junction microfluidic chip used for calcium carbonate crystal growth. (B) The fluorescein profile of this T-junction microfluidic chip. This profile was generated by delivering the fluorescein solution and de-ionised water into the chip of a velocity at 5.2mm/s. (C) Cartoon of Y-type microfluidic channels with straight reaction channel. (D) The fluorescein profile of the Y-type channel illustrated the emerging of two solutions. This profile was achieved at a velocity at 5.1 mm/s.

In order to precisely control crystal formation, a commercial computational software (Comsol) was used to construct a complete set of concentration gradient profiles for both ions and proteins, as well as in-channel distribution of supersaturation ratios (S). Crystal on-chip formation was controlled by both supersaturation ratios (S) and mass concentrations.

2.3.1.1 Modelling for concentration profile

There are several equilibria when sodium carbonate (Na_2CO_3) and calcium chloride ($CaCl_2$) dissolve in de-ionised water or MOPS buffer (100 mM, pH 7.5) (Table 2.2). All these

equilibria were considered to construct the concentration gradient profiles. In order to construct a complete set of on-chip concentration gradient profiles for Ca^{2+} and CO_3^{2-} ions, a two-dimensional plot was designed, where the x-axis presents the mass lateral diffusion across reaction microfluidic channels (100 µm in T-junction channel and 250 µm in Y-type channel), and the y-axis represents the flow distance along microfluidic channel.

In computational modelling, the first simulation was calculated for the ion concentrations only. Under such conditions, 10 mM calcium chloride solution was delivered through the right channel and 10 mM sodium carbonate through the left in the T-junction device at velocity of 5.2 mm/s. To construct mass concentration with diffusion modelling, diffusion coefficients of each ion were induced in this calculation (Table 2.3). The concentration profile was constructed using the Nernst-Planck equation in the software of Consol.

In the later experiments, simulation on concentration gradient was repeated with consideration of both ion and protein diffusion across the channels. Under such circumstance, 50 mM of $CaCl_2$ and 50 µg/ml of protein were used as initial concentration in modelling calculation. In this modelling simulation, the diffusion coefficients of both protein and ions were involved. The diffusion coefficients of large protein molecules were significantly lower than ions such as Ca^{2+} and CO_3^{2-} (Table 2.3).

Equilibrium	K value
$H^+ + OH^- \Leftrightarrow H_2O$	$1\times 10^7 dm^3/mol$
$CO_3^{2-} + H^+ \Leftrightarrow HCO_3^-$	$2.25 \times 10^6\ dm^3/mol$
$HCO_3^- + H^+ \Leftrightarrow H_2CO_3$	$2.13\times 10^{10}\ dm^3/mol$
$MOPS^- + H^+ \Leftrightarrow HMOPS$	$1.58 \times 10^7\ dm^3/mol *$

Table 2.2 Acid bases and MOPS equilibria and corresponding K value at 25°C.

Several equilibria were considered for construction of the concentration gradient profile. * indicates a calculated value from the pKa data (Verdoes et al., 1992).

Species	Diffusion coefficients (m^2/s)
HCO_3^-	1.185×10^{-9}
CO_3^{2-}	9.23×10^{-10}
H_2CO_3	1.185×10^{-9}
H^+	9.31×10^{-9}
Na^+	1.33×10^{-9}
OH^-	5.27×10^{-9}
Ca^{2+}	7.92×10^{-9}
Cl^-	2.03×10^{-9}
$MOPS^-$	1.185×10^{-10}
MOPSH	1.185×10^{-10}
BSA	5.21×10^{-11}
28kDa EP	8.20×10^{-11} *
EEP	8.20×10^{-11} *
C1q domain	15.50×10^{-11} *

Table 2.3 Diffusion coefficients of ions and proteins for mass diffusion in laminar flow microfluidic system.

* indicates a calculated value based on the comparison to BSA according to the molecular weight (Meechai et al., 1999, Guiot et al., 2000, Lide, 2006)

2.3.1.2 Modelling for on-chip surpersaturation ratio (S)

Having determined protein and ion concentration gradient profiles, the supersaturation ratio (S) is the other key factor which influences on-chip crystal distribution. The supersaturation ratio (S) is effectively a measure of the driving force of crystallisation such that systems with high S values tend to precipitate readily. This ratio can be calculated using the equation 2.1. Ion activity was calculated using the extended Debye-Hückel equation. A two-dimensional plot of supersaturation ratio distribution was constructed, with x-axis standing for the lateral diffusion distance and y-axis for the supersaturation ratio.

$$S = \sqrt{\frac{\Upsilon_{Ca^{2+}} \times \Upsilon_{CO_3^{2-}}}{K_{CaCO_3}}} \qquad \textbf{(Equation 2.1)}$$

Where K_{CaCO3} is the solubility constant of calcium carbonate (mol^2/dm^6)

$\Upsilon_{CO3^{2-}}$ is the activity of CO_3^{2-} (dm^3/mol)

$\Upsilon_{Ca^{2+}}$ is the activity of Ca^{2+} (dm^3/mol)

2.3.2 Micro-fabrication of microfluidic chips

Soft lithography is a diverse set of techniques encompassing replica moulding structures using elastomeric materials, such as polydimethylsiloxane (PDMS). This technique is used for the fabrication process of microfluidic devices as well as surface patterning using PDMS, i.e. microcontact printing (μCP) (Whitesides et al., 2001).

In this project, microfluidic chips were fabricated by casting PDMS against a Si mask with SU-8 microfluidic channel patterns. The Si substrates were thoroughly cleaned using solvents (in the order of ethanol, acetone and then isopropanol) during sonication for 5 min for each solvent. Samples were then rinsed with Milli Q™ water and dried under a nitrogen stream. Positive photoresist SU-8 series was spun evenly onto the substrate surface at 2000 rpm for 30 s. Prebaking of SU-8 coated samples on a hotplate (95 °C) for 10min was required to set down the resist for ultraviolet (UV) exposure. This is followed by an exposure using UV light through the dark field mask with designed channel features. Si sample was exposed in hard-contact mode for 20 s and then baked again on a hotplate (95 °C) for 10 min. The development process was followed using the SU-8 developer for 10 min to create the channel features on the substrate with the correct height.

Replica moulding with PDMS was required to achieve a negative replica structure of channels. This process requires pouring PDMS pre-polymer against SU-8 patterned Si substrate and curing at 70 °C in an oven for 2 hours. The PDMS pre-polymer is composed of PDMS elastomer and its curing agent at a ratio of 10:1. After peeling off the PDMS stamps, an irreversible microfluidic chip with microfluidic channels is achieved by exposing both PDMS and glass substrates to oxygen plasma at 50 V for 2 min and then bonding together. Alternatively, the clean PDMS chip can be clamped to a clean glass substrate directly to create the reversible microfluidic chip with inter-connected microfluidic channels. This technique was used for crystallisation in this project, which enables further crystal analysis using SEM and Raman spectroscopy (Figure 2.2).

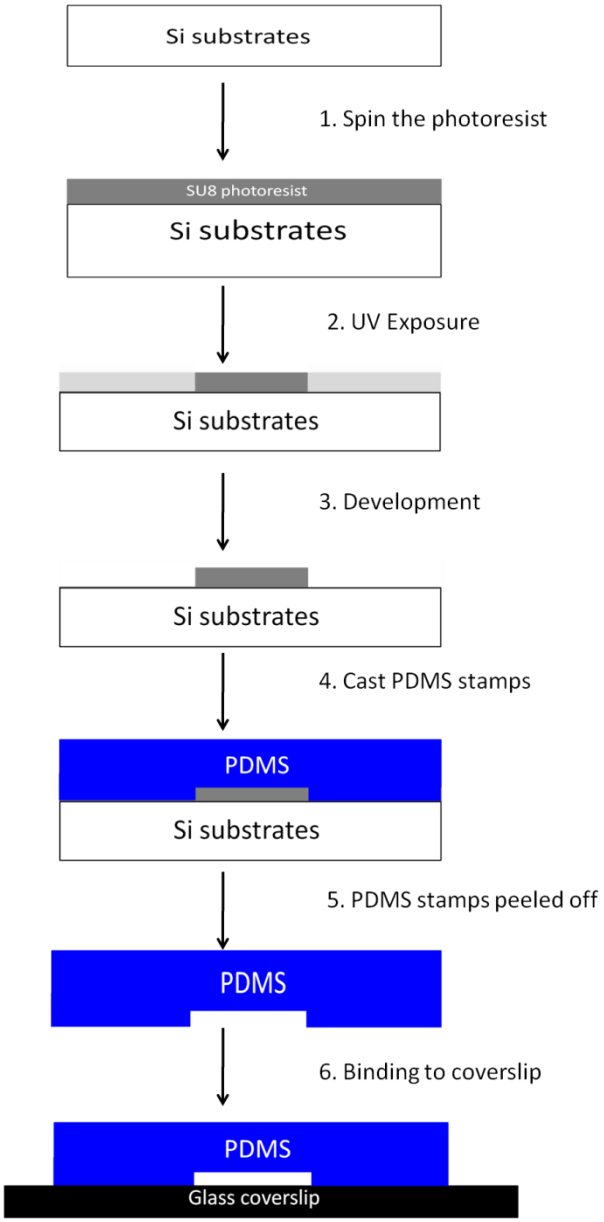

Figure 2.2. Schematic illustration of micro-fabrication process for microfluidic chips.

Si substrates were cleaned using solvents: (1) Photoresist was evenly spun onto substrate surface and soft-baked at 95 °C for 10 min. (2 and 3) The SU-8 is illuminated with UV light through the photomask to cross-link the SU8 and uncross-linked SU-8 was removed to leave the channel features with proper height. (4) PDMS was cast against the mask. (5 & 6) After curing, stamps were peeled off the mask and bound to coverslip to make microfluidic chips. Two different types of microfluidic devices were fabricated and used in this project. In the beginning of the project, a T-junction channel with all channels having a uniform cross section of 130 µm (width) x 100 µm (height) and a long reaction channel length (>5 cm) was designed for crystal growth (Figure 2.1A). Later in this project, a Y-type channel with uniform cross section of 250 µm (width) x 50 µm (height) with a 2 cm long straight reaction channel was fabricated for protein functional screenings (Figure 2.1C).

Fluorescein solution and de-ionised water were run through both types of microfluidic devices to investigate the dynamic flow rate profile. For each device, a continuous supplement of both fluorescein solution and Milli Q™ water were delivered into two inlets with a precise control on flow rate by KD scientific (KDS) pumps: 2 µl/min for the T-junction channel and 2.5 µl/min for the Y-type channel. For each experiment, flow profiles were monitored using a laser confocal scanning microscopy (Carl Zeiss LSM510, Germany) under 20x optical lens. An excitation laser of 488 nm was used with 505-530 emission filters to collect the fluorescence signals. Fluorescence profiles were analysed by the software from Zeiss LSM. In both microfluidic chips, a sharp interface of two solutions occurred in the junction where they first met (Figure 2.1B&D). As the laminar flow progress along the mcrofluidic channels, the mass diffusion across the channel makes this interface more blurred.

2.3.3 Microfluidic experimental setting for on-chip crystallisation

Calcium chloride ($CaCl_2$) and sodium carbonate (Na_2CO_3) were used as reaction reagents for calcium carbonate crystallisation. To identify the influence of biomolecules on crystallisation, additives were mixed with reagents prior to delivery into the microfluidic device. Each reaction solution was freshly prepared in an eppendorf™ tube in total volume of 1 ml. Macromolecules were mixed with $CaCl_2$ only, Na_2CO_3 only or both solutions to create different conditions for crystal on-chip precipitation (Table 2.4). In addition, the blank condition with MOPS buffer (100mM, pH 7.5) only was also screened for comparison. Proteins were initially mixed with reagents prior to delivery into the microfludic channel. Solutions were delivered into microfluidic chip *via* 1 ml syringes and clean tubes with inner diameter of 0.35 mm. The reagent delivery into the channel was precisely controlled by syringes and pumps (KD Scientific). MOPS buffer (100 mM, pH 7.5), polyacrylic acid (PAA) and proteins from Table 2.1 were screened to assess their influence on *in vitro* calcium carbonate crystallisation in Table 2.4.

	$CaCl_2$	Na_2CO_3
Condition 1	+	-
Condition 2	+	+
Condition 3	-	+
Condition 4	-	-

Table 2.4 Proteins in reaction reagents for crystallisation.

Proteins and additives were used with different reagents to create more crystallisation conditions. Where + stands for bio-molecules were added and - stands no bio-molecules added. All samples were prepared in the same methods.

All microfluidic experiments were observed *via* an Olympus Ix70 microscope under 20 x optical lens. Video and image recordings were processed during real-time crystallisation from two solutions merging in the reaction channel for on-chip crystallisation. After crystal formation, chips were rinsed with methanol to preserve crystals and used for further analysis. Each experiment was repeated three times.

2.3.4 Bulk system for calcium carbonate crystallisation

In order to compare crystal formation in the microfluidic system, a conventional bulk system was prepared. Extrapallial proteins used for this bulk system crystallisation were prepared in an analogous manner (Table 2.4) to create the same reaction conditions as in the microfluidic system. All reaction reagents were prepared in a total volume of 1 ml. In every set of experimental conditions, reagent solutions were mixed rapidly (with 500 μl of each) for 1 min and left for 5min for crystal growth. Crystallisation mediums were filtered using a 0.2 μm nylon membrane (Whatman, England) and then rinsed with methanol to ensure crystal stability. Crystals on the membranes were characterised by Raman spectroscopy for polymorph identification, and then coated with gold/palladium for SEM analysis.

2.4 Microcontact printing (μCP) patterns for crystal precipitation

2.4.1 Microcontact printing (μCP) of protein patterns

Similar to the fabrication process of microfluidic devices, microcontact printing requires the creation of a Si mask or template with designed patterns using photolithography. In brief, the Si substrates were evenly coated with positive photoresist SU-8 and exposed to UV light through a photomask with designed patterns. The post-baking with samples on a hotplate (95 °C) and development using developer were followed in order to create the designed patterns on the mask. Cleaning process with solvents was followed for future use.

After fabrication, the silicon elastomer (PDMS) and its curing reagent in the ratio of 10:1 were poured against the mask to create negative replica PDMS stamps. After cured elevated temperature at 70 °C for 2 hours, solid polymer stamps were ready for replicating the opposite of desired structures. After peeled off the mask, PDMS stamps and glass substrates were cleaned with solvents and dried with a stream of nitrogen. In order to enhance the immobilisation of biomolecules on substrate surface, both hydrophobic PDMS stamps and hydrophilic glass substrates were treated with oxygen plasma at 50 V for 5 min (Bhattacharya et al., 2005). This is followed by inking stamps with microcontact printing solutions. In this study, about 500 μl of microcontact printing solution was left on each stamp for 5 min for molecular surface binding. Stamps were dried with a steam of N_2 to leave thin layers of biomolecule on the surface.

The next stage is to transfer the biomolecules from PDMS substrate surface. PDMS stamps were simply placed against the glass substrates with appropriate pressure for physical contact, leaving thin layers of biomolecules in the defined regions on the glass substrate. The stamps were then removed from the substrates to leave inked substrates ready for future use (Figure 2.3A). After the whole process of microcontact printing, well-developed glass substrates with localised biomolecule restricted to the only desired areas can be achieved (Figure 2.3B).

In this project, microcontact printing provides the substrates with protein templates for crystallisation. In order to investigate the influence of extrapallial proteins as template on calcium carbonate *in vitro* crystallisation, microcontact printing solutions were prepared as Table 2.5. Polyacrylic acid (PAA) and bovine serum albumin (BSA) were used as positive and

negative controls to compare the influence on crystallisation of the target protein, the expressed major extrapallial fluid (EEP) protein from *M. edulis*.

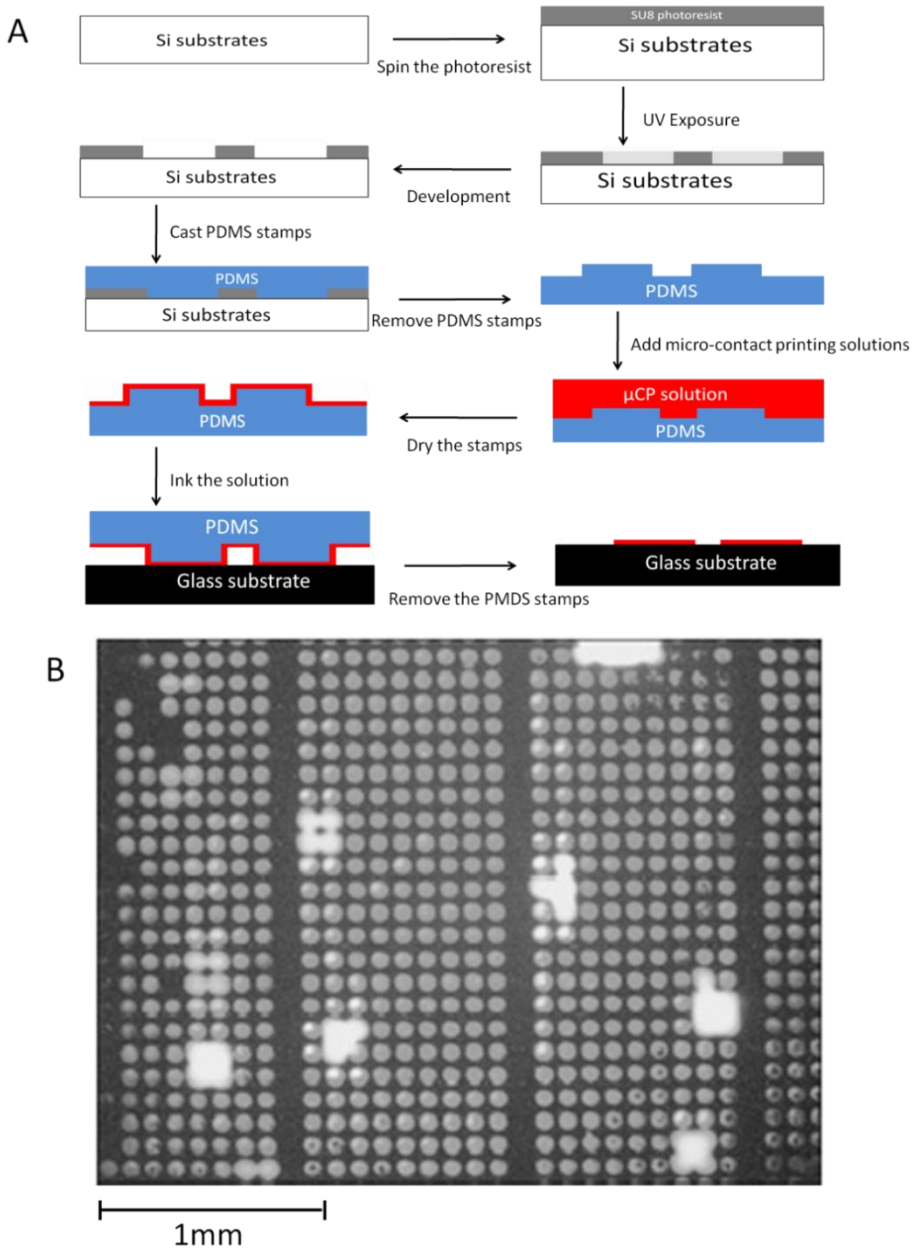

Figure 2.3. Schematic illustration of microcontact printing fabrication.

(A) After cleaning with solvents, Si substrates were coated with positive photoresist. The UV exposure with dark field dot-patterned mask was processed for 25 s in hard-contact mould. Development is to create the mask with dotted patterns. PDMS stamps were prepared by casting against silicon mask at 70 °C for 2hours and then removed. PDMS stamps were wet with microcontact printing solutions for 5min and then dried with N_2 to leave thin layers of molecules on the surface. Stamps were pressed onto the glass substrates surface to ink solution. Afterwards, stamps were removed to leave thin layers of molecules on the surface. (B) Microcontact printing samples after process. Well-inked FITC-BSA solution dispersed on the substrate surface in defined areas only.

2.4.2 Calcium carbonate crystallisation on patterned substrates

Since there are two sets of μCP solutions used in the μCP process (Table 2.5), two different crystallisation methods were required. As to the μCP substrates with proteins and Ca^{2+} (Set A in Table 2.5), the patterned substrates were placed upside down in a petri dish, by supporting the edges. The petri dish was filled with 1 M Na_2CO_3 solution and incubated at 25 ºC for 12 hours (Figure 2.4A). However, as to the μCP patterns with protein/polymer only (Set B in Table 2.5), the substrates were incubated in a slow diffusion system with ammonium carbonate for crystal growth. Under this circumstance, the patterned substrates were placed upside down in 1 M $CaCl_2$ solution, held in the edges. Both ammonium carbonate powder and $CaCl_2$ solution were placed in a sealed dessicator chamber, crystals were incubated using the slow diffusion of CO_2 into $CaCl_2$ solution.

In both crystallisation methods, the patterned glass substrates were removed from the petri dish and cleaned with de-ionised water after crystal formation. Crystal polymorph was identified by Raman spectroscopy using 632.81nm laser as an excitation light. Samples were coated with gold/palladium for crystal morphology observation by SEM.

	μCP set A	μCP set B
Condition 1	1 M $CaCl_2$ +50 μg/ml EEP	50 μg/ml EEP
Condition 2	1 M $CaCl_2$ + 50 μg/ml BSA	50 μg/ml BSA
Condition 3	1 M $CaCl_2$ +1% PAA	1% PAA

Table 2.5 Components of microcontact printing (μCP) solution.

Different biomolecules used in preparing microcontact printing (μCP) solutions for comparison to the target protein: EEP protein.

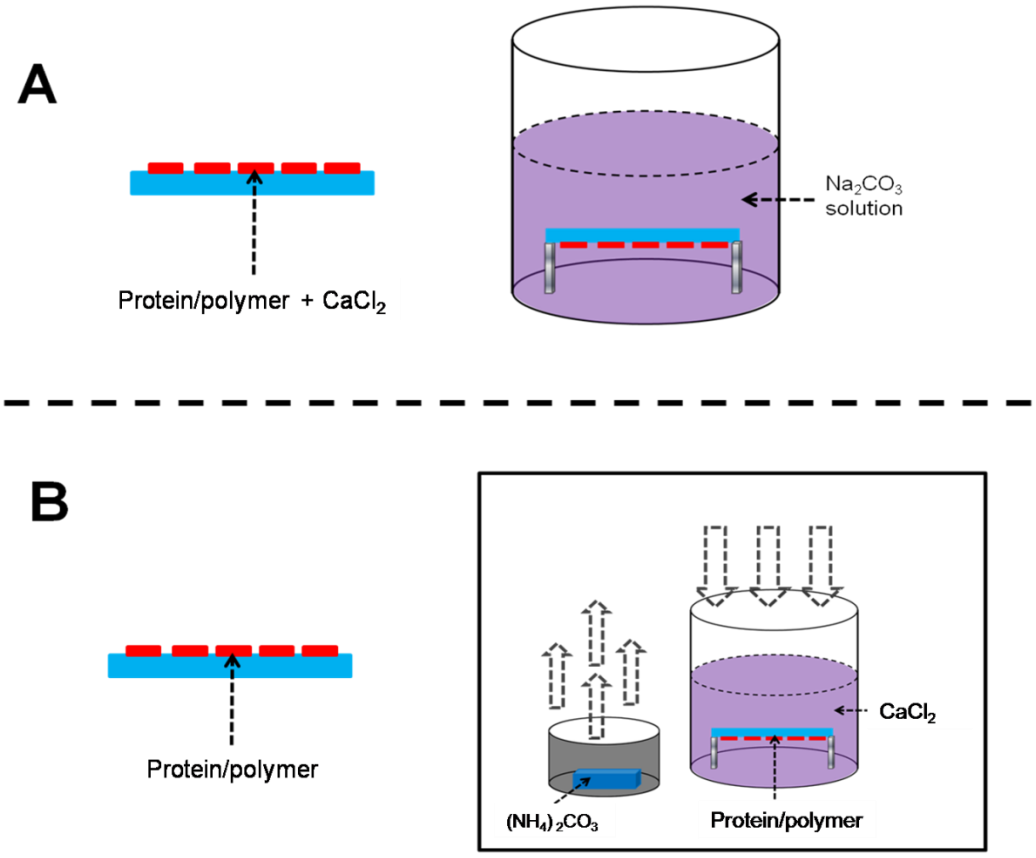

Figure 2.4. Illustrations of crystal incubation methods with µCP patterns.

Two types of crystallisation systems have been processed according to the different µCP patterns. (A) When the protein/peptide and calcium were both printed, the substrates were placed in Na_2CO_3 for crystallisation. (B) When the substrates were patterned with protein/peptide only, the substrates were incubated with ammonium carbonate in the slow diffusion system.

2.5 Raman Spectroscopy and scanning electron microscopy (SEM)

Raman spectroscopy is a non-destructive spectroscopic technique that provides a unique spectrum for each inorganic polymorph structure (Dandeu et al., 2006). It is widely used in chemistry and biology. For Raman spectroscopy, a fixed laser was used as an excitation light, which does not change the wavelength during analysis. Under this circumstance, the Raman shift was caused by the vibrational changes according to the chemical bonds, which are specific to the molecular structure (Truchet et al., 1995, Dandeu et al., 2006). Therefore, different polymorphs can be identified from the Raman spectra. Raman analysis can be performed as a point spectral analysis using submicron size samples. It can also be performed in two-dimensional Raman mapping analysis on flat samples.

Raman spectroscopy readily distinguishes between the three major crystalline polymorphs of calcium carbonate (Dandeu et al., 2006). The strongest peak from Raman detection of calcium carbonate is in the range of 1050 to 1100 cm^{-1}, which exists in all three polymorphs (Figure 2.5). Vaterite can be easily distinguished from other polymorphs with the shoulder peak of 1074 adjacent to main peak at 1091 cm^{-1}. In addition, the characteristic peaks of vaterite 115, 267 and 300 cm^{-1}, are overlapped (Figure 2.5). Although both calcite and aragonite have the main peak at 1086 and minor peak ~710 cm^{-1}, the characteristic peak is the shift at 282 cm^{-1} for calcite and 213 cm^{-1} for aragonite (Figure 2.5).

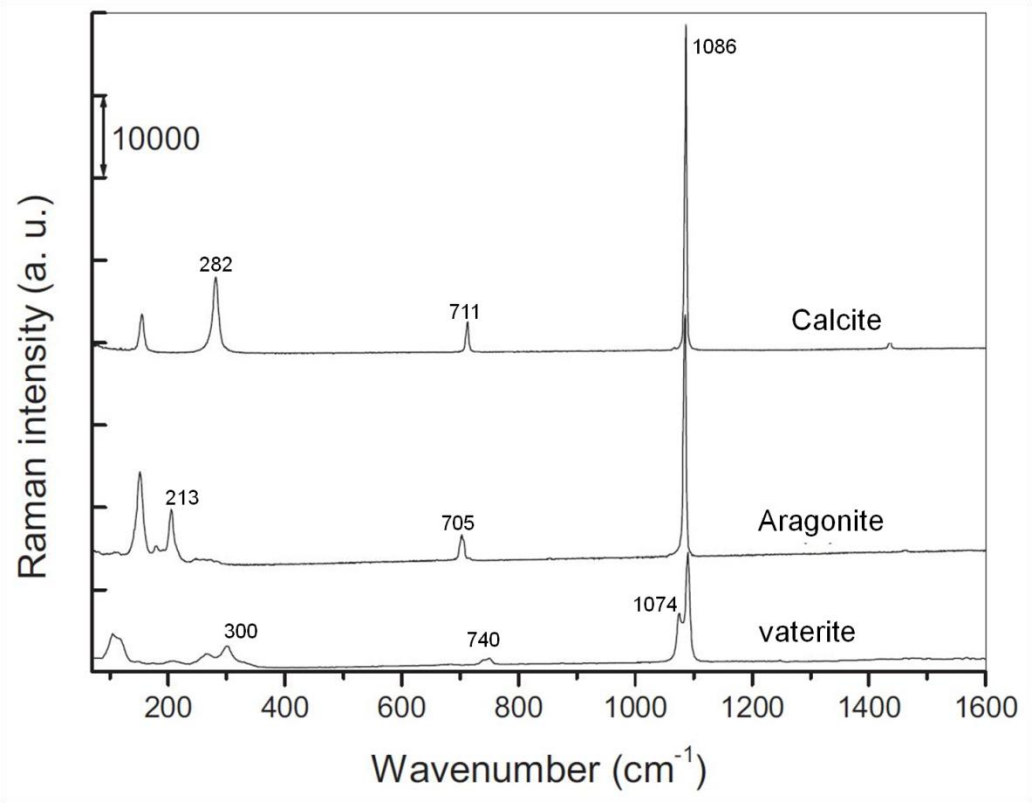

Figure 2.5. Raman spectra of $CaCO_3$ polymorphs.

Specific spectra were identified according to the different structures, with different characteristic Raman shift in the range of wavenumber from 100 to 400 cm^{-1} (Dandeu et al., 2006).

In this study, Raman spectroscopy has been used for the identification of calcium carbonate polymorphs formed in the microfluidic device, bulk system and on microcontact printing samples. A LabRam INV Raman spectrometer (Jobin Yvon Ltd) was used. For the off-chip Raman analysis, crystal samples were located under an optical microscope with 50x optical lens with Raman spectroscopy. Spectra were obtained using a 632.81 nm laser beam as the

excitation light source. An integration time of 20 seconds was used for each spectrum. An average of three spectra was recorded for each crystal. *In-situ* Raman spectroscopy was designed to record crystal growth from initial stage of the experiments.

Crystal morphologies were initially observed using an optical microscope during crystal growth. In microfluidic system, after crystals formed, PDMS were peeled off the glass coverslip and both were coated with gold/palladium for scanning electron microscopy (SEM) imaging. Crystal off-chip analysis used a Hitachi S4700 SEM at high vacuum mode at an accelerating voltage of 10 kV for coated samples.

In microcontact printing (μCP) experiments, SEM and Energy Dispersive X-ray Spectrometry (EDS or EDX) were used for both printed patterns and crystal analysis. Samples were dried and coated with gold/palladium, and then analysed using Hitachi S4700 SEM at an accelerating voltage of 10kV. Energy Dispersive X-ray Spectrometry (EDS), an analytical technique detecting emitted X-ray from investigated samples, is widely used in conjunct with scanning electron microscopy (SEM) or Transmission electron microscopy (TEM) (Newbury, 2005). In this study, EDS was used to detect the calcium distribution on the patterned substrates. Two types of sample were used for EDS: the printed patterns without $CaCO_3$ crystals and the patterned substrates with crystals after incubation. EDS was carried out in an SEM (Hitachi S4700) at accelerating voltage of 10 kV and current at 10 μA.

Chapter 3

Computational modelling for crystallisation

3

3.1 Introduction:

3.1.1 Principles of microfluidics

Microfluidics provides a set of fluidic-unit platforms for (bio-) chemical research, i.e. drug delivery (Teng et al., 1999, Weigl et al., 2003, Kang et al., 2008), combinatory chemistry (Price and Kricka, 2007) and protein crystallisation (Teh et al., 2008). Typically, microfluidic channels are tens to hundreds of microns wide. This offers great advantages over traditional experimental systems, providing fast screening with a large surface to consumption volume ratios. According to the dominating liquid propulsion, microfluidics could be divided into five subgroups: capillary, pressure-driven, centrifugal, electro-kinetic and acoustic systems (Mark et al., 2010).

The laminar flow phenomenon is a characteristic feature in microfluidic system. Without any turbulence in microfluidic system, laminar flows were controlled by external pressures, such as syringe pumps (Mark et al., 2010). Previous studies demonstrated that parallel streams have been achieved allowing a wide range of flow rates and channel diameters.

Under these conditions, the characteristic lengths of the channel are L and H respectively for the y- and x-axis (Figure 3.1). The u, *v* are presented as the respective velocity in two-dimensional channel of flow-through (L in y-axis) and lateral diffusion (H in x-axis) (Figure 3.1). However, with L>>H in the microfluidic devices used in this project, the flow streams (x-axis) were considered as parallel streams. Under such circumstance, the flow delivery is determined by the Reynolds (R_e) number for fluidic types.

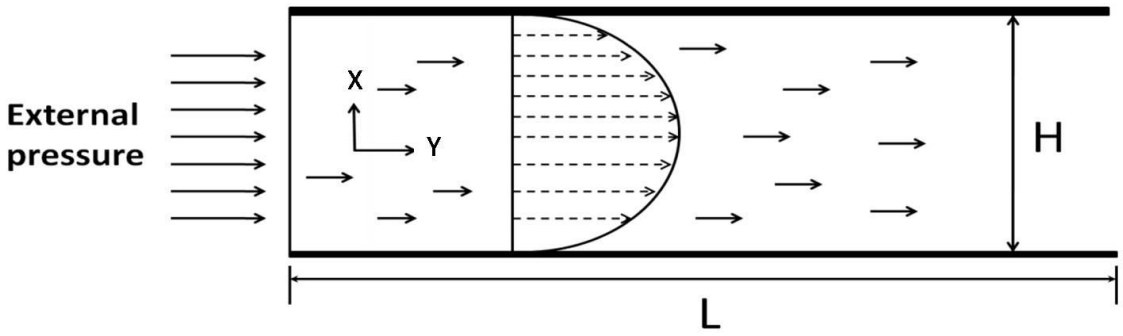

Figure 3.1. Illustrates of pressure-driven flow in a parallel microfluidic channel with channel height (H) and length (L).

The Reynolds number (R_e) is used to characterise different fluidic regimes, laminar or turbulent. R_e can be defined as the ratio of inertial force to viscous force (Mark et al., 2010). Laminar flow occurs at low Reynolds numbers (R_e<2000), where viscous forces are dominant. It is characterized by smooth, constant fluid motion. However, high Reynolds numbers (R_e>2000) occur in turbulent flow with dominated by inertial forces dominate.

3.1.2 Mass transport in diffusion microfluidic mode

With appropriate flow rate, parallel fluidic streams will form in the main reaction channel. By varying the ratios of flow rates of solutions, the interface between the solutions can be changed (Kuczenski et al., 2007). As mentioned before, lateral diffusion controls the mass exchange between the adjacent flow streams in this system. Times for transport of ions and proteins were calculated by considering both the flow rate (*y*-axis) and lateral diffusion (*x*-axis), given by the dimensionless ratio, the Peclet number (P_e). To present the result of mass transportation, a two-dimensional profile of ionic distribution was created using the extended Nernst-Planck equation.

3.1.3 Supersaturation ratios for $CaCO_3$ crystallisation

The supersaturation ratio (S) of calcium carbonate ($CaCO_3$) in aqueous solution is fundamental for understanding the biomineral crystallisation. This ratio is the driving force for crystal precipitation and accounted for prediction of calcium carbonate crystal formation. Theoretically, in both seeded and unseeded conditions, supersaturation is achieved by altering reagent ion concentrations in reaction solutions. The supersaturation ratio (S) has already been described in Section 2.3 in Chapter 2.

In this project, we designed the pressure-driven laminar flow microfluidic devices with R_e<<2000 to build on-chip crystallisation system with two reagent solutions. Mass concentration gradient profiles were required to present the normalised ions and proteins in the channel to demonstrate the influence on $CaCO_3$ crystallisation. In addition, supersaturation ratio (S) calculation along the channel will illustrate the crystal on-chip distribution. Thus, commercial simulation software (Comsol) was used to construct both concentration gradients and supersaturation ratios to simulate on-chip crystallisation *via* this novel platform.

3.2 Results:

3.2.1 Modelling results with only ion diffusion

In the beginning of this project, we used the total wild-type extrapallial (TWEP) proteins for crystal growth. Proteins were added into both calcium chloride and sodium carbonate solutions prior to crystallisation experiments (Table 2.2 in Chapter 2). Therefore, after delivery into the microfluidic channels, only ion concentration gradient was generated under this condition. Modelling of mass transportation was considered according to ion diffusion only to influence crystal precipitation.

3.2.1.1 Modelling results on mass transportation

In order to show the modelling results, a two-dimensional profile is constructed to represent the ion concentration gradients. The distance on the x-axis (Dx) is the lateral diffusion distance and the distance y-axis (Dy) is the fluidic running distance along the channel. Figure 3.2 shows that the concentrations vary in the channel when 10 mM of Na_2CO_3 is delivered in one inlet channel and 10mM $CaCl_2$ in the other. At the initial meeting of two solutions (Dy=0), the concentration of Ca^{2+} is 10 mM in one channel and none in the other. Immediately after that, a close to half-Gaussian concentration profile of Ca^{2+} has formed. Concentration gradients gradually decrease as the solutions running through the devices (Dy increases). As the distance increases from the start of the channel (Dy=30 mm), the fluidic concentration of Ca^{2+} equilibrates to ~5mM. A similar profile is presented for CO_3^{2-} ion in the other channel with an analogous profile to Ca^{2+} ions. Distributions of on-chip concentration gradients have been generated from the start point towards the outlet of device.

This set of modelling results demonstrates the well distributed ion concentrations along the channel in the laminar flow microfluidic devices. In this modelling, a steep step concentration gradient has been generated from the initial joint point of two solutions (Dy=0), without any lateral diffusion. As flow proceeds along the length of the device (Dy=1.0 mm), the concentration profile is getting less steep since ions diffused into the other streams in the channel. After long distances (Dy>10 mm), the concentration profile approaches flat, which denotes the ion concentration profile across the whole channel.

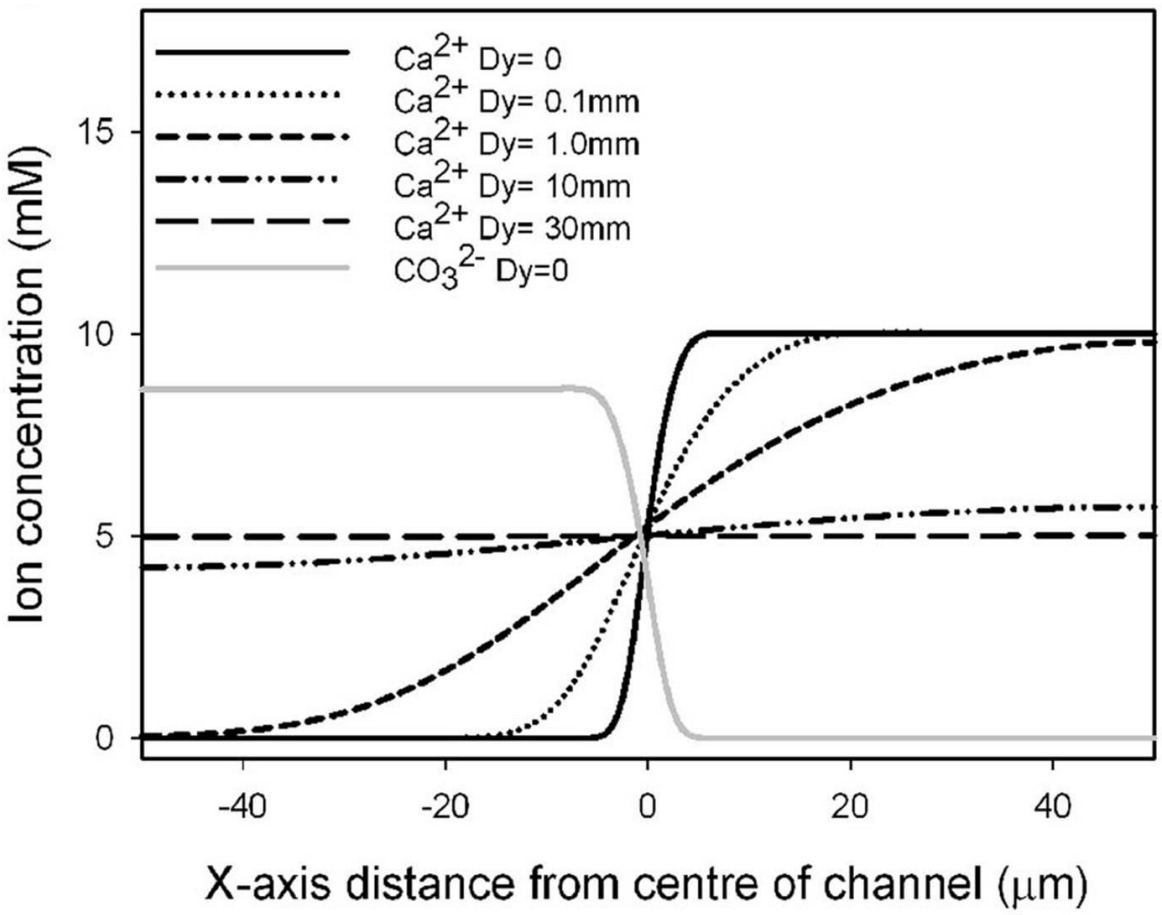

Figure 3.2.On-chip ion concentration gradient modelling.

Concentration profiles of Ca^{2+} and CO_3^{2-} show across the channel at different distances in the direction of flow (Dy). Results are presented in the absence of precipitation of calcium carbonate.

3.2.1.2 Modelling of supersaturation ratio (S) profile

For calcium carbonate crystallisation, supersaturation ratio (S) is a precondition for crystal precipitation. In this study, supersaturation ratios in the channel were calculated to present

crystal precipitation mathematically. It has been calculated using the equation 2.1 in Section 2.3.1.2.

Figure 3.3 demonstrates that a well distributed supersaturation ratio occurred in the channel. The simulation result of supersaturation ratios (S) indicates that there is a sharp peak in the centre of channel in the initial stage of solutions merging (Dy=0). This indicates that only a single line of crystals will form on this interface in the initial joining of two reagent solutions. As the solutions run through the device (Dy increases), the supersaturation ratio profile becomes symmetrically wider. This widening profile predetermines that crystals will be dispersed across the whole channel rather than forming a single line. When solutions travelled a long distance towards the outlet (Dy≥30 mm), the profile is almost flat with high value of ~50% of supersaturation. This profile implies that the crystals will be evenly dispersed across the whole channels under this condition.

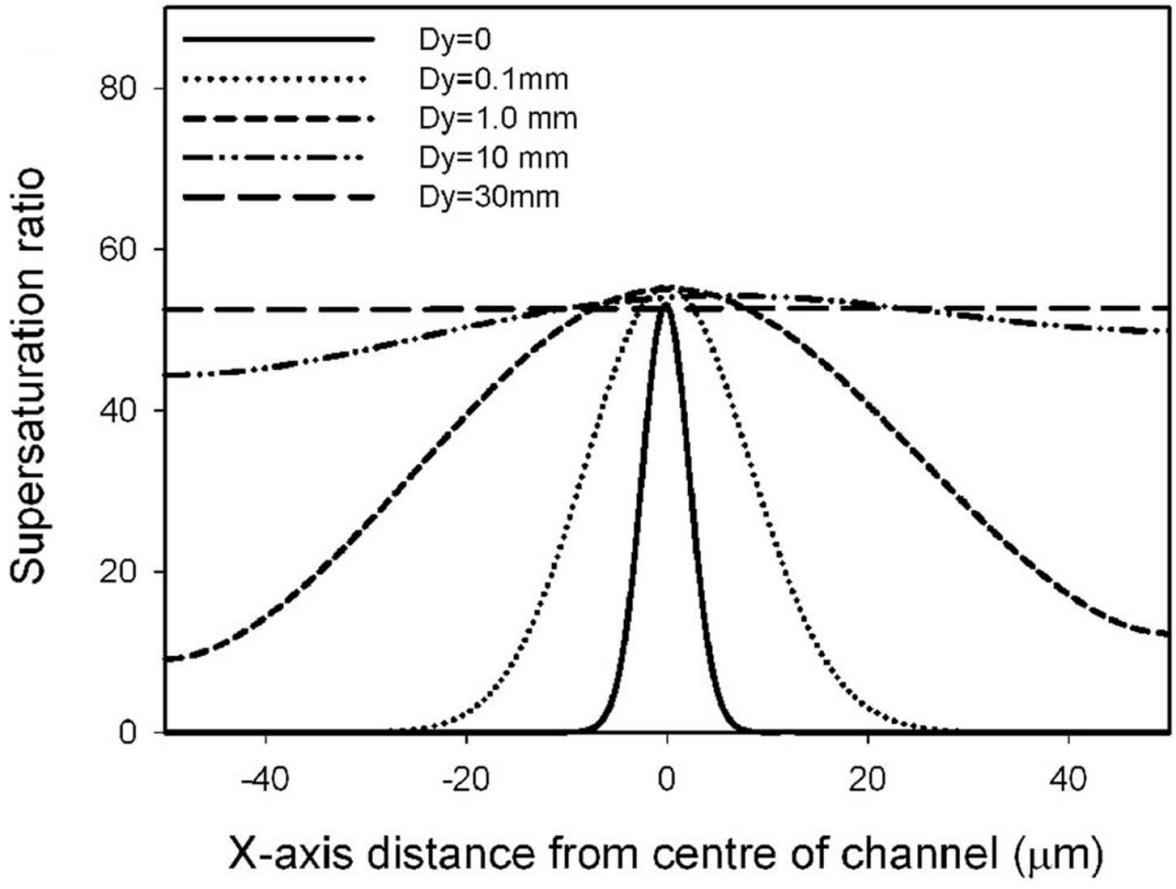

Figure 3.3. Simulation on supersaturation ratio in de-ionised condition.

Profiles for supersaturation of Ca^{2+} and CO_3^{2-} corresponding to the flow distances (Dy). The supersaturation ratio was calculated with the activities estimated from the localized pH and the concentrations of Na^+, Ca^{2+}, CO_3^{2-}, and Cl^-.

3.2.1.3 On-chip crystallisation in de-ionised conditions

In order to test the computational modelling results, real time crystallisation experiments were set up according to the modelling conditions. On-chip crystallisation was set up with 10 mM $CaCl_2$ and 10 mM Na_2CO_3 solutions at a flow rate of 2 μl/min. During crystallisation, optical image recording captured the crystal on-chip distribution in this laminar flow microfluidic system. Crystal on-chip formation was determined by analysing the real time crystallisation images with different flow rate distance (Dy) along the microfluidic channels (Figure 3.4). An interface formed immediately when two solutions merged in the channel (Figure 3.4A). After the induction time for crystal precipitation, a single line of crystals formed on this interface (Figure 3.4B). As the solutions ran along the channel (Dy>0), the dispersed crystals predominately formed in Na_2CO_3 side in this microfluidic channel (Figure 3.4C). Near the outlet of the channel, where the concentration gradients are thoroughly balanced, crystals were uniformly dispersed across the entire width of the channel (Figure 3.4D). This set of results confirms the predictions from the Comsol modelling, that on-chip crystallisation is under the control of localised ion concentration gradients and supersaturation ratios across the channels.

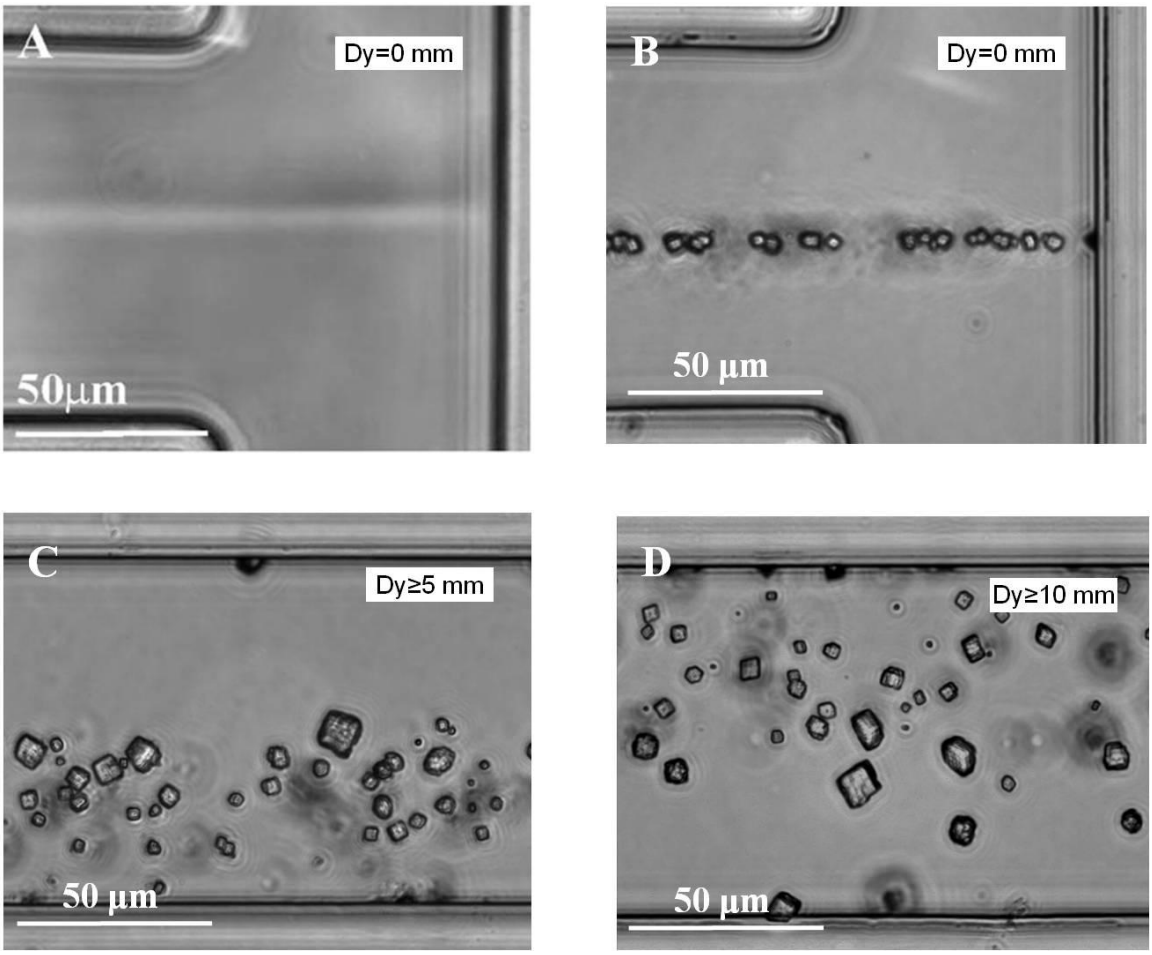

Figure 3.4. On-chip crystal formation with 10 mM Na_2CO_3 and 10 mM $CaCl_2$ in de-ionised water.

(A) Interface arrow of two solutions delivery into microfluidic channel. (B) Single stream of individual crystals formed on the interface after induction time for crystal precipitation at initial interface. (C) Crystals formed in the Na^+ side with Dy increase. (D) Well-dispersed crystals formed in the channel near the outlet of channel.

This experiment demonstrates the usefulness of computational modelling as precursors to real time crystal nucleation experiments. At the initial interface, a single line of individual crystals is formed in the real experiment, which was induced by a sharp peak in the supersaturation ratio in the modelling calculation. At the outlet of channel, a flat supersaturation ratio profile in the model implied that the crystals would be uniformly distributed across the channel. This is coincident with the experimental results which showed the well-dispersed crystals across the whole channel at the end of this laminar flow microfluidic device.

However, there is a discrepancy between the observation from computational modelling on

crystal growth and real-time crystallisation. After solutions running along the channel (Dy>1.0 mm), the wider supersaturation ratio profile suggests that crystals will precipitate in the central areas of the channel rather than forming a single line (Figure 3.4B). But real crystallisation results revealed that crystals precipitating towards the side of the Na_2CO_3 solution (Figure 3.4C). An explanation for this phenomenon is the effect of pH differential of $CaCl_2$ and Na_2CO_3 solutions. The crystal precipitation was inhibited by the initial low pH of the calcium chloride solution (pH 4.9). The diffusion process mixed with the slightly alkalinity sodium carbonate solution (pH 9.5), crystals were accelerated by the high pH of Na_2CO_3 solution.

To investigate the variation of local pH in the microfluidic channel, the pH indicator phenolphthalein (0.1 mM), was added into both $CaCl_2$ and Na_2CO_3 solutions prior to injecting into the microfluidic channels for crystallisation. The results clearly showed the interface between the low pH of $CaCl_2$ and high pH of Na_2CO_3 solutions, which remained for a long distance (~5 mm) from the joint point (Figure 3.5). This interface finally disappears when the ions are balanced across the channel after running along towards the end of the channel. Confirming the modelling prediction under this condition, a single line of crystals formed in the initial stage of two merged solutions. This was followed by most crystals precipitated in the Na_2CO_3 channel side, with higher pH than the $CaCl_2$ side. This *in-situ* crystallisation experiment in the presence of the pH indicator clearly demonstrated that crystal formation is controlled by the pH differentials. Crystallisation is accelerated by higher pH conditions and inhibited in acidic conditions.

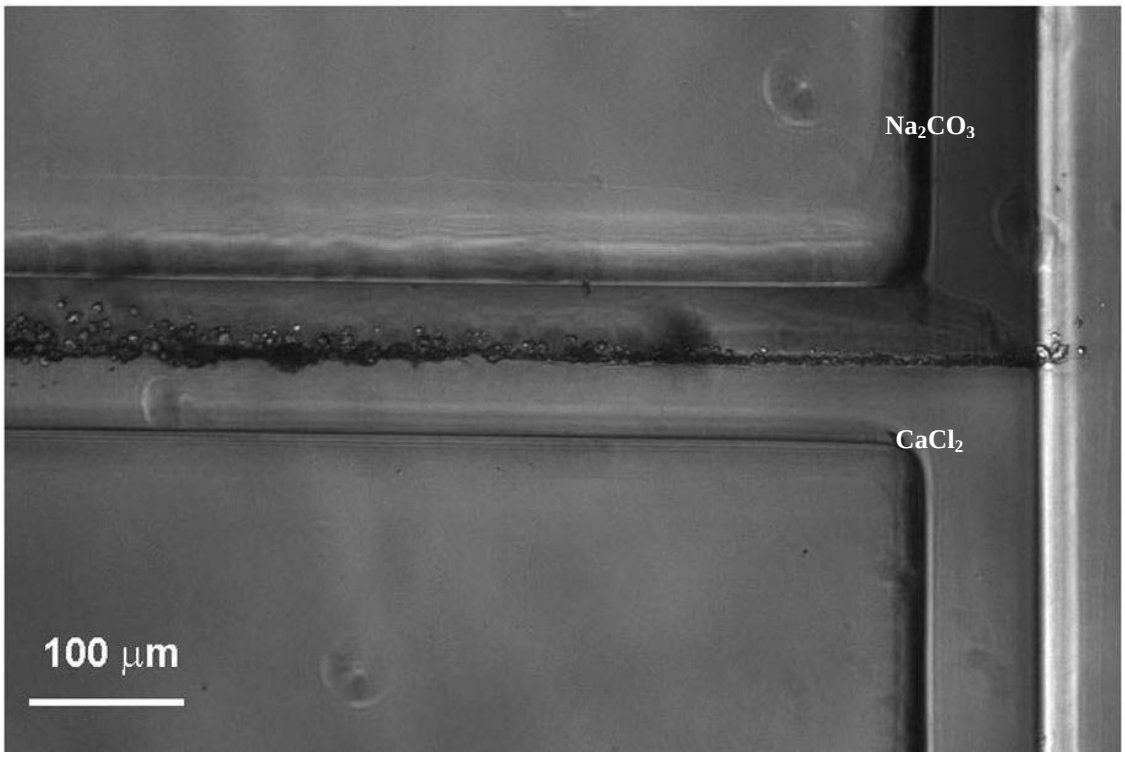

Figure 3.5. On-chip crystallisation in presence of 0.1 mM phenolphthalein.

The pH indicator, phenolphthalein presented in both solutions indicates the pH profile in microfluidic channel. In the condition of pH>9.5, phenolphthalein appears dark under 548 nm illumination.

This set of combination work of systematic computational simulation and experimental confirmation demonstrated the opportunity for trial experiments of calcium carbonate crystallisation using microfluidics. In a laminar flow system, calcium carbonate on-chip crystallisation seems to be dependent on ion diffusion and pH gradient. These experiments highlighted the need to control the pH of both solutions. As a consequence, the MOPS buffer was used to provide a pH buffered condition for crystallisation in subsequent experiments.

3.2.2 Modelling results with both protein and ion diffusion

The above work has demonstrated the advantage of computational simulation in the condition where the lateral diffusion of proteins was estimated. However, within the later work in this project, more reaction conditions were required to investigate the influence of mussel proteins on $CaCO_3$ crystallisation. Macromolecules including proteins and polymers were added into $CaCl_2$ only, Na_2CO_3 only or both solutions to create more scenarios to investigate their effects on crystallisation (Table 2.2 in Chapter 2). Therefore, computational modelling was required

to demonstrate the mathematical control of both ion and protein concentration on crystal formation under this situation.

3.2.2.1 Modelling of mass transportation with EP protein

Understanding the protein influence on mineral formation is an important feature of calcium carbonate crystallisation studies. Under the conditions of the lateral diffusion over the microfluidic channel existing in both ions and proteins, the computational fluid dynamic software (Comsol) is again used to construct the complete set of concentration profiles of on-chip distributions for Ca^{2+}, CO_3^{2-} and proteins.

To eliminate the pH influence on crystal precipitation, MOPS buffer (100 mM, pH 7.5), a physiologically relevant pH for this protein, has been used to keep all reagents within this pH range. A two-dimensional concentration profile was used in this simulation modelling. Although there is a right-angle turn at 10 mm along the channel, its effects on mass contribution was negligible. In comparison to previous simulation work, the simulation of a pH buffered system required the consideration of acid-based and MOPS equilibria at pH 7.5, which was presented in Table 2.2 in Chapter 2. Mass diffusion coefficients (Table 2.3 in Chapter 2) were used in concentration gradient profile calculation.

Previous modelling demonstrated the similar concentration profile achieved for both Ca^{2+} and CO_3^{2-} ions. In addition, protein concentration gradients are generated as proteins are delivered into microfluidic device with only one reagent in this set of experimental design. Therefore, Ca^{2+} ion and the wild-type major 28 kDa extrapallial (WEP) protein are selected for concentration profile in this computational modelling. This concentration profile was calculated by considering both flow running distance (y-axis) and lateral diffusion distance (x-axis). The bigger diffusion coefficient of proteins compared to small ions (Table 2.3 in Chapter 2) implies a much lower lateral diffusion speed of protein molecules than Ca^{2+}. In the condition where protein and calcium were delivered only in one channel, both calcium and protein will diffuse across the channel throughout the whole length of the microfluidic channels. As a consequence, both protein and calcium ion will have a similar concentration gradient profile.

With a low diffusion coefficient (shown in Table 2.3 in Chapter 2), the protein concentration gradient will remain along the length of channel. After delivery the 50 µg/ml of EP protein as initial concentration into one inlet, a sharp gradient profile is generated across the channel (Figure 3.6, red dash line). After flow running of 10 mm along the channel, this concentration gradient still remains with less steep steps (Figure 3.6, red lines). The Ca^{2+} concentration

reduces rapidly along the channel (Figure 3.5, black lines). The initial concentration of 50 mM $CaCl_2$ was delivered into one side of the channel, a sharp gradient profile is generated, similar to the WEP protein. But ions were uniformly dispersed across the entire channel by 10 mm down in the channel (Dy=10 mm). Therefore, over long channel distance (Dy≥10 mm), the protein concentration gradient still remains mainly with balanced ion concentration across the channel. As mentioned preciously, after delivery into the microfluidic channel at the same flow rate, the CO_3^{2-} will have the similar concentration profile as Ca^{2+}, not presented in this simulation work. This set of modelling results indicates a great range of scenarios of concentration gradient with proteins and ions being achieved for on-chip calcium carbonate crystal formation.

The long distance of microfluidic channel (~5 cm), allows both the protein and ion concentrations to eventually be balanced across the microfluidic channel. This set of diffusion modelling presents the opportunity to screen the influence of biomineral proteins on crystal growth with a vast range of conditions along this long channel microfluidic device. Under such circumstance, different crystallisation conditions will be generated *via* delivering protein solutions into the laminar flow microfluidic devices. Therefore, biomineral protein influence on calcium carbonate crystallisation can be achieved by analysing the crystal formation along the whole microfluidic channel with different protein concentrations.

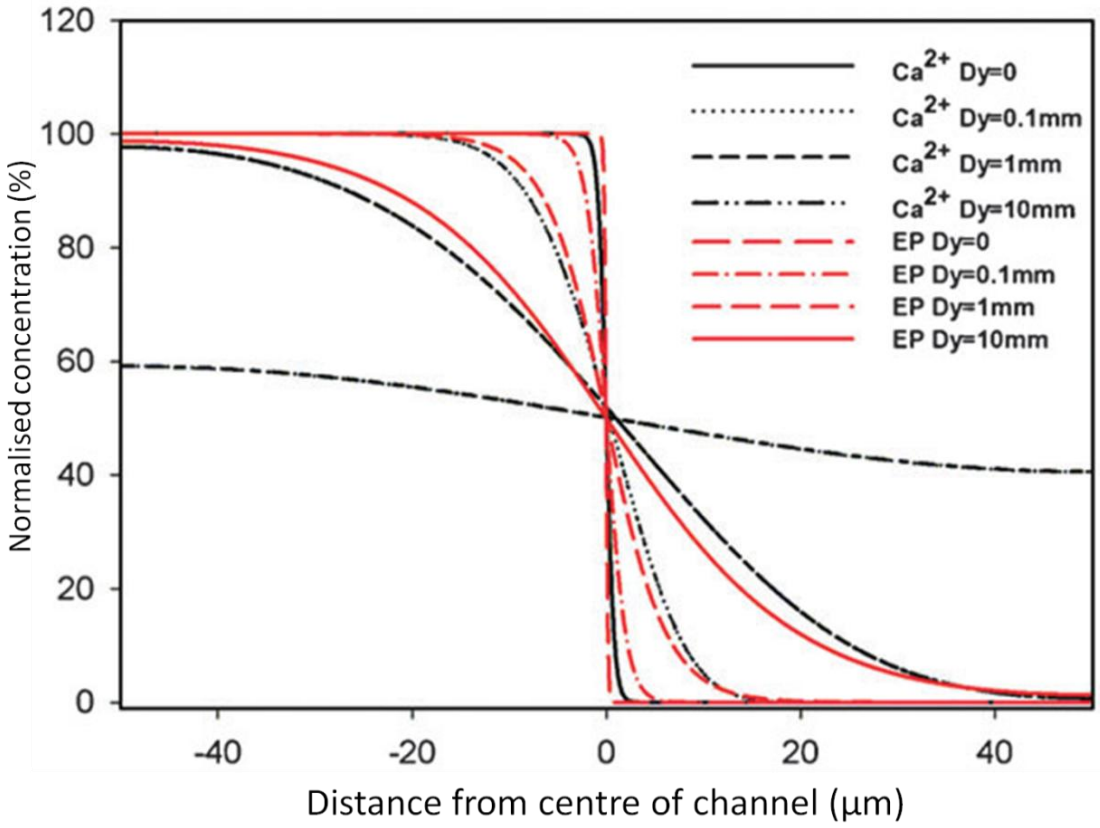

Figure 3.6. Illustration of concentration gradient profiles of EP and Ca^{2+} on-chip distribution.

Ions and protein have similar diffusion profile along the directions of stream flow (Dy). Protein has small diffusion rate, with concentration gradient remainning after running long distance (Dy>10 mm). Ionic gradient across the channel has been elimated after running long distance (Dy>10 mm).

3.2.2.2 Supersaturation ratio in the presence of protein diffusion

Under the buffered pH conditions, the calculation of the supersaturation ratio (S) is more complicated than for the previous work in de-ionised water. Using the same calculations and taking into account the MOPS and pH equilibria, the supersaturation ratio (S) of this system was constructed. This calculation indicates that the supersaturation ratio (S) varies under different conditions of pH and ion concentrations (Table 3.1). In the presence of the same concentration of 10 mM reagents, the supersaturation ratio is much higher in de-ionised water (53) than that in the buffer condition of pH 7.5 (3.4). Meanwhile, given the constant pH value, supersaturation ratio of $CaCO_3$ varies by the presence of the concentrations of Ca^{2+} and CO_3^{2-}. For example, the presence of 50 mM Na_2CO_3 and $CaCl_2$ in MOPS buffer (100mM, pH7.5) induced an S value of 7.4 while 10 mM Na_2CO_3 and 10 mM $CaCl_2$ in MOPS buffer (100mM, pH 7.5) induces an S value of 3.4.

The supersaturation ratio profile was presented as a two-dimensional plot with x-axis representing for the lateral distance of the channel (Dx) and distance y-axis for the flow rate distance (Dy). Under this pH buffered condition, the supersaturation ratio of calcium carbonate was presented in Figure 3.7. The results imply a similarity in overall shape of the supersaturation distribution to that of a non-buffered system. There is a sharp peak in the middle of channel in the initial stage after sample delivery (Dy=0 mm). Supersaturation ratio profile broadens across the channel on the sample continuous along the device (Dy increases) and finally flattens across the whole channel after distance of Dy≥30 mm.

System	Supersaturation ratio
10 mM Na_2CO_3 in DI water, pH 11.0 10 mM $CaCl_2$ in DI water, pH 4.9	53
10 mM Na_2CO_3 in 100mM MOPS buffer, pH 7.5 10 mM $CaCl_2$ in 100mM MOPS buffer, pH 7.5	3.4
50 mM Na_2CO_3 in 100mM MOPS buffer, pH 7.5 50 mM $CaCl_2$ in 100mM MOPS buffer, pH 7.5	7.4

Table 3.1 The maximum supersaturation ratio in different systems.

The formation of bicarbonate and carbonate is determined by the pH of the system. Based on the equilibrium between H_2CO_3, HCO_3^-, CO_3^{2-}, bicarbonate is dominant in the system consisting of 50 mM Na_2CO_3 and 50 mM $CaCl_2$ in 100 mM MOPS buffer at pH 7.5. The concentration of bicarbonate is 46.9mM in comparison to 0.07 mM of carbonate accounting for the much lower supersaturation ratios of $CaCO_3$ in the MOPS buffer system (100mM, pH 7.5).

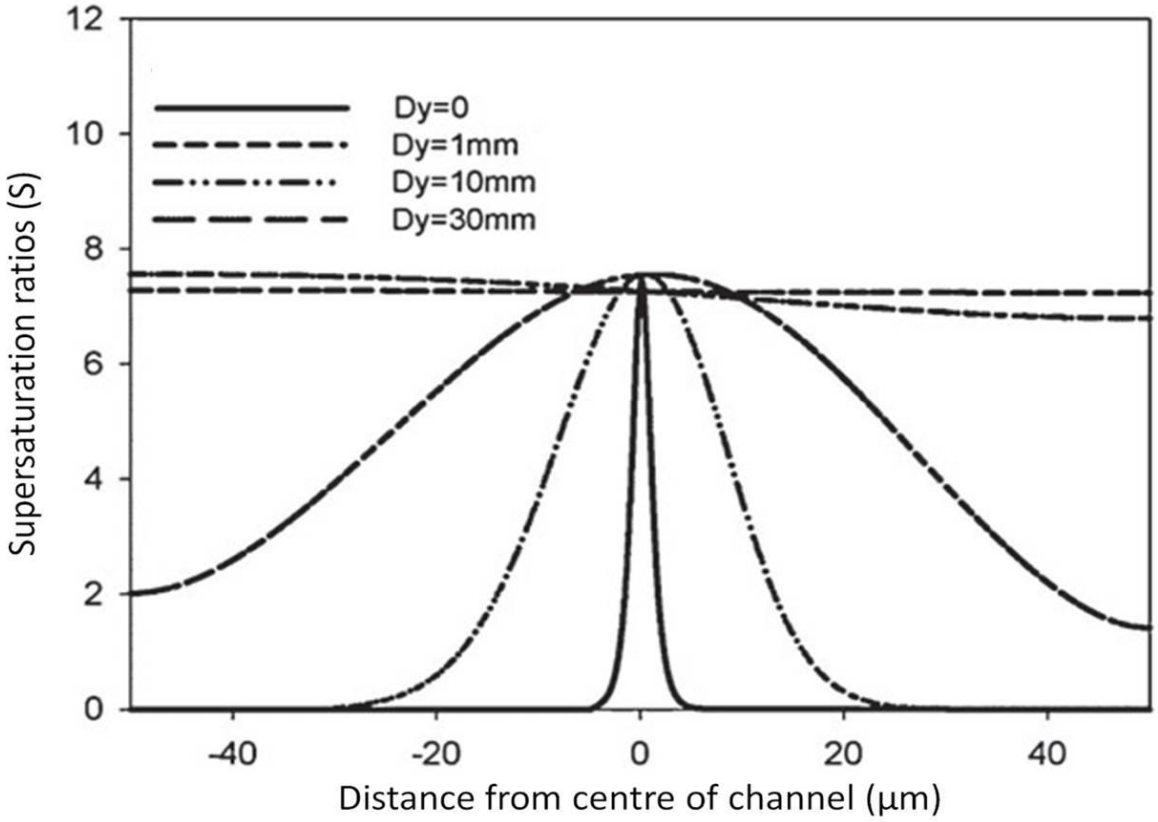

Figure 3.7.Simulation of supersaturation ratio in pH buffered condition.

Supersaturation ratio differs across the channel along the distances in flow direction (Dy). The various acid-base equilibrium and the MOPS buffer (100mM, pH7.5) were taken into account in the simulation. The supersaturation ratio was same calculated as previous non-buffered system.

This set of computational modelling results predicts the distribution of crystals along the microfluidic channel in this pH controlled condition. The simulation predicts that a single line of crystals will form in the channel in the initial stage of the two merged solutions (Dy<1 mm). Thereafter crystals will be more dispersed across the channel and finally crystals become well separated in the channel at the outlet. In addition, after delivering the same concentration of $CaCl_2$ and Na_2CO_3 solutions, a lower crystal density will occur in the channel in this pH controlled condition than the non-buffered de-ionised water conditions in previous work.

In this PhD project, two types of microfluidic channels are used: the T-junction channel and Y-type channel. In our experiments, same reagent solutions are running at similar velocity for both microfluidic channels: 5.2 mm/s for T-junction channel and 5.1 mm/s for Y-type channel. As a consequence, the similar computational modelling results are achieved, as presented in T-junction channel mentioned above, with steep step profile for the concentration gradient and central peaks profile for the supersaturation ratio (S).

3.2.2.3 Real time experiments with both protein and ion diffusion

To investigate the crystallisation in this pH buffered condition in microfluidic devices, real time on-chip crystallisation experiments are required. According to the modelling settings, 10 μg/ml of protein were added to $CaCl_2$ solution only, with all reagents bufferred in MOPS buffer (100 mM, pH 7.5). Crystallisation reagents of 10 mM $CaCl_2$ and 10 mM Na_2CO_3 solutions, were used for on-chip crystallisation. Two solutions were delivered at flow rate of 2 μl/min, controlled by syringe pumps. *In-situ* optical image recordings were required to determine the crystal on-chip distribution under this condition.

Under the condition of equal pH 7.5 in the presence of functional protein, overall investigation demonstrated that fewer crystals precipitated in the channel than in the de-ionised conditions. As to the initial stage of the interface, a line of individual crystals occurs in the centre of the channel (Figure 3.8A). This phenomenon remains for some flow distances (Dy≥1 mm) towards the outlet (Figure 3.8B). The stream of crystals start to disperse across the channel further towards the outlet (Figure 3.8C). Finally, crystals were well separated across the whole channel with protein and ion diffused into the other stream (Figure 3.8D). This real time crystallisation experiment demonstrates the crystal distribution throughout the whole channel in the buffered pH conditions.

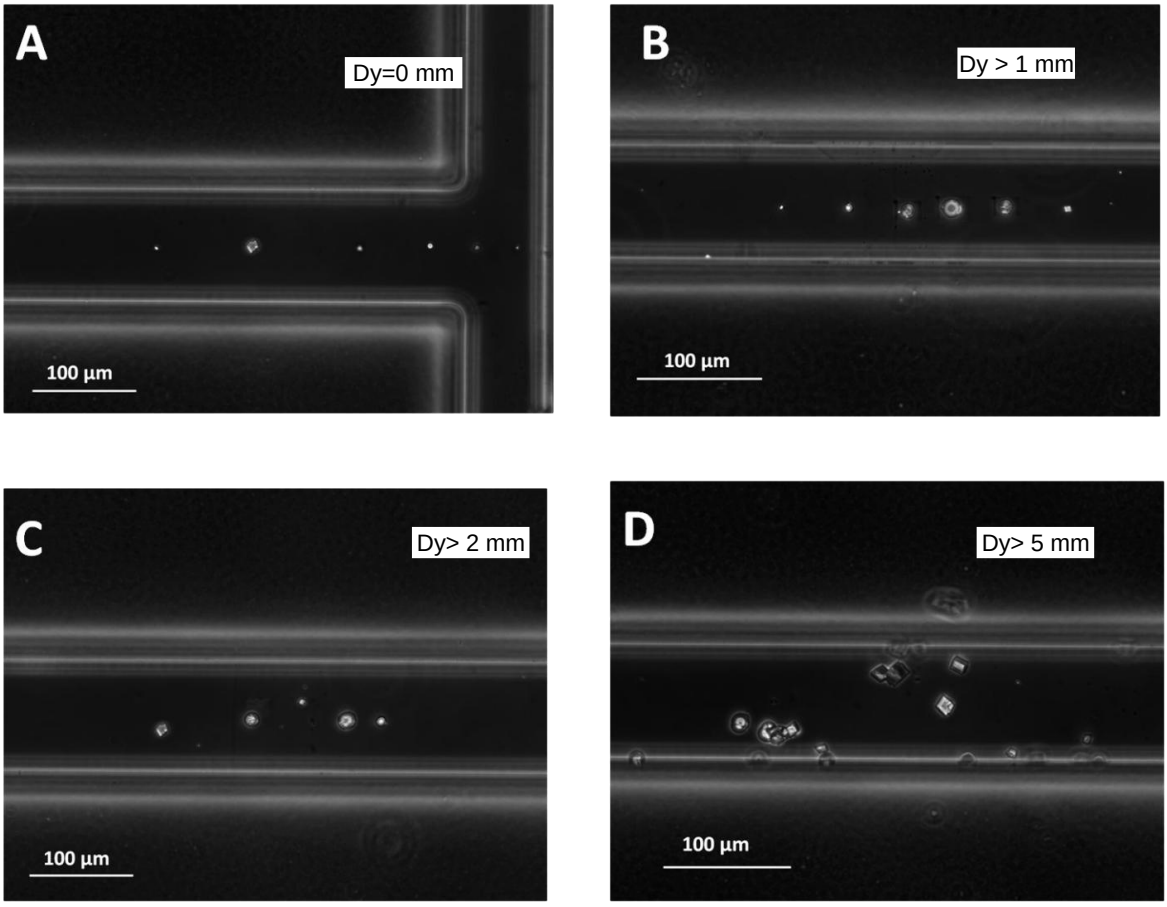

Figure 3.8. Optical images of the crystal precipitation in microfluidic channels.

Optical graphs show crystal distribution along the channel.(A) A line of individual crystals formed with Dy=0 mm and (B) remains for a long distance of Dy>1 mm. Crystals dispersed across the channel under mass diffusion (Dy> 2mm) (C) and finally across the whole channel (D).

This set of computational modelling results represents the crystal distribution in the microfluidic channels with the presence of both proteins and ion concentration gradients. The supersaturation profile demonstrated the crystal distribution in this microfluidic channel.Under the buffered pH (7.5) conditions, low supersaturation ratios (S) indicated lower crystal density than that in de-ionised water system. The coincidence between the computational modelling prediction and real time crystallisation experiments reveal the usefulness of this combination of modelling prediction and real-time confirmation experiments for crystal growth control. The modelling calculation reveals the ion and protein concentration gradient profile throughout the channel, which can be used for calcium carbonate on-chip crystallisation to investigate the protein influence on crystal formation control.

3.3 Discussion:

Compared to the mineral crystallisation in the de-ionised conditions, biomineralisation is a much more complicated process. There are three major steps for this processes, each exerting precise control. The first step is the templation of biomineral nucleation from the interaction from organisms. During the nacre formation, mantle cells are orchestrating the whole process, probably from assembling the chitin before mineralisation. Also, a local microenvironment for mineralisation is controlled by cells delivering the mineral-loaded vesicles into the nucleation site (Nudelman et al., 2006). In addition, biomineral properties are controlled by ions and organic molecules as a mineralisation modifier *in vivo*. During molluscan shell formation, the existing acidic proteins are thought to induce and control mineralisation to form the nacreous layer structures (Addadi et al., 2006). Finally, biomineral structures are perfectly regulated from the localized microenvironment (Xu et al., 2007). Take the example of nacre formation, the crystal first grows vertically along the *c*-axis until it reaches the limitation of chitin, and then grows laterally to form the tablet structure (Addadi et al., 2006). Meanwhile *in vitro* crystallisation experiments in the presence of functional peptides or proteins demonstrated the influence of specific proteins on crystal formation, i.e. the promotion of amorphous calcium carbonate (ACC) (Aizenberg et al., 1996, Lévêque et al., 2004, Politi et al., 2008). Therefore, it is important to investigate calcium carbonate crystallisation under the precise control of these functional biomineral proteins.

Computational modelling demonstrates the advantages of applying microfluidics to *in vitro* calcium carbonate crystallisation. In this pressure-driven laminar flow microfluidic system, the supersaturation ratio profile was calculated to predict the crystal on-chip distribution. Real time on-chip crystal distribution coincides with the prediction of supersaturation ratio profile in modelling results. This combination of the computational modelling and real time experiments demonstrated the well controlled crystal formation by the on-chip supersaturation ratios.

After reagent solution was delivered into the laminar flow microfluidic system, ions and proteins were transferred in both lateral mass diffusion (x-axis) and advection (y-axis) throughout the channel simutaneously. The modelling results denote a large number of crystallisation conditions have been achieved with specific ion and protein concentrations in each part of the microfluidic channel. Under these circumstances, crystals would be precisely controlled by the microenviroment of localised ions and proteins. Proteins that are potentially involved in biomineralisation can be screened using this approach for calcium carbonate crystallisation. The influence of biomineral proteins, the potential morphology and polymorph

control on crystallisation, can be determined by analysing the on-chip crystal formation along the microfluidic channel.

Chapter 4

Established protocols of microfluidics for $CaCO_3$ on-chip crystallisation

4

4.1 Introduction

4.1.1 $CaCO_3$ *in vitro* crystallisation system

A key issue in the study of biomineralisation is how biological molecules control crystal nucleation and orientation *in vivo* (Lowenstam and Weiner, 1989, Addadi and Weiner, 1992, Belcher et al., 1996, Yan et al., 2007). This is fairly difficult to determine as biological systems are complex, with many possible pathways for *in vivo* control (Nudelman et al., 2006, Addadi et al., 2006, Cartwright and Checa, 2007). Therefore, relatively simplified *in vitro* crystallisation systems have been used to control crystal nucleation and growth.

In the *in vitro* systems, additives such as proteins (Belcher et al., 1996, Gotliv et al., 2003), polymers (Ma et al., 2007, Pokroy et al., 2007), low molecular compounds (Gebauer et al., 2009, Wang et al., 2009b) and ions (Wilbur and Bernhardt, 1984, Loste et al., 2003b, Politi et al., 2010) are investigated for their effects on crystallisation. For example, magnesium has a vital impact on $CaCO_3$ crystallisation. Early *in vitro* experiments confirmed that crystal inhibition was achieved by Mg, by prolonging the induction time for crystal growth (Wilbur and Bernhardt, 1984). This was followed by experiments on stabilising amorphous calcium carbonate using $MgCl_2$ solution (Loste et al., 2003b, Politi et al., 2010). In addition, the ratio of [Mg]/[Ca] determined the crystal polymorph in aqueous conditions: low ratios produce calcite and a high ratio aragonite (Loste et al., 2003b, Dandeu et al., 2006, Falini et al., 2009). Not only Mg, other ions such as Sr^{2+} and K^{+} have also been used for *in vitro* crystallisation (Wasylenki et al., 2005, Gebauer et al., 2009, Falini et al., 2009).

In vitro, organic components are used to modify crystallisation in two main ways: either as additives in aqueous condition (Pietrzak et al., 1976, Suzuki et al., 2009, Dey et al., 2010) or serving as manufactured templates (Loste et al., 2003a, Aizenberg, 2004, Gower, 2008). In aqueous conditions, an acidic shell matrix protein from *P. fucata*, Aspein, was identified to induce calcite crystal formation in aqueous conditions (Takeuchi et al., 2008). They incubated

calcite crystals by adding 10 µg/ml Aspein as an additive into a reagent solution of Mg/Ca at a ratio of 5:1 for crystallisation. In addition, a double hydrophilic polymer consisting of polydiethylaminoethyl methacrylate (PDEAEMA) and polymethacrylic acid (PMMA) was used to induce pure branched aragonite crystals in aqueous conditions (Nassif et al., 2005). Polymers have also been used as organic templates to mediate crystal nucleation and orientation (Loste et al., 2003a, Dey et al., 2010, Li et al., 2011). Well-defined crystal topography with templated structure (~1 µm particle monolayer) was generated using a colloidal monolayer template in a bulk system (Meldrum and Ludwigs, 2007). In addition, printed templates with self-assembled monolayer (SAMs) of $HS(CH_2)_{15}CO_2H$ were used to control $CaCO_3$ nucleation and orientations in a slow diffusion bulk system (Aizenberg, 2004). All these findings demonstrate a range of *in vitro* systems that have been successfully used to control crystal nucleation and orientation.

In all these experiments, a bulk system with fixed reagent volumes was used, i.e. 500 ml solution was used to determine magnesium effect on crystallisation (Loste et al., 2003b). However, most studies demonstrated that additive concentrations influence crystallisation. In this chapter, we get into explore situation where the bulk process is not needed, but instead components are screened in an individual way to determine the order of events and subtle influence of each of the participants.

4.1.2 Laminar flow microfluidic system

The laminar flow microfluidic system provides a dynamic system with continuous flow for (bio-) chemical analysis in microlitres (Takayama et al., 2001, Ismagilov et al., 2001, Kuczenski et al., 2007). In the experimental design, reagent solutions containing proteins are delivered into the laminar flow microfluidic system. This method offers simultaneous control of microenvironments along the channel by locating [ion] and [protein] at different channel parts, which enables an opportunity to grow crystals in a number of conditions in a single channel. These conditions have been demonstrated from on-chip protein and ion concentration profiles using the computational modelling software (Comsol) in Section 3.2 in Chapter 3.

In order to establish a systematic screening method, extrapallial fluid proteins were used. The wild-type extrapallial proteins, existing in the cavity between the shell and organic mantle, are considered important for *in vivo* shell growth (Wilbur and Saleuddin, 1983, Wilbur and Bernhardt, 1984). The total wild-type extrapallial fluid proteins (TWEP) mixture is used for on-chip crystallisation. TWEP is the total proteins extracted from the extrapallial cavity from the bivalve *M. edulis,* which is made up of many proteins, some of which may, or may not, be

involved in biomineralisation.

4.2 Results

4.2.1 Fast crystal on-chip growth in aqueous conditions

Under appropriate control of the flow rate, the pressure-driven laminar flow system can generate a series of conditions with stable concentration gradients. In the first trial experiments on applying the microfluidic system to biomineral studies, a simple T-junction microfluidic device with ~5 cm long reaction channel was initially used (Figure 2.1 in Chapter 2). Calcium chloride ($CaCl_2$) and sodium carbonate (Na_2CO_3) were used as reagents, with both dissolved in de-ionised water without pH control. Aliquots of reagent solutions were continuously delivered into the microfluidic channels for on-chip crystallisation. In order to investigate the influence of reagent concentration on crystal formation, a range of concentrations were used, including 1 mM, 10 mM, 50 mM and 100 mM.

In the presence of very low concentration (1 mM) of both reagents, no crystals precipitated in the channel after constant delivery for 20 min. Crystals started to precipitate once a concentration of 10 mM was reached. In the presence of 10 mM $CaCl_2$ and Na_2CO_3 solutions, a line consisting of a few individual crystals formed, biased towards the CO_3^{2-} channel (Figure 4.1A). Compared to crystallisation with 10 mM reagents, when 20 mM was delivered into microfluidic channel, a stream of crystals formed in the Na_2CO_3 channel side with higher crystal density (Figure 4.1B). When a higher concentration of 50 mM was used, a stream of crystals with greater density formed in the channel (Figure 4.1C). However, in the presence of 100 mM, a large number of crystals precipitated across the whole channel (Figure 4.1D). This was a result of greater supersaturation ratio in the presence of high concentrations.

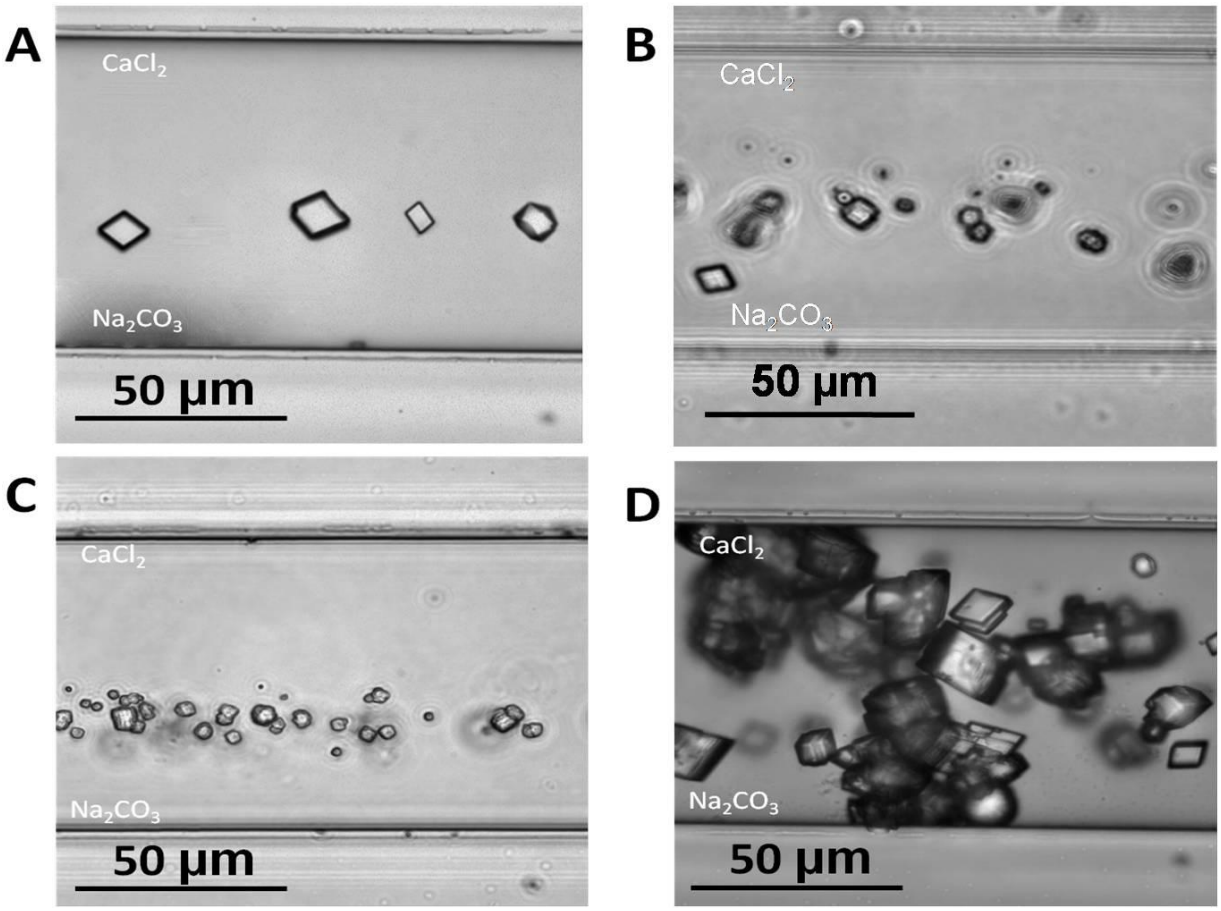

Figure 4.1. On-chip crystallisation with different reagent concentrations.

(A) Individual crystals aligned in a line in the CO_3^{2-} side of channel with 10 mM reagent solution. A stream of crystals formed in the presence of both (B) 20 mM and (C) 50 mM of reagents into the microfluidic channels. (D) High crystal density occurs cross the whole channel after delivering 100 mM reagents of both $CaCl_2$ and Na_2CO_3.

The reagent concentration influence is seen with high crystal density in the channel in the presence of highest reagent concentration (100 mM). This high density distribution would prevent the analysis of individual crystals. In addition, previous modelling has shown a range of reaction conditions being achieved using appropriate reagent concentrations such as 50 mM. As a consequence, a concentration of 50 mM for each reagent was used for protein screening in this project. This ensured sufficient crystals were produced while avoiding crystal 'overcrowding' in the channel, which would have enhanced the analysis of individual crystals by Raman spectroscopy.

4.2.2 Crystal off-chip analysis using Raman spectroscopy & SEM

The reversible sealed microfluidic chip enhances the off-chip analysis of crystal polymorph identification from Raman spectroscopy and morphology study *via* scanning electron microscope (SEM). With appropriate volume of reaction solutions, well-dispersed crystals formed on the surface of the glass substrate and PDMS channels of microfluidic chips. After crystal on-chip formation, methanol was run-through the channel to 'freeze' the crystals for further analysis.

Rhombohedral crystals were dominant in the microfluidic channel when both reagents were dissolved in de-ionised water without any additives (Figure 4.2). Micro-Raman spectroscopy was used for crystal polymorph identification. In this experiment, over 10 crystals were randomly selected for Raman spectra collection. The Raman results showed the same spectra for crystals investigated, with the strongest peak at 1086 cm^{-1}, and vibration bands of 710 cm^{-1}, 281 cm^{-1} and 155 cm^{-1}. These specific peaks identify the cubic structures as calcite crystals. Scanning electron microscope (SEM) images showed the well dispersed crystals in detail. All crystals have similar cubic morphology, aligning on the glass coverslip according to the microfluidic channel. Figure 4.2B shows crystals at the turn of the channel.

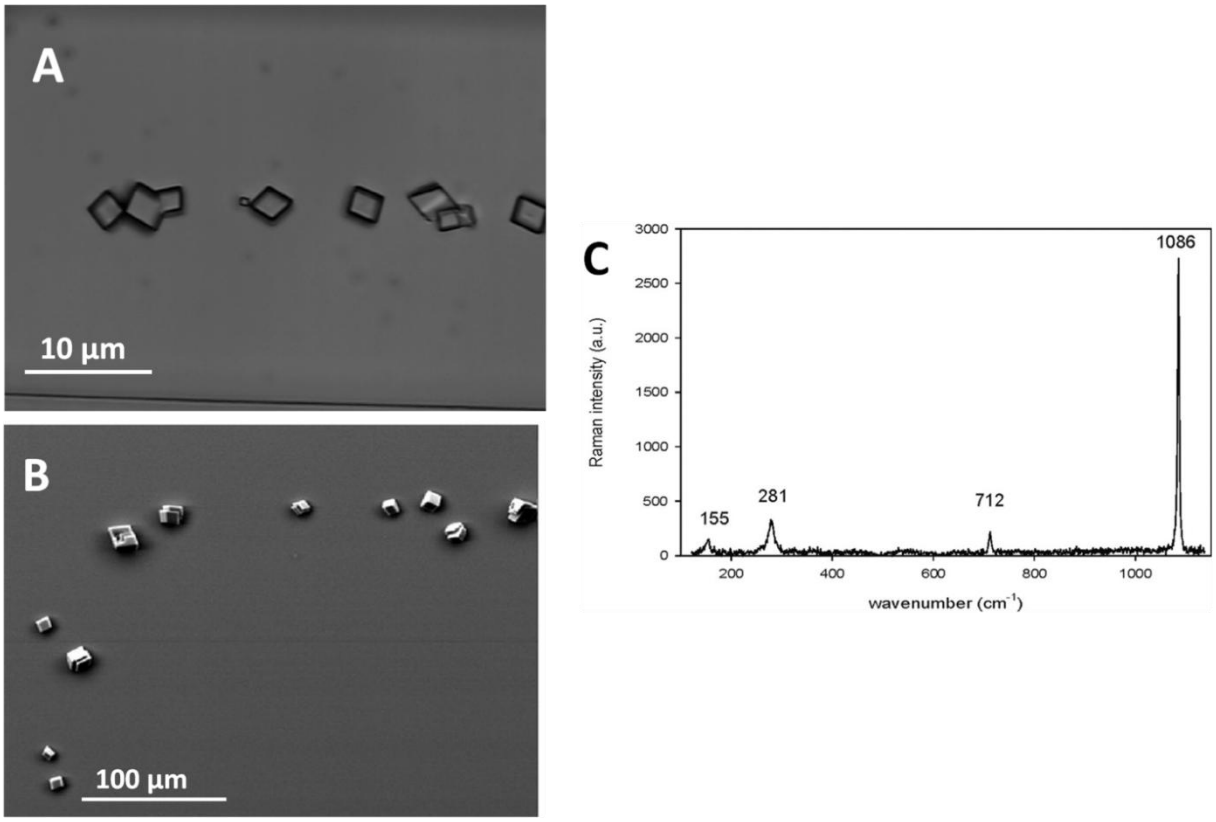

Figure 4.2. Off-chip analysis of crystals formed in microfluidic channels.

(A) Optical microscope image reveals a line of crystal formed in the channel with 10 mM $CaCl_2$ and 10 mM Na_2CO_3. (B) Scanning electron microscope (SEM) observation of crystals formed on the glass cover-slip of microfluidic chip. Well dispersed crystals formed along the channel figures. (C) Polymorph identification using Raman spectroscopy confirmed the crystals as calcite.

The combination of on-chip crystallisation and off-chip analysis presents a novel platform for biomineral studies. In the de-ionised water conditions, calcite was the dominant polymorph formed in a wide range of concentration gradients of $CaCl_2$ and Na2CO3 solutions.

4.2.3 On-chip screening of TWEP protein

In native conditions, calcium carbonate deposition under biological control is not as simple as the experiments above using $CaCl_2$ and Na_2CO_3 in de-ionised water. For some long time, the extrapallial fluid was considered important for molluscan *in vivo* shell formation (Wilbur and Bernhardt, 1984, Fritz et al., 1994, Weiner, 2008). Rich in inorganic and organic components, the extrapallial fluid supplies potential roles in the biomineralisation process including providing a microenvironment for $CaCO_3$ deposition (Crenshaw, 1972, Misogianes and

Chasteen, 1979).

The laminar flow microfluidic system provides an opportunity to screen these EP proteins using small volumes. In this trial experiment, the total wild-type extrapallial (TWEP) protein mixture is used for on-chip crystallisation in a T-junction channel. This T-junction microfluidic device enables comparison of crystal formation in different channel parts, from the initial stage to the end of channel, where different ion concentrations exist. To compare the results with TWEP protein, the same experiments were carried out using BSA and Tris buffer (100 mM, pH 7.5).

In the presence of TWEP protein, branched crystal clusters were firstly observed in microfluidic channel (Figure 4.3A). This cluster structure is similar to the synthetic aragonite formation (Dandeu et al., 2006). However, this is an unstable formation with continuous reagents running through the channel. Oval crystals, derived from these clusters, subsequently appeared in the microfluidic channel (Figure 4.3B). This is a unique phenomenon only existing in the presence of TWEP protein. It was not seen in the condition when Tris buffer (100mM, pH 7.5) or BSA was used.

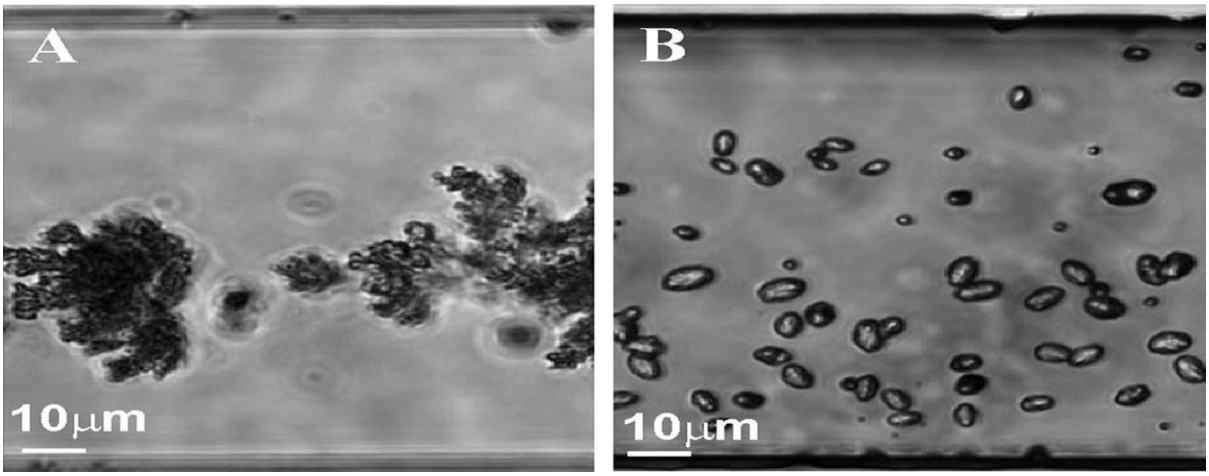

Figure 4.3. Optical images of $CaCO_3$ on-chip crystallisation with TWEP proteins.

(A) Unstable branched crystal clusters initially formed in the channel. (B) Subsequently, clusters transformed into stable ovoid-shaped crystals.

For each condition, five crystals were selected for Raman analysis. An average of three spectra was collected for each single crystal. The ovoid crystals (Figure 4.4A), formed in the presence of TWEP protein, were identified as calcite. Average Raman spectrum gives a strong signal at 1086 cm^{-1}, with characteristic peak at 281 cm^{-1} (Figure 4.4B). In contrast to the calcite crystals formed in the control experiments, the background spectrum of ovoid

calcite crystals is higher and the intensity ratio of the main peak (1086 cm^{-1}) compared to two other peaks (712 and 281 cm^{-1}) is lower (Figure 4.4B).

In the control experiment with BSA, both spherical and rhombohedral crystals precipitated in the channel (Figure 4.4C). The rhombohedral crystals were confirmed as calcite, with characteristic peaks at 1086 cm^{-1}, 710 cm^{-1}, 281 cm^{-1} and 155cm^{-1} (Figure 4.4D). The spherical crystals were identified as vaterite by Raman. Average Raman spectra presented spherical crystals with strong signals at 1073 cm^{-1} adjacent to the major peak at 1088 cm^{-1} (Figure 4.4F). Both crystals also appear in the experiment with buffer system only (Figure 4.4E).

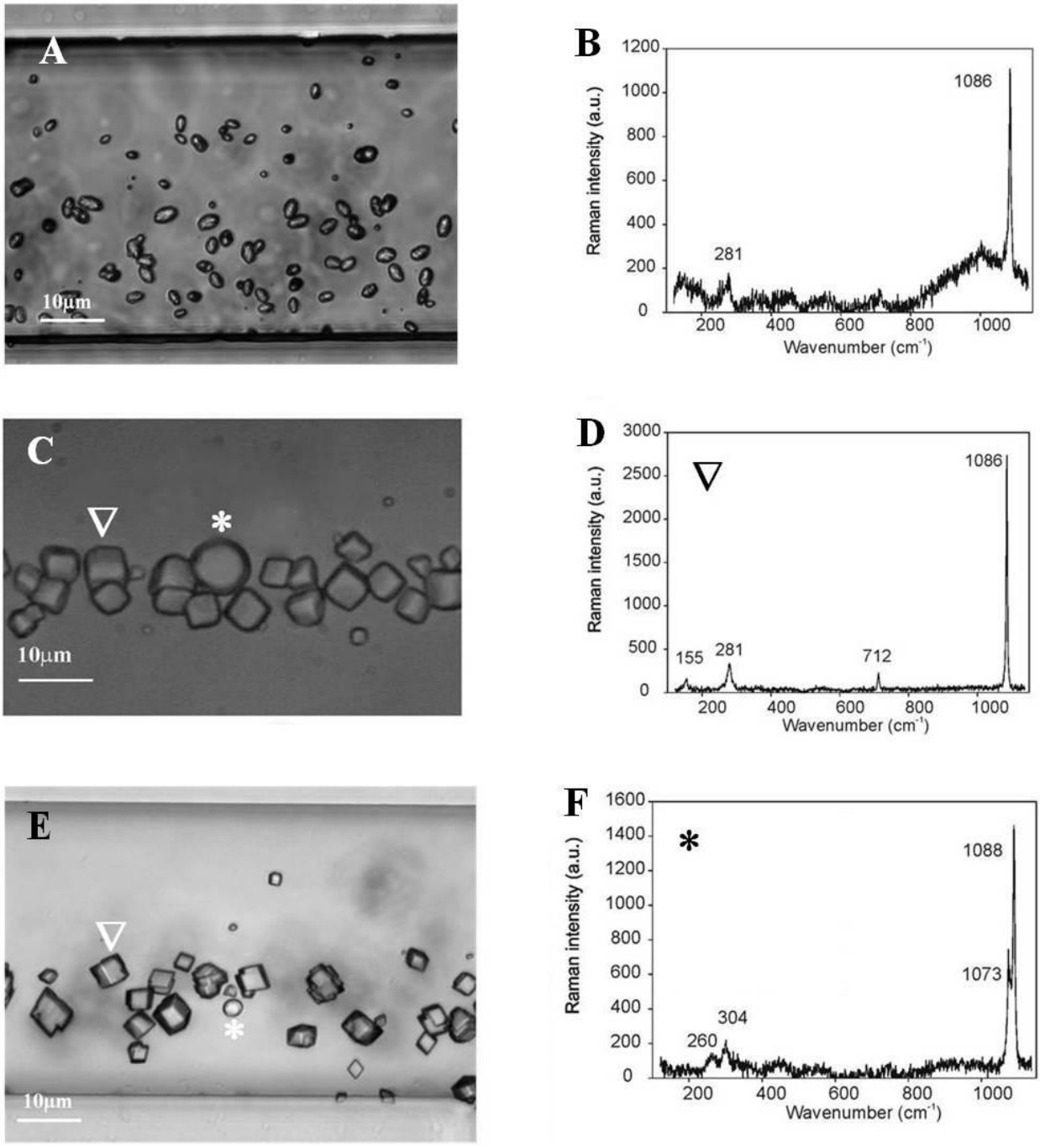

Figure 4.4.Fast screening of on-chip crystallisation.

(A) Ovoid-shaped crystals were dominant in the presence of TWEP protein mixture. (B) The Raman spectrum identified the ovoid crystal as calcite with calcite-like Raman spectra but with much higher background scattering. Similar phenomenon of both spherical and rhombohedral crystals has been generated in the control experiments of (C) BSA and (E) Tris buffer system only. Raman spectra presented (D) calcite and (F) vaterite crystals.

After polymorph identification from Raman spectra, scanning electron microscopy (SEM) was used to observe crystal morphology. In the presence of TWEP proteins, the ovoid crystals

were presented as peanut-shaped structures (Figure 4.5A). High-magnification SEM images revealed that these peanut-shaped crystals had a rough surface (Figure 4.5A, Insert). In the control experiments, both rhombohedral calcite and spherical vaterite crystals were observed in the channel (Figure 4.5B&C). The inserted high-resolution SEM images show the details of both the spherical vaterite (Figure 4.5B) and rhombohedral calcite crystals (Figure 4.5C) with smooth surfaces (Figure 4.5B&C, Inserts). However, BSA generated more vaterite crystals (Figure 4.5B), compared to that of the buffer system (Figure 4.5C).

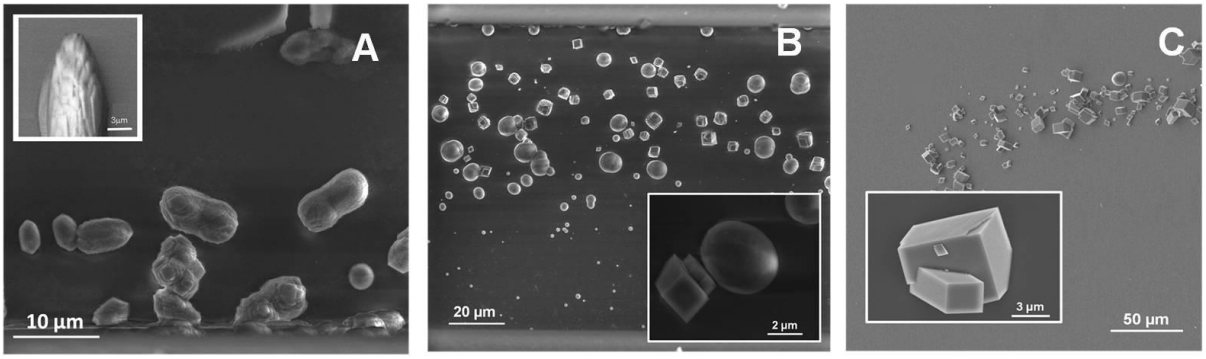

Figure 4.5. SEM images of on-chip crystallisation.

(A) In the presence of TWEP protein mixture, the ovoid calcite crystals were shown as peanut-shaped crystals. The insert high-magnification image represents the rough surface on the pea-nut shaped crystals. (B) In microfluidic channels, BSA induced spherical vaterite and rhobomhedral calcite crystals. (C) Similar phenomenon occurs in the Tris buffer (100mM, pH 7.5) conditions. The insert high-magnification SEM images show the details of both spherical and cubic calcite crystals.

The presence of TWEP protein induced ovoid calcite formation in microfluidic channels, illustrating the effect that TWEP protein has on crystal morphology. In the control experiments, calcite was the dominant polymorph, while again shows the influence of the TWEP protein.

4.2.4 *In-situ* Raman detection during crystal formation

In the biomineral process, calcium carbonate crystallisation is a kinetic process, controlling crystal morphology, size and orientation (Verdoes et al., 1992, Cölfen, 2007). Optical recording alone cannot distinguish which polymorph has been formed, since several different gross morphologies can exist within the same polymorph. The examples are the rhombohedral and peanut-shaped crystals identified as calcite in this study, as well as the nacre tablet and branch cluster crystals confirmed as aragonite. Therefore, monitoring crystal

polymorph switch during *in vitro* growth is important for understanding the crystallisation mechanism involved in the biomineral process.

Raman spectroscopy, the non-destructive and non-invasive analysis approach, has great application i.e. live cell analysis and synthetic structure detection (Maguregui et al., 2009). For this *in-situ* analysis, we integrated micro-Raman spectroscopy and the microfluidic device for crystal polymorph detection during on-chip growth. Real time Raman spectroscopy enables investigation on crystal formation from the very initial stage.

In this set of *in-situ* Raman experiments, the TWEP protein was used for crystal growth. All microfluidic chips were placed on the microscope with the Raman detector. Real-time Raman spectra were collected every 40 s during crystal formation. Initially, no significant spectrum appeared on the interface during the induction time. As flow progressed, a strong peak at 1086 cm^{-1} appears on initial crystal formation, but no significant peaks at 710 or 281 cm^{-1}. At this early stage, it is not possible to distinguish polymorph. With time increasing, all Raman peaks were getting stronger, at 1086, 710 and 281cm^{-1}, which identified the crystals as calcite (Figure 4.6). More spectra were collected during the investigation to identify that there was no polymorph switch during formation. It can be concluded that calcite was initially formed in the presence of TWEP proteins in the microfluidic system, without polymorph switch during crystal growth.

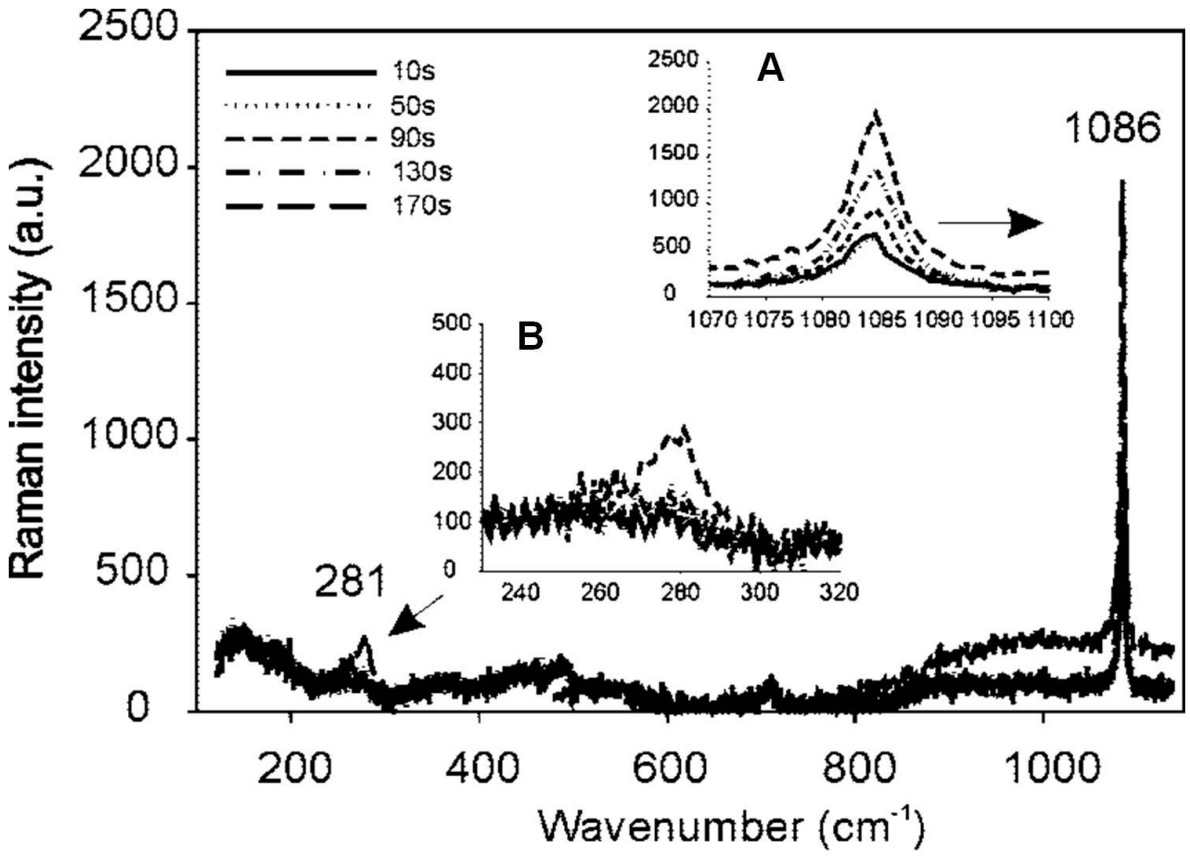

Figure 4.6. *In-situ* Raman spectroscopy of on-chip crystal formation with TWEP protein mixture.

Consecutive spectra were collected every 40 s from the initial joint of interface. (A) The Raman peak at 1086 cm^{-1} firstly appeared to show the calcium carbonate. (B) With time elapse, the peak of 281 cm^{-1} increased without any shift, which identified the crystal as calcite.

This is the first example of the integration of a microfluidic device with micro-Raman spectroscopy in biomineralisation study. It provides a platform to investigate the mechanism of crystal formation in the presence of functional macromolecules from initial stage of crystal precipitation. This has demonstrated an approach for real-time polymorph monitoring during crystallisation, which can be used for functional screening of biomineral proteins.

4.3 Discussion

The detailed mechanism of $CaCO_3$ crystal growth control during *in vivo* shell formation is poorly understood. We have demonstrated the microfluidic approach as an important tool in the rapid screening of biomineral extrapallial proteins during $CaCO_3$ *in vitro* crystallisation. In

this experiment, reversible sealed microfluidic device was developed. T-junction channel was designed to allow consistent laminar flow when the two solutions met in the channel. This uses a mass diffusion module to create a mass concentration gradient profile along the channel, as well as a large range of crystallisation conditions with different supersaturation ratio (S) (Chapter 3).

This study clearly shows the advantages of using a microfluidic approach for crystal formation over traditional methods. This technique consumes small quantities of functional proteins, but yields much information on rapid screening of biomineral proteins. In this laminar flow approach, crystal morphology control has been achieved using the extrapallial proteins, inducing ovoid calcite crystals. *In-situ* Raman spectroscopy indicates no polymorph switch during this calcite crystal formation in the presence of TWEP proteins. The result of this initial set of experiments provides a platform to study individual proteins that have been purified from the extracted extrapallial fluid.

Chapter 5

Functional screening of biomineral proteins using the microfluidic system

5

5.1 Introduction

5.1.1 Calcium carbonate polymorphs

As described in the general introduction, calcium carbonate, one of the most widely studied biominerals, has three main crystalline polymorphs (vaterite, aragonite and calcite) (Addadi et al., 2006, Meldrum and Ludwigs, 2007, De Paula and Silveira, 2009), two hydrated crystal forms (calcium carbonate monohydrate and calcium carbonate hexahydrate) (Peric et al., 1996, Nebel et al., 2008) and an amorphous calcium carbonate (ACC) precursor (Politi et al., 2008).

Calcite and aragonite are the most common polymorphs in the biosphere, both of which can occur in the mollusc shells (Marin and Luquet, 2005, Addadi et al., 2006, Nudelman et al., 2006). The mussel *Mytilus edulis* produces a well defined bimineralic shell structure with an outer layer of prismatic calcite and an inner layer of aragonite nacre (Cusack and Freer, 2008). This contiguous formation is under exquisite biological control from organic components (Addadi et al., 2006, Cusack and Freer, 2008).

In this chapter, calcium carbonate *in vitro* crystallisation is investigated in the presence of several individual extrapallial fluid proteins, including the major wild-type 28 kDa extrapallial (WEP) protein, the major expressed extrapallial (EEP) protein, the C1q domain and the wild-type extrapallial complex (WCEP) protein. All of these proteins were used to study crystallisation in the microfluidic system and also to compare these results with conventional bulk system experiments.

5.1.2 Molluscan extrapallial (EP) proteins

The extrapallial (EP) fluid, filling the cavity between organic mantle tissue and the inner shell surface, is considered to influence shell formation. This has been supported by the flat pearl

formation on inorganic substrates inserted into the extrapallial space of abalone *Haliotis rufescens* (Fritz et al., 1994, Zaremba et al., 1996). There are many inorganic ions in the extrapallial fluid, including K^+, Ca^{2+}, Mg^{2+}, Na^+, SO_4^{2-}, Cl^- and CO_3^{2-} (Crenshaw, 1972, Pietrzak et al., 1976). The components of the extrapallial fluid have calcium-binding capacity and as a consequence, the EP fluid has a calcium ion concentration of approximately 9.8 mM, with over 70% of the calcium bound to small molecules (Misogianes and Chasteen, 1979). Both the Ca^{2+}-binding ability and the spatial location of extrapallial fluid suggest that it has a potential role during shell formation (Wilbur and Bernhardt, 1984).

In recent decades, major advances in molecular biology have been used in the identification of molluscan proteins (Miyamoto et al., 1996, Marin et al., 2007, Takeuchi et al., 2008, Suzuki et al., 2009). The reverse transcription polymerase chain reaction (RT-PCR) has been widely used to generate the amplified DNA sequence allowing protein expression of biomineral proteins, which enhances the opportunity for functional studies of these molluscan shell matrix proteins (Takeuchi et al., 2008, Kong et al., 2009). Recently, RNA interference (RNAi), a molecular biology technique to silence the target gene expression, has been used to clarify the *in vivo* function of the Pif protein, which is involved in aragonite layer binding (Suzuki et al., 2009). Simultaneously, pyrosequencing techniques using expressed sequencing tags (ESTs) have been used to cover most of the diversity of matrix protein in *P. margaritifera* shell. This novel technique has also been used to encode of the shell matrix proteins, which indicates their implications on shell formation (Clark et al., 2010, Craft et al., 2010, Joubert et al., 2010).

Organic components of the extrapallial (EP) fluid from the bivalve *M. edulis* had been initially analysed by Misogianes and Chasteen (1979). In their studies, at least five proteins were confirmed from the extrapallial fluid using a disc gel electrophesis system. Hattan *et al.* (2001) illustrated that the major EP protein from *M. edulis* exists as a dimmer with a monomeric molecular weight of 28.3kDa and is highly glycosylated (estimated 14% of total mass is carbohydrate). This protein has a pI of 4.43 indicating an acidic protein with probable calcium-binding capacity. This calcium-binding interaction is coupled with changes to the protein secondary structure (increase in α-Helix, and reduction in β-sheet) (Hattan et al., 2001). These findings provide a starting point to investigate the mechanism of *in vivo* biomineralisation.

Yin *et al.* (2005) used molecular biology methods, including the reverse transcription polymerase chain reaction (RT-PCR) and rapid amplification of cDNA ends (RACE), to characterise the primary structure of the main extrapallial (EP) protein from *M. edulis*. They

determined that the major EP protein is composed of 236 amino acids of 24.3 kDa with an N-linked acidic glycan (~4kDa). This protein binds to Ca^{2+} and other divalent ions such as Mg^{2+}, Cd^{2+}, Mn^{2+} and Cu^{2+}. The amino acid sequencing and protein domain prediction indicate that the Ca^{2+}-binding sites and H^{+}-binding receptors are probably located towards N-terminus, which is rich in Ca^{2+}-binding amino acids, such as Asp. All these findings imply a potential role for this protein during biomineralisation, calcium transportation for shell growth and heavy metal detoxification (Yin et al., 2005).

5.1.3 Influence of EP proteins on crystallisation

Due to their calcium-binding abilities, molluscan extrapallial proteins may fulfill several functions during biomineralisation (Misogianes and Chasteen, 1979, Hattan et al., 2001, Yin et al., 2005). In order to determine the function of the extrapallial proteins, they have been used for *in vitro* crystallisation studies. Wilbur *et al.* (1984) used the extrapallial fluids (EPF) from both the oyster *Crassostrea virginica* and the clam *Mercenaria mercenaria* for crystallisation. The EPF inhibits crystallisation by prolonging the crystal induction time *(Wilbur and Bernhardt, 1984)*. A novel ~38 kDa EP protein from the pearl oyster *Pinctada funcata* was determined to be an amorphous calcium carbonate-binding protein (ACCBP), rich in acidic residues with its theoretical pH at 4.56 (Ma et al., 2007). Crystal binding experiments indicate this 38 kDa protein having crystal recognisation ability. This capacity to bind to specific polymorph potentially influences *in vivo* crystal deposition by protecting undesired crystal attachment (Ma et al., 2007).

The total wild-type extrapallial fluid (TWEP) protein mixture from the bivalve *M. edulis* (Figure 5.1A), has already been screened for calcium carbonate crystal formation in the laminar flow microfluidic system (Chapter 4 Section 4.2). Crystallisation results demonstrate the influence of TWEP on crystal growth, inducing ‘peanut’ shaped calcite crystals in the microfluidic channel (Yin et al., 2009).

Apart from the total wild-type extrapallial (TWEP) proteins, four different protein samples were screened to investigate the influence of individual EP proteins on crystallisation. Before the consideration of the synergistic effects on crystallisation between exrapallial proteins, all proteins are used to modify $CaCO_3$ on-chip crystallisation individually. This functional study experimental design will contribute to the understanding of potential influence from individual proteins and then how to control crystallisation collaboratively. In these experiments both wild-type and expressed proteins were used (Figure 5.1). The major wild-type 28 kDa extrapallial (WEP) protein (Figure 5.1B), directly extracted from living mussels, has already

been identified and characterised in previous work (Hattan et al., 2001, Yin et al., 2005). The properties and calcium-binding ability implied a possible involvement in crystallisation. Molecular biology techniques have been used to express the 28 kDa WEP, the major expressed extrapallial (EEP) protein (Figure 5.1C) and the C1q domain of this protein (Figure 5.1D). As to further characterise the WEP protein, the cDNA coding WEP protein was synthesised using GenScript. WEP cDNA was incorporated into plasmid pET21a which was further amplified in the *E.coli* System. Therefore, EEP protein has the same amino acid sequence as the WEP protein, but without the carbohydrate moiety (Figure 5.2A). The C1q domain is a 14 kDa (Figure 5.1D) C-terminal conserved domain of the EEP (Figure 5.2B). In addition, a wild-type complex was extracted from the extrapallial fluid and purified using ion exchange chromatography. Three bands from this complex are usually associated together in sodium dodecyl sulfate polyacrylamide gel electrophoresis (SDS-PAGE) (Figure 5.1E).

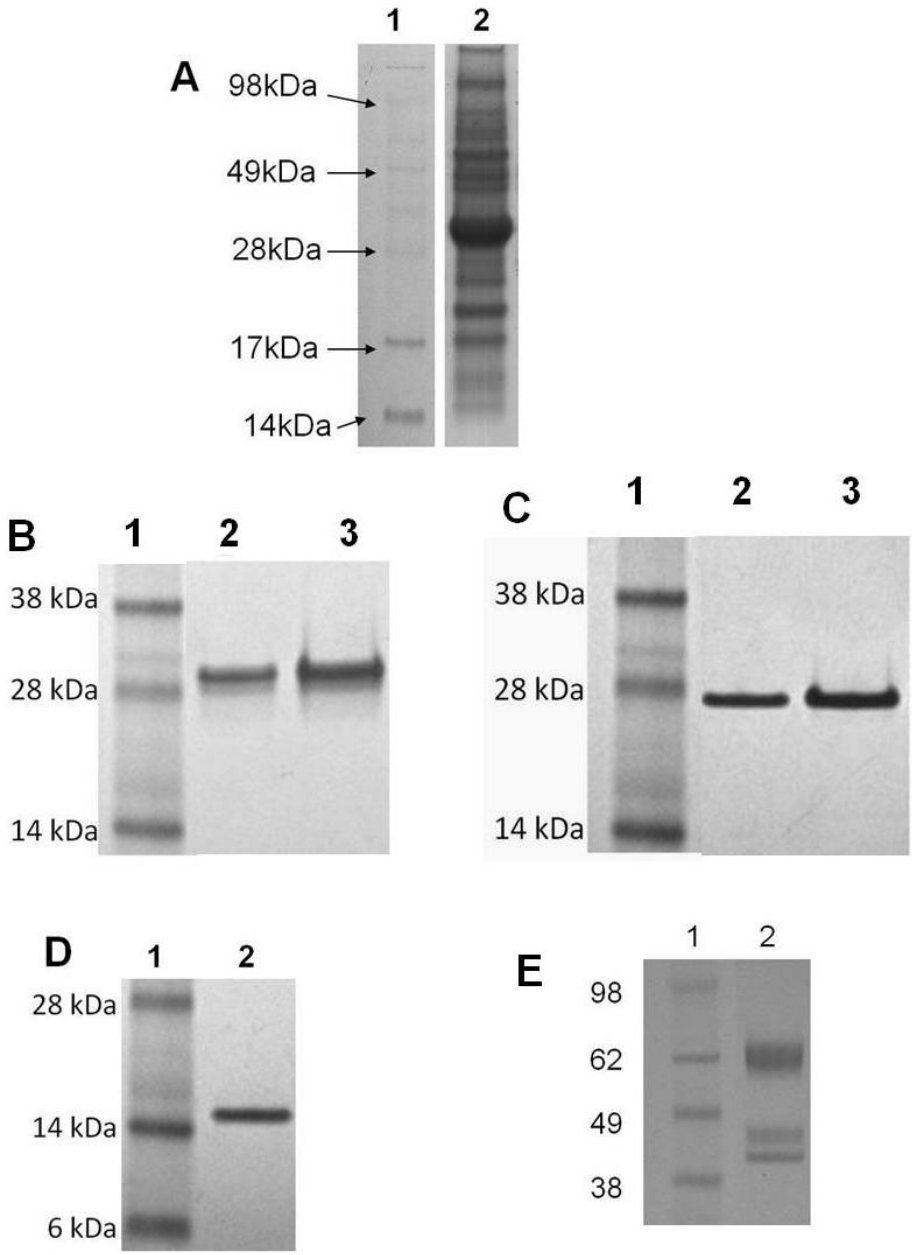

Figure 5.1. Electrophoretic analyses of extrapallial fluid proteins.

There are four individual extrapallial proteins used for functional screening on calcium carbonate crystallisation. Each sample was subjected to SDS-PAGE analysis on 10% gel and stained with Coomassie blue. (A) The total wild-type extrapallial (EP) proteins from *M.edulis* (lane 2). A multitude of proteins are present in this mixture. (B) The profile of the major wild-type 28 kDa extrapallial fluid (WEP) protein from *M. edulis* (lanes 2, 3). (C) The expressed major extrapallial fluid (EEP) protein from *E.coli* system (lanes 2, 3). (D) The conserved C-terminal domain, C1q domain has a molecular weight 14 kDa (lane 2). (E) The wild-type extrapallial fluid complex (WCEP) proteins from *M. edulis* (lane 2). There are three proteins associated together during protein purification in the range of 40 to 62 kDa. The lanes 1 in all images are the molecular protein standards presenting the molecular weight.

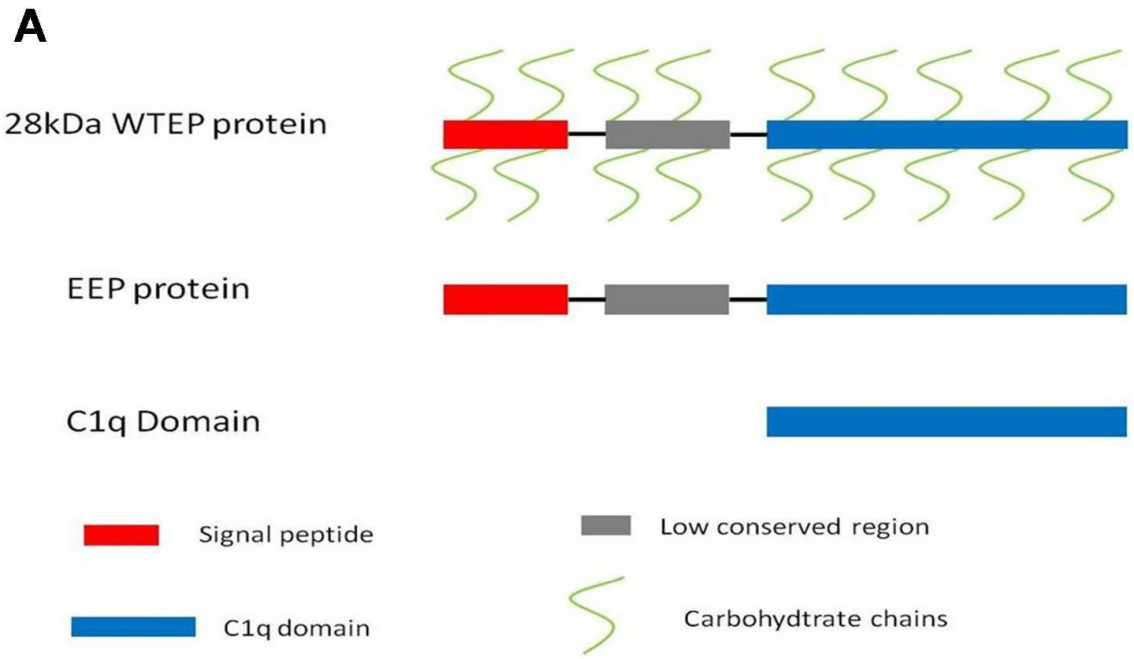

B

1	MGRYQISLLV	LFCVVSLFDQ	GLTNPVDDHH	GDDHHDAPIV	GHHDAFLKAE
51	FDLTSLNADL	EKFIHHEIEK	EIHDVENHTE	HNKHEIDELH	QEIKHLHEEV
101	EYFKSHHVAF	SAELTHPIEN	IAAEEIAHFD	KVRVNSGHAY	HADTGKFVAP
151	EEGFFYFSVT	ICTKRDSILE	MALHVNDHDE	MIIHADAEHL	ELGCASNSEI
201	VHLQKGDHVE	VVKHGADGVP	PFYIHTMSTF	TGFMLH	

Figure 5.2. Illustration of the major extrapallial fluid proteins in *M. eduis*.

In this functional screening study, three proteins related to the main EP protein are screened: the wild-type EP protein, expressed EP protein and the C1q domain. (A) Cartoon shows the protein components of all three screened main EP proteins. The 28 kDa WTEP protein is a glycosylated protein. EEP has the same amino acid sequence but without carbohydrate, C1q domain is the conserved C-terminal domain of the main extrapallial fluid protein. (B) Amino acid sequence of the main EP protein from mussel *M. edulis*. The red region indicates the conserved C1q domain.

All four EP proteins were screened to assess their roles on crystallisation in both conventional bulk conditions and microfluidic system. Using the microfluidic system, the combination of computational modelling and real-time on-chip crystallisation provides precise control of experimental conditions for crystallisation (Chapter 3). This advantage of generating a large number of scenarios with precise control over crystallisation cannot be achieved by the bulk system. This combination has been used to identify the influence of these four proteins on crystal distribution and morphology.

5.2 Results

5.2.1 Crystallisation with EP proteins in bulk system

There have been many investigations on the application of Ca^{2+}-binding acidic polymers, i.e. polyacrylic acid (PAA) and polyaspartic acid (poly-Asp) on $CaCO_3$ crystallisation (Gower and Odom, 2000, Park and Meldrum, 2004, Nassif et al., 2005, Cheng et al., 2007, Cölfen, 2007). Han *et al.* (2007) demonstrated that at low concentrations of PAA, amorphous calcium carbonate (ACC) spheres aggregated to form hollow structures. A twin-sphere structure has been generated in the presence of poly L-lysine (pLys) in a slow diffusion system (Yao et al., 2009). All these findings illustrate the modification effect of Ca^{2+}-binding polymers on crystal formation. In order to identify the influence of extrapallial (EP) proteins on $CaCO_3$ crystallisation, a conventional bulk precipitation approach using an eppendorf™ tube was used to study crystal growth. This has been described in Chapter 2.

Before crystallisation, all individual EP proteins, including the major wild-type 28 kDa extrapallial (WEP) protein, the wild-type extrapallial complex (WCEP) protein, the major expressed extrapallial (EEP) protein and the expressed C1q domain, were mixed with $CaCl_2$ only, Na_2CO_3 only, or both reagent solutions to create a range crystallisation conditions analogous to those used in microfluidics to determine the protein influence.

In the presence of 28 kDa WEP protein mixed with different reagents, calcite is the only precipitated polymorph in bulk conditions. Multilayer calcite structures have been achieved under this circumstance (Figure 5.3A).The insert is the high-magnification SEM image representing the crystal details in layered structures (Figure 5.3A, Insert). Calcite is also the dominant polymorph in the presence of the WCEP protein, with conventional rhombohedral morphologies (Figure 5.3B). However, in the presence of EEP protein, both layered calcite crystals and spherical vaterite crystals formed (Figure 5.3C). Similar results have been achieved in the presence of C1q domain (Figure 5.3D). The high-magnification SEM images represent the similar crystal results with spherical vaterite and layered calcite crystal formation (Figure 5.3C &D, Insert).

All these crystallisation experiments demonstrate the shortfall of the bulk system in identifying the EP protein function on crystallisation. The similar phenomenon of predominant calcite crystal formation occurs when WEP or WCEP was used for crystallisation in bulk system. The multilayer calcite and spherical vaterite crystals were generated by both EEP protein and C1q domain in bulk conditions. In addition, the same crystallisation results were achieved when

one specific EP protein was mixed with different reagents.

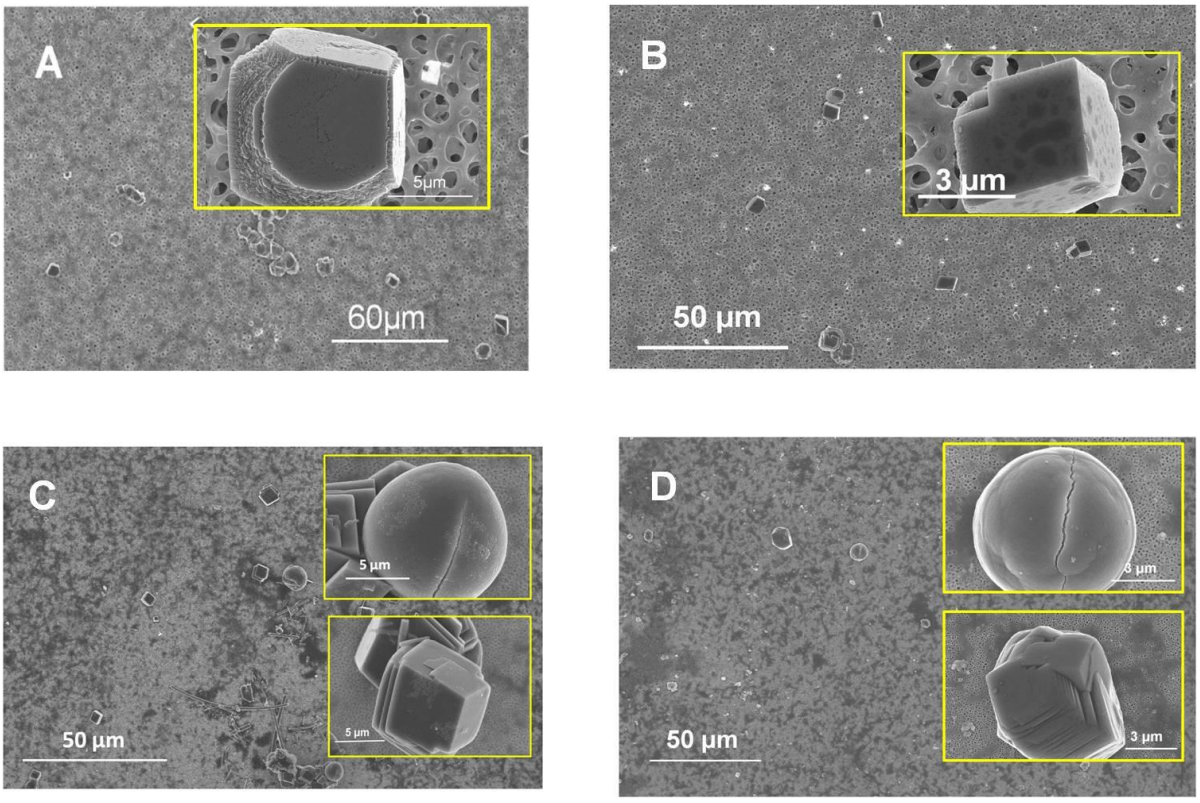

Figure 5.3. Crystallisation in bulk system.

When one EP protein is mixed with different reagents, same crystal formation was generated. This phenomenon occurs to all four individual EP proteins, with (A) multilayer calcite formation in WEP protein, (B) rhombohedral calcite crystal formation in WCEP protein, spherical vaterite and multilayer calcite crystal formation in both (C) EEP and (D) C1q domain. All inserted images are the high-magnification SEM images presenting the details of crystal morphologies.

5.2.2 Protein concentration determination for on-chip crystallisation

The above crystallisation results demonstrate that the conventional bulk system cannot fully enable the determination of protein influence on crystallisation. Therefore, the pressure-driven laminar flow microfluidic system has been used for EP protein functional screening.

The microfluidic system has been applied to biomineral studies with reaction reagents of $CaCl_2$ and Na_2CO_3 for crystallisation in non-buffered aqueous conditions (Chapter 4). The well controlled on-chip crystal distribution has been achieved by using 50mM reagents. For protein functional screening, the pH buffered condition of pH 7.5, a physiological pH for molluscan extrapallial fluid proteins, was used. Under this condition, mathematical calculations determined that there is a lower value for the maximum supersaturation ratio (S)

of 50 mM $CaCl_2$ and Na_2CO_3 solutions at this pH than in the non-buffer system. This 50 mM reagent concentration has also been confirmed by real-time crystallisation experiments with appropriate crystal density formed in microfluidic channel (Figure 4.4 in Chapter 4). Therefore, 50 mM $CaCl_2$ and Na_2CO_3 have been used from here on as the concentration during on-chip crystallisation in MOPS buffer (100 mM, pH 7.5)

Previous screening of EP protein mixture demonstrated the influences of total extrapallial fluid (TWEP) proteins on crystal morphological and polymorph control in microfluidic system. Since many mollusc biomineral proteins are assumed to have calcium-binding ability, they are assessed by mixing the proteins with different reaction reagents for crystallisation.

In functional screening studies, a key factor of protein influence on crystallisation is protein concentration. Based on the reagent concentration of 50 mM, the major wild-type 28kDa extrapallial (WEP) protein has been mixed with 50 mM $CaCl_2$ solution only for trial experiments for crystal growth, in a range from 1 to 100 µg/ml, since this protein has calcium-binding abilities. A blank condition without any protein was used for comparison (Figure 5.4A).

The results illustrate that protein concentration has a major impact on the control of crystal formation (Figure 5.4). Rhombohedral calcite crystals dominated on-chip formation with buffer only (Figure 5.4A). In the very low concentration (1 µg/ml) of 28 kDa WEP (Figure 5.4B), both rhombohedral calcite and spherical vaterite crystals precipitated in the channel. When the protein concentration is increased (10 µg/ml), the novel hollow lemon-shaped crystals formed in the channel (Figure 5.4C). At 50 µg/ml of WEP, lemon-shaped crystals dominated on-chip crystal formation (Figure 5.4D). The presence of the highest concentration (100 µg/ml) produces a similar result as the concentration of 50 µg/ml, with predominant lemon-shaped crystals in the microfluidic channel (Figure 5.4E). This set of experiments demonstrates the influence of protein concentration on crystal morphology.

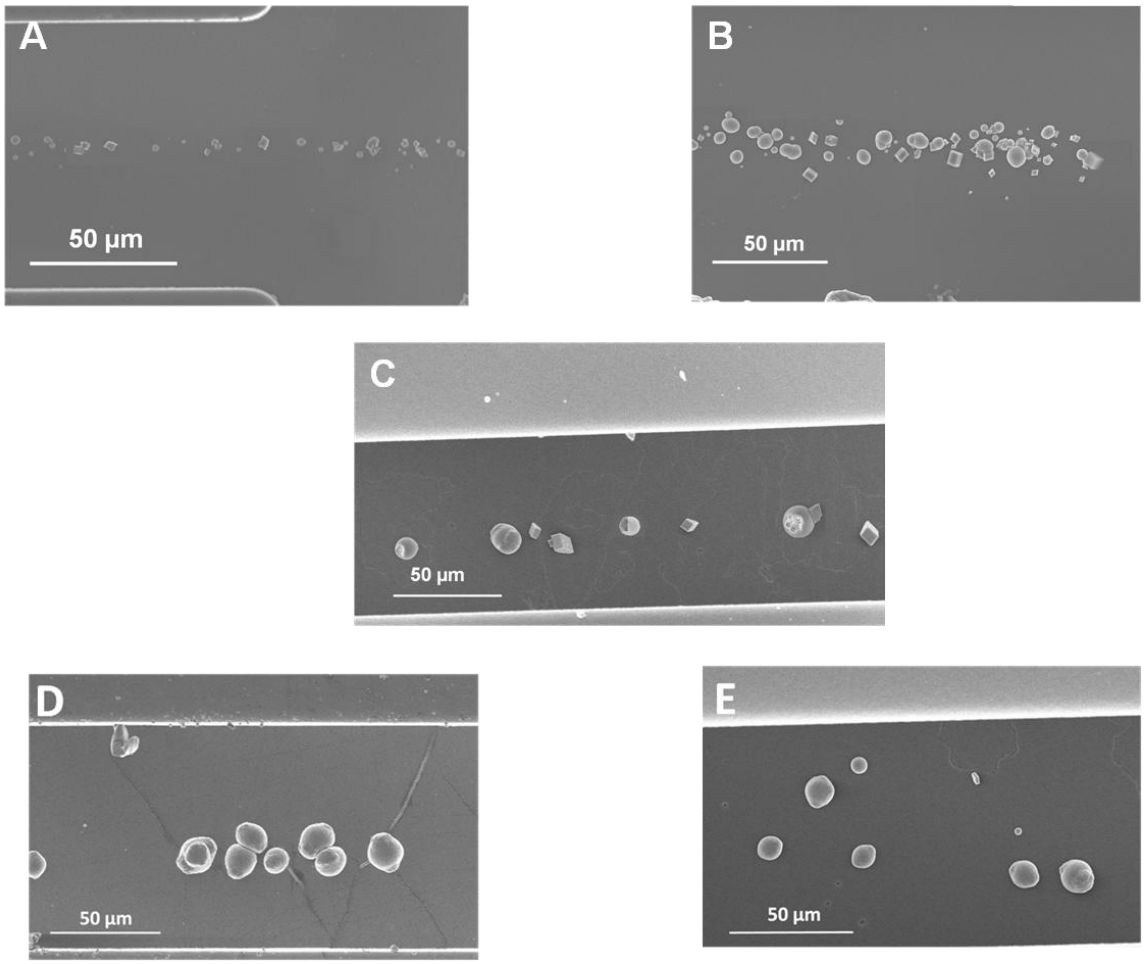

Figure 5.4. On-chip crystallisation with a range of concentrations of WEP protein.

Scanning electron microscopy images of crystals formed in microfluidic channel. A range of EP protein concentrations (0 to 100 µg/ml) have been used to assess protein concentration influence on crystallisation. (A) The rhombohedral calcite crystals dominated on-chip crystallisation in the condition of buffer system without any protein. (B) In the presence of very low concentration (1 µg/ml) of WEP protein, both rhombohedral calcite and spherical vaterite crystal precipitated in the channel. (C) The hollow lemon-shaped crystals were generated by the 28 kDa WEP from 10 µg/ml protein. (D) The relatively higher concentrations of 50 µg/ml induced predominant lemon-shaped crystals during on-chip formation. (E) Similar phenomenon with dominated lemon-shaped crystal formation occurs in the highest concentration of 100 µg/ml.

Since protein has a more marked effect on crystallisation in the range of 10 µg/ml and 50 µg/ml, these two concentrations were subsequently used as protein concentrations in functional screening experiments, including the major wild-type 28 kDa extrapallial (WEP) protein, the expressed main extrapallial (EEP) protein, the 14 kDa C1q domain and the wild-type extrapallial proteins complex (WCEP) proteins. To maintain an objective analysis and comparison of all these proteins, commercial calcium-binding protein (CBP) and polyacrylic

acid (PAA, Mw ~3500) were used as positive controls while BSA was used as a negative control during on-chip crystallisation. 100 mM MOPS buffer, pH 7.5, was used throughout this set of experiments. Prior to delivery into the microfluidic chip, all proteins and polymers are mixed with $CaCl_2$ only, Na_2CO_3 only and both solutions to create more diverse range of conditions to investigate protein influence on crystallisation (Table 2.1). Although a T-junction microfluic chip was used for initial experiments all the results for TWEP proteins and WEP protein, described here were obtained using Y-type microfluidic channel (250µm width x50µm depth x 2cm length) for all individual EP proteins.

5.2.3 Semi-quantitative analysis of on-chip crystallisation

Previous research indicates that extrapallial fluid has an inhibitory effect on crystallisation (Wilbur and Bernhardt, 1984). This inhibitory effect can be identified in the semi-quantitative analysis of protein screening in microfluidic system. Semi-quantitative analysis includes the crystal induction time and on-chip crystal distribution. In microfluidic system, the crystallisation induction time is defined as the time lag from the formation of the interface of the two solutions to the first crystal observed under 20x objective lens. In each case, a time of 90 s, after observation of first crystal, was used for crystal growth. To determine the crystal on-chip distribution, the images of all microfluidic chips were recorded. Recorded images were analysed using the software (Image J) to count the crystal numbers in the whole microfluidic channel under all conditions. Both the induction time and the induced on-chip crystal numbers are used to illustrate the influence of extrapallial fluid proteins on crystallisation.

Molluscan extrapallial proteins were screened using the same procedure as for $CaCO_3$ crystal growth (Section 2.3 in Chapter 2). The results demonstrate that crystal induction time varies depending on the reaction components. Shortest induction time (190 s) occurs in the absence of any protein, i.e. only in MOPS buffer (100 mM, pH 7.5) condition (Figure 5.5A). Different extrapallial fluid proteins induced similar induction times in the range of 300 to 350 s (Figure 5.5). But as to each individual protein, shorter induction time was generated by low concentration (10 µg/ml) (Figure 5.5A), compared to high concentration (50 µg/ml) (Figure 5.5B). This set of analysis demonstrates one aspect of the inhibition effect of proteins on crystal formation by prolonging the induction time for the first crystal to appear.

The inorganic buffer condition induces more crystals (crystal number>6500) than with any

biomineral protein (crystal number <4500) after the same crystallisation time. As to the presence of extrapallial fluid proteins, fewer crystals precipitate in the presence of high concentration (50 μg/ml) (Figure 5.5B) of protein than in the condition of low concentration (10 μg/ml) (Figure 5.5A).

This set of semi-quantitative analyses on both crystallisation induction time and on-chip distribution demonstrates the influence of extrapallial fluid protein on on-chip crystallisation. It illustrates that proteins can serve as inhibitors to crystal precipitation in aqueous conditions. This effect has been determined by the prolonged crystal induction time and reduced crystal numbers after on-chip formation. More information on protein influence during crystallisation can be achieved by analysing the morphologies of crystals formed in the presence of specific proteins.

In the laminar flow microfluidic system, the supersaturation ratio (S) profile has been constructed in modelling (Chapter 3), with a sharp peak in the middle of the channel in the beginning of the experiments, getting wider along the microfluidic channel, and finally flattening after a long flow rate distance (Dy) (Figure 3.7 in Chapter 3). This profile may influence the crystal numbers along the channel. In order to investigate the crystal on-chip distribution in the presence of biomineral proteins, the expressed extrapallial (EEP) protein was used for crystallisation. The result shows that the precipitated crystal number is increasing with increasing Dy (Figure 5.5C). But crystals have similar crystal size along the channel. This result can be explained by the wider distribution of supersaturation ratio (S) profile, with the increased supersaturation ratio across the channel when Dy increases.

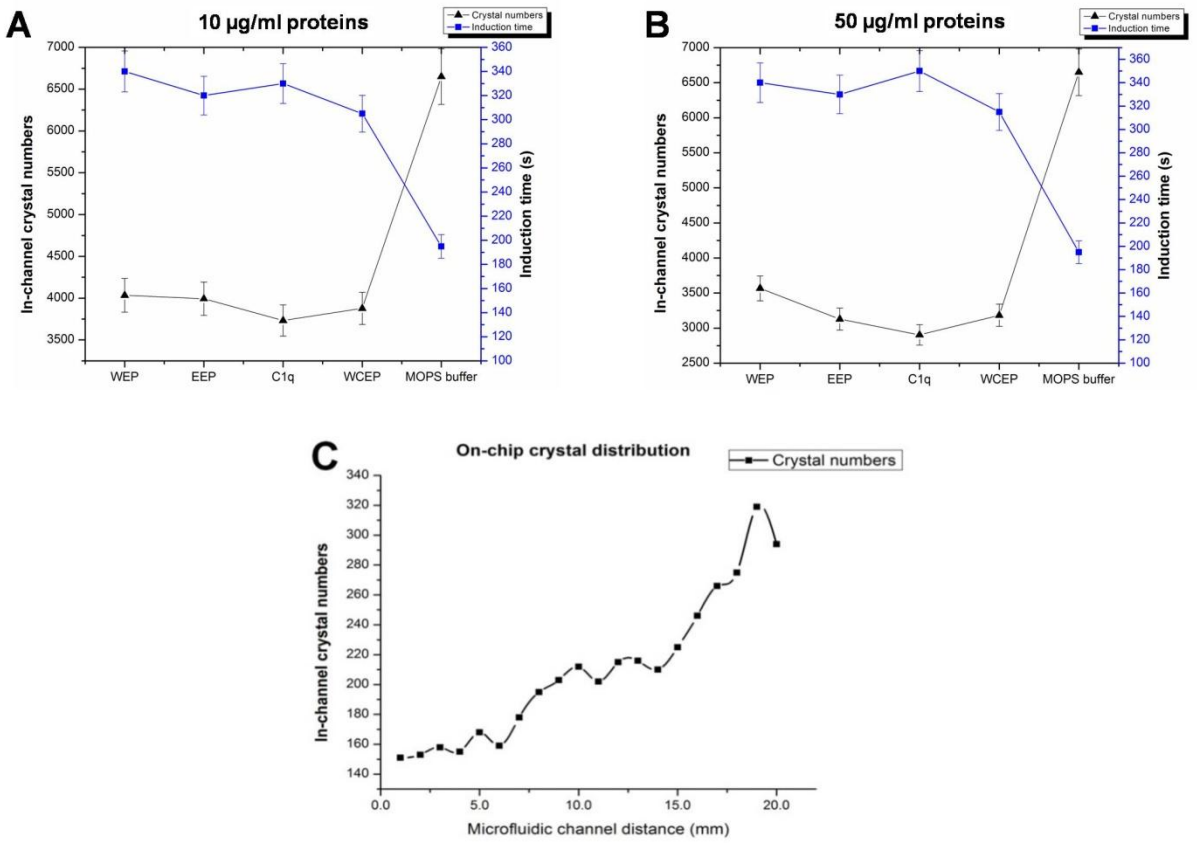

Figure 5.5. Semi-quantitative analysis of on-chip crystallisation.

Semi-quantitative analysis includes the crystallisation lag and the in-channel crystal numbers in the presence of extrapallial fluid proteins. (A) The presence of 10 µg/ml EP proteins mediates both crystallisation lag and in-channel crystal numbers, in contrast to the blank condition with buffer only. (B) The semi-quantitative analysis in the presence of 50 µg/ml extrapallial proteins, comparing to the buffer condition. (C) In the laminar flow microfluidic system, the in-channel crystal number is increasing along the channel in the presence of EEP.

5.2.4 Glycosylated major wild-type extrapallial (WEP) protein

In our initial experiments (Chapter 4), the total wild-type extrapallial (TWEP) protein from *M. edulis* induced oval calcite crystal formation on-chip. To investigate the influence of the major wild-type 28 kDa extrapallial (WEP) protein during on-chip crystallisation (Figure 5.6), it was screened at two concentrations. A high concentration of 50 µg/ml and a low concentration of 10 µg/ml were used. Both concentrations were screened using three conditions: protein mixed with $CaCl_2$ only, Na_2CO_3 only and both solutions (Table 2.1 in Chapter 2).

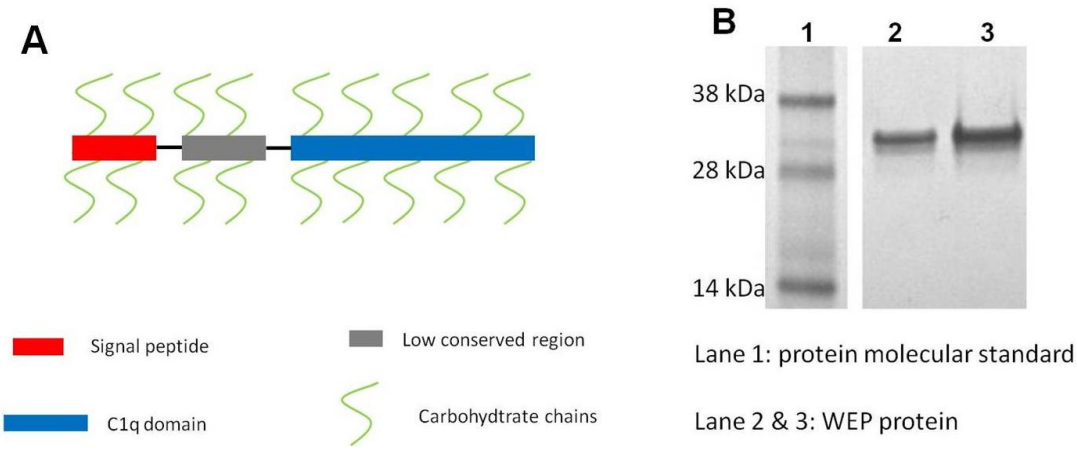

Figure 5.6. Illustration of the major wild-type 28 kDa extrapallial protein.

(A) Illustration of protein domains of the abundant wild-type extrapallial fluid protein from mussel *M. edulis*. (B) SDS-PAGE shows the molecular weight of this protein is approximately 28 kDa.

- *WEP in $CaCl_2$ solution only*

Using a microfluidic approach, it is realised that the influence of WEP protein on crystal growth critically depends on the solutions in which the protein is delivered. In the presence of 50 µg/ml WEP in 50 mM $CaCl_2$ solution, hollow lemon-shaped crystals dominate at the initial point of interface of the two solutions (Dy<1 mm) (Figure 5.7A). As the experiment progresses, the formed lemon-shaped structures are open at both ends indicating hollow structures (Figure 5.7B). Calcite crystals form further down the channel, after some flow rate distance (Dy >5 mm) (Figure 5.7C). Raman spectroscopy has identified both lemon-shaped and open structures as vaterite, with a shoulder peak at 1074 cm^{-1} near the major Raman shift at 1089 cm^{-1} (Figure 5.7E).

As mentioned, the computational simulation (Comsol) predicted the protein concentration profile along the microfluidic channel (Figure 3.7 in Chapter 3). The combination of the protein concentration gradient profile and real-time on-chip crystallisation reveals that WEP protein controlled crystal morphology. At high concentration in the initial stage of experiments, lemon-shaped crystals dominate at the beginning of the channel. The vaterite structures formed are more open as protein diffuses across the channel.

The presence of low concentration (10 µg/ml) WEP protein induces hollow vaterite structures in the channel, which is a similar result that occurs with 50 µg/ml WEP in $CaCl_2$ only. Under this condition, high-resolution SEM images show that most hollow crystals precipitate with a rough crystal surface composed of nano-granules (Figure 5.7D). A few calcite crystals also form along with the hollow vaterite crystals.

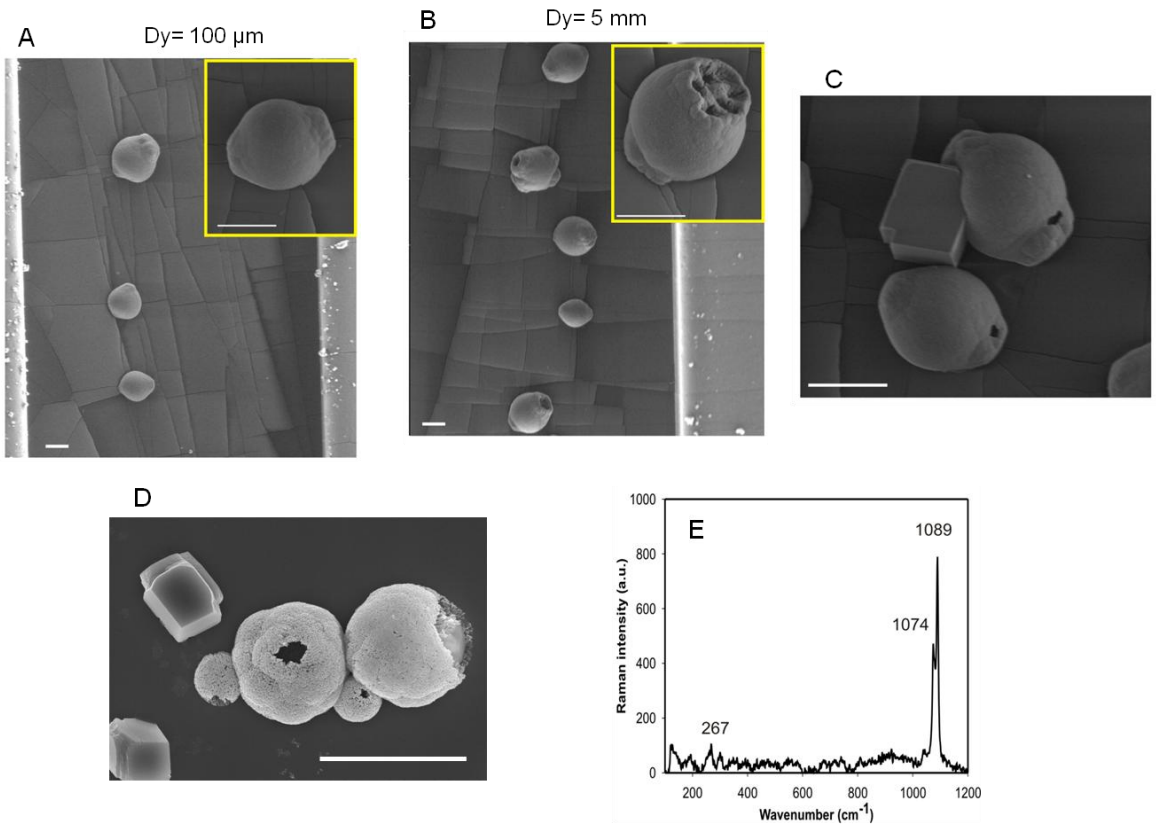

Figure 5.7. On-chip crystal formation with WEP present in $CaCl_2$ only.

SEM images of the crystals formed at the distances of (A) Dy=100 µm and (B) Dy=5 mm. High-resolution images are given in the inserts. The lemon-shaped crystal in A is closed whereas the one in B is open. (C) At Dy>5 mm, calcite crystals start forming in the channel. (D) High-magnification SEM image represents the hollow structure formation at the low concentration (10 µg/ml) of WEP in $CaCl_2$ only. (E) Raman spectrum of the lemon-shaped vaterite crystal. All scale bars 10 µm.

- *WEP in both reagent solutions and in Na_2CO_3 solution only*

When 50 µg/ml WEP is added into Na_2CO_3 solution only or both solutions, calcite is the only polymorph precipitated in the channel (Figure 5.8A). However, by comparing these crystals with classic rhombohedral calcite crystals formed in the inorganic condition without any protein (Figure 5.8C&D), the presence of WEP produces a multilayered structure (Figure 5.8A&B). This structure is composed of stacks of thin plates parallel to each other, although the edges are not perfectly aligned (Figure 5.8B). High-magnification SEM images also show that the rhombohedral calcite crystals form with smooth surface (Figure 5.8D). The identification of mineral polymorph from Raman spectroscopy has identified both structures as calcite, with the same Raman peaks at 1086, 712 and 281 cm^{-1} (Figure 5.8E). Similar structures have been generated under the conditions of low concentration (10 µg/ml) WEP protein mixed with both reagents or with Na_2CO_3 solution only. In comparison to the lemon-

shaped vaterite formation, this phenomenon probably demonstrates another possible way of the major extrapallial proteins in modifying crystal formation.

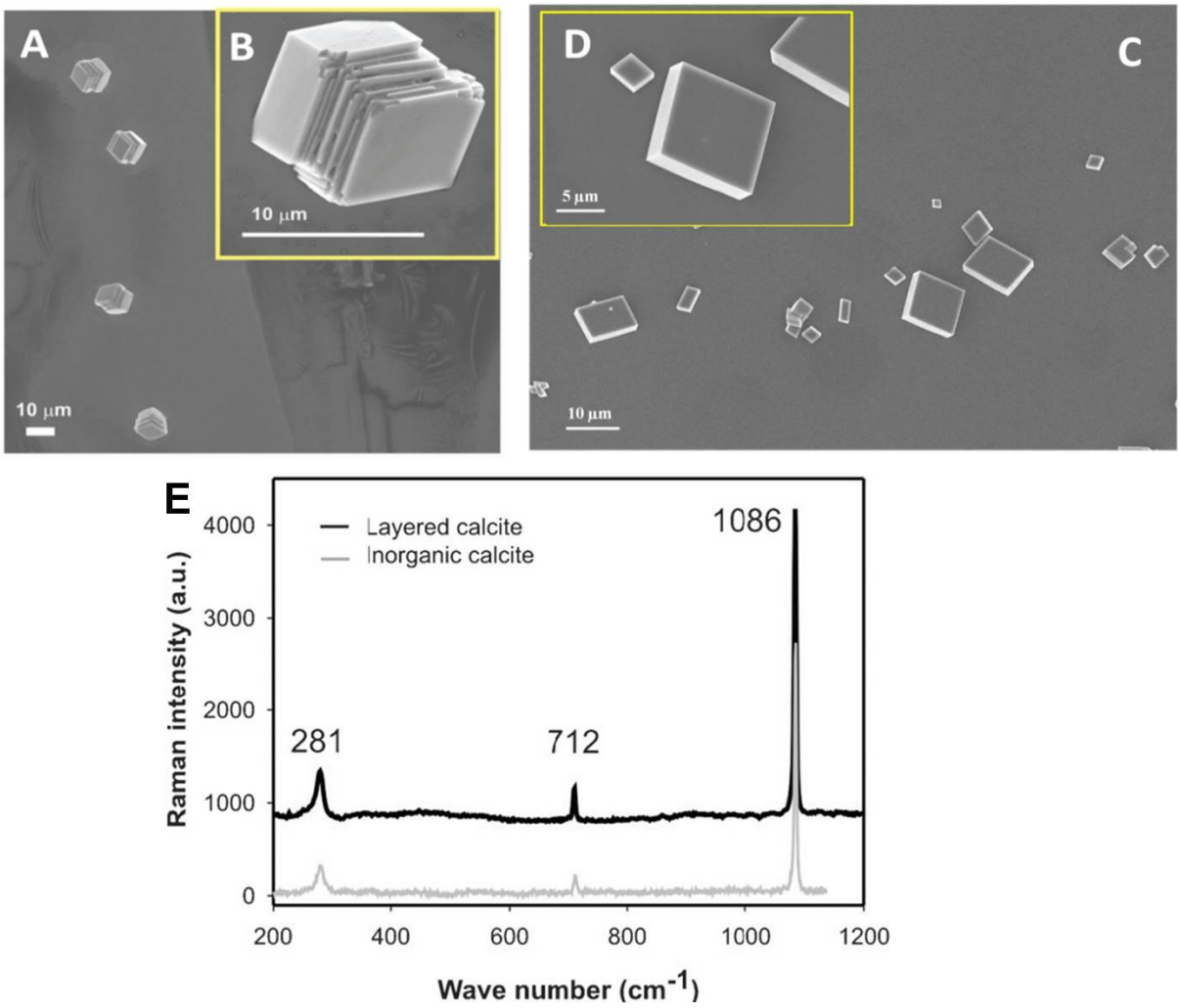

Figure 5.8. Crystal formation when WEP protein is present in Na_2CO_3 solution only or in both solutions.

(A) Layered crystals were the only product formed. The crystals aligned in the direction of flow and in the middle of the channel. (B) High magnification SEM image shows the layered structure under this condition. (C) Rhombohedral calcite crystals dominated on-chip formation without any protein. (D) High-magnification image shows calcite crystal with smooth surface in this condition. (E) Raman spectrum of the layered crystal shows that it is the same as standard rhombohedral calcite formed in pure inorganic solutions (inorganic calcite).

5.2.5 Non-glycosylated main expressed extrapallial (EEP) protein

EEP protein is a non glycosylated expressed protein with the same amino acid sequence as WEP protein. Therefore, the molecular weight of this protein is approximately 24 kDa, excluding the ~4 kDa N-glycan from WEP protein (Figure 5.9). This protein has been

screened in both the bulk condition and microfluidic system to determine the protein's influence on biomineral crystallisation.

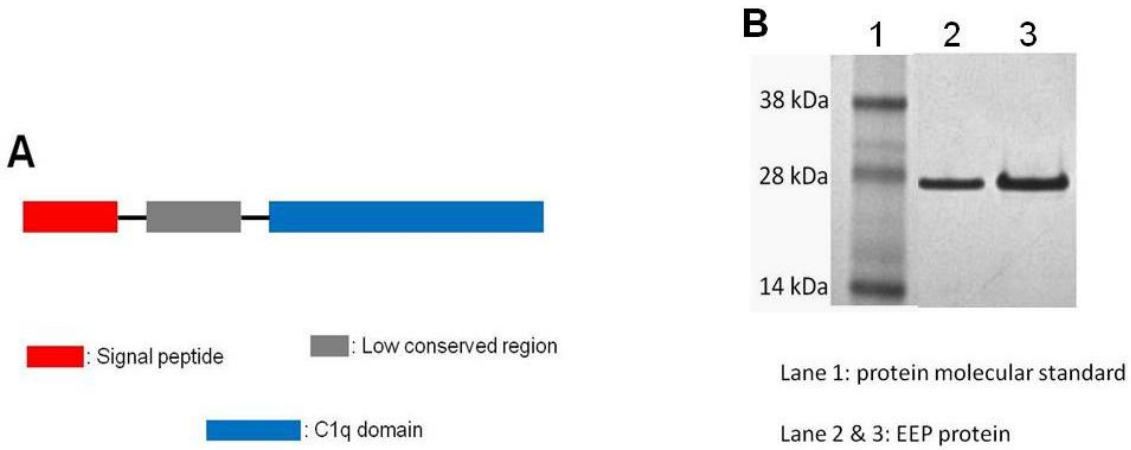

Figure 5.9. Illustration of the expressed major extrapallial fluid (EEP) protein.

(A) The illustration of protein domain demonstrates this protein as non-glycosylated protein with the same protein sequence as the abundant wild-type extrapallial fluid (WEP) protein. (B) SDS-PAGE reveals the molecular weight of this protein is approximating 28 kDa.

- *EEP in $CaCl_2$ only*

As with the WEP protein, the influence of EEP protein strictly depends on the location of the protein at delivery into the microfluidic channel. In the condition of 50 µg/ml EEP mixed in the $CaCl_2$ channel only, vaterite crystals dominated in the channel. From the beginning of the interface (Dy<1 mm), only a few crystals formed a single line at the interface (Figure 5.10A). High-magnification SEM image reveals the rough surface of these crystals (Figure 5.10A, Insert). After protein and ions diffusion across the channel (as Dy increases), the uniform lemon-shaped vaterite structures appeared in the channel. With progress towards the end of the device (Dy>10 mm), ions are completely distributed across the channel, and protein partially diffused with a concentration gradient still remaining. Under this condition, crystals of both lemon-shaped vaterite and rhombohedral calcite are well dispersed in the channel (Figure 5.10B). Similar results were found with the low concentration (10 µg/ml) of EEP in the $CaCl_2$side only (Figure 5.10C). After ion and protein diffusion across the channel, both lemon-shaped vaterite crystals and rhombohedral crystals formed in the channel.

This set of experiments reveals the influence on crystal polymorph from the EEP protein concentrations. In the beginning of the reaction channel, the presence of a high concentration of EEP induced vaterite crystals. As flow runs through the channel (Dy increase), protein and

ions diffuse across the channel. As a consequence, both calcite and vaterite are precipitated in the channel.

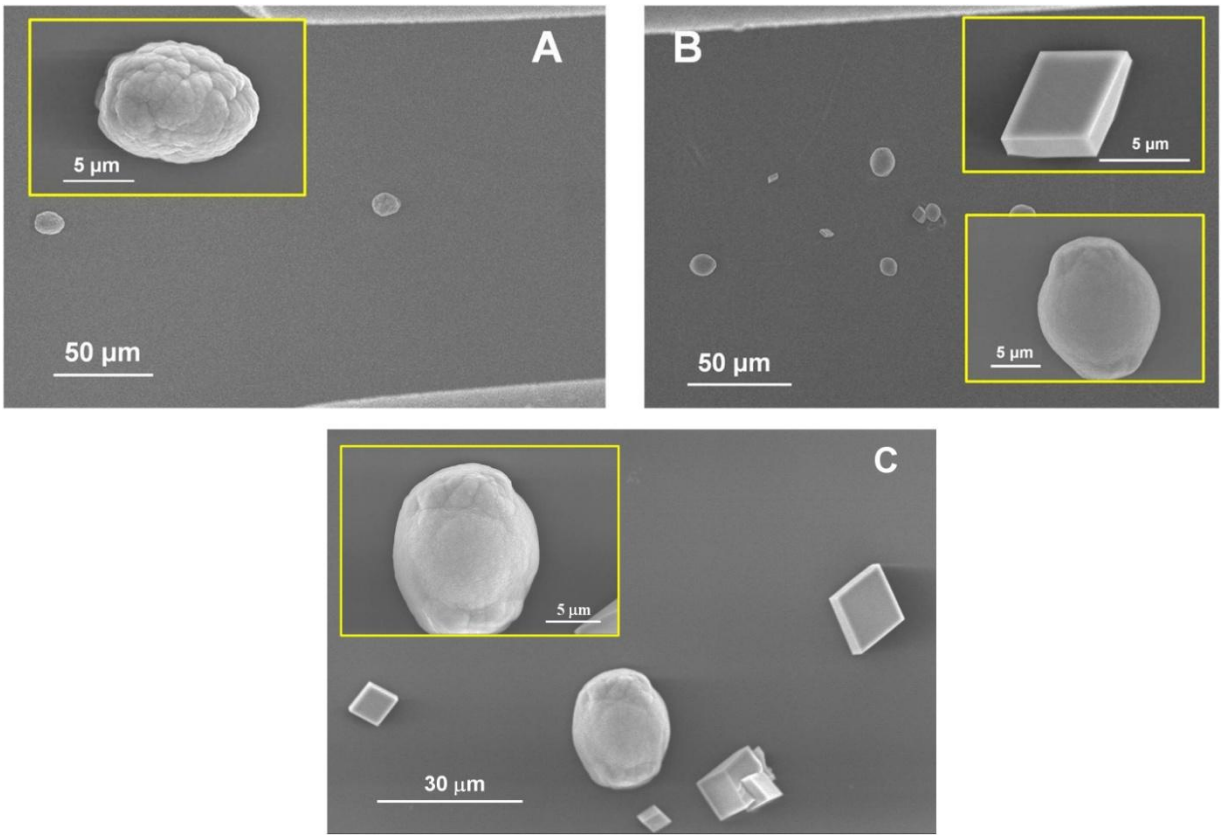

Figure 5.10. On-chip crystallisation with EEP protein in $CaCl_2$ only.

(A) When 50 μg/ml EEP was added in 50 mM $CaCl_2$ only, few crystals formed in a line in the beginning of the channel. (B) Crystals dispersed in the channel after mass diffusion into the other reagent streams. The inserted images present the details of crystal formation in this condition. (C) When 10 μg/ml EEP protein was added in 50 mM $CaCl_2$ only, the lemon-shaped vaterite and rhombohedral calcite crystals formed in the microfluidic channel. The inserted image shows the details of vaterite crystals with rough surface.

As shown above, when 50 μg/ml EEP protein was mixed with $CaCl_2$ solution only, crystal morphology and polymorphs vary along the channel, which is induced by the changing of protein and ion concentrations. Under this condition, the overview of crystal on-chip formation in the initial stages (Dy<2 mm) represents this phenomenon (Figure 5.11). In the very initial stage (Dy=0), protein is not diffused across the interface. Under this circumstance, vaterite formation is favoured, precipitating in the channel in the presence of high protein concentration and less diffusion. With Dy increasing, more crystals precipitated in the channel. Only a few rhombohedral calcite crystals start appearing in the channel after some distance (Dy≥1.8 mm), with EEP protein diffusion across the interface.

High-magnification SEM images reveal the details of the vaterite crystals precipitated in the channel at different Dy values. In the beginning of the channel, oval vaterite crystals precipitate, with a rough surface (Figure 5.11B). With increasing flow distance, lemon-shaped structures appear and are then formed uniformly in the latter section of the channel (Figure 5.11C&D). Calcite crystals start forming in the channel section of Dy≈2 mm. This set of results demonstrates the influence on crystal morphological control, polymorph selection and distributions using this laminar flow microfluidic system.

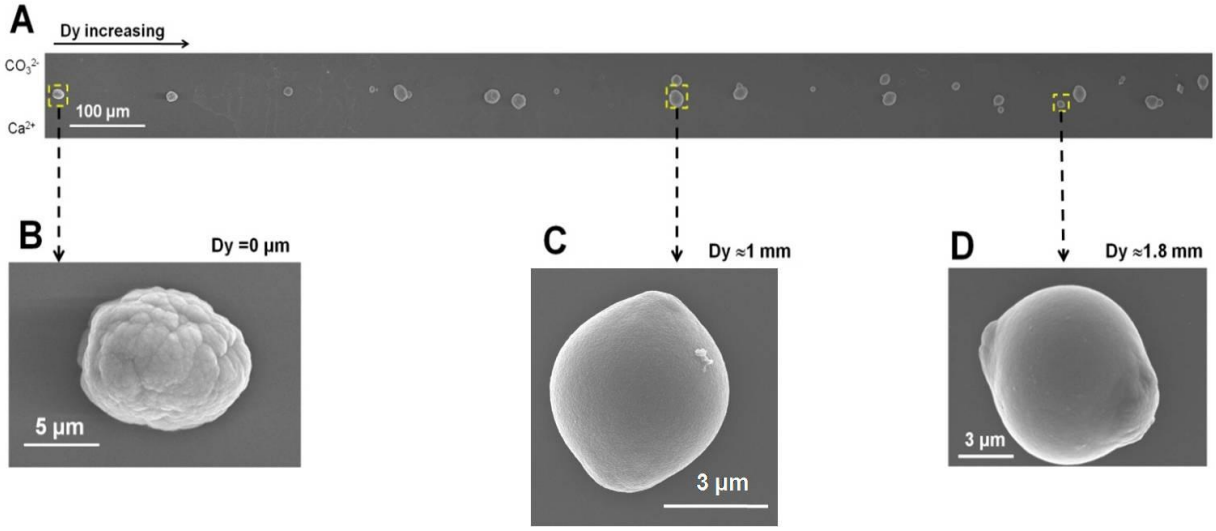

Figure 5.11. Overview of on-chip crystallisation with EEP protein in $CaCl_2$ only.

Calcium carbonate on-chip crystallisation in the condition of EEP protein mixed with 50 mM $CaCl_2$ solution only. (A) Representative SEM images demonstrate the crystal formation in the beginning stages of microfluidic channel (Dy<2 mm). In this condition, a line of individual vaterite crystals form in the beginning of the channel. Crystals start separating in the channel after mass diffusion during flow running (Dy≈1 mm). High-magnification SEM images reveal the details of vaterite formation in different channel sections (B, C and D).

- *EEP in both reagent solutions*

When the EEP protein is mixed with both $CaCl_2$ and Na_2CO_3 solutions prior to crystallisation, only ion concentration gradients remain across the channel with balanced protein concentration. Figure 5.12 demonstrates the on-chip crystallisation with EEP protein in both solutions. A stream of individual crystals forms at the interface of two solutions at the beginning of merging (Figure 5.12A). High-magnification SEM image reveals lemon-shaped structures form in this part of the channel (Figure 5.12A, insert). As the flow runs through the channel (Dy increases), both rhombohedral calcite and lemon-shaped vaterite crystals precipitated in the channel (Figure 5.12B). With a low concentration (10 µg/ml) of EEP protein mixed with both solutions, more crystals precipitated in the channel from the initial stage

(Figure 5.12C) to the latter channel part (Figure 5.12D). Under this condition, lemon-shaped vaterite crystals dominated on-chip formation. All the lemon-shaped crystals have been identified as vaterite by Raman spectroscopy with a characteristic shoulder peak at 1074 cm^{-1} nearby the major peak at 1091 cm^{-1} (Figure 5.12E).

In this set of experiments, the condition of mixing EEP protein with both reagents induces the formation of both rhombohedral calcite and 'lemon' vaterite. This result is different from the crystallisation in the condition of mixing both reagents with WEP protein containing carbohydrate, which generates layered calcite crystals only. The difference between the two sets experiments probably implies that the carbohydrate, present in the wild-type protein, and not on the expressed, may influence crystal formation.

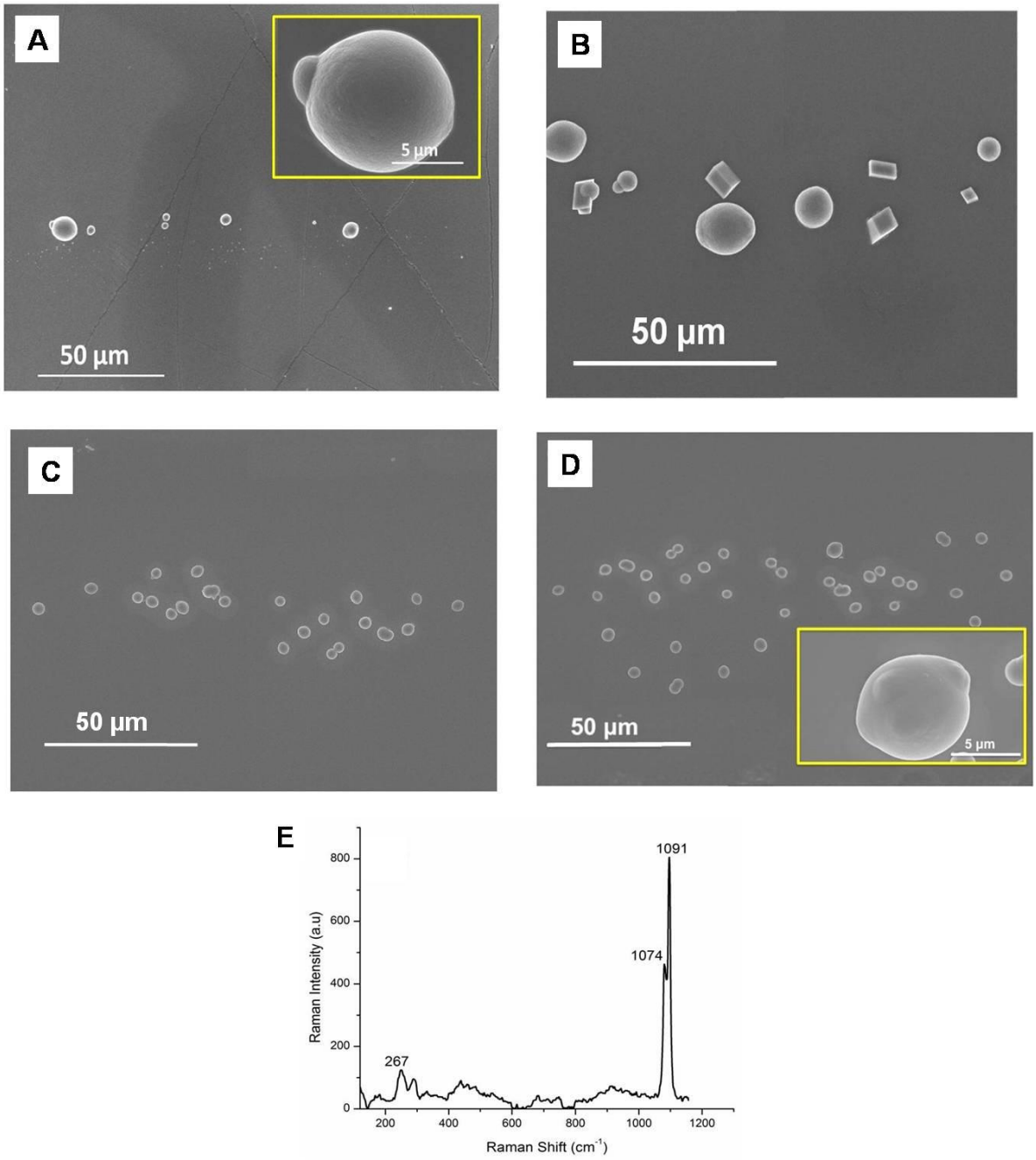

Figure 5.12. On-chip crystal formation in the presence of EEP in both solutions.

Lemon-shaped vaterite crystals dominate on-chip crystallisation in the presence of the EEP protein in both reagent solutions. (A) In the presence of 50 µg/ml EEP in both solutions, a single line of individual vaterite crystals precipitates in the initial stage of channel, high-magnification image showing the lemon-shaped structures. (B) Crystals start dispersing across the channel after ion diffusion. Vaterite dominated in-channel formation, from the initial stage (C) to the channel part with Dy increasing (D), when 10 µg/ml EEP was added in both solutions. The Insert is the high-resolution SEM image showing the lemon-shaped crystals under this condition. (E) Raman spectra confirmed the lemon-shaped crystals as vaterite, with characteristic should peak of 1074 cm^{-1} near the major shift of 1091 cm^{-1}.

- *EEP in Na_2CO_3 solution only*

In the presence of 10 µg/ml EEP in Na_2CO_3 solution only, both calcite and vaterite crystals precipitate in the channel (Figure 5.13). This condition induces a dominance of calcite crystals in the initial part of the reaction channel (Figure 5.13A), and more vaterite precipitate down the channel (Dy increases) (Figure 5.13D). High-resolution SEM images reveal the details of rhombohedral calcite (Figure 5.13B) and spherical vaterite crystals (Figure 5.13 C&E) forming in the channel. Compared to the results of low concentration of glycosylated major wild-type 28 kDa extrapallial fluid protein (WEP) in Na_2CO_3 solution only, the presence of non-glycosylated EEP induces vaterite crystal formation when protein added in Na_2CO_3 only. This comparison also implies the potential influence of carbohydrate on crystal morphology and polymorph discrimination.

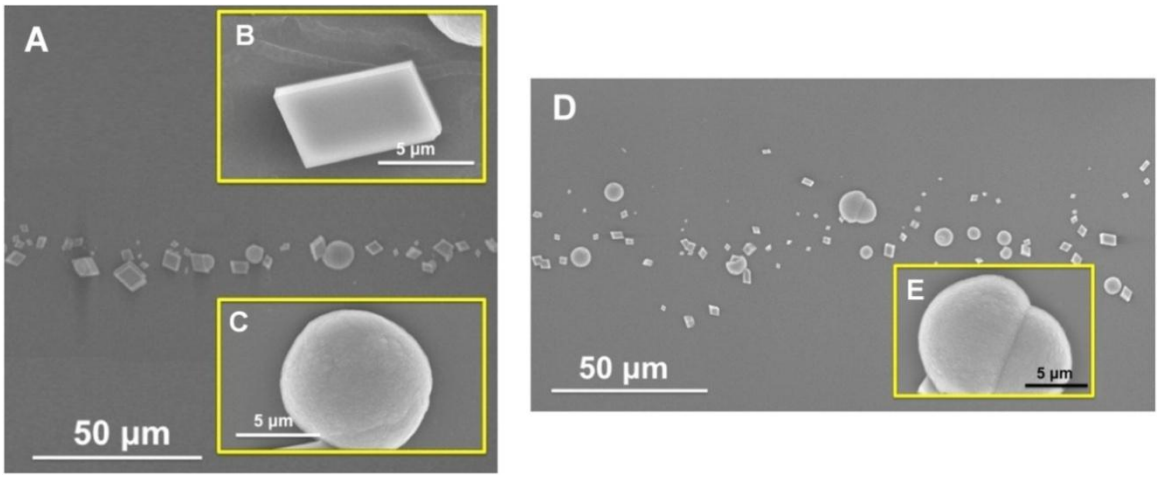

Figure 5.13.On-chip crystallisation with 10 µg/ml EEP protein in Na_2CO_3 solution only.

(A) SEM image of on-chip crystallisation in initial part of channel in presence of 10µg/ml EEP in Na_2CO_3 solution only. High-magnification SEM images represent the (B) rhombohedral calcite and (C) spherical vaterite crystals in this condition. (D) Crystals dispersed in the channel with Dy increasing. (E) High-magnification SEM image represents the spherical vaterite structures in this condition.

However, in the presence of high concentration (50 µg/ml) of expressed major extrapallial fluid protein (EEP) in sodium carbonate solution only, calcite dominated on-chip crystallisation. From the start of the initial interface of the two solutions, a line of individual crystals formed (Figure 5.14A). High-magnification images revealed that the hillock-shaped crystals formed in a line (Figure 5.14A, Insert). After protein and ions diffused into the other stream, the hillock-shaped crystals formed in the remainder of the channel (Figure 5.14B). The high-resolution microscopic images show that crystals have a columnar morphology with

two facets forming a cap, and one face generally decreasing towards the base of crystal. This uniform structure only formed in the microfluidic channel with 50 µg/ml EEP in Na_2CO_3 solution. Micro-Raman spectra identify this structure as calcite, with characteristic shifts at 1091, 710 and 139 cm^{-1}.

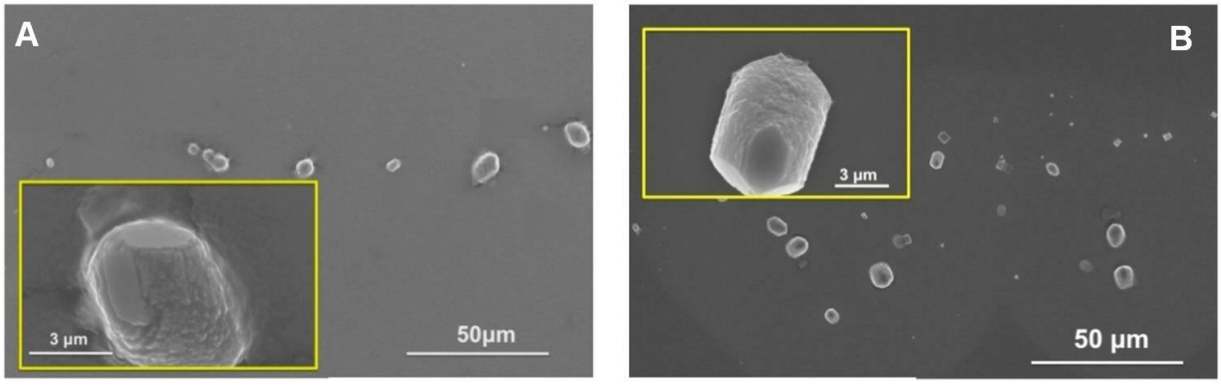

Figure 5.14. Representative SEM images of crystals formed in the microfluidic channel with 50 µg/ml EEP in Na_2CO_3 solution only.

(A) The crystal formed in a line in the beginning of microfluidic channel. The insert image represents the details of crystals in hillock-shaped. (B) After mass diffusion across the microfluidic channel, crystals randomly separated in the channel. The insert presents the crystals details with similar structure as that formed in the beginning of the channel.

5.2.6 Non-glycosylated conserved C1q domain

The C1q domain is a conserved C-terminal domain of the major extrapallial fluid protein from *M. edulis* (Figure 5.15). This domain has been provided from an *E.coli* protein expression system, as a consequence, devoid of carbohydrate (Figure 5.15A). SDS-PAGE has clearly showed the molecular weight of this domain as approximately 14kDa (Figure 5.15B). As with WEP and EEP proteins, this domain has been screened for crystallisation using microfluidics at two concentrations: 50 µg/ml and 10 µg/ml.

Figure 5.15. Illustration of the C1q domain.

(A) The amino acid sequence of the major extrapallial fluid protein from *M. edulis*. The red region is the conserved C-terminal domain, the C1q domain. (B) Protein purification using SDS-PAGE presents the molecular weight of this domain as ~14kDa.

- *C1q domain in $CaCl_2$ solution only*

The on-chip crystallisation results reveal that the influence of this domain again relies on which component the C1q domain is mixed with prior to crystal incubation in the microfluidic device. When C1q domain was added in $CaCl_2$ solution only, the lemon-shaped structures were induced in the channel (Figure 5.16). When 50 µg/ml C1q domain was mixed with $CaCl_2$ solution only, individual crystals aligned in a line in the middle of channel at the beginning of reaction channel (Dy<1mm) (Figure 5.16A). These crystals have been confirmed as lemon-shaped structures from the higher magnification SEM image (Figure 5.16B). Greater magnification SEM image reveals a rough surface on the lemon-shaped structures (Figure 5.16B, Insert). As the experiment proceeds (Dy>10 mm), both lemon-shaped vaterite and only a few rhombohedral calcite crystals precipitated across the whole channel, with lemon-shaped vaterite dominant (Figure 5.16C). High-magnification SEM image reveals the crystal as lemon-shaped structure (Figure 5.16D).

Similar crystallisation results have been generated when low concentration (10 µg/ml) C1q domain was added into $CaCl_2$ solution. In the initial stage of channel (Dy=0), crystals aligned in a line on the interface of two solutions, with lemon-shaped structures dominated crystal formation (Figure 5.16E). High-magnification SEM image presents the lemon-shaped structure with rough surface as well (Figure 5.16F). These results are similar to those recorded when the major expressed EP protein was used (Section 5.2.3). Micro-Raman spectroscopy was again used to identify the crystal polymorph. All these lemon-shaped structures have been identified as vaterite crystals.

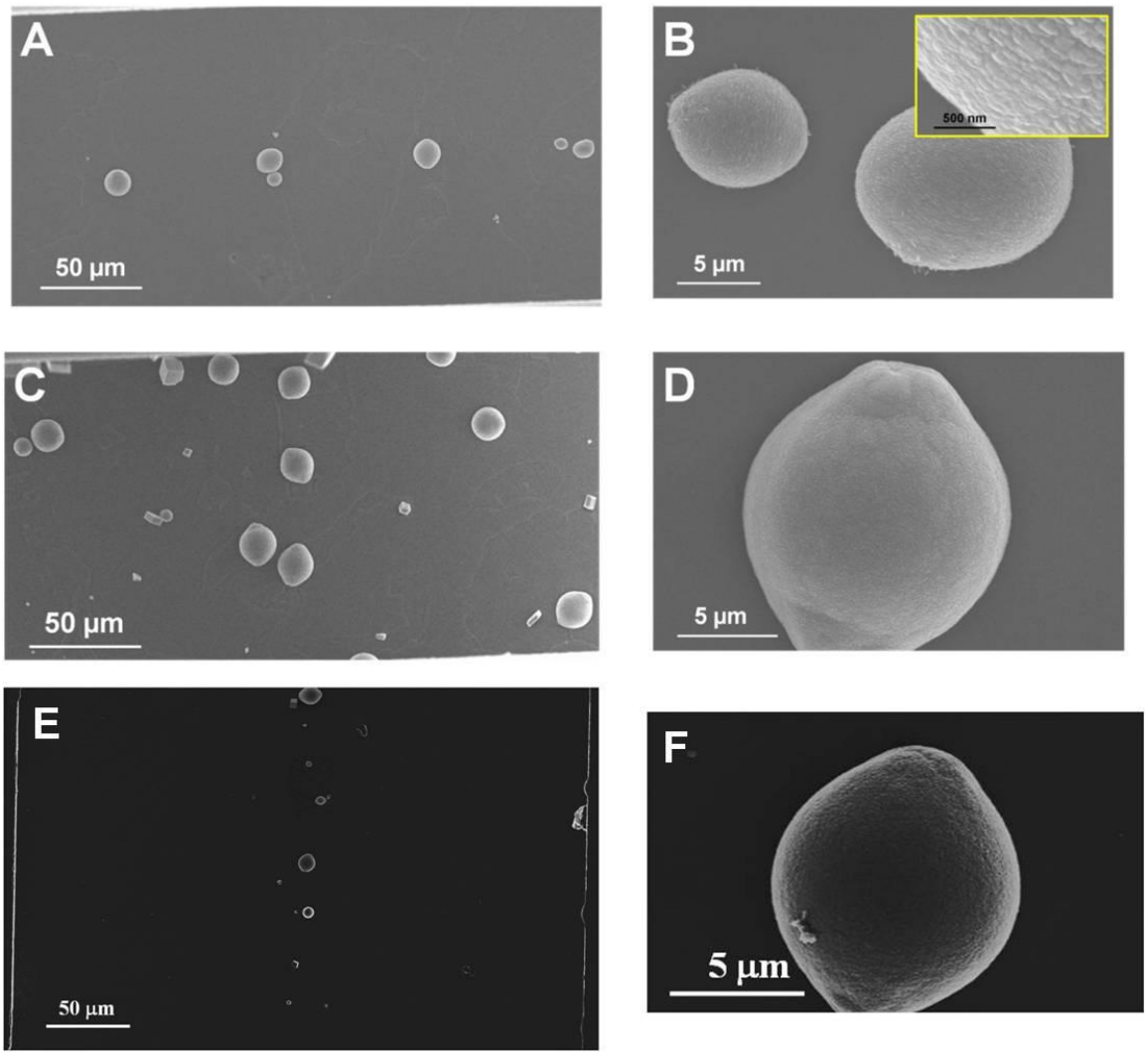

Figure 5.16. Representative SEM images of on-chip crystal formation with C1q domain in 50 mM $CaCl_2$ only.

When C1q domain was mixed with 50 mM $CaCl_2$ solution, lemon-shaped vaterite crystals dominated in-channel crystallisation. (A) A line of individual crystals formed in the channel at Dy<1 mm. (B) High-magnification images show the crystal initially formed as lemon-shaped structures. The insert Image represents details of crystal surface with nano-granules. (C) After diffusion, crystal randomly formed in the channel, including lemon-shaped vaterite and a few rhombohedral calcite crystals. (D) High-magnification images present the single lemon-shaped vaterite structure. (E) When 10 µg/ml C1q domain mixed with 50 mM $CaCl_2$ solution, a line of crystals formed in the channel, with vaterite crystals predominant. (F) High-resolution SEM image shows the vaterite crystals as 'lemon' structure.

- *C1q domain in both reagent solutions*

When the 50 µg/ml C1q domain is mixed with both reagents for on-chip crystallisation, a line of individual crystals including both rhombohedral calcite and lemon-shaped crystals appear at the beginning of the interface (Figure 5.17A). The insert reveals the crystal details with the

well-shaped 'lemon' structures (Figure 5.17A, Insert). As the experiment progresses (Dy>10 mm), the ion concentration balances across the channel. This balanced ion concentration induces crystals to be deposited separately in the channel (Figure 5.17B). Under this condition, both lemon-shaped vaterite and rhombohedral calcite crystals formed in the channel. Vaterite crystals have similar lemon-shaped structures along the whole channel. The presence of low concentration (10 μg/ml) of C1q domain mixed with both solutions induced the similar results as 50 μg/ml C1q domain, with vaterite crystals aligning a line in the beginning of channel (Figure 5.17C). The high-magnification SEM image shows the crystal as lemon-shaped structure. After protein diffusion across the channel, both lemon-shaped vaterite and rhombohedral calcite crystals dispersed in the channel (Figure 5.17D).

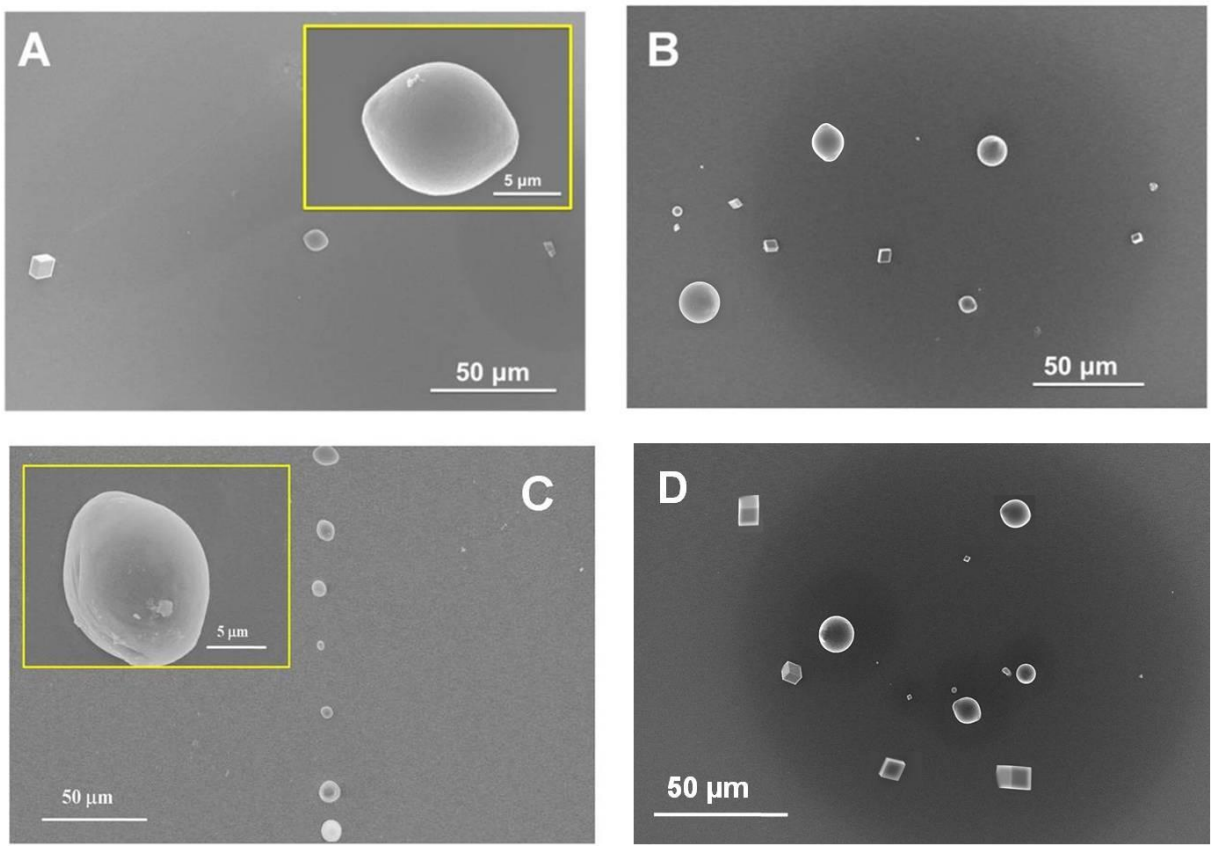

Figure 5.17. On-chip crystallisation in the condition of C1q domain mixed in both solutions.

When 50 μg/ml C1q domain is mixed with both reagent solutions, both lemon-shaped vaterite and rhombohedral calcite crystals dominated in the channel. (A) Few crystals precipitated in the beginning of the channel (Dy<1 mm). Both lemons-shaped and rhombohedral crystals formed. (B) After diffusion across the channel (Dy>10 mm), both kinds of crystals dispersed in the channel. (C) When 10 μg/ml C1q domain is mixed with both solutions, a line of crystals aligned in the beginning of channel. The insert high magnification SEM image shows the lemon-shaped crystals formed in the channel. (D) After protein diffusion across the channel, both calcite and vaterite dispersed in the channel.

- *C1q domain in Na_2CO_3 solution only*

Similarly to the major wild-type 28 kDa extrapallial protein (WEP) and the main expressed extrapallial fluid protein (EEP), the C1q domain has been screened in crystallisation trails in microfluidic channel with 50 mM Na_2CO_3 solution only. In the condition of 10 µg/ml C1q domain mixed with 50 mM Na_2CO_3 only, a single line of individual crystals precipitate in the channel in the beginning of the experiment (Dy<1 mm) (Figure 5.18A). High-magnification SEM images reveal that spherical vaterite crystals have formed. After the solutions progress towards the outlet (Dy>10 mm), crystals separated in the channel, including both rhombohedral calcite and spherical vaterite crystals (Figure 5.18B).

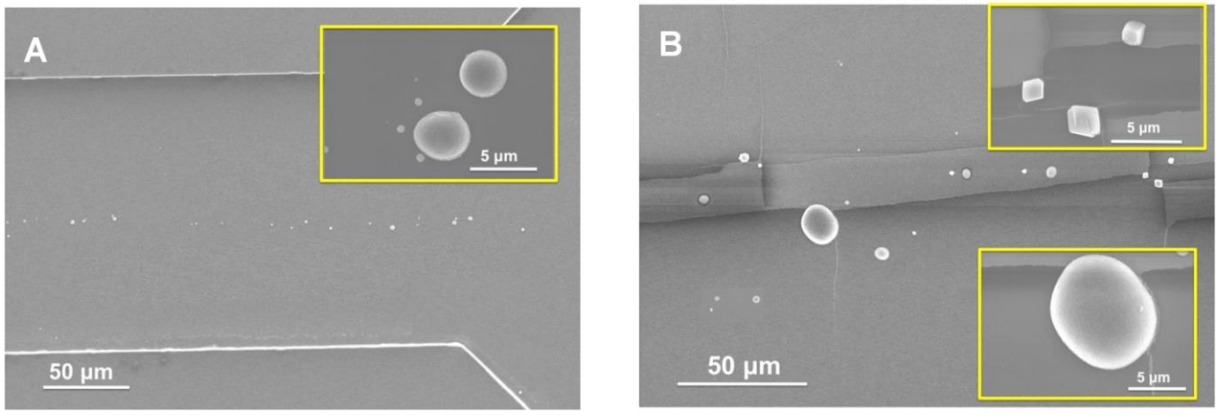

Figure 5.18. On-chip crystallisation with 10 µg/ml C1q in Na_2CO_3 only.

(A) Spherical vaterite crystals precipitated in the channel from the beginning of the channel. (B) When mass balance across the whole channel, both rhombohedral calcite and spherical vaterite crystals precipitated.

Under the condition of 50 µg/ml C1q domain in 50 mM Na_2CO_3 solution only, the in-channel crystal distribution is similar to that found for the low concentration of C1q domain, with crystals forming a single line in the beginning of channel (Dy<1 mm) (Figure 5.19A) and dispersing across the channel after Dy>10 mm (Figure 5.19C). Compared to the crystallisation with 10 µg/ml C1q domain in 50 mM Na_2CO_3 solution only, the presence of high protein concentration induces the crystal morphology changes. The significant change is that a multilayer calcite structure has been produced (Figure 5.19B&E). This layered calcite structure forms from the initial stage of Dy<1 mm (Figure 5.19B) and continues along the channel of Dy>10 mm (Figure 5.19E). Also, spherical vaterite crystals remain along the channel (Figure 5.19C).

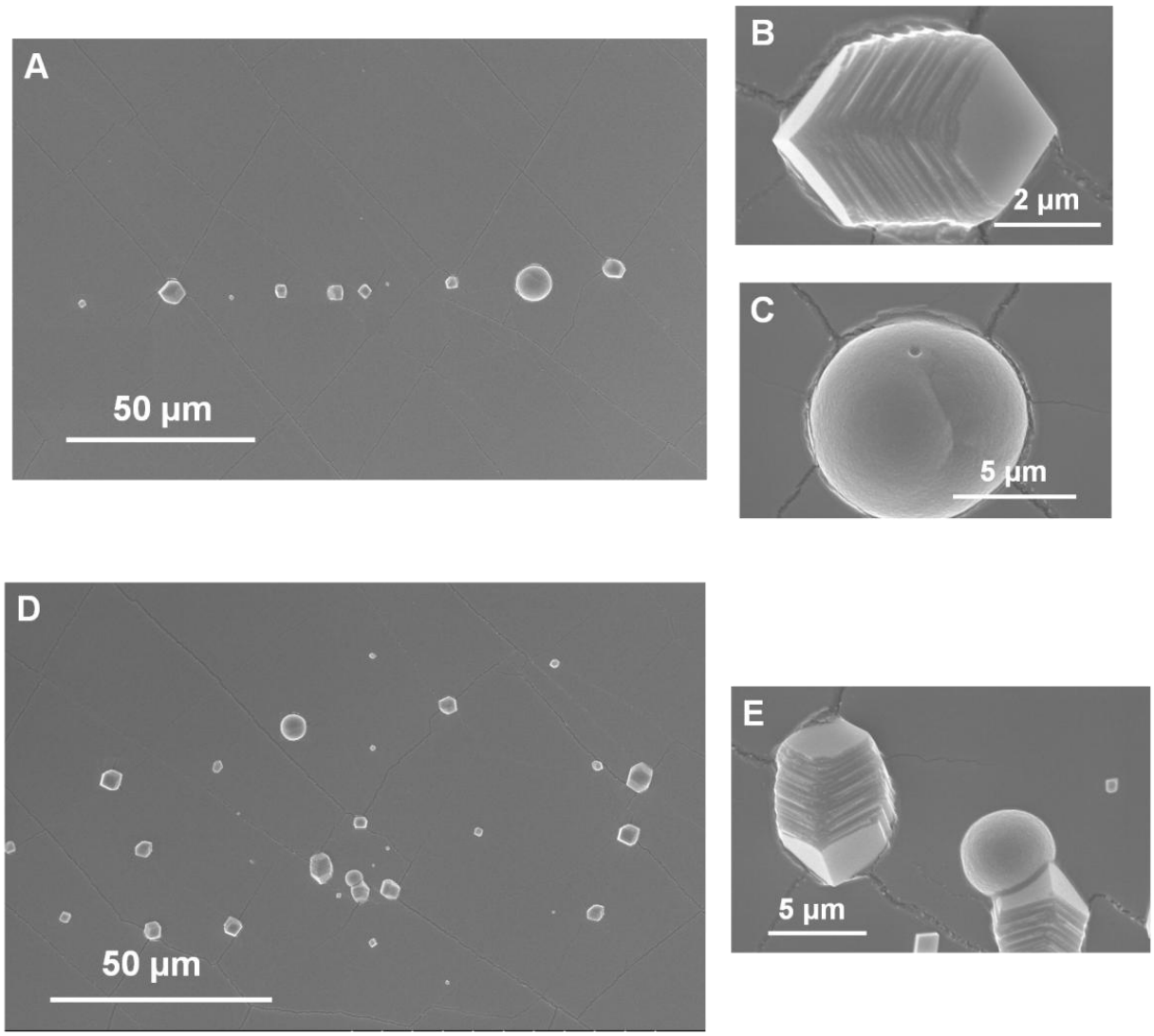

Figure 5.19. On-chip crystallisation with 50 µg/ml C1q domain in 50 mM Na_2CO_3 solution only.

In this condition, calcite crystals dominate on-chip formation. (A) The initial crystallisation shows a line consisting of individual crystals. This crystal formation includes both (B) layered calcite and (C) spherical vaterite formation. (D) After ion diffusion across the whole channel, crystals precipitated across the whole channel, including both multilayer and spherical structures (E).

5.2.7 Wild-type extrapallial complex (WCEP) protein

As well as the major extrapallial protein that was purified, other proteins were purified by my colleagues (Dr Khedidja Mosbahi and Dr Jiahong Jiang). During the protein purification using DE-52 anion exchange chromatography and analytical gel filtration chromatography, three proteins were co-eluted together, which appear to form a complex (Figure 5.20). Cross-linking experiments, using glutaraldehyde as a cross-linker confirmed that these proteins are

physically combined to form a complex. This complex consists of three proteins in the molecular weight (MW) range of 40 to 60 kDa. This complex was labelled as the wild-type extrapallial fluid complex protein (WCEP).

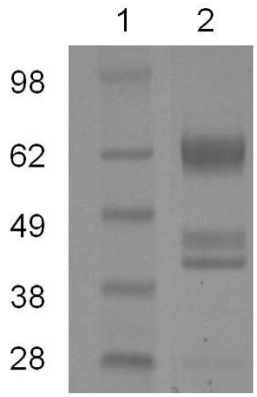

Figure 5.20. Electrophoretic analysis of WCEP protein.

SDS-PAGE analysis shows three bands, which stands for wild-type extrapallial f complex (WCEP) proteins (Lane 2). Lane 1 is the preloaded protein standard molecular weight markers.

- *WCEP in $CaCl_2$ solution only*

Unlike the other proteins, when WCEP is used, remarkably different results have been observed. Under the condition of 50 µg/ml WCEP added into 50 mM $CaCl_2$ solution only, calcite crystals dominate in-channel crystal formation (Figure 5.21A&B). In the initial stage in the reaction channel, individual crystals precipitate to form a line in the middle of channel, and the high-magnification SEM images show that these single crystals as multilayered structures (Figure 5.20, Insert). After some distance along the channel (Dy>10 mm), protein and ions diffuse across the interface, crystals randomly precipitate in the microfluidic channel (Figure 5.21B). The crystal details are shown in the high-resolution image: calcite formed by several layers (Figure 5.21A&B, Insert).

Similar results have been achieved in the presence of low concentration (10 µg/ml) of WCEP protein in $CaCl_2$ only. Crystals favour precipitating in a line in the initial stage of the channel (Dy<1 mm) (Figure 5.21C), and separated in the channel with Dy>10 mm (Figure 5.21D). However, the presence of a low concentration of WCEP induces more crystal precipitation in the channel. The high-magnification SEM images demonstrate the crystal details in both areas, in stratified structures (Figure 5.21C& D, Inserts).

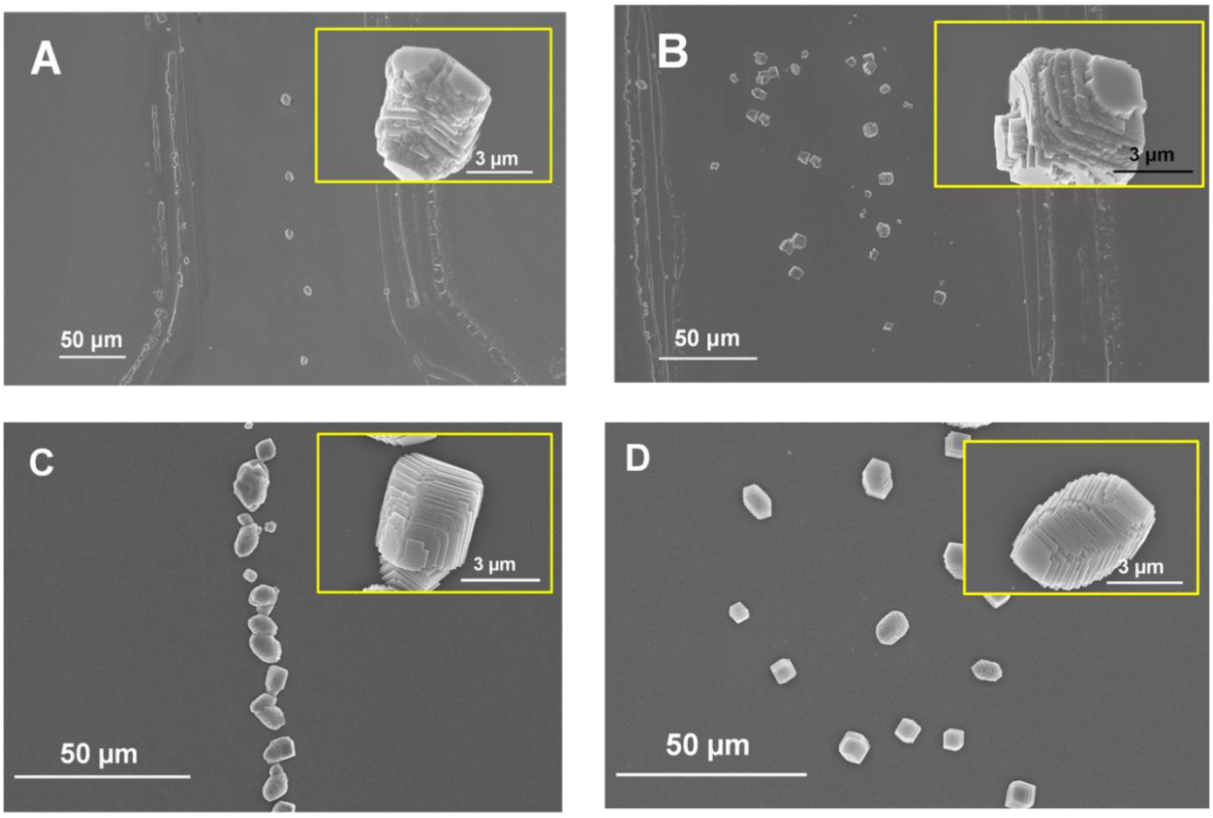

Figure 5.21. Crystal formation in the presence of WCEP in $CaCl_2$ solution only.

Calcite crystals dominate the on-chip crystallisation when WCEP protein was added in 50 mM $CaCl_2$ solution only. (A) In the presence of high concentration (50 µg/ml) of proteins, a line of individual crystals appeared in the beginning of the main channel. (B) Crystals separated across the channel after mass lateral diffusion. The inserted images present the individual crystals with layered structures respectively. (C) Similar phenomenon appears in the condition of low concentration (10 µg/ml) of proteins, with crystals aggregating in a line in the beginning of channel. (D) Well separated across the channel after protein and ion diffusion. The inserted high-resolution SEM images present the crystal formation of layers structures (The inserts in C&D).

- *WCEP in both reagent solutions*

When 50 µg/ml WCEP protein is present in both solutions, crystal morphology is changed, with both calcite and vaterite forming in the microfluidic channel (Figure 5.22). In the presence of WCEP in both solutions, a line of individual crystals forms in the channel with short flow distance (Dy<1 mm) (Figure 5.22A). Further down the microfluidic channel (Dy>10 mm), crystals are spread across the channel, with both spherical and rhombohedral crystals (Figure 5.22B). In this instance, calcite structures have been found embedded in the spherical vaterite crystal surface (Figure 5.22C). This bi-polymorph structure comprises layered calcite edges coming out from the spherical vaterite crystals (Figure 5.22C, Insert). This illustrates a

polymorph switch in the presence of WCEP in both reagent solutions. When 10 µg/ml WCEP protein was mixed with both solutions, similar crystallisation results were generated, with both vaterite and calcite crystals formed in the channel (Figure 5.22D). However, compared to the presence of high concentration of WCEP protein, the presence of 10 µg/ml protein induces more calcite crystals.

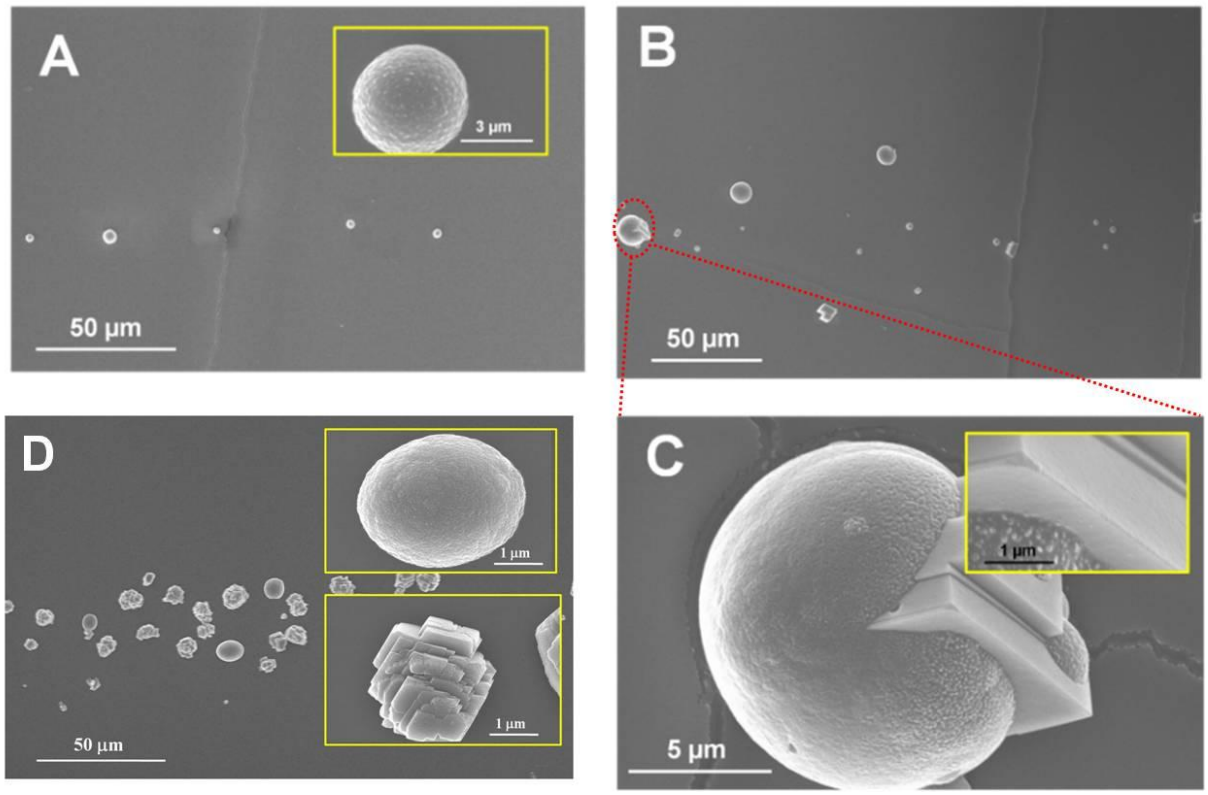

Figure 5.22. On-chip crystallisation in the present of WCEP mixed with both solutions.

When 50 µg/ml WCEP protein was mixed with both reagents, vaterite and calcite precipitated in the microfluidic channel. (A) Few crystals were aligned in the beginning of channel. The inserted high-magnification image confirmed these crystals as spherical vaterite. (B) At Dy>10 mm, crystals of calcite and vaterite are dispersed in the channel. (C) High-resolution SEM image reveals the rough surface of the vaterite structure, with layered calcite crystal growing out from the surface. The insert image presents the details of layered structures. (D) When 10µg/ml WCEP protein was mixed with both reagent solutions, both vaterite and calcite crystals precipitated in the channel. The inserted images show the details of vaterite and calcite crystals formed in this condition.

- *WCEP in Na_2CO_3 solution only*

When this complex was mixed with Na_2CO_3 solution only, spherical vaterite crystals dominantly formed in the microfluidic channel. A stream of crystals initially formed without any mass diffusion across the interface of two streams (Figure 5.23A). In this condition, many

spherical vaterite structures are precipitated in the channel with only a few calcite crystals. After mass diffusion, randomly separated crystals appear in the channel instead of the single line. Calcite crystals formed in the channel after some distance (Dy>5 mm) (Figure 5.23B). When a low concentration (10 µg/ml) of WCEP protein was added in Na_2CO_3 solution only, a similar result was obtained (Figure 5.23C), with both calcite and spherical vaterite crystals precipitated in the channel.

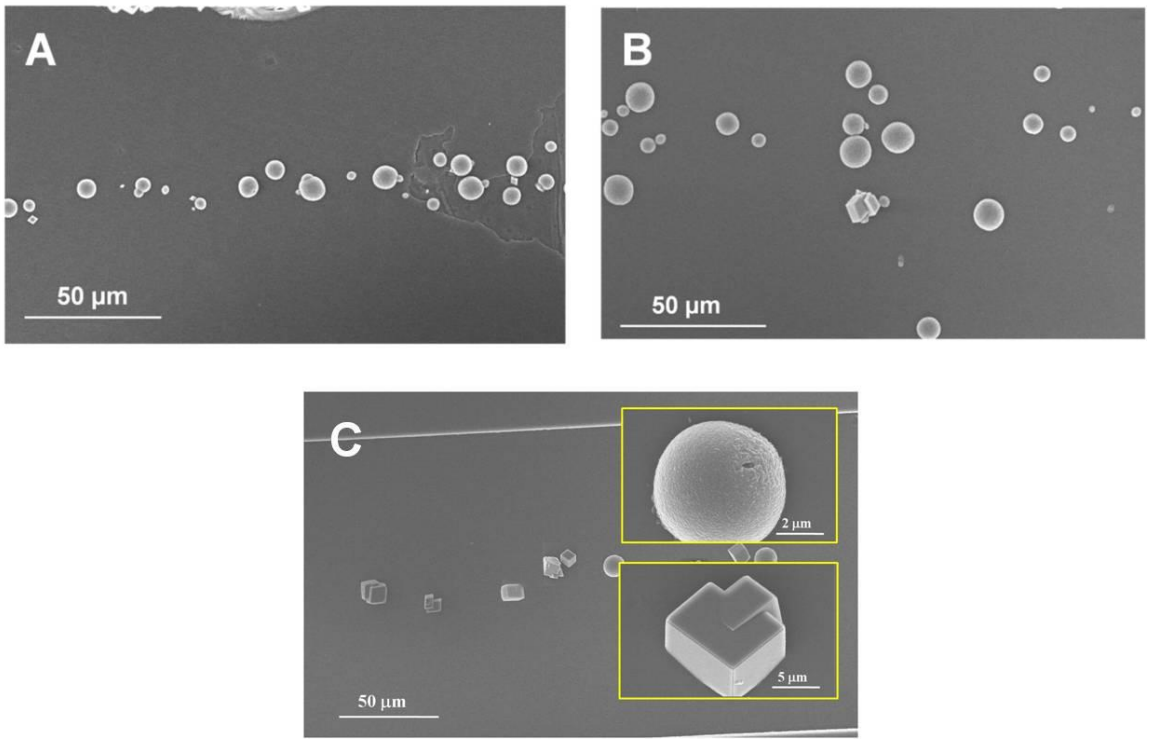

Figure 5.23. On-chip crystallisation with WCEP in Na_2CO_3 solution.

High concentration (50 µg/ml) of WCEP mixed with 50 mM Na_2CO_3 solution only, spherical vaterite crystals dominate in the channel. (A) A line of crystals formed in the centre of the microfluidic channel in the beginning of the reaction channel (Dy<1 mm). (B) The diffusion of ions and proteins with Dy>5 mm induces well dispersed crystals including both calcite and vaterite. (C) When low concentration (10 µg/ml) of WCEP protein mixed with 50 mM Na_2CO_3 solution, both calcite and spherical vaterite crystals precipitated in the channel. The inserted images show the structure details of both calcite and vaterite crystals.

This set of on-chip crystallisation studies show a lack of polymorph selection in the presence of WCEP in Na_2CO_3 solution only. Both conventional spherical vaterite and rhombohedral calcite crystals precipitate in the channel under this condition. Compared to the on-chip crystal formation with other extrapallial fluid proteins in Na_2CO_3 solution only, the presence of WCEP is the only protein that does not induce multilayered calcite crystals.

5.2.8 Positive and negative controls on crystallisation

The on-chip functional screening of extrapallial fluid proteins clearly demonstrates that the influence of EP proteins on $CaCO_3$ formation strictly depends on the components carried with the protein. This phenomenon can be explained by protein calcium-binding abilities, which has generated novel structures in *in vitro* crystallisation experiments (Falini et al., 1996, Belcher et al., 1996, Pokroy et al., 2007). As a consequence, both positive and negative control experiments were conducted on-chip, to compare with the results shown for the EP proteins. Commercial calcium-binding protein (CBP), purchased from Sigma Aldrich, was used as a positive control, while bovine serum albumin (BSA) was used as a negative control since it is a non-biomineral protein. Polyacrylic acid (PAA, 1%), with molecular weight of ~3500 was used for on-chip crystallisation as a positive control. All these control experiments were conducted in an analogous manner to the previous experiments with EP proteins, mixing with different reaction reagents to create the same scenarios for crystal growth.

- *Calcium-binding protein (CBP)*

In the presence of CBP, crystal formation is similar to that observed for the major wild-type 28 kDa extrapallial fluid protein (WEP). Hollow vaterite structures and calcite crystals formed when high concentration (50 µg/ml) of CBP added into $CaCl_2$ solution only (Figure 5.24A). The results imply that the protein's calcium-binding ability has impacted on crystal formation, inducing hollow lemon-shaped crystals. However, the hollow vaterite structures formed with CBP are different from those formed in the presence of WEP protein. With WEP protein, the hollow structure has a rough surface composed of nano-granules (Section 5.2.3). The CBP protein generated the hollow structure with a thin smooth wall (Figure 5.24A) and rhombohedral calcite (Figure 5.24B). It is assumed that this difference in the outer wall of these structures is attributable to the differences in the structure of the two calcium-binding proteins. In other conditions of on-chip screening with the CBP protein, calcite is the only polymorph precipitated in the microfluidic chips (Figure 5.24C). High-resolution SEM images indicate the calcite crystal structure with several layers in the presence of CBP protein (Figure 5.24D).

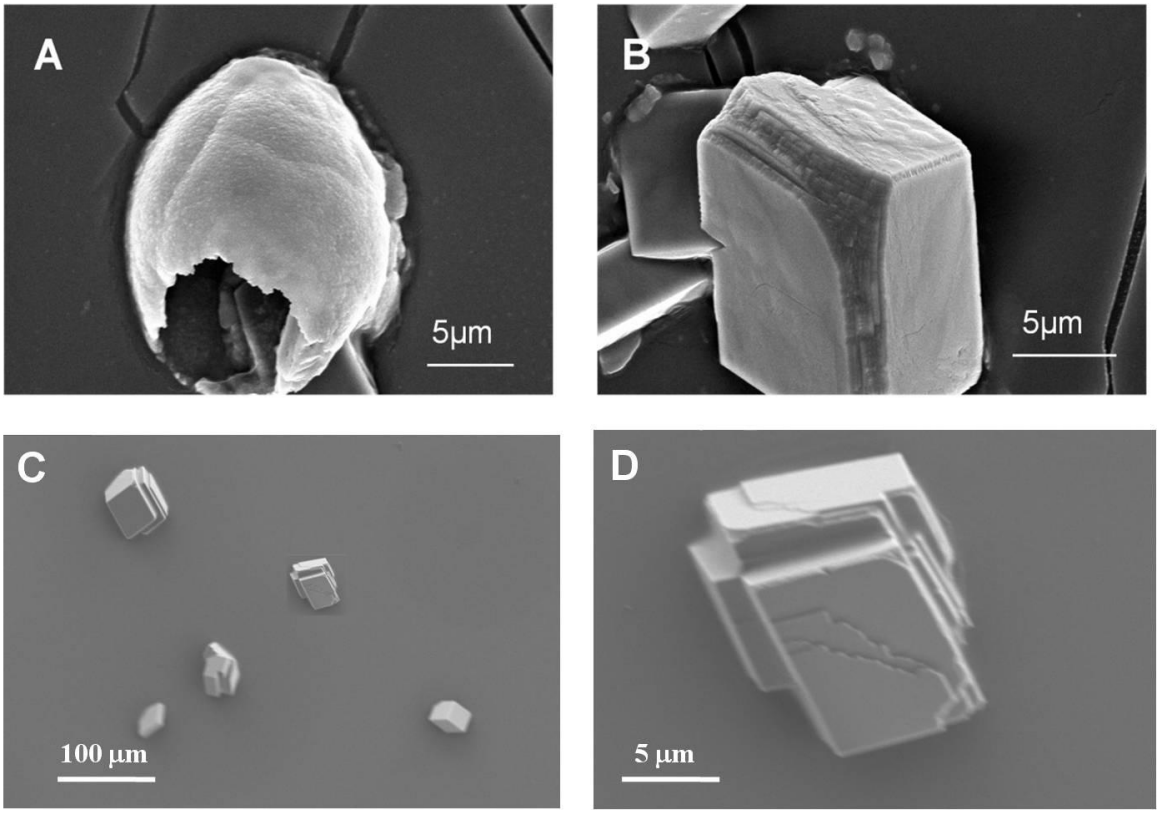

Figure 5.24. On-chip crystal formation with calcium-binding protein.

Calcium-binding protein in $CaCl_2$ solution only gave rise to both open, thin shell vaterite (A) and rhombohedral calcite (B) crystal formation. (C) All other conditions gave calcite crystals in the channel. (D) High-magnification SEM image shows the calcite crystal details in the condition of CBP in both solutions.

- *Polyacrylic acid (PAA)*

Polyacrylic acid (PAA), which has strong calcium-binding characteristics, was also used as a positive control. Three different reaction conditions (Table 2.2 in Chapter 2) were used to illustrate the influence of PAA on crystallisation.

In all conditions of PAA mixed with different reagents, similar results were achieved, with the spherical vaterite crystals, having a rough surface composed with nano-granules and multilayered calcite crystals (Figure 5.25), either PAA is dissolved in $CaCl_2$ solution only (Figure 5.25A), Na_2CO_3 solution only (Figure 5.25B) or in both solutions (Figure 5.25C). High-magnification SEM images show that vaterite crystal structures have a rough surface with nano-granules (Figure 5.25D). The calcite crystals have been confirmed by high-magnification SEM images indicating layered structures in all conditions in the presence of PAA.

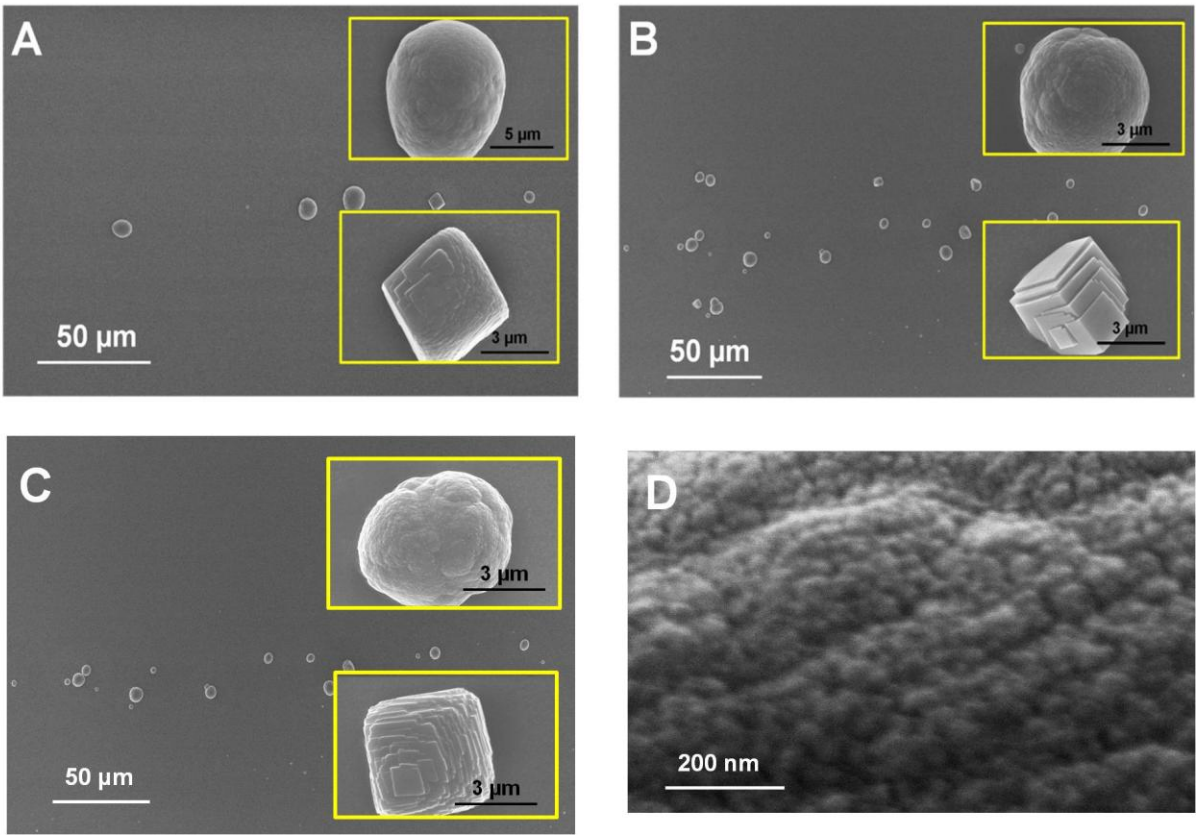

Figure 5.25. On-chip crystallisation in the presence of polyacrylic acid.

Polyacrylic acid (PAA) was used as a positive control for $CaCO_3$ on-chip crystallisation. (A) When PAA is in the $CaCl_2$ solution, both calcite and vaterite crystals formed in the microfluidic-channel. (B) Both spherical vaterite and layered calcite crystals formed in the channel in the condition of PAA in Na_2CO_3 solution only. (C) Similar crystallisation results, with vaterite and calcite crystals, occurred when PAA was added in both reagents. All inserted images show the individual crystals with structure details: calcite in layered structures and vaterite crystals having rough surfaces. (D) Higher magnification SEM image shows the surface details of vaterite crystals.

- *Bovine serum albumin (BSA)*

Bovine serum albumin (BSA) only has calcium-binding ability when the BSA concentration is greater than 3 g/ml (Besarab et al., 1981). Therefore, it can be assumed that there is unlikely to be calcium-binding occurring in the presence of 50 µg/ml BSA. In microfluidic system, BSA serves as a non-functional protein control at a concentration of 50 µg/ml. Although BSA has been mixed with $CaCl_2$ only, Na_2CO_3 only and both solution to create more crystallisation conditions, both rhombohedral calcite and spherical vaterite crystals formed in all these conditions (Figure 5.26A). The high-magnification SEM image represents the details of crystal morphologies with smooth surfaces, appearing on both vaterite and calcite (Figure 5.26 B&C). It is worth noting that when BSA is used, no hollow lemon-shaped crystals are formed

in any condition tried using microfluidic device.

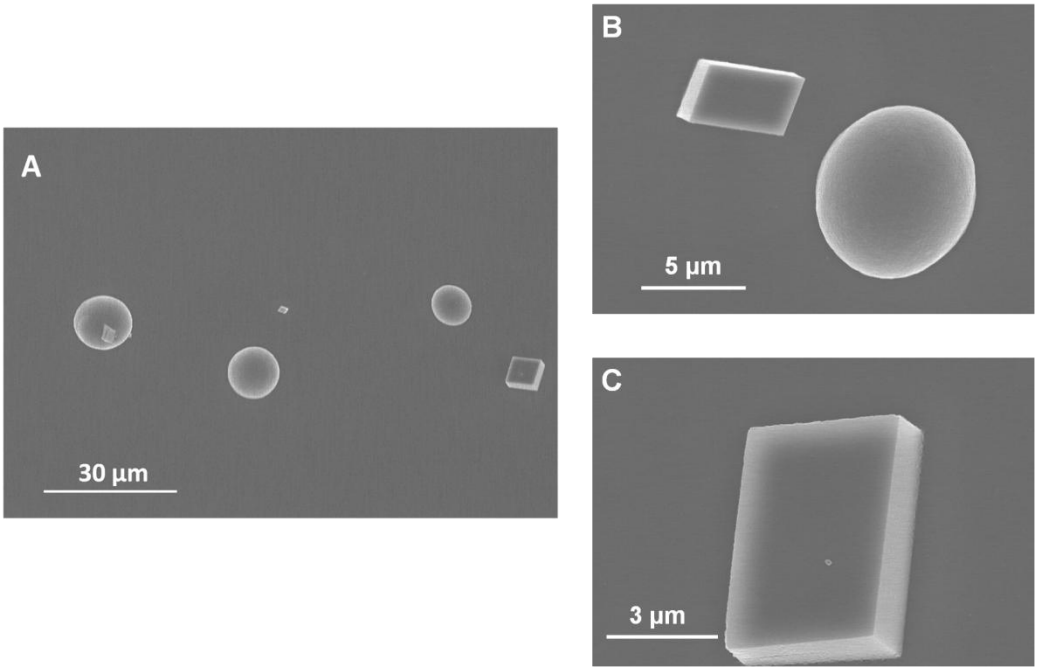

Figure 5.26. On-chip crystallisation in the presence of BSA.

(A) In all three conditions in the presence of BSA, both spherical vaterite and rhombohedral calcite crystals formed in the microfluidic channel. (B, C) Both structures have regular smooth surfaces (B , C).

5.2.9 On-chip crystallisation without proteins

A negative control without any protein, only 100mM MOPS buffer (pH 7.5), was also used to study crystal growth in the microfluidic channel. In the absence of any functional protein, rhombohedral calcite crystals are abundant in the channel (Figure 5.27A). High-resolution SEM image display conventional rhombohedral calcite precipitated in the microfluidic channel (Figure 5.27B). Raman spectroscopy identifies these crystals as calcite, with characteristic shifts at 1086, 712, 281 and 155 cm^{-1} (Figure 5.27C). In addition, semi-quantitative analysis indicates that this inorganic condition induced more crystals with a shorter induction time, compared to that when extrapallial proteins were present (Figure 5.4 in Section 5.2.3).

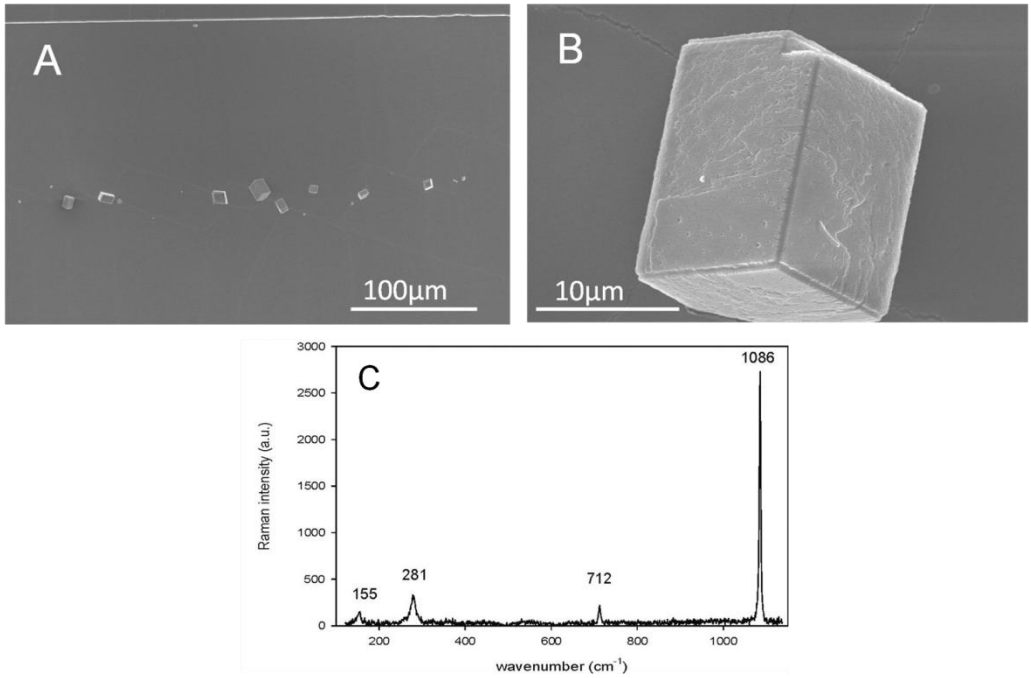

Figure 5.27. Crystal formation in inorganic buffer system.

(A) Overview of crystals formed in the microfluidic channel in the buffer system without any protein. Calcite is the abundant polymorph in this inorganic condition. (B) High-resolution SEM image shows the details of the rhombohedral calcite crystals. (C) Raman spectrum identified the rhombohedral crystals as inorganic calcite with major peak of characteristic Raman shifts at 1086 cm^{-1} and minor peaks at 155 and 281 cm^{-1}.

5.2.10 *In-situ* Raman detection of on-chip vaterite formation

In biomineral studies, vaterite is the least stable polymorph among the three major crystalline polymorphs: calcite, aragonite and vaterite. In the protein screening experiments, lemon-shaped vaterite crystals are induced by three main extrapallial proteins during crystallisation. These vaterite crystals are assumed to be a result of the influence of the protein-Ca^{2+} binding ability. This interesting structure has been only found in the presence of main extrapallial fluid proteins and the CBP protein.

In order to investigate the protein-mineral interaction during lemon-shaped vaterite formation, *in-situ* Raman spectroscopy was used during on-chip crystallisation. This combination of Raman detection and real-time on-chip crystallisation was used to detect calcite crystal formation in the presence of total wild-type extrapallial fluid (TWEP) proteins in the microfludic device (Section 4.2.4 in Chapter 4). It confirmed that the oval calcite crystals are stable structures during crystallisation.

In-situ Raman spectroscopy was used again during on-chip crystallisation with the major expressed extrapallial (EEP) protein in 50 mM $CaCl_2$ solution only, which had induced the lemon-shaped crystals. Real-time Raman spectra were collected every 20 seconds, during the crystallisation. Initially, there are no characteristic peaks except the channel background of the interface of the two solutions (Figure 5.28). As time lapses, the characteristic peak for vaterite formation of a shoulder at 1074 cm^{-1} appears. With continuous flow the spectrum gets stronger without any further change.

The amplified investigation on the characteristic peaks of vaterite in the range of 1050 to 1120 cm^{-1} show the major Raman shifts during the crystallisation (Figure 5.28A). The significant vaterite characteristic of a of shoulder at 1074 cm^{-1} adjacent to the major peak at 1091 cm^{-1} starts forming after 20 seconds. After this, both peaks get stronger without any shift during crystallisation. All these investigations confirm that there is no polymorph switch during the vaterie on-chip formation, with stable lemon-shaped vaterite formation in the presence of EEP.

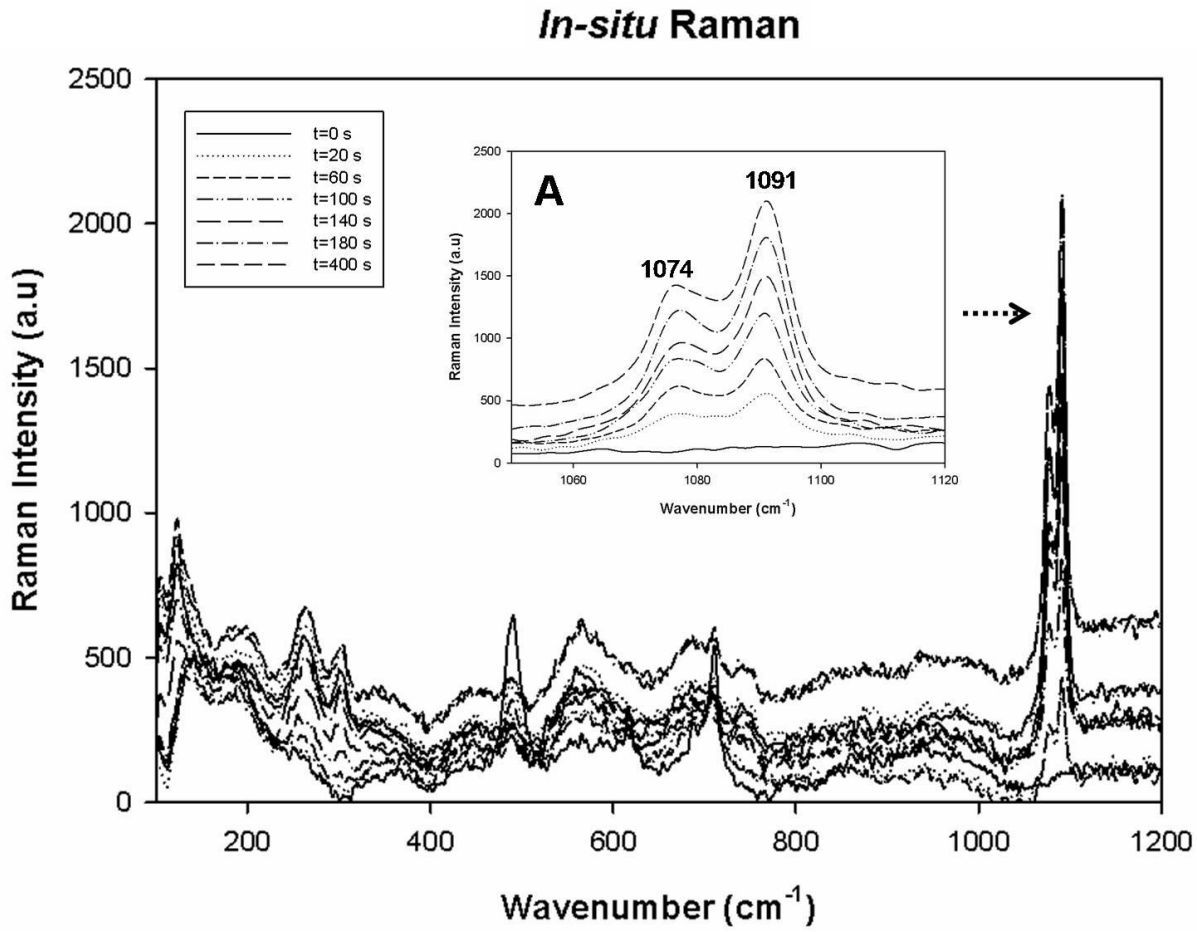

Figure 5.28. *In-situ* Raman spectra of on-chip crystallisation of vaterite in the presence of EEP protein.

Consecutive spectra are collected every 20 s from the initial the interface. (A) The characteristic peaks of vaterite crystal in the range of wavelength of 1050 to 1120 cm^{-1} were presented during crystallisation.

5.3 Discussion

5.3.1 $CaCO_3$ crystal distribution in the laminar flow microfluidic system

Understanding the function of biomineral proteins during *in vitro* crystallisation is fundamentally important for the investigation on the mechanism of the biomineralisation process. Previous studies have presented numerous experimental conditions required for protein function on crystallisation control (Belcher et al., 1996, Gotliv et al., 2005, Hou and Feng, 2006, Takeuchi et al., 2008, Feng et al., 2009, Suzuki et al., 2009).

In the pressure-driven laminar flow microfluidic system, mass transport into other streams is driven by the lateral diffusion. Therefore, a large number of scenarios have been created in the channel, with localised ions and proteins for crystal morphology and polymorph control. Combination of computational modelling and real-time experiments illustrates the influence of protein and ion concentration profiles on crystal morphology and polymorph. When EEP protein is mixed with $CaCl_2$ only, the decreasing of protein concentration along the channel (Dy increasing) induced the changing of roughness of lemon-shaped vaterite surface, simultaneously produced calcite crystals (Figure 5.11 in Section 5.2.5).

As shown above, different crystal structures have been generated in microfluidic channel in presence of different biomineral proteins. The summary of all crystallisation results with high concentration (50 μg/ml) biomineral proteins mixed with different reagents have been listed in Table 5.1. In addition, all control experimental results have also been presented for the comparison to functional biomineral proteins. All these results indicate the modification on crystal morphology and polymorph have been achieved from biomineral proteins.

In addition, in the laminar flow microfluidic system, crystal distribution is strictly controlled by the on-chip supersaturation ratio (S) profile. In the buffered pH condition, individual crystals formed in a line at the beginning, when the two solutions merge. This phenomenon has been predicted by the supersaturation ratio modelling results showing a sharp peak in the middle of the channel. With flow running along the channel (Dy increases), crystals start to spread in the channel, with a broader profile of supersaturation ratio. Finally, crystals are randomly distributed in the channel with a flatten supersaturation ratio profile after a long distance (Dy>10 mm).

Protein	Conditions in microfluidic	Crystallisation results
WEP	WEP in $CaCl_2$	Hollow lemon-shaped vaterite
	WEP in both solutions	Multilayered calcite
	WEP in Na_2CO_3	Multilayered calcite
EEP	EEP in $CaCl_2$	Lemon-shaped vaterite
	EEP in both solutions	Lemon-shaped vaterite
	EEP in Na_2CO_3	Multilayered calcite
C1q	C1q in $CaCl_2$	Lemon-shaped vaterite
	C1q in both solutions	Lemon-shaped vaterite
	C1q in Na_2CO_3	Multilayered calcite
WCEP	WCEP in $CaCl_2$	Layered calcite crystals
	WCEP in both solutions	Vaterite switch to layered calcite
	WCEP in Na_2CO_3	Round vaterite and rhombohedral calcite
PAA	PAA in $CaCl_2$	Vaterite with rough surface and multilayered calcite
	PAA in both solutions	
	PAA in Na_2CO_3	
CBP	CBP in $CaCl_2$	Hollow vaterite
	CBP in both solutions	Multilayered calcite
	CBP in Na_2CO_3	Multilayered calcite
BSA	CBP in $CaCl_2$	Round vaterite and rhombohedral calcite
	BSA in both solutions	
	BSA in Na_2CO_3	
MOPS buffer		Rhombohedral calcite dominated

Table 5.1 Summary of on-chip crystallisation results in different conditions.

The on-chip $CaCO_3$ crystallisation varies in different conditions. This table summarises the crystallisation results with high concentration (50 μg/ml) of biomineral proteins in microfluidic channel mixed with different reagents. Control experimental results including positive controls (PAA and CBP) and negative controls (BSA and MOPS buffer) are also listed in the table.

5.3.2 Vaterite crystal formation in the microfluidic system

In the functional screening experiments on $CaCO_3$ on-chip crystallisation, vaterite crystals formed in the channel when organic additives are mixed with $CaCl_2$ solution only, except in the presence of wild-type extrapallial fluid complex (WCEP) proteins. An overview of vaterite

formation illustrates that different morphologies have been achieved with different proteins (Figure 5.29). Classic spherical vaterite structures formed with smooth surfaces in the channel with BSA (Figure 5.29A). The lemon-shaped hollow structures precipitated in the channel in the presence of calcium-binding protein (CBP) in $CaCl_2$ solution only (Figure 5.29B). This structure also precipitated in the channel in the presence of biomineral proteins including the major wild-type 28 kDa extrapallial (WEP) protein (Figure 5.29C), the major expressed extrapallial (EEP) protein (Figure 5.29D) and the C1q domain (Figure 5.29E).

Previous studies illustrated the calcium-binding capacity of the 28 kDa WEP (Yin et al., 2005). Since EEP protein has the same amino acid sequence as the WEP protein, this protein is assumed to also have a similar calcium-binding capacity. The same prediction applies to the C1q domain since it is the C-terminal domain of EEP. The on-chip crystallisation results of screening all three proteins produced lemon-shaped crystals. Therefore, this specific structure is likely to be the product of the presence of calcium-binding capacity of extrapallial fluid proteins.

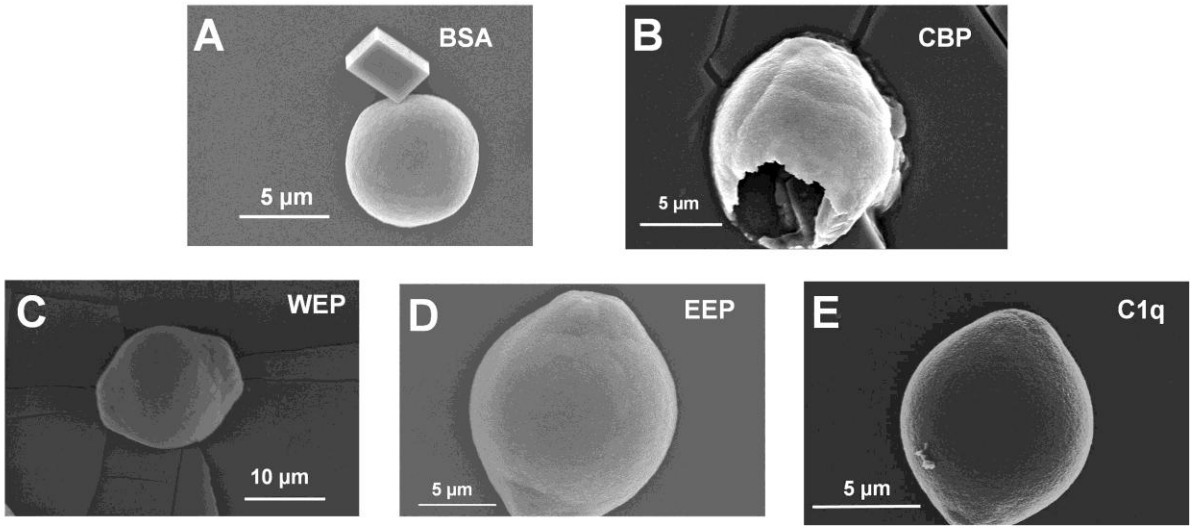

Figure 5.29. Vaterite crystal on-chip formation in the presence of different additives.

Vaterite crystals precipitated in the channel when proteins added to the $CaCl_2$ solution only, except for the WCEP protein. (A) Spherical vaterite crystal formed in the presence of non-functional protein, BSA, with smooth crystal surfaces. (B) Hollow vaterite structures precipitated in the channel in the condition of CBP protein in $CaCl_2$ solution only. Lemon-shaped structures formed in the channel in the presence of biomineral proteins of 28 kDa WEP (C), EEP (D) and 14kDa C1q (E).

High-magnification SEM images reveal the sub-micron surface details of the vaterite crystals formed in the presence of the glycosylated WEP (Figure 5.30A) and the non-glycosylated EEP (Figure 5.30B). The hollow vaterite crystals have a porous surface composed of nano-granules of diameter of ~30 nm (Figure 5.30A). However, in the presence of non-glycosylated EEP protein, there is no direct evidence identifying the lemon-shaped vaterite as hollow structures. High-resolution SEM images show that these lemon-shaped crystals also have a rough surface with nano-granules (Figure 5.30B). This set of results shows the possible effect of carbohydrate chains on crystal morphological control. The linked carbohydrate moiety probably enhances the hollow structure formation composed within crystals. These hollow structures are composed of nano-granules (40 nm), which form in aqueous condition with the interaction between the protein and inorganic ions. This phenomenon can be explained by the hypothesis of protein modification on crystal morphologies (Cölfen and Mann, 2003, Gao et al., 2006).

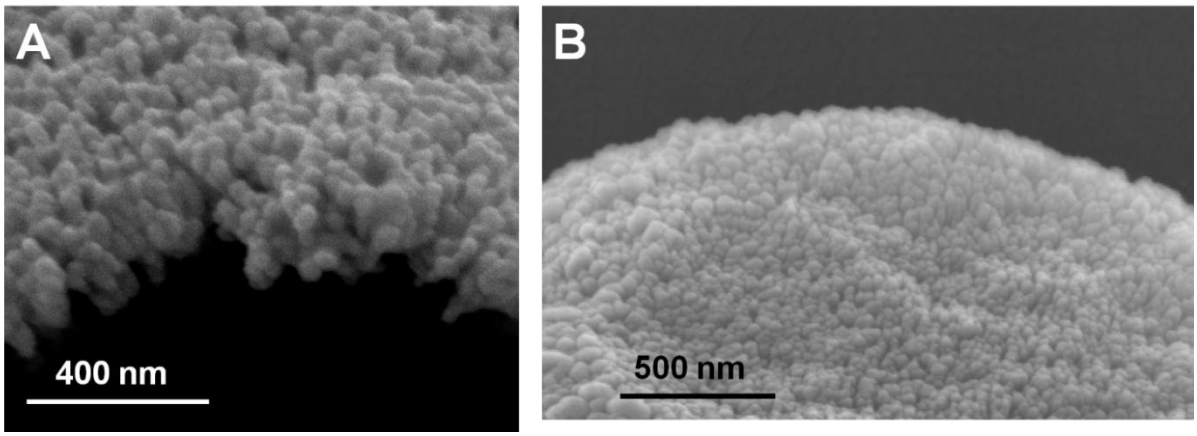

Figure 5.30. High-magnification SEM images of vaterite crystal surface details.

(A) High-magnification SEM images demonstrate the thin crystal shell of hollow vaterite formed in the condition of glycosylated 28 kDa WEP in $CaCl_2$ solution only. The surface is composed with nano-granules. (B) High-magnification SEM image presents the surface details of vaterite crystals formed in the condition of the non-glycosylated EEP protein in $CaCl_2$ solution only.

The possible mechanisms of protein-mineral interaction during lemon-shaped crystal formation in this dynamic system are shown in Figure 5.31. During the sample preparation, proteins were added to the $CaCl_2$ solution, complex with Ca^{2+}. This complex induces the formation of nucleation clusters with proteins. Some of these cluster units aggregate to form the vaterite nano-particles in the presence of extrapallial proteins. Afterwards, nano-particles assemble together to form a nucleation oval template. With continuous supplement of reagent solutions, nucleation clusters attach onto the template and the lemon-shaped crystals form in

the channel. According to the different structure of biomineral proteins, especially the glycosylated chains in the WEP protein, the hollow structures formed in the channel under the control of the protein aggregation with linked carbohydrate. In addition, in this dynamic system, protein concentration varies in different parts of the microfluidic channel. Roughness of vaterite crystal surface may vary according to the protein concentrations.

As to the WCEP protein, spherical vaterite crystals formed when protein is mixed with Na_2CO_3 only or both reagents, which is not following the pathway of lemon-shaped crystals. The possible mechanism of WCEP protein on crystallisation control will be discussed below.

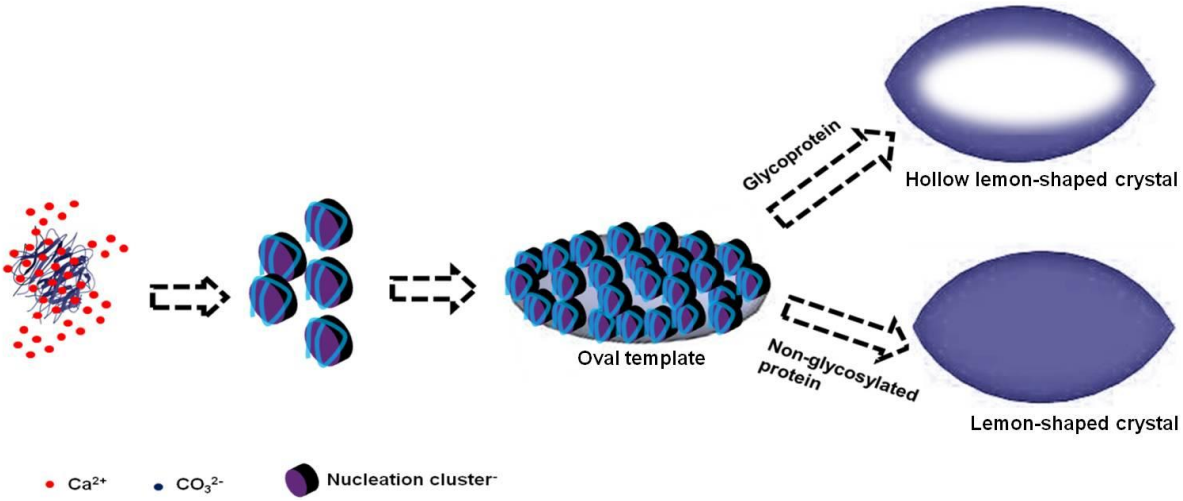

Figure 5.31. Schematic illustration of pathway of lemon-shaped vaterite formation.

When main extrapallial proteins are mixed with Ca^{2+} solution prior to crystallisation, Ca^{2+} ions are captured by proteins in aqueous conditions. This leads the formation of nucleation clusters with proteins. It is followed by the oval crystal template formation, which generate the lemon-shaped crystals. The presence of glycoproteins induces the hollow crystals.

5.3.3 The calcite formation in the microfluidic system

In the on-chip screening experiments, the condition of mixing organic additives with Na_2CO_3 solution only induced calcite crystal formation. However, the influence of organic additives can be illustrated by comparing the calcite crystal morphologies in all these conditions (Figure 5.32). The conventional calcite crystals formed in the BSA condition confirms the negative control of this protein (Figure 5.32A). On the other hand, the positive control of PAA (Figure 5.32B) and CBP (Figure 5.32C) induced layered calcite structures. Similar multilayer calcite structures form in the presence of all the biomineral proteins: C1q domain (Figure 5.32D), WEP protein (Figure 5.32E) and EEP protein (Figure 5.32F).

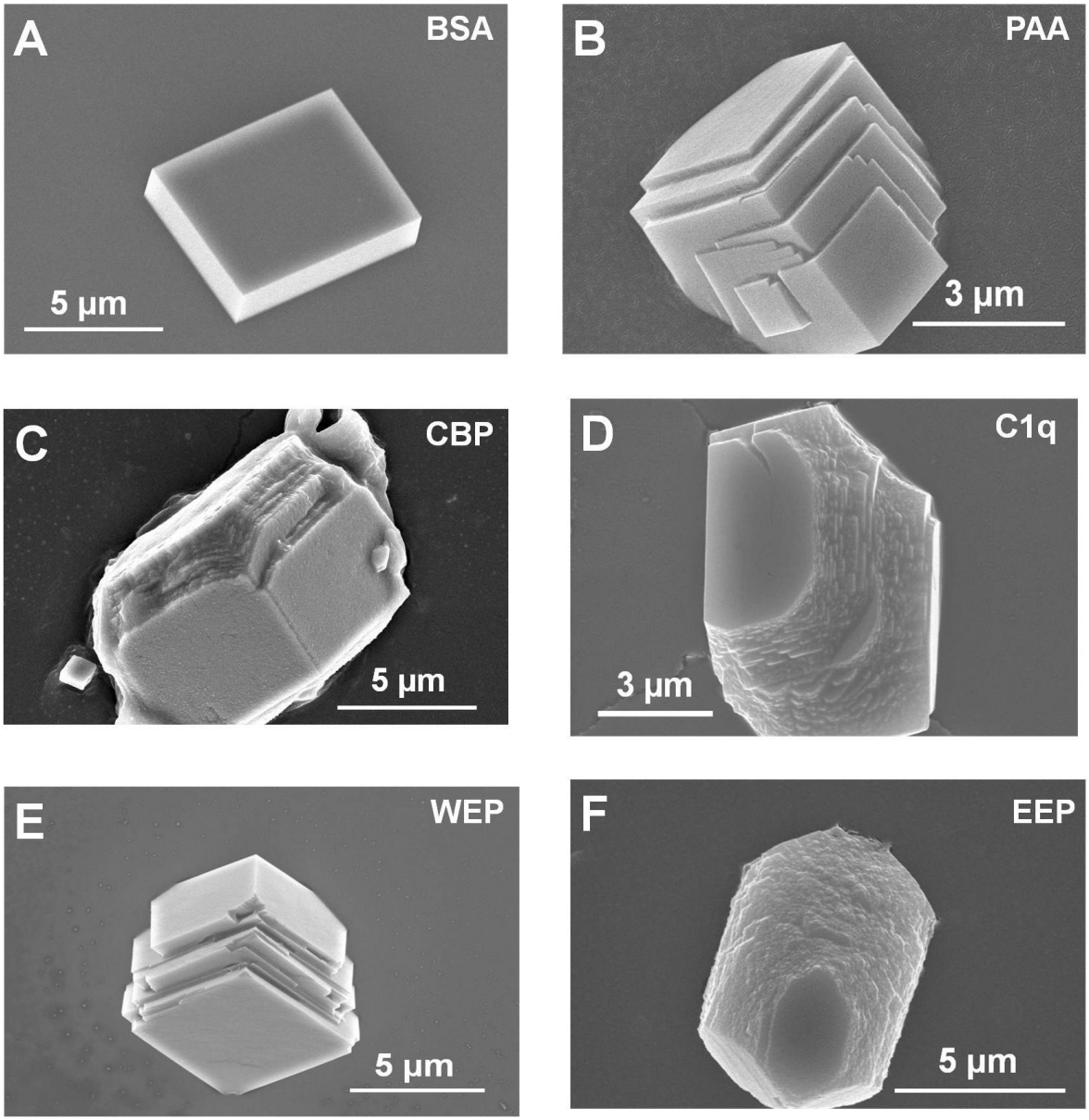

Figure 5.32. Calcite on-chip formation in the presence of different proteins.

In microfluidic crystallisation experiments, proteins and polymers were mixed with sodium carbonate only prior to delivery into the channel. Different calcite morphologies formed in the microfluidic channel with different proteins of BSA (A), PAA (B), CBP (C), C1q (D), WEP (E) and EEP (F).

Among all these calcite crystals, the most interesting structure is the hillock type structure (Figure 5.32F). These hillock shaped crystals formed in the presence of EEP protein in sodium carbonate solution only, with two facets forming the cap and one facet decreasing towards the base (Figure 5.33A). Similar calcite morphology had also been found in previous crystallisation work by Orme *et al.* (2001). They used the chiral peptides (L- and D-aspartic acid) to form this hillock type calcite crystals (Figure 5.33B), and then used AFM to identify

crystal topography (Figure 5.33C). They combined *in-situ* atomic force microscope (AFM) and peptide molecular modelling studies to illustrate the amino acid specific binding sites for crystal geometrical modification (Orme et al., 2001). Their work provides the mechanical hypothesis on the functional peptide effect on mediating crystallisation by adsorbing onto the crystal surface during crystal growth.

As similar crystal structures have been produced during on-chip screening experiments (Figure 5.33A), the EEP protein is assumed to bind to the crystal surfaces inducing geometrical structure modification. In the microfluidic system, when the extrapallial proteins are mixed with sodium carbonate solution only, there are no precursors such as protein-Ca^{2+} complex are likely to pre-exist to mediate crystal formation in aqueous conditions. Hence, during crystal formation the EEP protein may bind, or be adsorbed onto, the crystal surface mediating crystal growth in a stepwise manner. Afterwards, the protein binding process induces multilayer structure formation in the microfluidic channel. A similar mechanism can be applied to the formation of other layered calcite structures. According to the difference in the amino acid components and spatial structure of each protein or polymer, different multilayer calcite structures form in the microfluidic channel in the presence of different organic additives.

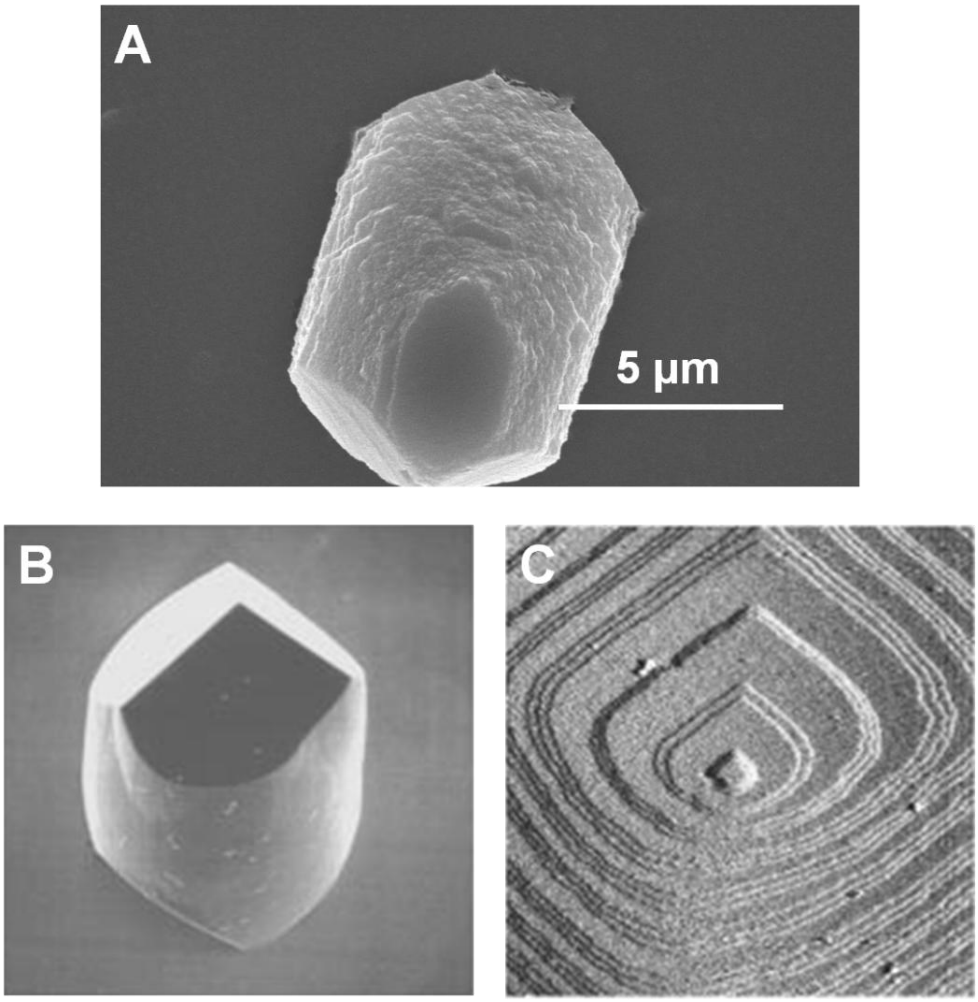

Figure 5.33. Hillock-shaped calcite formed in the presence of additives.

(A) The hillock-shaped calcite formed in microfluidic system in the condition of 50 µg/ml EEP protein in 50 mM Na_2CO_3 solution only. (B) The growth of hillock calcite crystal formed in the presence of chiral amino acid L-Asp. (C) AFM analysis of the crystal topography (Orme et al., 2001).

5.3.4 Possible pathways of crystal formation in microfluidics

Since the microfluidic system provides opportunities to screen the extrapallial fluid proteins by mixing with different reagents, the crystallisation mechanism can be varied. When the main extrapallial proteins (WEP, EEP and C1q) are mixed with the calcium chloride solution only, lemon-shaped structures precipitated in the microfluidic channel. The multilayer calcite structures are induced under the conditions when main EP proteins are introduced in sodium carbonate solution only.

The mixing of main EP proteins in $CaCl_2$ solution only induces the lemon-shaped vaterite structure. As discussed in Section 5.3.2, the mechanism of this ovoid crystal formation is

probably from the formation of nucleation cluster with proteins, which presented in Figure 5.34A.

When biomineral proteins are mixed with Na_2CO_3 only, nucleation clusters form without any protein. Proteins then recognise and bind to the cluster surface of calcium ion. The protein attachment onto the crystal surface mediates the classic rhombohedral calcite crystal formation into layered structures (Figure 5.34B). This layered crystal structure formed in the presence of functional polymers has been published previously (Orme et al., 2001).

When the major extrapallial proteins are mixed with both reagents, proteins are likely to binding to calcium and therefore follow the pathway of Figure 5.34A to produce lemon-shaped structures. This prediction has been confirmed by the experiments of EEP protein and C1q domain. However, this crystallisation process can be disturbed by the carbohydrate moiety during crystallisation, i.e. the major wild-type 28 kDa extrapallial (WEP) protein inducing multilayer calcite structures when mixed with both reagents.

In the negative control experiments, neither calcite nor vaterite crystals have been identified as morphological modifications using BSA. Both polymorphs precipitate in the microfluidic channel by a typical aggregation pathway in aqueous conditions (Cölfen and Mann, 2003).

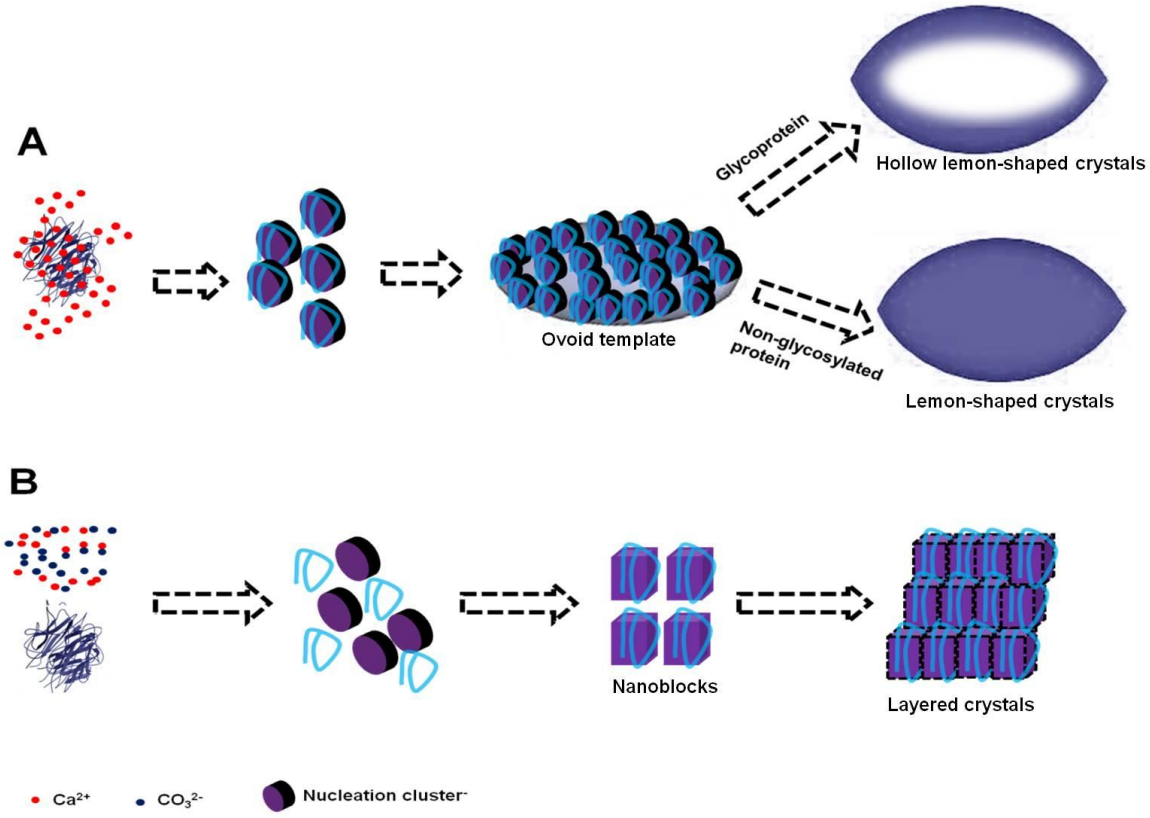

Figure 5.34. Schematic illustrations of possible pathways of on-chip crystallisation macromolecules.

There are two possible pathways of crystallisation in microfluidics when the macromolecules are delivered in different reaction reagents. (A) The schematic pathways of lemon-shaped crystal formation, which has been described as Figure 5.31. (B) When the biomineral proteins are mixed with CO_3^{2-} only before nucleation, nucleation clusters form without protein. Proteins attach onto the crystal surface during precipitation.

However, the possible mechanism on crystal formation in the presence of the wild-type extrapallial complex (WCEP) protein is unclear. Since the WCEP complex is eluted and isolated at the beginning of the anion exchange process, it is much less strongly bound to the exchange, which suggests that it has few calcium-binding sites. Of course, as it is a complex it may have as many calcium-binding domains but these have been excluded, or pushed internally into the complex and thus unavailable for calcium-binding. When introduced into the $CaCl_2$ side, few Ca^{2+} ions are taken out of solution and hence the proposed mechanism for the lemon-shaped crystal does not occur. On the other hand, when placed into the Na_2CO_3 side, the complex may be disrupted, thus making the calcium binding amino acids available and hence we get vaterite crystal forming.

Another possibility is the function of inducing calcite crystal formation of the WCEP, the calcite-inducing protein. Only calcite crystals formed in the channel when 50 mM $CaCl_2$ was

mixed with this complex, in either high or low protein concentrations. This can be supported by the existence of the bi-polymorphs structures in the condition of WCEP in both reagent solution and vaterite formation in WCEP-Na_2CO_3 conditions. Compared to the negative control, this set of proteins is assumed to induce calcite formation during crystallisation. The calcite inducing function has been identified to a matrix protein from oyster *P. fucata* in previous work (Takeuchi et al., 2008).

However, aragonite is a key component during the shell formation of mussel *M. edulis*, which has not been found in any experiment in our microfluidic system using extrapallial proteins. The missing structure of aragonite can be induced by the synergistic effects from several EP proteins in natural conditions. This has been eliminated in our functional studies when screening individual EP proteins for crystallisation. In addition, the inorganic additives in extrapallial fluid, such as Mg^{2+}, can also be involved to induce aragonite formation.

5.4 Conclusion

Calcium carbonate biomineralisation is a complicated process, which produces well defined inorganic structures with a number of macromolecules involved in the process, including proteins, glycoproteins and carbohydrates (Weiner and Hood, 1975, Falini et al., 1996, Addadi et al., 2006, Weiner, 2008). Extrapallial fluid from mussels have been used to study their effects on crystallisation, since this fluid is rich in inorganic and organic components (Crenshaw, 1972, Weiner and Hood, 1975). The total extrapallial fluid (TWEP) proteins from the mussel *M. edulis* have been screened for crystal formation in the microfluidic system in our previous results, where they induced oval crystal structures (Chapter 4). In this chapter, individual extrapallial fluid proteins including the wild-type glycosylated proteins and expressed non-glycosylated proteins are used for $CaCO_3$ on-chip crystallisation.

In the microfluidic system, reversible sealed devices have been developed to create designed channel devices. Laminar flow microfluidic channel allows constant laminar flow formation when two solutions meet in the channel. This type of microfluidic system uses mass diffusion to create a large range of crystallisation scenarios with mass concentration gradients and different supersaturation ratio (S) along the channel, which enables precise functional screening of biomineral proteins during *in vitro* crystallisation.

The combination of on-chip crystallisation and off-chip analysis provides a novel platform for biomineral *in vitro* crystallisation studies. The accurate control of crystal formation can be achieved by the microenvironment of localized protein and ion concentrations. Crystals

localized in different regions of the channel with different morphologies and polymorphs illustrate the influence of the protein concentration gradient on crystal formation. The crystallisation results indicate that crystal on-chip distribution is controlled by the supersaturation ratio (S) profile. In addition, the *in-situ* Raman spectroscopy enhances the opportunity to investigate the crystal formation from the very initial stages. The result produces stable lemon-shaped vaterite formation. These stabile vaterite crystals confirmed the protein influence during crystallisation, with EP proteins possibly integrating with ions and stabilising the vaterite formation.

This study presents the advantages of using the microfluidic approach for crystal formation over traditional methods. This technique combines the computational modelling of on-chip concentration prediction and real-time crystallisation. Protein concentrations control both crystal morphology and polymorph outcome. According to the protein calcium-binding capacities, two possible pathways for crystal formation are proposed. The lemon-shaped crystal structures are mediated by calcium-binding capacity of the extrapallial fluid proteins from the very initial stage of nucleation. However, the multilayer calcite structures are probably formed by an organic macromolecules attachment process. Both structures define the protein influence on crystal morphological control in microfluidic system.

Chapter 6

Crystallisation on microcontact printing (μCP) organic patterns

6

6.1 Introduction

6.1.1 Organic matrices in biomineral crystallisation

Biomineral analysis indicates that the formation of most biominerals is controlled by two major types of organic components: soluble organic hydrophilic components, which include proteins, glycoproteins and polypeptides; and insoluble organic matrix components such as collagen and chitin (Lowenstam and Weiner, 1989, Nudelman et al., 2006, Addadi et al., 2006). The insoluble organic components play critical roles during biomineralisation, providing a template for initial crystal nucleation, exerting influence on crystal formation including crystal orientation and morphology (Lowenstam and Weiner, 1989, Dove et al., 2003, De Paula and Silveira, 2009). Nacre, mother of pearl, is an important biomineral example composed of both organic and inorganic components. As to molluscs, the hypothesis presented for nacre growth includes four different organic zones: a central spot rich in carboxylates, a surrounding ring-shaped area of sulfates, a intertabular matrix area rich in carboxylates and sulfates and a space between the intertabular matrix and ring-shaped area containing carboxylates (Nudelman et al., 2006). Addadi *et al.* provided a model for nacre formation, which comprised two layers of chitin with crystal nucleation sites and gel-like silk fibroin proteins filling the space in between (Addadi et al., 2006). This matrix is assembled prior to crystallisation. The silk gel phase controlled crystallisation by stabilising amorphous calcium carbonate (ACC), until in contact with the nucleation sites. During crystal formation, acidic proteins were incorporated into crystals, adjusting crystal chemical and soluble properties (Addadi et al., 2006). These findings denote the critical roles provided by organic templates in the initial crystallisation process.

6.1.2 *In vitro* crystallisation with templates

In previous studies, numerous organic and inorganic materials were used as templates to modify calcium carbonate crystallisation, including Langmuir monolayer substrates (Mann et al., 1988, Mann et al., 1993), imprinted self-assembled monolayers (SAMs) on inorganic substrates (Kuther et al., 1998, Aizenberg et al., 1999) and insoluble macroporous substrates (Meldrum and Seshadri, 2000, Hetherington et al., 2011). Steric acid was initially used as a Langmuir monolayer to control crystal nucleation since it provided a functional surface (Mann et al., 1988). Self-assembled monolayers (SAMs) of alkylthiols on a Si surface was used to control $CaCO_3$ crystal nucleation, with crystallisation accelerated in the polar regions and suspended in the rest of the methyl-terminated regions (Aizenberg et al., 1999). In addition, Li and Estroff (2007) used the carboxylate-terminated self-assembled monolayers (SAMs) substrates coupled with agarose hydrogel to control crystal nucleation and morphology simultaneously. In their crystallisation system, calcite crystals, the only observed polymorph, precipitated primarily on the surface with SAMs of alkanethiols (Li and Estroff, 2007a). Meanwhile, insoluble 3-D substrates, including a polymer with sea urchin skeletal structure or colloid particle monolayer substrate, were used for crystallisation. Single calcite crystals within the template polymer structure precipitated in the presence of a rigid sponge-like polymeric sea-urchin plate (Park and Meldrum, 2004, Meldrum and Ludwigs, 2007). In their experiments, double diffusion technique was used to grow microporous crystals, after the polymer replicated identical structure to the original sea urchin template (Meldrum and Ludwigs, 2007). Moreover, well-defined crystal topography with patterned individual crystal faces has been achieved from micrometer to nano-meter scale *via* crystallisation on colloidal monolayer templates (Meldrum and Ludwigs, 2007, Finnemore et al., 2009). Thin films (120 nm thick) composed of polystyrene or polyvinyl pyridine have been also used to pattern individual calcite crystal faces (Meldrum and Colfen, 2008, Kim et al., 2010). All these findings demonstrated the applications of templated substrates in controlling crystal precipitation, orientation, polymorph and morphology.

6.1.3 Microcontact printing (μCP)

Microcontact printing (μCP), an efficient and quick method to exploit the adsorption of organic components on a variety of surfaces, was initially described by Whiteside's co-workers (Wilbur et al., 1996, Xia and Whitesides, 1998).The application of μCP in patterning proteins has advanced in biosensor, cell biology and tissue engineering research (Chen et al., 1997, Bhatia et al., 1999, Hodgson et al., 2007). For example, in cell biology studies, microcontact

printing provides protein patterns to control cell morphologies (Chen et al., 1997), orientation (Altomare et al., 2010) and segregations (Hynd et al., 2007, Hodgkinson et al., 2007). These examples illustrate that protein-patterned substrates can be achieved from this simple, reliable and efficient way of direct patterning *via* microcontact printing.

Currently, there is no published work describing μCP of biomineral proteins on $CaCO_3$ crystallisation research. This chapter firstly establishes a novel platform for crystallisation studies by using μCP extrapallial (EP) protein patterns for functional screening on *in vitro* crystallisation. In this study, the major expressed extrapallial (EEP) protein has been used as the target protein to create protein patterns for crystal growth. This protein has been shown to control $CaCO_3$ crystal growth in the microfluidic system (Section 5.2.5 in Chapter 5). In order to identify any genuine effects from the EEP protein, control experiments were employed, including a positive control with polyacrylic acid (PAA) with its strong calcium-binding capacity and a negative control with bovine serum albumin (BSA), neither of which is involved in biomineralisation.

6.2 Results

6.2.1 The fabrication of microcontact printing (μP) patterns

In order to achieve the patterns without denaturing the proteins, proteins or polymer substrates are directly 'inked' onto substrates using microcontact printing (μCP). During μCP process used here, only the substrates (PDMS and glass coverslip) are treated by oxidation from an oxygen plasma to make both PDMS and glass substrate surfaces hydrophilic, no further treatment was used. Moreover, in our microcontact printing (μCP), there is no 'click' chemistry process as normally used on glass substrates e.g. surface modification with triazole group (Link and Tirrell, 2003). All of these treatments may enhance protein immobilisation on substrate, but are likely to denature the acidic biomineral proteins.

After the micro-fabrication process, PDMS stamps were produced for the μCP. In this project, both square and circular PDMS stamps have been used for printing. Figure 6.1A presents the square PDMS patterns used in this project, patterns fabricated in dimension of 100 μm (wide) x 20 μm (height). After the μCP process, protein and polymer patterns were generated on the glass substrate surface. Fluorescein isothiocyanate-labelled bovine serum albumin (FITC-BSA) was localised in the designed regions only (Figure 6.1B&C). This provides an opportunity to control the $CaCO_3$ crystal distributions after crystallisation takes place on the

patterned substrates.

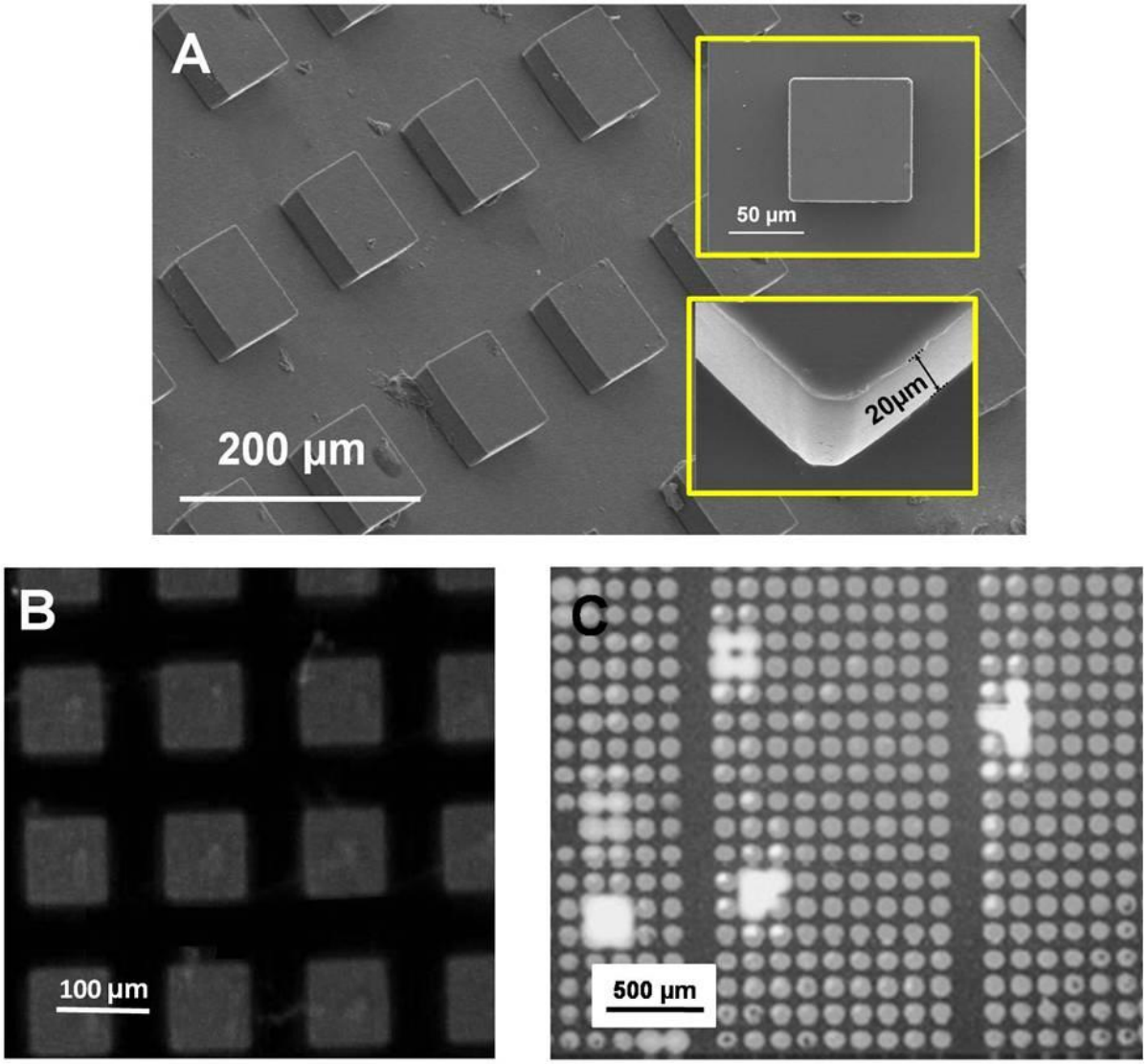

Figure 6.1. Microncontact printing patterns.

(A) Oblique view SEM image of PDMS stamp for microcontact printing (μCP). The inserted images are the high-magnification SEM micrographs showing patterns with 20 μm height and 100 μm wide. (B) After microcontact printing, proteins are localised in defined areas according to the PDMS stamp. (C) Round patterns generated using a circular PDMS stamps.

6.2.2 Crystallisation on μCP patterns using a soaking system

For this set of μCP experiments, protein and polymer are transferred onto the substrates with $CaCl_2$ solution (1 M), which was initially designed as the only calcium source to control crystal distribution. Thereafter, patterned substrates are soaked in Na_2CO_3 solution (1 M) for crystal

growth (Figure 2.4A in Chapter 2). Polyacrylic acid (PAA), the EEP protein and BSA were used in an analogous way.

In the presence of PAA-$CaCl_2$ patterns, crystals only precipitated on the patterned regions on glass substrates after a 12 hour incubation period (Figure 6.2). Stamps with circular features resulted in the formation of round patterns on the substrate with PAA-$CaCl_2$ solution (Figure 6.1C). After incubation using this patterned substrate, crystals formed on the patterned regions only (Figure 6.2).

High-resolution SEM images reveal the morphological details of precipitated crystals. Crystals form with a similar diameter of approximately 2 μm. High-resolution images show the crystal morphology in detail, which is composed of nano-particles (Figure 6.2C&D). Although the crystal morphology is not identical, these structures can be easily identified as aggregates formed from several nano-blocks (~500 nm) (Figure 6.2C&D). These crystals are the products of the presence of PAA-$CaCl_2$ patterns, which controlled crystallisation in aqueous condition. These crystals are determined as calcite by micro-Raman spectroscopy with characteristic peaks at 139 and 269, 711 and 1086 cm^{-1}.

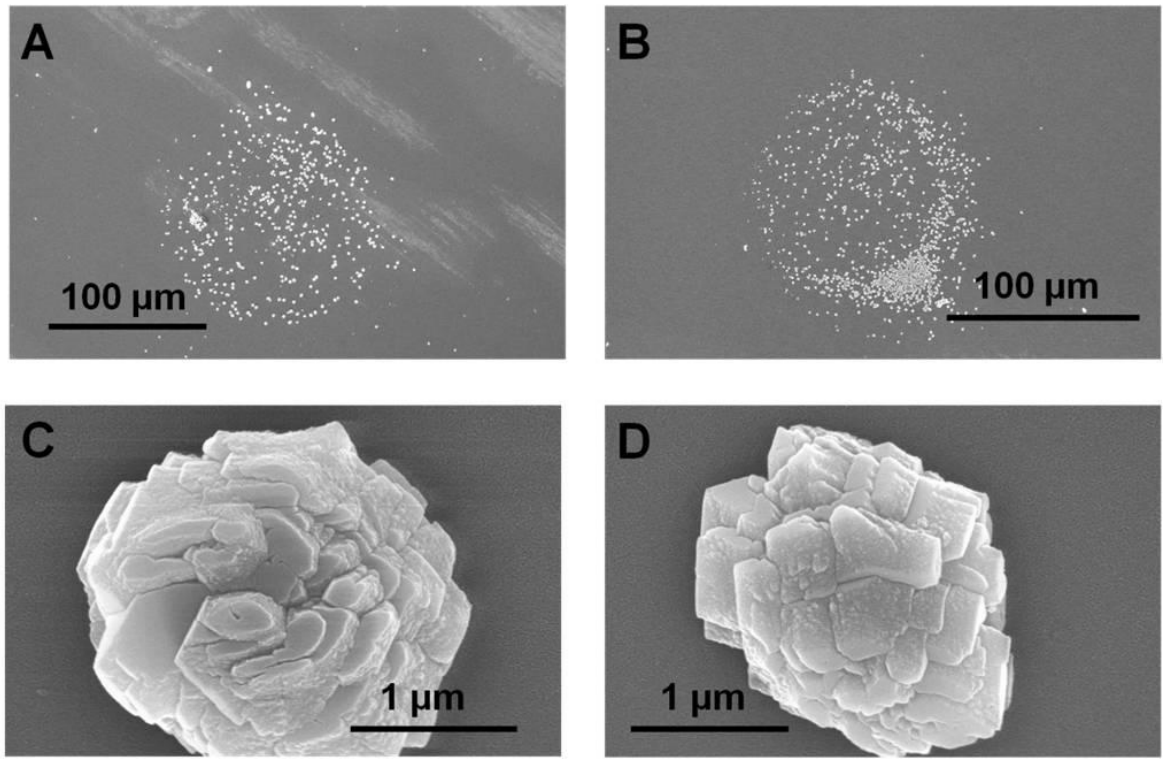

Figure 6.2. Representative SEM images of crystals formed on μCP patterned substrates.

(A, B) Since the dotted PDMS stamps have been used in this μCP process, the crystals precipitated on the dotted patterns only. (C, D) The respective high-magnification SEM images present the details of the crystals formed on the patterns. The crystals have diameters of ~2 μm, consisting of blocks of nano-structures.

After crystallisation, three spots were selected for chemical analysis *via* energy dispersive spectroscopy (EDS): one in the patterned area and two others in the non-patterned region. The EDS analysis clearly shows that there is a significant difference in chemical composition between the two areas (Figure 6.3). There are strong signals in both the calcium and carbon spectral range in the patterned areas (Figure 6.3B). However, there is no peak identifying either calcium or carbon from the spot analysis of two non-patterned areas, which have identical spectra (Figure 6.3C& D). These findings demonstrate polyacrylic acid (PAA) as an effective substrate to mediate crystallisation when serving as template.

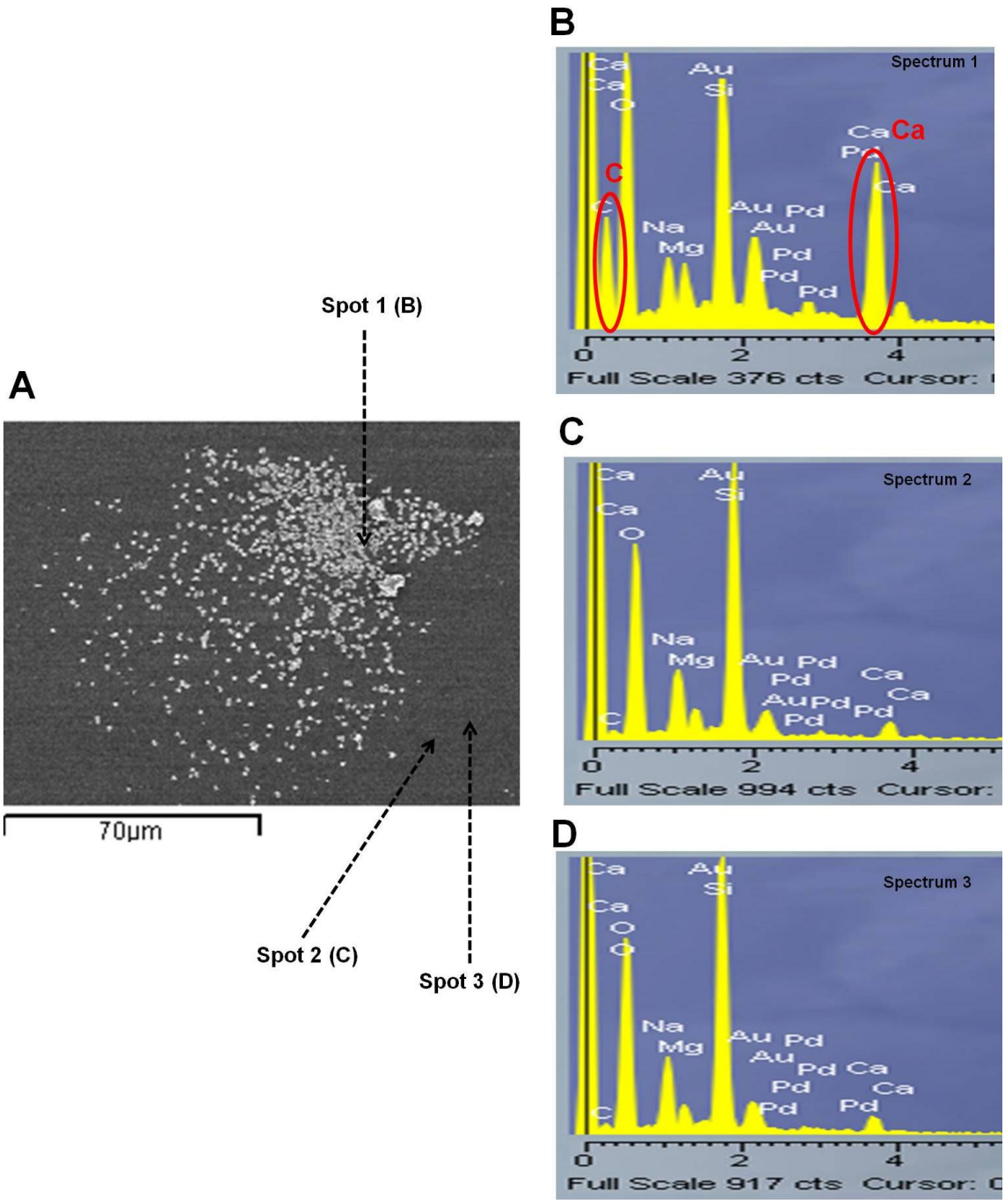

Figure 6.3. Energy dispersive spectroscopy (EDS) detection of printed PAA-$CaCl_2$ patterns.

(A) The SEM image represents the crystals only precipitated on the regions of µCP patterns. (B) EDS spectra of area in the patterned area. Both calcium and carbon were detected in this area. (C, D) EDS spectra of non-patterned regions. In the non-patterned areas, there is neither calcium nor carbon detected.

In an analogous manner to the PAA experiments, the same procedures were used for the expressed major extrapallial fluid protein (EEP) to create patterns on the glass substrate. In this condition, 50 μg/ml EEP protein was printed onto the substrate alone with 1 M $CaCl_2$ solution (Figure 6.4A).

After incubation, there was no evidence of crystals having precipitated on the substrates when using the EEP-$CaCl_2$ pattern substrates. This lack of crystal formation may be due to several possibilities. The first possibility is that only protein had been localised on the substrate surface during the μCP process, without any calcium ions. However, there are several other possibilities, i.e. insufficient Ca^{2+} was provided by the patterns to form crystals or the dissolving of EEP protein during soaking the substrates in solution.

In order to answer these questions, EDS was used again for chemical analysis prior to the crystallisation. After microcontact printing (μCP), the patterned substrate was used for EDS analysis, in the same way as PAA-$CaCl_2$ pattern with crystals. Two different areas were selected for EDS spectra comparison: one in the patterned region and the other outside the patterned region (Figure 6.4). The protein patterns can be easily observed from SEM images, with square patterns on the surface (Figure 6.4A). Energy dispersive spectroscopy (EDS) was used to distinguish the patterns from the non-patterned areas by chemical composition analysis. However, the results are the same for both regions (Figure 6.4B and C). There is no calcium detected in the patterned areas, although the protein and Ca^{2+} were printed onto the surface *via* μCP. The same result occurs when $CaCl_2$ solution is patterned with 50 μg/ml BSA onto glass surface. These results may prove that calcium ions were not printed onto surface. Alternatively, the EDS results will not distinguish calcium spectra because of the shortfall of EDS on surface chemical analysis with extremely thin protein layers. These results demonstrate the shortcoming of EDS on surface chemical analysis with thin protein layers. No crystals precipitated on the patterned substrates after applying the EEP/BSA patterns for crystallisation. Even increasing the incubation time to 24 hours makes no difference.

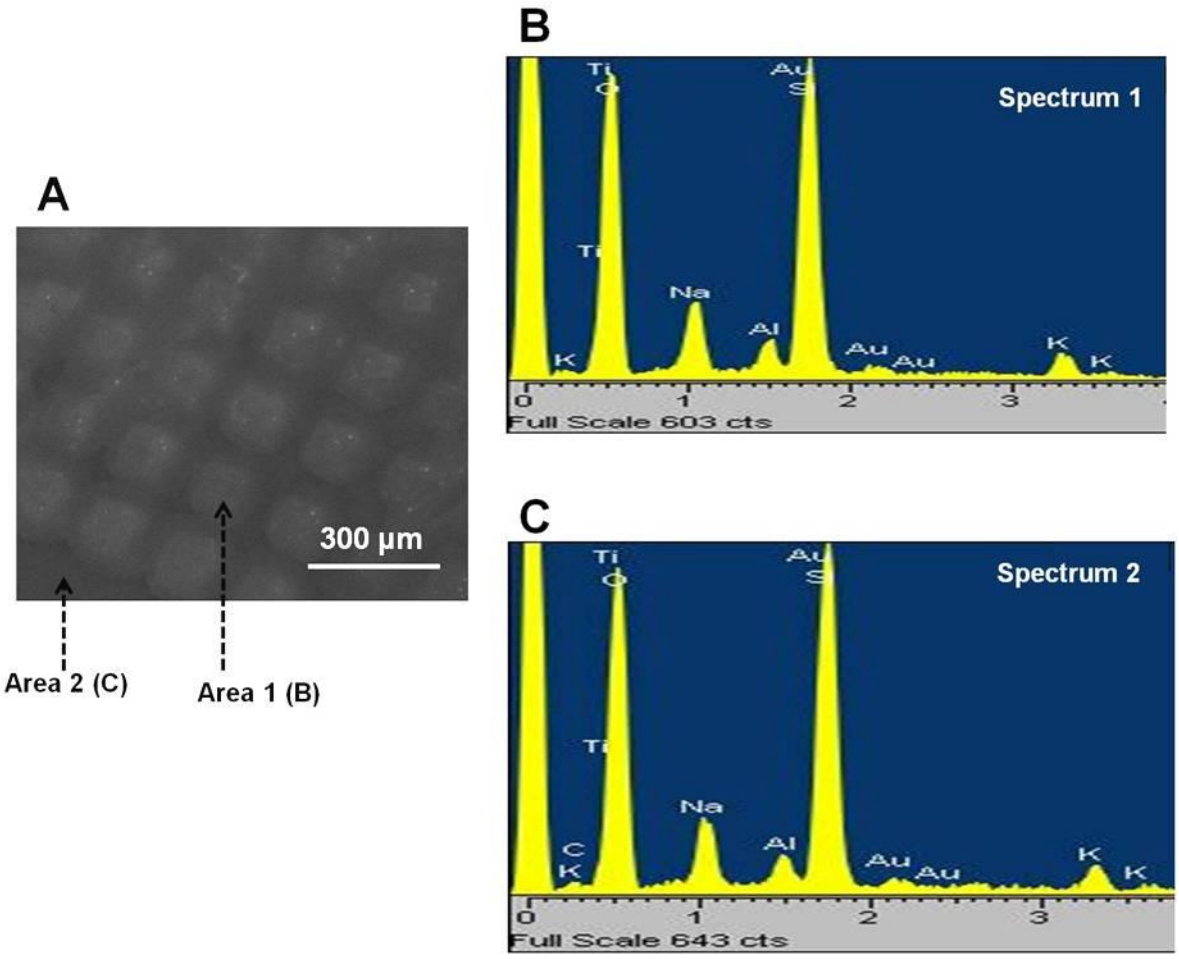

Figure 6.4. EDS analysis of the μCP patterns with EEP protein.

The SEM image represents the printed patterns on the glass substrates. (A) In this condition, 50 μg/ml EEP protein and 1M $CaCl_2$ solution were initially patterned onto the surface via μCP. Two areas were selected for EDS detection: area 1 (B) in the patterned regions and area 2 (C) outside of the patterns.

6.2.3 Crystallisation in a slow diffusion system

In the soaking crystallisation system with imprinted calcium-protein/polymer patterns, only PAA, the polymer with strong calcium-binding ability, successfully induced crystal formation. Calcite crystals composed of nano-blocks precipitated only on the PAA patterns during incubation. To eliminate the influence of the incubation process on crystal formation, a conventional slow diffusion system with $(NH_4)_2CO_3$ powder was used for crystal growth (Figure 2.4B in Chapter 2). Under this condition, the μCP solution was changed, with only proteins or polymer patterned on the substrate, excluding the $CaCl_2$ solution. In this set of experiments, 1% PAA was initially used to create the patterned substrates, via the same

microcontact printing (μCP) process as described above. The patterned substrates were placed upside down in 1M $CaCl_2$ solution to enact a slow diffusion system in a sealed desiccator with solid $(NH_4)_2CO_3$ powder.

Well patterned glass substrates were achieved after the microcontact printing process with appropriate pressure. After incubation for 4 hours at 25 °C, crystals precipitated on the patterned substrate. Substrates were then removed from the petri dish and cleaned for further analysis. Crystals are easily observed using an optical microscope since the average crystal size is approximately 50 μm. The SEM images show that crystals randomly deposit on the substrate in both patterned and non-patterned areas (Figure 6.5A). Crystal morphology is presented by high-magnification SEM images (Figure 6.5B&C). Two different types of crystals already formed on the substrates, the classic rhombohedral structures with smooth surface (Figure 6.5B) and multilayered structures (Figure 6.5C). This layered structure is similar to the multilayered structure formation already observed in the microfluidic system (Figure 5.32 in Chapter 5).

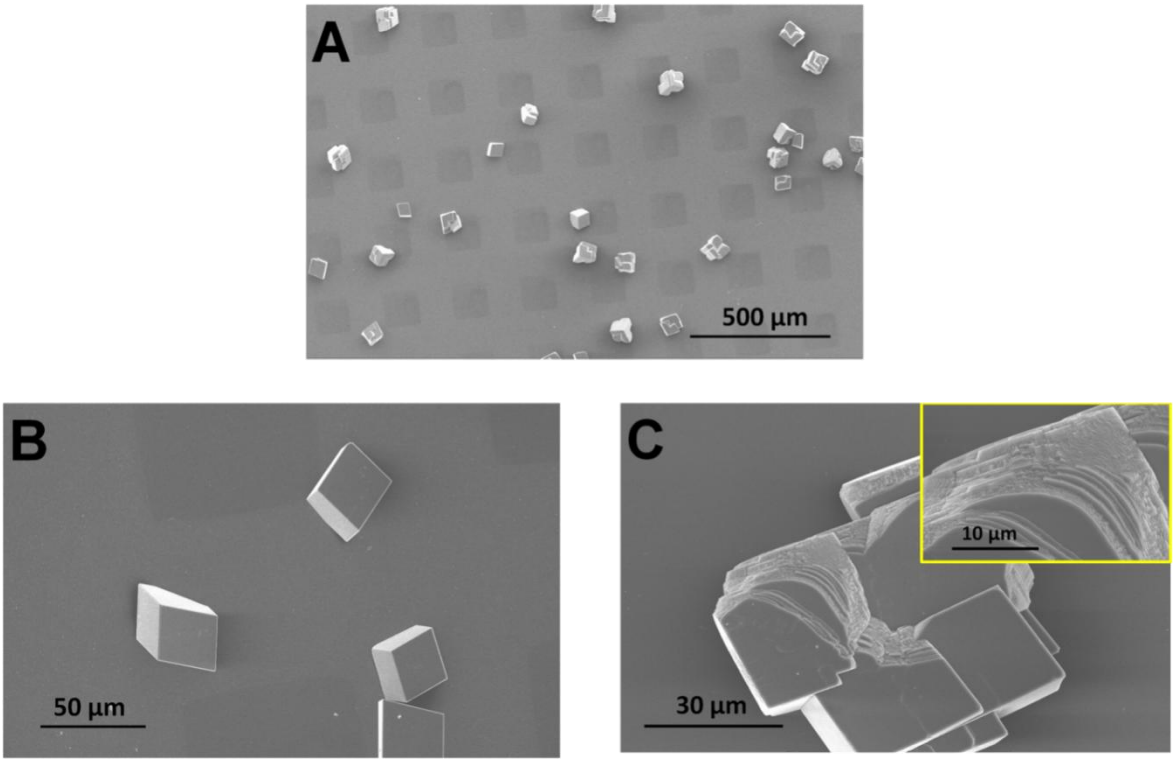

Figure 6.5. Representative SEM images of crystals formed on the patterned glass substrates in the slow diffusion system.

(A) Glass substrates were pre-patterned with 1% polyacrylic acid (PAA) only and used for crystal growth in a slow diffusion approach. $CaCO_3$ crystals in various morphologies precipitated on the patterned substrates randomly. High-magnification SEM images present the (B) classic rhombohedral calcite crystals and (C) layered structures formed on the same substrates. The insert greater-magnification SEM image presents the layered structures on crystal surface.

Micro-Raman spectroscopy was used to determine which polymorph was produced (Figure 6.6). Both the rhombohedral and multilayer structures are calcite, with characteristic Raman shifts at 139, 268, 710 and 1091 cm^{-1}. This experiment using PAA patterns for crystallisation in a slow diffusion system with ammonium carbonate shows that there is no control over crystal morphology.

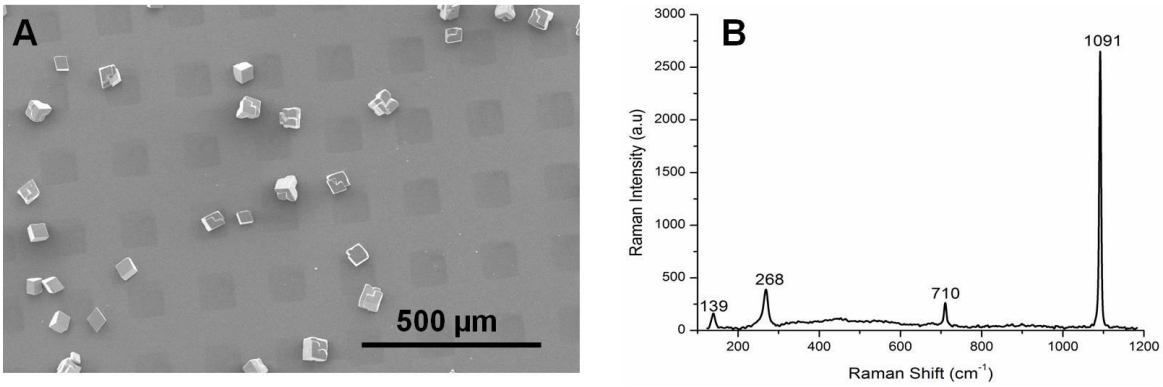

Figure 6.6. Polymorph characterisation of crystals formed on the patterned substrates.

(A) The SEM image shows the randomly distributed crystal on the substrate. (B) The characteristic Raman spectroscopy identifies all precipitated crystals as calcite, with characteristic Raman shift at 1091, 710, 268 and 139 cm^{-1}.

The PAA patterns were originally assumed to control the crystal nucleation by capturing the calcium ions from the initial stage of nucleation in aqueous conditions. However, the random deposition and different morphologies illustrate the non-specific control over crystal formation in this slow diffusion system with imprinted PAA patterns.

6.3 Discussion:

This chapter demonstrates the applications of μCP protein patterning for $CaCO_3$ crystallisation studies. Without any surface chemical modification, the PAA-$CaCl_2$ solution patterns using a direct μCP process can be used for calcium carbonate crystallisation.

6.3.1 Possible mechanism of organic templates over crystallisation

- *Crystallisation in the soaking system*

In the soaking system, crystals only precipitated onto the patterned regions on the substrate surface. This phenomenon is induced by the polymer template to mediate crystal formation. The crystallisation method in the presence of μCP organic patterns is analogous to the organic matrix moderating (OMM) crystallisation system, which has been described in previous work (Cölfen and Mann, 2003). Their research illustrated the mechanisms of three potential pathways to control the crystal distribution and orientation using an organic matrix (Figure 6.7). In their studies, the conventional pathway is organic matrix mediating the crystallisation from the capture of cations from the aqueous solution. This is followed by

clustering which controls crystal orientation (Figure 6.7A). In the soaking crystallisation experiments, the calcium is only provided from the μCP patterns. This procedure produced crystals with a nano-block structure which only nucleated in patterned regions. It shows that the process probably followed the pathway A in Figure 6.7. In addition, in the organic matrix templating system, the organic templates are assumed to be lowering energy barriers allowing calcium carbonate homogeneous precipitation (Dey et al., 2010).

When the organic additive is changed from PAA to BSA, calcium is in insufficient quantities attracted to the BSA on the patterned substrates after μCP. Thus, the printed BSA pattern, lacking calcium ions will not induce $CaCO_3$ crystals. This is consistent with the experimental design, with 50 μg/ml BSA as a negative control.

- *Crystallisation in the slow diffusion system*

During crystallisation experiments in the slow diffusion system, there is no specific crystallisation control. Crystals randomly deposited on the substrate surface, with two different morphologies. This phenomenon can be explained by either of two pathways in the organic matrix mediating (OMM) system (Figure 6.7B&C). The classic rhombohedral structures with smooth surfaces probably formed according to the pathway B in Figure 6.7. Ions aggregated to form amorphous calcium carbonate and then crystalline nuclei in aqueous condition. Crystals then bind to the patterns after transforming into calcite. The layered structures probably form via the crystallisation pathway C in Figure 6.7. Amorphous phases form on the pattern surface and then modified by the organic matrix to form the multilayered structures.

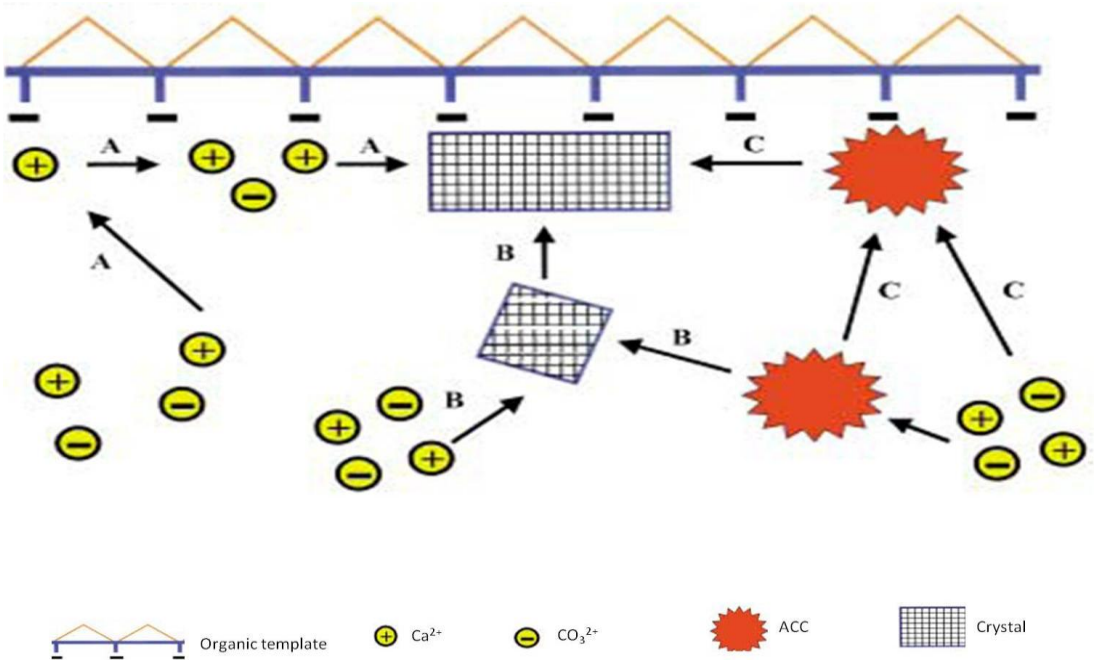

Figure 6.7. Schematic illustration of crystallisation pathway in the organic matrix mediating system.

In the presence of two-dimensional organic matrix template, there are several potential ways to control crystallisation. (A) The classic pathway is from the binding of aqueous cations to matrix. It is followed by the cluster formation and finally orientated crystals. (B) Matrix can bind the crystalline nuclei already formed in aqueous condition, either directly from ions or transformed via amorphous clusters. (C) An alternative pathway is the amorphous particle formation by ions binding to matrix, which leads the formation of orientated crystals (Cölfen and Mann, 2003).

6.3.2 Unsuccessful crystallisation using protein patterns

When the major expressed extrapallial (EEP) protein was printed on the substrate with calcium ions, no crystals formed on the glass substrate in the soaking crystallisation system. The EDS results indicated that there was no calcium present on the patterns. There are several possible explanations for the contrast between the predicted and experimental results. The most likely is the calcium-binding capacity of the EEP protein compared to PAA. As the EEP protein (50 μg/ml) added into 1 M $CaCl_2$ solution, there is little Ca^{2+} binding to the protein. After the μCP process, thin layers of protein are printed on the substrate surface, with an extremely low concentration of calcium ions. There is insufficient calcium ion concentration on the imprinted patterns to lead to crystal precipitation. Moreover, the high solubility of the protein may also prevent crystal deposition because the protein itself is removed.

Previous work has demonstrated control on crystal nucleation by the alkanethiols SAMs with a range of functionalities on a Si substrate surface, with highly orientated single crystal grown in a slow diffusion crystallisation system (Aizenberg et al., 1999). They used the slow diffusion system of carbon dioxide or ammonium carbonate into a 1M $CaCl_2$ solution to mediate the crystal formation (Aizenberg et al., 1999, Li and Estroff, 2007b, Kim et al., 2010). The same crystal incubation system of ammonium carbonate vapour diffusion has also been used with PAA patterns on glass substrates in this project, which yields non-specific control on crystal deposition in the slow diffusion system. Crystals randomly deposit on the substrate surface, with two different morphologies.

Taking an overview of the successful use of microcontact printing (μCP) substrates, surface modifications with functional residues are required (Aizenberg et al., 1999, Li and Estroff, 2007a). These studies have demonstrated the importance of substrate surface modification with covalent biomolecules immobilisation for successful applications.

However, a simple method was used to create the protein patterns, where all proteins and polymers were directly printed onto the substrate. According to the μCP procedure, the PDMS stamps and glass substrates were only treated using oxygen plasma treatment for the hydrophilic surface according to previous work of Bhattacharya *et al.,* (2005). The experimental results proved that calcium ions had not been immobilised on glass substrates by direct printing. One possibility to solve this non-specific crystallisation is to combine the microcontact printing (μCP) process with fuctionalisation of designed regions with proteins and blocking the remaining areas with other organic components, the ‘click’ chemistry, which has been used for cell biology and biochemistry studies (Kolb et al., 2001, Kolb and Sharpless, 2003).

Chapter 7

Conclusion and future work

7

7.1 Aim of the investigation

The aim of this project was to develop a novel technique to analyse the function of extrapallial protein in the biomineralisation process. Understanding the biological control exerted by these proteins in crystal formation will give details on protein-mineral interactions during crystallisation. The influence of extrapallial proteins on crystallisation has been established by studying the crystallisation process in detail in the presence of a range of biomineral proteins in the microfluidic device and also by microcontact printing (μCP) patterns. Microfluidics enhances the opportunity of controlling the speed of solution delivery, diffusion gradient and supersaturation ratio. By localising the microenvironment of protein and ion concentrations in the channels, the laminar flow microfluidic system has allowed us to study several aspects of the biomineralisation process simultaneously in a very short time span.

The following chapter summarises the main findings of this project and the investigations on the microfluidic applications on the biomineral protein screening for calcium carbonate *in vitro* crystallisation.

7.2 Advantages of using microfluidic system for biomineral screening

Understanding of biomineral protein function during *in vitro* crystallisation is fundamentally important for the investigation in the biomineralisation process. Many crystallisation systems have been provided to investigate the mechanism of additive control over crystal morphologies and polymorphs during formation (Kitano et al., 1962, Aizenberg et al., 1999, Zheng et al., 2003, De Yoreo and Dove, 2004, Pokroy et al., 2007, Politi et al., 2007, Gower, 2008, Dey et al., 2010, Hetherington et al., 2011, Li et al., 2011). In their crystallisation methods, a large range of experimental conditions are required, including variation in protein and ion concentrations. All these findings suggest several simultaneous conditions are

required for biomineral protein functional studies.

In this project, the pressure-driven laminar flow microfluidic system was used for crystallisation. In this approach, the mass transport is driven by lateral diffusion into adjacent streams after two solutions are delivered into the channel. As the diffusion coefficients determine the movement of protein and ions, their concentration profile on-chip can be constructed using commercial simulation software (i.e. Comsol). This approach has been used to investigate the influence of protein and ion concentration on crystal morphology. As described in Chapter 5, in the present of EEP protein in $CaCl_2$ solution only, the on-chip crystal morphology varies according to the protein and ion concentrations along the microfluidic channels. These concentration profiles have also provided an insight into polymorph selection during the on-chip formation. Take the example of EEP protein in $CaCl_2$ solution only again, calcite crystals start to precipitate in the channel after protein and ions diffused across the channel with Dy increasing. This phenomenon of polymorph selection occurs in almost all crystallisation experiments in the presence of biomineral proteins in laminar flow microfluidic system. This novel approach demonstrates that the stable localised mass concentrations along the channels control crystal morphology and polymorph.

Not only is crystal morphology and polymorph modified, but also the crystal distribution is strictly controlled in this laminar flow microfluidic system. The supersaturation ratio (S) is also an essential condition in calcium carbonate crystallisation. Computational modelling has generated the on-chip supersaturation ratio profile, which accurately predicted the crystal distributions along the channel. The modelling prediction has been confirmed by the real-time crystallisation experiments, with a single line of crystal forms at the beginning of channel, and well separated crystals across the channel after a long flow rate distance (Dy).

These advantages outlined above cannot be achieved using a conventional bulk system for crystallisation. In the bulk conditions, there is no significant difference between the results generated by the conditions of one specific biomineral protein mixed with different reaction reagents. Moreover, in the bulk system, there is no continuous supply of reagents during crystallisation. Thus the parameters of crystal precipitation are changing all the time, including the supersaturation ratio, organic additive concentration and ion concentrations. It is therefore difficult to detect the best conditions to generate the desired mineral formation such as porous structures.

In addition, the combination of on-chip crystallisation using microfluidic system and Raman spectroscopy real-time detection provides another opportunity to thoroughly investigate

crystallisation from the initial stage. The *in-situ* Raman confirmed the formation of stable lemon-shaped vaterite crystals and stable ovoid calcite structures induced by the extrapallial proteins.

7.3 Crystallisation controlled by extrapallial fluid proteins

As described by previous researchers, some of extrapallial proteins are defined as acidic proteins and considered to contribute significantly to the biomineral processes (Misogianes and Chasteen, 1979, Lowenstam and Weiner, 1989). Also previous work was published on the 28kDa main EP protein from *M. edulis* defining it as an acidic glycoprotein with calcium-binding capacities (Hattan et al., 2001, Yin et al., 2005). The extrapallial fluid proteins, screened in this project, include total wild-type extrapallial fluid (TWEP) protein, the major wild-type 28 kDa extrapallial (WEP) protein, the abundant expressed extrapallial (EEP) protein, C1q domain and the wild-type extrapallial complex (WCEP) proteins were screened.

Initially, the total wild-type extrapallial (TWEP) protein mixture was used to study its effect on crystallisation in the laminar flow microfluidic system. The protein mixture was added into both solutions and produced ovoid calcite crystals. This structure has been identified as a stable structure without any polymorph switch during formation by *in-situ* Raman detection.

In this study, a set of the major EP proteins have been systematically screened using microfluidics for crystallisation, including the glycosylated WEP protein, the non-glycosylated EEP protein and non-glycosylated C1q domain. The novel structure of lemon-shaped vaterite crystals were produced in the microfluidic channel when these proteins were introduced in the $CaCl_2$ solution only. The vaterite crystals are considered to be induced by the calcium-binding property of these proteins. This calcium-binding ability probably modifies the crystallisation from the initial stage in aqueous conditions, as forming the complex of EP-Ca^{2+}. The EP-Ca^{2+} complex is assumed to be the precursor to these novel structures. Although the potential pathways were discussed in previous chapters, the exact mechanism of control under the protein-mineral interactions is unclear. This complex probably mediates crystal formation by forming a template and thereafter to form the lemon-shaped structures. In this microfluidic screening assay, different lemon-shaped structures have been produced by the presence of different proteins.

However, protein function is not only determined by the protein amino acid sequence. The protein secondary or tertiary structures may be as important in determining protein function during the biomineralisation process. Therefore, the structural proteomic information of all

these EP proteins will enhance the illustration of protein functions during calcium carbonate crystallisation. The 28 kDa WEP protein has been confirmed as a glycoprotein with a considerably long N-terminal carbohydrate moiety. This carbohydrate domain may influence the crystal formation producing well defined hollow structures composed of nano-granules. The chemical composition of the carbohydrate and the spatial structure of the protein may provide ideas for the mechanism of the pathway as to how these hollow vaterite crystals form.

Meanwhile, the multilayer calcite structure formation is a common feature in the microfluidic system, when the main extrapallial proteins are added in Na_2CO_3 solution only. Similar structures have been generated by the positive control conditions with identified calcium-binding additives. The synthesis of this type of crystal is considered to be the process of adsorption of protein onto the crystal surface during growth. This shows an alternative pathway where protein can control crystallisation. Hence, two different pathways have been addressed for protein influence when present in different reagents.

As to the wild-type extrapallial complex (WCEP) proteins, its 'upside down' effect on biomineral crystallisation is really interesting and may provide a subtle key as to how bimineralic structures can be generated simultaneously.

7.4 Microcontact printing patterns for $CaCO_3$

Microcontact printing (µCP) has previously provided organic patterns with a number of wide applications, such as biological assays in cell culture, DNA analysis and tissue engineering (Chen et al., 1997, Mrksich et al., 1997, Offenhausser et al., 2007, Rozkiewicz et al., 2007b). In this study, polyacrylic acid (PAA) has been used as model substrate to create the imprinted patterns for calcium carbonate crystallisation. The PAA patterns totally controlled the crystal deposition and morphology when PAA and $CaCl_2$ are both printed on the patterns. However, when the same procedures were used with the EEP protein, there was no crystal precipitation on the substrate. This can be explained by the protein's calcium-binding capacity or the protein pattern stability.

As to further application of protein patterning for crystallisation, surface modification is probably needed. The immobilisation of the biomolecules can be achieved by several protocols, such as 'click' chemistry with functional carboxylated groups to immobilise proteins. Other improvements may also contribute to a more useful application of µCP patterns for crystallisation, i.e. the positive µCP with etching techniques and employing crosslink polymers between the surface and organic molecules (Perl et al., 2009).

7.5 Future work

Amorphous calcium carbonate (ACC) has been recognised as an important phase during crystallisation, aggregating to form different structures under the mediation of different additives (Aizenberg et al., 1996, Weiss et al., 2002, Politi et al., 2004, Ma et al., 2007, Cölfen, 2007, Pichon et al., 2008, Wang et al., 2009a, Njegic-Dzakula et al., 2010). The ACC phase has been investigated by many researchers using the slow crystallisation system. However, the design of the laminar flow process produces a well separated concentration profile for crystal growth, which, in turn, stimulates fast crystal formation without any ACC detection in the channel. In addition, we only focused on the on-chip crystallisation in the presence of different additives to analyse the biomineral protein functions. Crystal formation from the outlet collection solution in the different conditions has not been investigated.

Therefore, it would be interesting to fabricate a microfluidic system that could stabilise amorphous calcium carbonate formation. In previous work, methanol or ethanol has been used to quench the crystals formed during on-chip formation. Thus, organic solvent could be used in microfluidic channels to stabilise ACC during the on-chip formation. A simple design of microfluidic device could be used, with two additional inlets to deliver ethanol into the channels (Figure 7.1). This device design stimulates the slow lateral diffusion of two reaction reagent solutions ($CaCl_2$ and Na_2CO_3) in the initial stage of mixing. The target proteins or peptides are initially delivered into the central inlet with each reagent in each side for crystallisation. With the same microfluidic principles, all three streams are forming the laminar flow system with diffusion controlling mass transportation. After the flow runs in the channel, ethanol is delivered into the channel to ’freeze’ the mineral phase as a stable amorphous phase. These ACC structures can be collected from the outlet and used for further analysis including SEM or TEM. During solution delivery, crystals may precipitate in the microfluidic channel before ethanol injection. The crystallisation in this area is modified by the localised micro-conditions of protein and ion concentrations, which is similar to the crystallisation in our existing laminar flow microfluidic system.

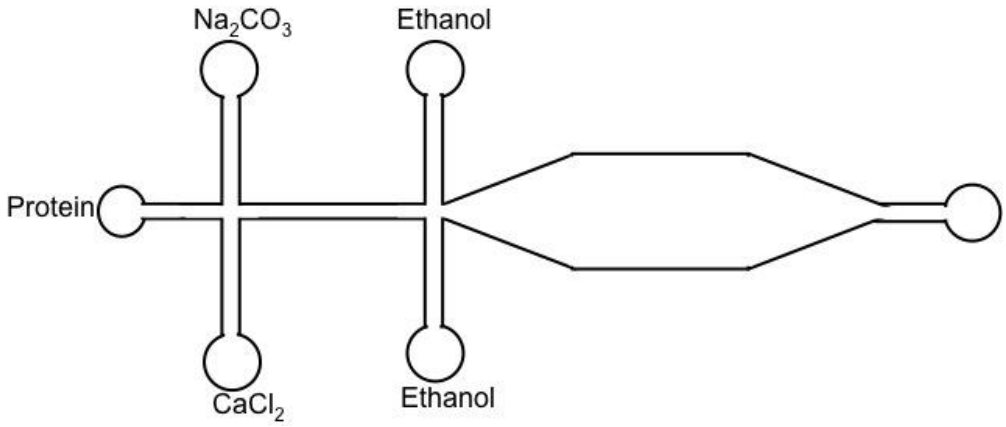

Figure 7.1. Illustration of T-junction microfluidic device for ACC formation.

Revised T-junction laminar flow microfluidic channel system can be used for calcium carbonate crystallisation for stable amorphous calcium carbonate formation. Laminar flow system stimulates the crystallisation control with diffused protein and ion concentrations in the long narrow reaction channel. After ethanol injected into system, amorphous calcium carbonate will be stabilised in the main reaction chamber and collected for analysis.

References:

ADDADI, L., JOESTER, D., NUDELMAN, F. & WEINER, S. 2006. Mollusk Shell Formation: A Source of New Concepts for Understanding Biomineralization Processes. *Chemistry – A European Journal,* 12**,** 980-987.

ADDADI, L., MORADIAN, J., SHAY, E., MAROUDAS, N. G. & WEINER, S. 1987. A chemical-model for the cooperation of sulfates and carboxylates in calcite crystal nucleation-relevance to biomineralization. *Proceedings of the National Academy of Sciences of the United States of America,* 84**,** 2732-2736.

ADDADI, L. & WEINER, S. 1992. Control and desing principles in biological mineralization. *Angewandte Chemie-International Edition in English,* 31**,** 153-169.

AIZENBERG, J. 2004. Crystallization in Patterns: A Bio-Inspired Approach. *Advanced Materials,* 16**,** 1295-1302.

AIZENBERG, J., BLACK, A. J. & WHITESIDES, G. M. 1999. Control of crystal nucleation by patterned self-assembled monolayers. *Nature,* 398**,** 495-498.

AIZENBERG, J., LAMBERT, G., ADDADI, L. & WEINER, S. 1996. Stabilization of amorphous calcium carbonate by specialized macromolecules in biological and synthetic precipitates. *Advanced Materials,* 8**,** 222.

AIZENBERG, J., TKACHENKO, A., WEINER, S., ADDADI, L. & HENDLER, G. 2001. Calcitic microlenses as part of the photoreceptor system in brittlestars. *Nature,* 412**,** 819-822.

ALTOMARE, L., RIEHLE, M., GADEGAARD, N., TANZI, M. & FARE, S. 2010. Microcontact printing of fibronectin on a biodegradable polymeric surface for skeletal muscle cell orientation. *International Journal of Artificial Organs,* 33**,** 535-543.

ANDERSSON, H. & BERG, A. V. D. 2004. Microfabrication and microfluidics for tissue engineering: state of the art and future opportunities. *Lab on a Chip,* 4**,** 98-103.

ARCHIBALD, D. D., QADRI, S. B. & GABER, B. P. 1996. Modified calcite deposition due to

ultrathin organic films on silicon substrates. *Langmuir,* 12**,** 538-546.

ARIAS, J. L. & FERN NDEZ, M. S. 2003. Biomimetic processes through the study of mineralized shells. *Materials Characterization,* 50**,** 189-195.

ARIAS, J. L. & FERNÁNDEZ, M. A. S. 2008. Polysaccharides and Proteoglycans in Calcium Carbonate-based Biomineralization. *Chemical Reviews,* 108**,** 4475-4482.

BAIN, C. D. & WHITESIDES, G. M. 1988. Molecular-Level Control over Surface Order in Self-Assembled Monolayer Films of Thiols on Gold. *Science,* 240**,** 62-63.

BEEBE, D. J., MENSING, G. A. & WALKER, G. M. 2002. Physics and applications of microfluidics in biology. *Annual Review of Biomedical Engineering,* 4**,** 261-286.

BEHRENS, P. & BAEUERLEIN, E. (eds.) 2007. *Handbook of Biomineralization - Biomimetic and Bioinspired Chemistry,* Weinheim: WILEY-VCH Verlag GmbH & Co.

BELCHER, A. M., WU, X. H., CHRISTENSEN, R. J., HANSMA, P. K., STUCKY, G. D. & MORSE, D. E. 1996. Control of crystal phase switching and orientation by soluble mollusc-shell proteins. *Nature,* 381**,** 56-58.

BERNARD, A., RENAULT, J. P., MICHEL, B., BOSSHARD, H. R. & DELAMARCHE, E. 2000. Microcontact Printing of Proteins. *Advanced Materials,* 12**,** 1067-1070.

BESARAB, A., DEGUZMAN, A. & SWANSON, J. W. 1981. Effect of albumin and free calcium concentrations on calcium-binding invitro. *Journal of Clinical Pathology,* 34**,** 1361-1367.

BHATIA, S. N., BALIS, U. J., YARMUSH, M. L. & TONER, M. 1999. Effect of cell-cell interactions in preservation of cellular phenotype: cocultivation of hepatocytes and nonparenchymal cells. *The FASEB Journal,* 13**,** 1883-1900.

BHATTACHARYA, S., DATTA, A., BERG, J. M. & GANGOPADHYAY, S. 2005. Studies on surface wettability of poly(dimethyl) siloxane (PDMS) and glass under oxygen-plasma treatment and correlation with bond strength. *Journal of Microelectromechanical Systems,* 14**,** 590-597.

BOLZE, J., PENG, B., DINGENOUTS, N., PANINE, P., NARAYANAN, T. & BALLAUFF, M. 2002. Formation and Growth of Amorphous Colloidal $CaCO_3$ Precursor Particles as Detected by Time-Resolved SAXS. *Langmuir,* 18**,** 8364-8369.

C LFEN, H. 2007. Bio-inspired Mineralization Using Hydrophilic Polymers. *In:* NAKA, K. (ed.) *Biomineralization II.* Springer Berlin / Heidelberg.

C LFEN, H. & MANN, S. 2003. Higher-order organization by mesoscale self-assembly and transformation of hybrid nanostructures. *Angewandte Chemie-International Edition,* 42**,** 2350-2365.

CARTWRIGHT, J. H. E. & CHECA, A. G. 2007. The dynamics of nacre self-assembly. *Journal of the Royal Society Interface,* 4**,** 491-504.

CARVALHO, A., GEISSLER, M., SCHMID, H., MICHEL, B. & DELAMARCHE, E. 2002. Self-Assembled Monolayers of Eicosanethiol on Palladium and Their Use in Microcontact Printing. *Langmuir,* 18**,** 2406-2412.

CHAKRABORTY, D. & CHAKRABORTY, S. 2010. Microfluidic Transport and Micro-scale Flow Physics: An Overview. *Microfluidics and Microfabrication***,** 1-85.

CHEN, C. S., MRKSICH, M., HUANG, S., WHITESIDES, G. M. & INGBER, D. E. 1997. Geometric Control of Cell Life and Death. *Science,* 276**,** 1425-1428.

CHENG, X., VARONA, P. L., OLSZTA, M. J. & GOWER, L. B. 2007. Biomimetic synthesis of calcite films by a polymer-induced liquid-precursor (PILP) process: 1. Influence and incorporation of magnesium. *Journal of Crystal Growth,* 307**,** 395-404.

CLARK, M. S., THORNE, M. A. S., VIEIRA, F. A., CARDOSO, J. C. R., POWER, D. M. & PECK, L. S. 2010. Insights into shell deposition in the Antarctic bivalve Laternula elliptica: gene discovery in the mantle transcriptome using 454 pyrosequencing. *Bmc Genomics,* 11.

COSTA, N. & MAQUIS, P. M. 1998. Biomimetic processing of calcium phosphate coating. *Medical Engineering & Physics,* 20**,** 602-606.

CRAFT, J. A., GILBERT, J. A., TEMPERTON, B., DEMPSEY, K. E., ASHELFORD, K.,

TIWARI, B., HUTCHINSON, T. H. & CHIPMAN, J. K. 2010. Pyrosequencing of Mytilus galloprovincialis cDNAs: Tissue-Specific Expression Patterns. *PLoS ONE,* 5**,** e8875.

CRENSHAW, M. A. 1972. Inorganic composition of molluscan extrapallial fluid. *Biological Bulletin,* 143**,** 506-512.

CUSACK, M., FRASER, A. C. & STACHEL, T. 2003. Magnesium and phosphorus distribution in the avian eggshell. *Comparative Biochemistry and Physiology Part B: Biochemistry and Molecular Biology,* 134**,** 63-69.

CUSACK, M. & FREER, A. 2008. Biomineralization: Elemental and Organic Influence in Carbonate Systems. *Chemical Reviews,* 108**,** 4433-4454.

CUSACK, M., PARKINSON, D., FREER, A., P REZ-HUERTA, A., FALLICK, A. E. & CURRY, G. B. 2008. Oxygen isotope composition in Modiolus modiolus aragonite in the context of biological and crystallographic control. *Mineralogical Magazine,* 72**,** 569-577.

CUSACK, M., PEREZ-HUERTA, A., DALBECK, P., CHUNG, P. & LEE, M. R. 2009. Comparison of calcite crystallographica texture in the shells of the Rhynchonelliform brachipod, Terebratulina retusa and the Bivalve Mollusc, Mytilus edulis. *Applications of Texture Analysis,* 201**,** 587-593.

DABBS, D. M. & AKSAY, I. A. 2000. Self-assembled ceramics produced by complex-fluid templation. *Annual Review of Physical Chemistry,* 51**,** 601-622.

DALBECK, P. & CUSACK, M. 2006. Crystallography (Electron Backscatter Diffraction) and Chemistry (Electron Probe Microanalysis) of the Avian Eggshell. *Crystal Growth & Design,* 6**,** 2558-2562.

DANDEU, A., HUMBERT, B., CARTERET, C., MUHR, H., PLASARI, E. & BOSSOUTROT, J. M. 2006. Raman spectroscopy - A powerful tool for the quantitative determination of the composition of polymorph mixtures: Application to $CaCO_3$ polymorph mixtures. *Chemical Engineering & Technology,* 29**,** 221-225.

DAVEY, R. J., CARDEW, P. T., MCEWAN, D. & SADLER, D. E. 1986. Rate controlling processes in solvent-mediated phase transformations. *Journal of Crystal Growth,* 79**,**

648-653.

DE LEEUW, N. H. 2002. Molecular Dynamics Simulations of the Growth Inhibiting Effect of Fe^{2+}, Mg^{2+}, Cd^{2+}, and Sr^{2+} on Calcite Crystal Growth. *The Journal of Physical Chemistry B,* 106**,** 5241-5249.

DE PAULA, S. M. & SILVEIRA, M. 2009. Studies on molluscan shells: Contributions from microscopic and analytical methods. *Micron,* 40**,** 669-690.

DE VILLIERS J. P. R. 1971. Crystal structures of aragonite, strontianite and witherite. *American Mineralogist,* 56.

DE YOREO, J. J. & DOVE, P. M. 2004. Shaping crystals with biorriolecules. *Science,* 306**,** 1301-1302.

DEY, A., DE WITH, G. & SOMMERDIJK, N. A. J. M. 2010. In situ techniques in biomimetic mineralization studies of calcium carbonate. *Chemical Society Reviews,* 39**,** 397-409.

DOVE, P. M., DE YOREO, J. J. & WEINER, S. 2003. *Biomineralization--Review in Mineralogy & Geochemistry,* Washington, DC, American Mineralogical Society.

EHRLICH, H., MALDONADO, M., SPINDLER, K.-D., ECKERT, C., HANKE, T., BORN, R., GOEBEL, C., SIMON, P., HEINEMANN, S. & WORCH, H. 2007. First evidence of chitin as a component of the skeletal fibers of marine sponges. Part I. Verongidae (demospongia: Porifera). *Journal of Experimental Zoology Part B: Molecular and Developmental Evolution,* 308B**,** 347-356.

EL-ALI, J., SORGER, P. K. & JENSEN, K. F. 2006. Cells on chips. *Nature,* 442**,** 403-411.

ENGLAND, J., CUSACK, M., DALBECK, P. & PEREZ-HUERTA, A. 2007. Comparison of the crystallographic structure of semi nacre and nacre by electron backscatter diffraction. *Crystal Growth & Design,* 7**,** 307-310.

FAATZ, M., GROHN, F. & WEGNER, G. 2004. Amorphous calcium carbonate: Synthesis and potential intermediate in biomineralization. *Advanced Materials,* 16**,** 996-1000.

FALINI, G., ALBECK, S., WEINER, S. & ADDADI, L. 1996. Control of aragonite or calcite

polymorphism by mollusk shell macromolecules. *Science,* 271**,** 67-69.

FALINI, G., FERMANI, S., TOSI, G. & DINELLI, E. 2009. Calcium Carbonate Morphology and Structure in the Presence of Seawater Ions and Humic Acids. *Crystal Growth & Design,* 9**,** 2065-2072.

FENG, Q. L., FANG, Z., YAN, Z. G., XING, R., XIE, L. P. & ZHANG, R. Q. 2009. The structure-function relationship of MSI7, a matrix protein from pearl oyster Pinctada fucata. *Acta Biochimica Et Biophysica Sinica,* 41**,** 955-962.

FENG, Q. L., LI, H. B., PU, G., ZHANG, D. M., CUI, F. Z., LI, H. D. & KIM, T. N. 2000. Crystallographic alignment of calcite prisms in the oblique prismatic layer of Mytilus edulis shell. *Journal of Materials Science,* 35**,** 3337-3340.

FINNEMORE, A. S., SCHERER, M. R. J., LANGFORD, R., MAHAJAN, S., LUDWIGS, S., MELDRUM, F. C. & STEINER, U. 2009. Nanostructured Calcite Single Crystals with Gyroid Morphologies. *Advanced Materials,* 21**,** 3928-3932.

FRANKEL, R. B. & BAZYLINSKI, D. A. 2003. Biologically Induced Mineralization by Bacteria. *Reviews in Mineralogy and Geochemistry,* 54**,** 95-114.

FREER, A., GREENWOOD, D., CHUNG, P., PANNELL, C. L. & CUSACK, M. 2009. Aragonite Prism−Nacre Interface in Freshwater Mussels Anodonta anatina (Linnaeus, 1758) and Anodonta cygnea (L. 1758). *Crystal Growth & Design,* 10**,** 344-347.

FRITZ, M., BELCHER, A. M., RADMACHER, M., WALTERS, D. A., HANSMA, P. K., STUCKY, G. D., MORSE, D. E. & MANN, S. 1994. Flat pearls from biofabrication of organized composites on inorganic substrates. *Nature,* 371**,** 49-51.

GAO, Y.-X., YU, S.-H., CONG, H., JIANG, J., XU, A.-W., DONG, W. F. & C LFEN, H. 2006. Block-Copolymer-Controlled Growth of $CaCO_3$ Microrings. *The Journal of Physical Chemistry B,* 110**,** 6432-6436.

GAULDIE, R. W. 1996. Biological factors controlling the carbon isotope record in fish otoliths: Principles and evidence. *Comparative Biochemistry and Physiology Part B: Biochemistry and Molecular Biology,* 115**,** 201-208.

GEBAUER, D., C LFEN, H., VERCH, A. & ANTONIETTI, M. 2009. The multiple roles of additives in $CaCO_3$ crystallization: A quantitative case study. *Advanced Materials,* 21**,** 435-439.

GEBAUER, D., VOLKEL, A. & COLFEN, H. 2008. Stable Prenucleation Calcium Carbonate Clusters. *Science,* 322**,** 1819-1822.

GOTLIV, B.-A., KESSLER, N., SUMEREL, J. L., MORSE, D. E., TUROSS, N., ADDADI, L. & WEINER, S. 2005. Asprich: A novel aspartic acid-rich protein family from the prismatic shell matrix of the bivalve Atrina rigida. *Chembiochem,* 6**,** 304-314.

GOTLIV, B. A., ADDADI, L. & WEINER, S. 2003. Mollusk shell acidic proteins: In search of individual functions. *Chembiochem,* 4**,** 522-529.

GOWER, L. A. & TIRRELL, D. A. 1998. Calcium carbonate films and helices grown in solutions of poly(aspartate). *Journal of Crystal Growth,* 191**,** 153-160.

GOWER, L. B. 2008. Biomimetic Model Systems for Investigating the Amorphous Precursor Pathway and Its Role in Biomineralization. *Chemical Reviews,* 108**,** 4551-4627.

GOWER, L. B. & ODOM, D. J. 2000. Deposition of calcium carbonate films by a polymer-induced liquid-precursor (PILP) process. *Journal of Crystal Growth,* 210**,** 719-734.

GUIOT, ENESCU M., ARRIO B., JOHANNIN G., ROGER G., TOSTI S., TFIBEL F., M ROLA F., BRUN A., P., G. & P., F.-A. M. 2000. Molecular Dynamics of Biological Probes by Fluorescence Correlation Microscopy with Two-Photon Excitation. *Journal of Fluorescence,* 10**,** 413-419.

HAEBERLE, S. & ZENGERLE, R. 2007. Microfluidic platforms for lab-on-a-chip applications. *Lab on a Chip,* 7**,** 1094-1110.

HARRISON, D. J., MANZ, A., FAN, Z., LUEDI, H. & WIDMER, H. M. 1992. Capillary electrophoresis and sample injection systems integrated on a planar glass chip. *Analytical Chemistry,* 64**,** 1926-1932.

HATTAN, S. J., LAUE, T. M. & CHASTEEN, N. D. 2001. Purification and characterization of a novel calcium-binding protein from the extrapallial fluid of the mollusc, Mytilus edulis.

Journal of Biological Chemistry, 276**,** 4461-4468.

HETHERINGTON, N. B. J., KULAK, A. N., KIM, Y.-Y., NOEL, E. H., SNOSWELL, D., BUTLER, M. & MELDRUM, F. C. 2011. Porous single crystals of calcite from colloidal crystal templates: ACC is not required for nanoscale templating. *Advanced Functional Materials,* 21**,** 948-954.

HODGKINSON, G. N., TRESCO, P. A. & HLADY, V. 2007. The differential influence of colocalized and segregated dual protein signals on neurite outgrowth on surfaces. *Biomaterials,* 28**,** 2590-2602.

HODGSON, L., CHAN, E. W. L., HAHN, K. M. & YOUSAF, M. N. 2007. Combining surface chemistry with a FRET-based biosensor to study the dynamics of RhoA GTPase activation in cells on patterned substrates. *Journal of the American Chemical Society,* 129**,** 9264-9265.

HOU, W. T. & FENG, Q. L. 2006. Morphologies and growth model of biomimetic fabricated calcite crystals using amino acids and insoluble matrix membranes of Mytilus edulis. *Crystal Growth & Design,* 6**,** 1086-1090.

HYND, M. R., FRAMPTON, J. P., DOWELL-MESFIN, N., TURNER, J. N. & SHAIN, W. 2007. Directed cell growth on protein-functionalized hydrogel surfaces. *Journal of Neuroscience Methods,* 162**,** 255-263.

ISMAGILOV, R. F., ROSMARIN, D., KENIS, P. J. A., CHIU, D. T., ZHANG, W., STONE, H. A. & WHITESIDES, G. M. 2001. Pressure-Driven Laminar Flow in Tangential Microchannels: an Elastomeric Microfluidic Switch. *Analytical Chemistry,* 73**,** 4682-4687.

JOUBERT, C., PIQUEMAL, D., MARIE, B., MANCHON, L., PIERRAT, F., ZANELLA-CLEON, I., COCHENNEC-LAUREAU, N., GUEGUEN, Y. & MONTAGNANI, C. 2010. Transcriptome and proteome analysis of Pinctada margaritifera calcifying mantle and shell: focus on biomineralization. *Bmc Genomics,* 11.

KANG, L., CHUNG, B. G., LANGER, R. & KHADEMHOSSEINI, A. 2008. Microfluidics for drug discovery and development: From target selection to product lifecycle management. *Drug Discovery Today,* 13**,** 1-13.

KIM, Y.-Y., RIBEIRO, L., MAILLOT, F., WARD, O., EICHHORN, S. J. & MELDRUM, F. C. 2010. Bio-Inspired Synthesis and Mechanical Properties of Calcite–Polymer Particle Composites. *Advanced Materials,* 22**,** 2082-2086.

KIMURA, H., YAMAMOTO, T., SAKAI, H., SAKAI, Y. & FUJII, T. 2008. An integrated microfluidic system for long-term perfusion culture and on-line monitoring of intestinal tissue models. *Lab on a Chip,* 8**,** 741-746.

KITANO, Y. 1962. The Behavior of Various Inorganic Ions in the Separation of Calcium Carbonate from a Bicarbonate Solution. *Bulletin of the Chemical Society of Japan,* 35**,** 1973-1980.

KITANO, Y., PARK, K. & HOOD, D. W. 1962. Pure Aragonite Synthesis. *J. Geophys. Res.,* 67**,** 4873-4874.

KOLB, H. C., FINN, M. G. & SHARPLESS, K. B. 2001. Click chemistry: Diverse chemical function from a few good reactions. *Angewandte Chemie-International Edition,* 40**,** 2004.

KOLB, H. C. & SHARPLESS, K. B. 2003. The growing impact of click chemistry on drug discovery. *Drug Discovery Today,* 8**,** 1128-1137.

KONG, Y., JING, G., YAN, Z., LI, C., GONG, N., ZHU, F., LI, D., ZHANG, Y., ZHENG, G., WANG, H., XIE, L. & ZHANG, R. 2009. Cloning and Characterization of Prisilkin-39, a Novel Matrix Protein Serving a Dual Role in the Prismatic Layer Formation from the Oyster Pinctada fucata. *Journal of Biological Chemistry,* 284**,** 10841-10854.

KONHAUSER, K. O. 1998. Diversity of bacterial iron mineralization. *Earth-Science Reviews,* 43**,** 91-121.

KUCZENSKI, B., LEDUC, P. R. & MESSNER, W. C. 2007. Pressure-driven spatiotemporal control of the laminar flow interface in a microfluidic network. *Lab on a Chip,* 7**,** 647-649.

KUMAR, A. & WHITESIDES, G. M. 1993. Features of gold having micrometer to centimeter dimensions can be formed through a combination of stamping with an elastomeric stamp and an alkanethiol ``ink'' followed by chemical etching. *Applied Physics Letters,*

63**,** 2002-2004.

KUO, C. K. & MA, P. X. 2001. Ionically crosslinked alginate hydrogels as scaffolds for tissue engineering: Part 1. Structure, gelation rate and mechanical properties. *Biomaterials,* 22**,** 511-521.

KUTHER, J., SESHADRI, R., KNOLL, W. & TREMEL, W. 1998. Templated growth of calcite, vaterite and aragonite crystals onself-assembled monolayers of substituted alkylthiols on gold. *Journal of Materials Chemistry,* 8**,** 641-650.

L V QUE, I., CUSACK, M., DAVIS, S. A. & MANN, S. 2004. Promotion of Fluorapatite Crystallization by Soluble-Matrix Proteins from Lingula Anatina Shells. *Angewandte Chemie International Edition,* 43**,** 885-888.

LANGE, S. A., BENES, V., KERN, D. P., HORBER, J. K. H. & BERNARD, A. 2004. Microcontact printing of DNA molecules. *Analytical Chemistry,* 76**,** 1641-1647.

LANTING, B. & BARFETT, J. 2006. Encapsulated calcium carbonate suspensions: a drug delivery vehicle sensitive to ultrasound disruption. *Mcgill J Med,* 9**,** 108-10.

LAU, B. T. C., BAITZ, C. A., DONG, X. P. & HANSEN, C. L. 2007. A complete microfluidic screening platform for rational protein crystallization. *Journal of the American Chemical Society,* 129**,** 454-455.

LAVAN, D. A., MCGUIRE, T. & LANGER, R. 2003. Small-scale systems for in vivo drug delivery. *Nat Biotech,* 21**,** 1184-1191.

LEE, I., MORALES, R., ALBITER, M. A. & ZAERA, F. 2008. Synthesis of heterogeneous catalysts with well shaped platinum particles to control reaction selectivity. *Proceedings of the National Academy of Sciences***,** 15241-15246.

LEVI-KALISMAN, Y., FALINI, G., ADDADI, L. & WEINER, S. 2001. Structure of the Nacreous Organic Matrix of a Bivalve Mollusk Shell Examined in the Hydrated State Using Cryo-TEM. *Journal of Structural Biology,* 135**,** 8-17.

LI, H. & ESTROFF, L. A. 2007a. Hydrogels Coupled with Self-Assembled Monolayers: An in Vitro Matrix To Study Calcite Biomineralization. *Journal of the American Chemical*

Society, 129**,** 5480-5483.

LI, H. & ESTROFF, L. A. 2007b. Porous calcite single crystals grown from a hydrogel medium. *CrystEngComm,* 9**,** 1153-1155.

LI, H., FUJIKI, Y., SADA, K. & ESTROFF, L. A. 2011. Gel incorporation inside of organic single crystals grown in agarose hydrogels. *CrystEngComm***,** 1060-1062.

LIDE, D. R. 2006. *Handbook of Chemistry and Physics*, GRC press.

LINK, A. J. & TIRRELL, D. A. 2003. Cell Surface Labeling of Escherichia coli via Copper(I)-Catalyzed [3+2] Cycloaddition. *Journal of the American Chemical Society,* 125**,** 11164-11165.

LITMAN, D. J., LEE, R. H., JEONG, H. J., TOM, H. K., STISO, S. N., SIZTO, N. C. & ULLMAN, E. F. 1983. AN INTERNALLY REFERENCED TEST STRIP IMMUNOASSAY FOR MORPHINE. *Clinical Chemistry,* 29**,** 1598-1603.

LOO, Y. L., WILLETT, R. L., BALDWIN, K. W. & ROGERS, J. A. 2002. Additive, nanoscale patterning of metal films with a stamp and a surface chemistry mediated transfer process: Applications in plastic electronics. *Applied Physics Letters,* 81**,** 562-564.

LOOTENS, D., CAPEL, F., DURAND, D., NICOLAI, T., BOULENGUER, P. & LANGENDORFF, V. 2003. Influence of pH, Ca concentration, temperature and amidation on the gelation of low methoxyl pectin. *Food Hydrocolloids,* 17**,** 237-244.

LOSTE, E., DIAZ-MARTI, E., ZARBAKHSH, A. & MELDRUM, F. C. 2003a. Study of calcium carbonate precipitation under a series of fatty acid Langmuir monolayers using brewster angle microscopy. *Langmuir,* 19**,** 2830-2837.

LOSTE, E., WILSON, R. M., SESHADRI, R. & MELDRUM, F. C. 2003b. The role of magnesium in stabilising amorphous calcium carbonate and controlling calcite morphologies. *Journal of Crystal Growth,* 254**,** 206-218.

LOVE, J. C., ESTROFF, L. A., KRIEBEL, J. K., NUZZO, R. G. & WHITESIDES, G. M. 2005. Self-Assembled Monolayers of Thiolates on Metals as a Form of Nanotechnology. *Chemical Reviews,* 105**,** 1103-1170.

LOWENSTAM, H. 1981. Minerals formed by organisms. *Science,* 211**,** 1126-1131.

LOWENSTAM, H. & WEINER, S. 1989. *On Biomineralization,* New York, Oxford University Press.

MA, Z. J., HUANG, J., SUN, J., WANG, G. N., LI, C. Z., XIE, L. P. & ZHANG, R. Q. 2007. A novel extrapallial fluid protein controls the morphology of nacre lamellae in the pearl oyster, Pinctada fucata. *Journal of Biological Chemistry,* 282**,** 23253-23263.

MACDONALD, J., FREER, A. & CUSACK, M. 2010. Alignment of Crystallographic c-Axis throughout the Four Distinct Microstructural Layers of the Oyster Crassostrea gigas. *Crystal Growth & Design,* 10**,** 1243-1246.

MAGUREGUI, M., KNUUTINEN, U., CASTRO, K. & MADARIAGA, J. M. 2009. Raman spectroscopy as a tool to diagnose the impact and conservation state of Pompeian second and fourth style wall paintings exposed to diverse environments (House of Marcus Lucretius). *Journal of Raman Spectroscopy,* 41**,** 1110-1119.

MANN, K., WEISS, I. M., ANDR , S., GABIUS, H.-J. & FRITZ, M. 2000. The amino-acid sequence of the abalone (Haliotis laevigata) nacre protein perlucin. *European Journal of Biochemistry,* 267**,** 5257-5264.

MANN, S. 2001. *Biomineralization - Principles and Concepts in Bioinorganic Materials Chemistry,* Oxford, Oxford University Press.

MANN, S., ARCHIBALD, D. D., DIDYMUS, J. M., DOUGLAS, T., HEYWOOD, B. R., MELDRUM, F. C. & REEVES, N. J. 1993. Crystallization at Inorganic-organic Interfaces: Biominerals and Biomimetic Synthesis. *Science,* 261**,** 1286-1292.

MANN, S., HEYWOOD, B. R., RAJAM, S. & BIRCHALL, J. D. 1988. Controlled crystallization of CaCO3 under stearic acid monolayers. *Nature,* 334**,** 692-695.

MANZ, A., GRABER, N. & WIDMER, H. M. 1990. Miniaturized total chemical analysis systems: A novel concept for chemical sensing. *Sensors and Actuators B: Chemical,* 1**,** 244-248.

MARIN, F., AMONS, R., GUICHARD, N., STIGTER, M., HECKER, A., LUQUET, G.,

LAYROLLE, P., ALCARAZ, G., RIONDET, C. & WESTBROEK, P. 2005. Caspartin and Calprismin, Two Proteins of the Shell Calcitic Prisms of the Mediterranean Fan Mussel Pinna nobilis. *Journal of Biological Chemistry,* 280**,** 33895-33908.

MARIN, F. & LUQUET, G. 2004. Molluscan shell proteins. *Comptes Rendus Palevol,* 3**,** 469-492.

MARIN, F. & LUQUET, G. 2005. Molluscan biomineralization: The proteinaceous shell constituents of Pinna nobilis L. *Materials Science & Engineering C-Biomimetic and Supramolecular Systems,* 25**,** 105-111.

MARIN, F., LUQUET, G., MARIE, B. & MEDAKOVIC, D. 2007. Molluscan Shell Proteins: Primary Structure, Origin, and Evolution. *Current Topics in Developmental Biology.* Academic Press.

MARIN, F., PEREIRA, L. & WESTBROEK, P. 2001. Large-Scale Fractionation of Molluscan Shell Matrix. *Protein Expression and Purification,* 23**,** 175-179.

MARK, D., HAEBERLE, S., ROTH, G. A. N., VON STETTEN, F. & ZENGERLE, R. 2010. Microfluidic lab-on-a-chip platforms: requirements, characteristics and applications. *Chemical Society Reviews,* 39**,** 1153-1182.

MARSH, M. E., CHANG, D. K. & KING, G. C. 1992. Isolation and characterization of a novel acidic polysaccharide containing tartrate and glyoxylate residues from the mineralized scales of a unicellular coccolithophorid alga Pleurochrysis carterae. *Journal of Biological Chemistry,* 267**,** 20507-20512.

MATSUSHIRO, A., MIYASHITA, T., MIYAMOTO, H., MORIMOTO, K., TONOMURA, B. I., TANAKA, A. & SATO, K. 2003. Presence of Protein Complex is Prerequisite for Aragonite Crystallization in the Nacreous Layer. *Marine Biotechnology,* 5**,** 37-44.

MEECHAI, N., JAMIESON, A. M. & BLACKWELL, J. 1999. Translational Diffusion Coefficients of Bovine Serum Albumin in Aqueous Solution at High Ionic Strength. *Journal of Colloid and Interface Science,* 218**,** 167-175.

MELDRUM, F. C. & COLFEN, H. 2008. Controlling Mineral Morphologies and Structures in Biological and Synthetic Systems. *Chemical Reviews,* 108**,** 4332-4432.

MELDRUM, F. C. & LUDWIGS, S. 2007. Template-Directed Control of Crystal Morphologies. *Macromolecular Bioscience,* 7**,** 152-162.

MELDRUM, F. C. & SESHADRI, R. 2000. Porous gold structures through templating by echinoid skeletal plates. *Chemical Communications***,** 29-30.

MENG, D. D. & KIM, C. J. 2008. Micropumping of liquid by directional growth and selective venting of gas bubbles. *Lab on a Chip,* 8**,** 958-968.

MISOGIANES, M. J. & CHASTEEN, N. D. 1979. A chemical and spectral characterization of the extrapallial fluid of Mytilus edulis. *Analytical Biochemistry,* 100**,** 324-334.

MIYAMOTO, H., MIYASHITA, T., OKUSHIMA, M., NAKANO, S., MORITA, T. & MATSUSHIRO, A. 1996. A carbonic anhydrase from the nacreous layer in oyster pearls. *Proceedings of the National Academy of Sciences,* 93**,** 9657-9660.

MOURA, G., VILARINHO, L. & MACHADO, J. 2000a. The action of Cd, Cu, Cr, Zn, and Pb on fluid composition of Anodonta cygnea (L.): organic components. *Comparative Biochemistry and Physiology Part B: Biochemistry and Molecular Biology,* 127**,** 105-112.

MOURA, G., VILARINHO, L., SANTOS, A. C. & MACHADO, J. 2000b. Organic compounds in the extrapalial fluid and haemolymph of Anodonta cygnea (L.) with emphasis on the seasonal biomineralization process. *Comparative Biochemistry and Physiology Part B: Biochemistry and Molecular Biology,* 125**,** 293-306.

MRKSICH, M., DIKE, L. E., TIEN, J., INGBER, D. E. & WHITESIDES, G. M. 1997. Using Microcontact Printing to Pattern the Attachment of Mammalian Cells to Self-Assembled Monolayers of Alkanethiolates on Transparent Films of Gold and Silver. *Experimental Cell Research,* 235**,** 305-313.

MRKSICH, M. & WHITESIDES, G. M. 1995. Patterning self-assembled monolayers using microcontact printing: A new technology for biosensors? *Trends in Biotechnology,* 13**,** 228-235.

MURAYAMA, E., TAKAGI, Y., OHIRA, T., DAVIS, J. G., GREENE, M. I. & NAGASAWA, H. 2002. Fish otolith contains a unique structural protein, otolin-1. *European Journal of*

Biochemistry, 269**,** 688-696.

NAKA, K., KEUM, D.-K., TANAKA, Y. & CHUJO, Y. 2000. Control of crystal polymorphs by a 'latent inductor': crystallization of calcium carbonate in conjunction with radical polymerization of sodium acrylate in aqueous solution. *Chemical Communications***,** 1537-1538.

NASSIF, N., GEHRKE, N., PINNA, N., SHIRSHOVA, N., TAUER, K., ANTONIETTI, M. & C LFEN, H. 2005. Synthesis of Stable Aragonite Superstructures by a Biomimetic Crystallization Pathway. *Angewandte Chemie International Edition,* 44**,** 6004-6009.

NEBEL, H., NEUMANN, M., MAYER, C. & EPPLE, M. 2008. On the Structure of Amorphous Calcium Carbonate: A Detailed Study by Solid-State NMR Spectroscopy. *Inorganic Chemistry,* 47**,** 7874-7879.

NEWBURY, D. E. 2005. Misidentification of Major Constituents by Automatic Qualitative Energy Dispersive X-ray Microanalysis: A Problem that Threatens the Credibility of the Analytical Community. *Microscopy and Microanalysis,* 11**,** 545-561.

NJEGIC-DZAKULA, B., FALINI, G., BRECEVIC, L., SKOKO, Z. & KRALJ, D. 2010. Effects of initial supersaturation on spontaneous precipitation of calcium carbonate in the presence of charged poly-l-amino acids. *Journal of Colloid and Interface Science,* 343**,** 553-563.

NUDELMAN, F., CHEN, H. H., GOLDBERG, H. A., WEINER, S. & ADDADI, L. 2007. Spiers Memorial Lecture Lessons from biomineralization: comparing the growth strategies of mollusc shell prismatic and nacreous layers in Atrina rigida. *Faraday Discussions,* 136**,** 9-25.

NUDELMAN, F., GOTLIV, B. A., ADDADI, L. & WEINER, S. 2006. Mollusk shell formation: Mapping the distribution of organic matrix components underlying a single aragonitic tablet in nacre. *Journal of Structural Biology,* 153**,** 176-187.

NUDELMAN, F., PIETERSE, K., GEORGE, A., BOMANS, P. H. H., FRIEDRICH, H., BRYLKA, L. J., HILBERS, P. A. J., DE WITH, G. & SOMMERDIJK, N. A. J. M. 2010. The role of collagen in bone apatite formation in the presence of hydroxyapatite nucleation inhibitors. *Nat Mater,* 9**,** 1004-1009.

NYS, Y., GAUTRON, J., GARCIA-RUIZ, J. M. & HINCKE, M. T. 2004. Avian eggshell mineralization: biochemical and functional characterization of matrix proteins. *Comptes Rendus Palevol,* 3**,** 549-562.

OFFENHAUSSER, A., BACKER-MEFFERT, S., DECKER, T., HELPENSTEIN, R., GASTEIER, P., GROLL, J. A. R., MALLER, M., RESKA, A., SCHA?FER, S., SCHULTE, P. & VOGT-EISELE, A. 2007. Microcontact printing of proteins for neuronal cell guidance. *Soft Matter,* 3**,** 290-298.

ORME, C. A., NOY, A., WIERZBICKI, A., MCBRIDE, M. T., GRANTHAM, M., TENG, H. H., DOVE, P. M. & DEYOREO, J. J. 2001. Formation of chiral morphologies through selective binding of amino acids to calcite surface steps. *Nature,* 411**,** 775-779.

P REZ-HUERTA, A., CUSACK, M., MCDONALD, S., MARONE, F., STAMPANONI, M. & MACKAY, S. 2009. Brachiopod punctae: A complexity in shell biomineralisation. *Journal of Structural Biology,* 167**,** 62-67.

PARK, R. J. & MELDRUM, F. C. 2004. Shape-constraint as a route to calcite single crystals with complex morphologies. *Journal of Materials Chemistry,* 14**,** 2291-2296.

PEREIRA-MOURI S, L., ALMEIDA, M.-J., RIBEIRO, C., PEDUZZI, J., BARTH LEMY, M., MILET, C. & LOPEZ, E. 2002. Soluble silk-like organic matrix in the nacreous layer of the bivalve Pinctada maxima. *European Journal of Biochemistry,* 269**,** 4994-5003.

PERIC, J., VUCAK, M., KRSTULOVIC, R., BRECEVIC, L. & KRALJ, D. 1996. Phase transformation of calcium carbonate polymorphs. *Thermochimica Acta,* 277**,** 175-186.

PERL, A., REINHOUDT, D. N. & HUSKENS, J. 2009. Microcontact Printing: Limitations and Achievements. *Advanced Materials,* 21**,** 2257-2268.

PICHON, B. P., BOMANS, P. H. H., FREDERIK, P. M. & SOMMERDIJK, N. 2008. A quasi-time-resolved CryoTEM study of the nucleation of $CaCO_3$ under langmuir monolayers. *Journal of the American Chemical Society,* 130**,** 4034-4040.

PIETRZAK, J. E., BATES, J. M. & SCOTT, R. M. 1976. Constituents of unionid extrapallial fluid: pH and metal-ion composition. *Hydrobiologia,* 50**,** 89-93.

PINNA, N., WEISS, K., URBAN, J. & PILENI, M. P. 2001. Triangular CdS nanocrystals: Structural and optical studies. *Advanced Materials,* 13**,** 261-264.

POKROY, B., KAPON, M., MARIN, F., ADIR, N. & ZOLOTOYABKO, E. 2007. Protein-induced, previously unidentified twin form of calcite. *Proceedings of the National Academy of Sciences of the United States of America,* 104**,** 7337-7341.

POLITI, Y., ARAD, T., KLEIN, E., WEINER, S. & ADDADI, L. 2004. Sea Urchin Spine Calcite Forms via a Transient Amorphous Calcium Carbonate Phase. *Science,* 306**,** 1161-1164.

POLITI, Y., BATCHELOR, D. R., ZASLANSKY, P., CHMELKA, B. F., WEAVER, J. C., SAGI, I., WEINER, S. & ADDADI, L. 2010. Role of Magnesium Ion in the Stabilization of Biogenic Amorphous Calcium Carbonate: A Structure−Function Investigation. *Chemistry of Materials,* 22**,** 161-166.

POLITI, Y., MAHAMID, J., GOLDBERG, H., WEINER, S. & ADDADI, L. 2007. Asprich mollusk shell protein: in vitro experiments aimed at elucidating function in $CaCO_3$ crystallization. *Crystengcomm,* 9**,** 1171-1177.

POLITI, Y., METZLER, R. A., ABRECHT, M., GILBERT, B., WILT, F. H., SAGI, I., ADDADI, L., WEINER, S. & GILBERT, P. U. P. A. 2008. Transformation mechanism of amorphous calcium carbonate into calcite in the sea urchin larval spicule. *Proceedings of the National Academy of Sciences,* 105**,** 17362-17366.

POUGET, E. M., BOMANS, P. H. H., GOOS, J. A. C. M., FREDERIK, P. M., DE WITH, G. & SOMMERDIJK, N. A. J. M. 2009. The Initial Stages of Template-Controlled $CaCO_3$ Formation Revealed by Cryo-TEM. *Science,* 323**,** 1455-1458.

PRICE, C. P. & KRICKA, L. J. 2007. Improving Healthcare Accessibility through Point-of-Care Technologies. *Clin Chem,* 53**,** 1665-1675.

ROZKIEWICZ, D. I., BRUGMAN, W., KERKHOVEN, R. M., RAVOO, B. J. & REINHOUDT, D. N. 2007a. Dendrimer-mediated transfer printing of DNA and RNA microarrays. *Journal of the American Chemical Society,* 129**,** 11593-11599.

ROZKIEWICZ, D. I., GIERLICH, J., BURLEY, G. A., GUTSMIEDL, K., CARELL, T., RAVOO,

B. J. & REINHOUDT, D. N. 2007b. Transfer printing of DNA by "Click" chemistry. *Chembiochem,* 8**,** 1997-2002.

RUIZ, A., BUZANSKA, L., GILLILAND, D., RAUSCHER, H., SIRGHI, L., SOBANSKI, T., ZYCHOWICZ, M., CERIOTTI, L., BRETAGNOL, F., COECKE, S., COLPO, P. & ROSSI, F. 2008. Micro-stamped surfaces for the patterned growth of neural stem cells. *Biomaterials,* 29**,** 4766-4774.

RUIZ, S. A. & CHEN, C. S. 2007. Microcontact printing: A tool to pattern. *Soft Matter,* 3**,** 168-177.

SAAVEDRA, C. & BACH RE, E. 2006. Bivalve genomics. *Aquaculture,* 256**,** 1-14.

SAMATA, T., HAYASHI, N., KONO, M., HASEGAWA, K., HORITA, C. & AKERA, S. 1999. A new matrix protein family related to the nacreous layer formation of Pinctada fucata. *FEBS Letters,* 462**,** 225-229.

SARASHINA, I. & ENDO, K. 1998. Primary structure of a soluble matrix protein of scallop shell; implications for calcium carbonate biomineralization. *American Mineralogist,* 83**,** 1510-1515.

SARASHINA, I. & ENDO, K. 2006. Skeletal matrix proteins of invertebrate animals: Comparative analysis of their amino acid sequences. *Paleontological Research,* 10**,** 311-336.

SAUTER, C., DHOUIB, K. & LORBER, B. 2007. From macrofluidics to microfluidics for the crystallization of biological macromolecules. *Crystal Growth & Design,* 7**,** 2247-2250.

SCHEFFEL, A., GRUSKA, M., FAIVRE, D., LINAROUDIS, A., PLITZKO, J. M. & SCH LER, D. 2006. An acidic protein aligns magnetosomes along a filamentous structure in magnetotactic bacteria. *Nature,* 440**,** 110-114.

SHEN, X., BELCHER, A. M., HANSMA, P. K., STUCKY, G. D. & MORSE, D. E. 1997. Molecular Cloning and Characterization of Lustrin A, a Matrix Protein from Shell and Pearl Nacre of Haliotis rufescens. *Journal of Biological Chemistry,* 272**,** 32472-32481.

SHOJI, S., ESASHI, M. & MATSUO, T. 1988. Prototype miniature blood gas analyser

fabricated on a silicon wafer. *Sensors and Actuators,* 14**,** 101-107.

SIA, S. K. & WHITESIDES, G. M. 2003. Microfluidic devices fabricated in poly(dimethylsiloxane) for biological studies. *Electrophoresis,* 24**,** 3563-3576.

SONG, H., CHEN, D. L. & ISMAGILOV, R. F. 2006. Reactions in Droplets in Microfluidic Channels. *Angewandte Chemie International Edition,* 45**,** 7336-7356.

STEPHENS, C. J., LADDEN, S. F., MELDRUM, F. C. & CHRISTENSON, H. K. 2010. Amorphous Calcium Carbonate is Stabilized in Confinement. *Advanced Functional Materials,* 20**,** 2108-2115.

SUBBURAMAN, K., PERNODET, N., KWAK, S. Y., DIMASI, E., GE, S., ZAITSEV, V., BA, X., YANG, N. L. & RAFAILOVICH, M. 2006. Templated biomineralization on self-assembled protein fibers. *Proceedings of the National Academy of Sciences of the United States of America,* 103**,** 14672-14677.

SUZUKI, M., SARUWATARI, K., KOGURE, T., YAMAMOTO, Y., NISHIMURA, T., KATO, T. & NAGASAWA, H. 2009. An Acidic Matrix Protein, Pif, Is a Key Macromolecule for Nacre Formation. *Science,* 325**,** 1388-1390.

TAKAYAMA, S., OSTUNI, E., LEDUC, P., NARUSE, K., INGBER, D. E. & WHITESIDES, G. M. 2001. Laminar flows: Subcellular positioning of small molecules. *Nature,* 411**,** 1016-1016.

TAKEUCHI, T., SARASHINA, I., IIJIMA, M. & ENDO, K. 2008. In vitro regulation of $CaCO_3$ crystal polymorphism by the highly acidic molluscan shell protein Aspein. *FEBS Letters,* 582**,** 591-596.

TEH, S.-Y., LIN, R., HUNG, L.-H. & LEE, A. P. 2008. Droplet microfluidics. *Lab on a Chip,* 8**,** 198-220.

TENG, H. H., DOVE, P. M. & DEYOREO, J. J. 1999. Reversed calcite morphologies induced by microscopic growth kinetics: insight into biomineralization. *Geochimica et Cosmochimica Acta,* 63**,** 2507-2512.

TERRY, S. C., JERMAN, J. H. & ANGELL, J. B. 1979. A gas chromatographic air analyzer

fabricated on a silicon wafer. *Electron Devices, IEEE Transactions on,* 26**,** 1880-1886.

THEIL, E. C., MATZAPETAKIS, M. & LIU, X. F. 2006. Ferritins: iron/oxygen biominerals in protein nanocages. *Journal of Biological Inorganic Chemistry,* 11**,** 803-810.

TRUCHET, M., DELHAYE, M. & BENY, C. 1995. Identification of calcium carbonates (calcite, aragonite and vaterite) by Raman-Castaing microprobe; Application to biomineralisations. *Analusis,* 23**,** 516-518.

TSUKAMOTO, D., SARASHINA, I. & ENDO, K. 2004. Structure and expression of an unusually acidic matrix protein of pearl oyster shells. *Biochemical and Biophysical Research Communications,* 320**,** 1175-1180.

VAN LINTEL, H. T. G., VAN DE POL, F. C. M. & BOUWSTRA, S. 1988. A piezoelectric micropump based on micromachining of silicon. *Sensors and Actuators,* 15**,** 153-167.

VERDOES, D., KASHCHIEV, D. & VAN ROSMALEN, G. M. 1992. Determination of nucleation and growth rates from induction times in seeded and unseeded precipitation of calcium carbonate. *Journal of Crystal Growth,* 118**,** 401-413.

VOLKMER, D., FRICKE, M., AGENA, C. & MATTAY, J. 2004. Interfacial electrostatics guiding the crystallization of CaCO3 underneath monolayers of calixarenes and resorcarenes. *Journal of Materials Chemistry,* 14**,** 2249-2259.

WANG, D., WALLACE, A. F., DE YOREO, J. J. & DOVE, P. M. 2009a. Carboxylated molecules regulate magnesium content of amorphous calcium carbonates during calcification. *Proceedings of the National Academy of Sciences,* 106**,** 21511-21516.

WANG, X., KONG, R., PAN, X., XU, H., XIA, D., SHAN, H. & LU, J. R. 2009b. Role of Ovalbumin in the Stabilization of Metastable Vaterite in Calcium Carbonate Biomineralization. *The Journal of Physical Chemistry B,* 113**,** 8975-8982.

WASYLENKI, L. E., DOVE, P. M., WILSON, D. S. & DE YOREO, J. J. 2005. Nanoscale effects of strontium on calcite growth: An in situ AFM study in the absence of vital effects. *Geochimica et Cosmochimica Acta,* 69**,** 3017-3027.

WEIGL, B. H., BARDELL, R. L. & CABRERA, C. R. 2003. Lab-on-a-chip for drug

development. *Advanced Drug Delivery Reviews,* 55**,** 349-377.

WEIGL, B. H. & YAGER, P. 1999. Microfluidic Diffusion-Based Separation and Detection. *Science,* 283**,** 346-347.

WEINER, S. 2008. Biomineralization: A structural perspective. *Journal of Structural Biology,* 163**,** 229-234.

WEINER, S. & DOVE, P. M. 2003. An overview of biomineralization processes and the problem of the vital effect. *Biomineralization,* 54**,** 1-29.

WEINER, S. & HOOD, L. 1975. Soluble-protein of organic matrix of mollusk shells-potential template for shell formation. *Science,* 190**,** 987-988.

WEINER, S. & TRAUB, W. 1984. Macromolecules in mollusk shells and their functions in biomineralization. *Philosophical Transactions of the Royal Society of London Series B-Biological Sciences,* 304**,** 425-434.

WEINER, S., TRAUB, W. & WAGNER, H. D. 1999. Lamellar Bone: Structure-Function Relations. *Journal of Structural Biology,* 126**,** 241-255.

WEINER, S. & WAGNER, H. D. 1998. The material bone: Structure mechanical function relations. *Annual Review of Materials Science,* 28**,** 271-298.

WEISS, I. M., TUROSS, N., ADDADI, L. & WEINER, S. 2002. Mollusc larval shell formation: amorphous calcium carbonate is a precursor phase for aragonite. *Journal of Experimental Zoology,* 293**,** 478-491.

WHEELER, A. P., RUSENKO, K. W., GEORGE, J. W. & SIKES, C. S. 1987. Evaluation of calcium binding by molluscan shell organic matrix and its relevance to biomineralization. *Comparative Biochemistry and Physiology Part B: Comparative Biochemistry,* 87**,** 953-960.

WHITESIDES, G. M., OSTUNI, E., TAKAYAMA, S., JIANG, X. & INGBER, D. E. 2001. Softlithography in biology and biochemistry *Annual Review of Biomedical Engineering,* 3**,** 335-373.

WILBUR, J. L., KUMAR, A., BIEBUYCK, H. A., KIM, E. & WHITESIDES, G. M. 1996. Microcontact printing of self-assembled monolayers: Applications in microfabrication. *Nanotechnology,* 7**,** 452-457.

WILBUR, J. L., KUMAR, A., KIM, E. & WHITESIDES, G. M. 1994. Microfabrication by microcontact printing of self-assembled monolayers. *Advanced Materials,* 6**,** 600-604.

WILBUR, K. M. & BERNHARDT, A. M. 1984. Effects of amino acids, magnesium, and molluscan extrapallial fluid on crystallization of calcium carbonate- In vitro experiments. *Biological Bulletin,* 166**,** 251-259.

WILBUR, K. M. & SALEUDDIN, A. S. M. 1983. Shell formation. *The Mollusca. Volume 4. Physiology. Part 1.***,** 253-287.

XIA, Y., KIM, E. & WHITESIDES, G. M. 1996a. Microcontact Printing of Alkanethiols on Silver and Its Application in Microfabrication. *Journal of The Electrochemical Society,* 143**,** 1070-1079.

XIA, Y. N., KIM, E., MRKSICH, M. & WHITESIDES, G. M. 1996b. Microcontact printing of alkanethiols on copper and its application in microfabrication. *Chemistry of Materials,* 8**,** 601-603.

XIA, Y. N. & WHITESIDES, G. M. 1998. Soft lithography. *Annual Review of Materials Science,* 28**,** 153-184.

XU, A. W., MA, Y. R. & COLFEN, H. 2007. Biomimetic mineralization. *Journal of Materials Chemistry,* 17**,** 415-449.

XU, H., LING, X. Y., VAN BENNEKOM, J., DUAN, X., LUDDEN, M. J. W., REINHOUDT, D. N., WESSLING, M., LAMMERTINK, R. G. H. & HUSKENS, J. 2009. Microcontact Printing of Dendrimers, Proteins, and Nanoparticles by Porous Stamps. *Journal of the American Chemical Society,* 131**,** 797-803.

YAN, Z., FANG, Z., MA, Z., DENG, J., LI, S., XIE, L. & ZHANG, R. 2007. Biomineralization: Functions of calmodulin-like protein in the shell formation of pearl oyster. *Biochimica et Biophysica Acta (BBA) - General Subjects,* 1770**,** 1338-1344.

YAO, Y., DONG, W. Y., ZHU, S. M., YU, X. H. & YAN, D. Y. 2009. Novel Morphology of Calcium Carbonate Controlled by Poly(L-lysine). *Langmuir,* 25**,** 13238-13243.

YIN, H. B., JI, B. Z., DOBSON, P. S., MOSBAHI, K., GLIDLE, A., GADEGAARD, N., FREER, A., COOPER, J. M. & CUSACK, M. 2009. Screening of Biomineralization Using Microfluidics. *Analytical Chemistry,* 81**,** 473-478.

YIN, Y., HUANG, J., PAINE, M. L., REINHOLD, V. N. & CHASTEEN, N. D. 2005. Structural characterization of the major extrapallial fluid protein of the mollusc Mytilus edulis: Implications for functions. *Biochemistry,* 44**,** 10720-10731.

YUE, W., PARK, R. J., KULAK, A. N. & MELDRUM, F. C. 2006. Macroporous inorganic solids from a biomineral template. *Journal of Crystal Growth,* 294**,** 69-77.

ZAREMBA, C. M., BELCHER, A. M., FRITZ, M., LI, Y., MANN, S., HANSMA, P. K., MORSE, D. E., SPECK, J. S. & STUCKY, G. D. 1996. Critical Transitions in the Biofabrication of Abalone Shells and Flat Pearls. *Chemistry of Materials,* 8**,** 679-690.

ZENGERLE, R., ULRICH, J., KLUGE, S., RICHTER, M. & RICHTER, A. 1995. A bidirectional silicon micropump. *Sensors and Actuators A: Physical,* 50**,** 81-86.

ZHANG, C. & ZHANG, R. 2006. Matrix Proteins in the Outer Shells of Molluscs. *Marine Biotechnology,* 8**,** 572-586.

ZHANG, Y., XIE, L., MENG, Q., JIANG, T., PU, R., CHEN, L. & ZHANG, R. 2003. A novel matrix protein participating in the nacre framework formation of pearl oyster, Pinctada fucata. *Comparative Biochemistry and Physiology Part B: Biochemistry and Molecular Biology,* 135**,** 565-573.

ZHENG, B., ROACH, L. S. & ISMAGILOV, R. F. 2003. Screening of Protein Crystallization Conditions on a Microfluidic Chip Using Nanoliter-Size Droplets. *Journal of the American Chemical Society,* 125**,** 11170-11171.

Appendix

Appendix 1:

Materials	Supplier
Calcium chloride	Sigma Aldrich
Sodium carbonate	Sigma Aldrich
Magnesium chloride	Sigma Aldrich
Ammonium carbonate	Sigma Aldrich
MilliQ™ water	Millipore
Calcium binding protein	Sigma Aldrich
Bovine serum albumin	Sigma Aldrich
Methonal	BDH
Acetone	BDH
Isopropernal	BDH
Microcon concentrators	Millport
0.2 µm nylon filter	Whatman
Tris buffer	Sigma Aldrich
MOPS buffer	Sigma Aldrich
Polydimethylsiloxane	SYLGARD® Ltd
Polydimethylsiloxane curing agent	SYLGARD® Ltd
Polyacrylic acid	Sigma Aldrich
SU-8 series photoresists	MicroChem Inc
Silicon dioxide wafer	Si-mat Ltd
Fluorescein	Sigma Aldrich
FITC-BSA	Sigma Aldrich

Appendix 2:

Modelling results on Y-type laminar flow microfluidic channel

Since the Y-type microfluidic channel and the T-junction channel are both laminar flow microfluidic system with similar flow speeds: 5.1 mm/s for T-junction channel and 5.2 mm/s for the Y-type channel, similar computational modelling results have been generated on either on-chip mass concentration profile or supersaturation ratio profile.

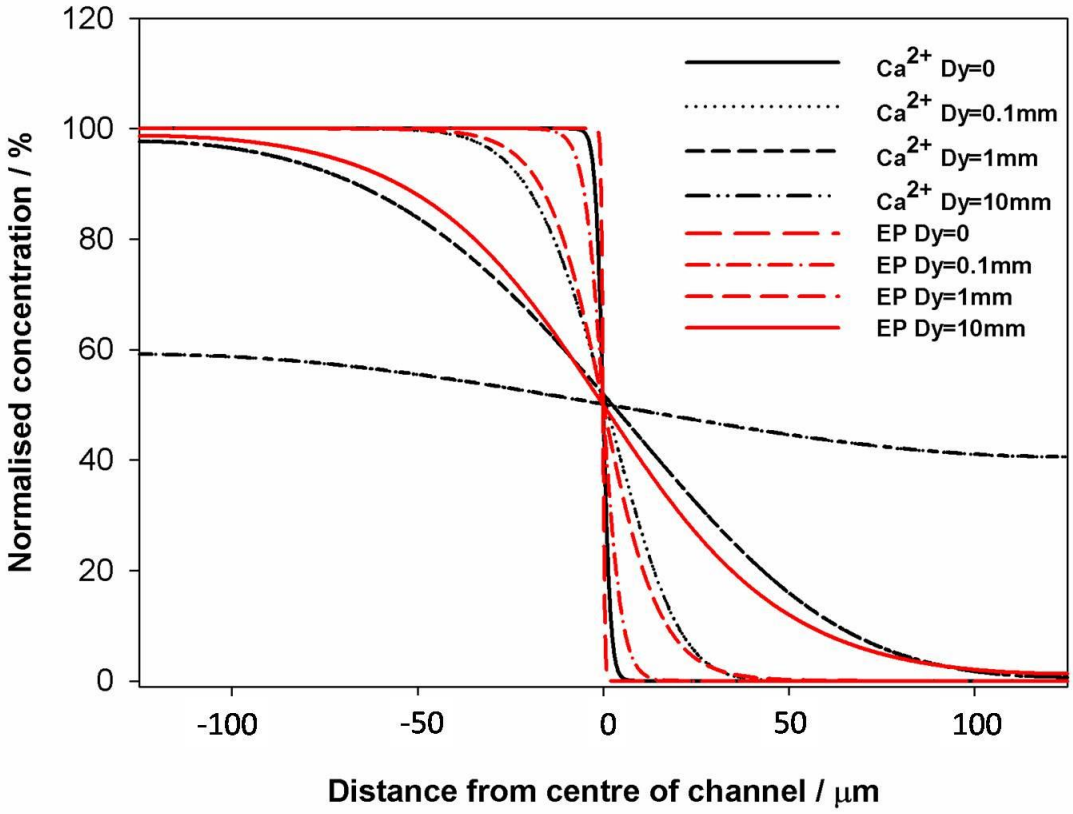

Figure S1. On-chip concentration profile in Y-type microfluidic channel

In the Y-type channel, ions and proteins have similar diffusion profile along flow rate distance (Dy) in the channel. Protein has small diffusion rate, with concentration gradient remaining after running long distance (Dy>10 mm). Ionic gradient has been eliminated after well diffused across the channel.

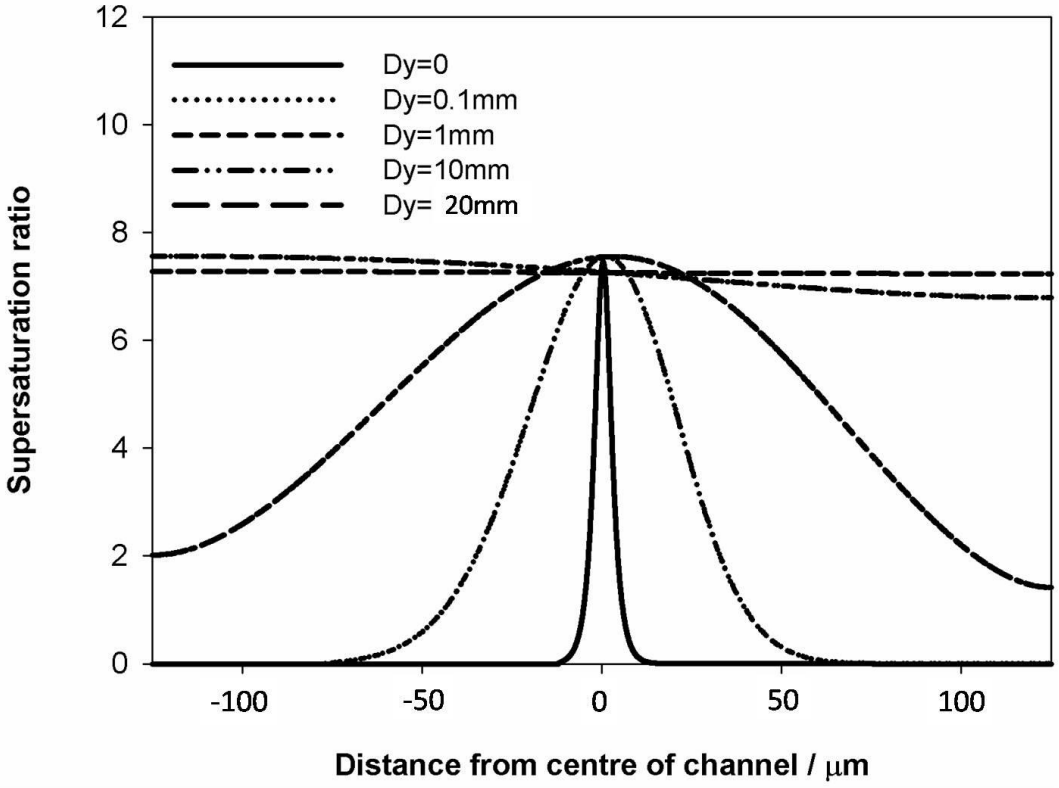

Figure S2. Supersaturation ratio (S) in Y-type microfluidic channel.

In the Y-type microfluidic channel, supersaturation ratio (S) profile varies along the flow rate distance (Dy). This profile has a sharp peak in the centre in the beginning of the channel, and boarders across the channel with Dy increasing.

Papers arising for this thesis:

YIN, H. B., JI, B. Z., DOBSON, P. S., MOSBAHI, K., GLIDLE, A., GADEGAARD, N., FREER, A., COOPER, J. M. CUSACK, M. 2009. Screening of Biomineralization Using Microfluidics. *Analytical Chemistry,* 81**,** 473-478.

JI, B., CUSACK, M., FREER, A., DOBSON, P., GADEGAARD, N., YIN, H. 2010, Control of Crystal Polymorph in Microfluidics Using Molluscan 28kDa Ca^{2+}-binding Protein. *Integrative Biology*, 2, 528-535